



TECHNISCHE
UNIVERSITÄT
WIEN

DISSERTATION

Der Ligand bestimmt den Cluster: Einfluss und Möglichkeiten zur Modifizierung der Liganden an Goldnanoclustern

ausgeführt am

Institut für Materialchemie
der Technischen Universität Wien

unter der Anleitung von

Prof. Dr. Günther Rupprechter
Dr. Noelia Barrabés Rabanal

durch

Vera Truttmann



Wien, Februar 2022



TECHNISCHE
UNIVERSITÄT
WIEN

DOCTORAL THESIS

The Ligand Shapes the Cluster: Influences and Modification Possibilities of Protecting Ligands on Gold Nanoclusters

carried out at the

Institute of Materials Chemistry
of TU Wien

under the supervision of

Prof. Dr. Günther Rupprechter
Dr. Noelia Barrabés Rabanal

by

Vera Truttmann
Am grünen Prater 10/27
1020 Wien

EIDESSTATTLICHE ERKLÄRUNG: Ich erkläre hiermit an Eides statt, dass ich die vorliegende Arbeit selbstständig verfasst, andere als die angegebenen Quellen/Hilfsmittel nicht benutzt, und die den benutzten Quellen wörtlich und inhaltlich entnommenen Stellen als solche kenntlich gemacht habe.

STATUTORY DECLARATION: I hereby declare that I have authored this thesis independently, that I have not used other than the declared sources/resources, and that I have explicitly marked all material which has been quoted either literally or by content from the used sources.

Es ist nicht alles Gold, was glänzt.

Aber, es glänzt auch nicht alles, was Gold ist, sollte man billig hinzusetzen.

Tagebücher von Christian Friedrich Hebbel (1813–1863),
deutscher Lyriker und Dramatiker

All that glitters is not gold.

But, not all glitters that is gold, one should add appreciatively.

(inofficial translation)

Diaries of Christian Friedrich Hebbel (1813–1863),
German poet and dramatist

Kurzfassung

Durch Liganden geschützte Goldnanocluster zeigen bemerkenswerte katalytische Aktivität, sowie elektronische, geometrische und chirale Eigenschaften, die sich stark von jenen des unreaktiven Goldes in metallischer Form unterscheiden und dadurch für eine Vielzahl von Anwendungen attraktiv sind. Zudem können solche Cluster auch monodispers hergestellt werden, was es ermöglicht, Struktur–Wirkungsbeziehungen zu untersuchen. Einer der bedeutendsten Einflussfaktoren auf beispielsweise die Größe und Form, aber auch die Stabilität und Reaktivität oder Chiralität von Goldnanoclustern entsteht durch die Liganden. Bereits eine kleine Veränderung im organischen Rest kann die Clustereigenschaften nachhaltig verändern. Ein wichtiges Ziel der Goldnanoclusterchemie ist es daher, diese von den Liganden hervorgerufenen Änderungen zu verstehen und gezielt einsetzen zu können. Im Rahmen dieser Arbeit werden drei Bereiche, in denen Clusterliganden eine wichtige Rolle spielen, näher untersucht, und zwar (1) Chiralität, (2) Synthesestrategien für Goldnanocluster und (3) heterogene Katalyse.

Einige Goldnanocluster zeigen intrinsisch chirale Eigenschaften, die durch chirale Au–Liganden Schnittstellen und/oder durch chirale Kernstrukturen hervorgerufen werden. Es ist jedoch oftmals ein kompliziertes Unterfangen, die Cluster als reine Enantiomere zu erhalten, da es den Einsatz speziell angepasster Separationstechniken erfordert. Daher wurde eine direkte Synthesestrategie mit einem chiralen Thiolliganden eingesetzt und zwei verschiedene intrinsisch chirale Nanocluster, nämlich Au₃₈ und Au₁₄₄, in ungewöhnlich hoher Ausbeute erhalten, wohingegen kein Anstieg in der Menge des erhaltenen achiralen Au₂₅ Clusters beobachtet werden konnte. Ein Vergleich der gemessenen Circular Dichroism Spektren mit publizierten Spektren einzelner Enantiomere von Au₃₈ und Au₁₄₄ deutete darauf hin, dass enantiomerenreine Clusterproben erhalten wurden. Das zeigt, dass Direktsynthese mit chiralen Liganden ein sehr wirksames Mittel ist, um gezielt chirale Goldnanocluster in hoher Ausbeute zu erhalten.

Zudem wurden auch Dichtefunktionalrechnungen der Au₂₅ und Au₃₈ Cluster durchgeführt, mit dem Ziel, geeignete Modellstrukturen für die weitere Untersuchung ihrer chiralen Eigenschaften zu erhalten.

Zielgerichtetes Clusterdesign lässt sich aber beispielsweise auch durch sogenannte Ligandenaustausch-induzierte Größe/Struktur Transformationen bewerkstelligen. Dabei wird ein Ausgangscluster einer großen Menge an Thiolatliganden ausgesetzt und dadurch selektiv in einen anderen Cluster von unterschiedlicher Größe und/oder Geometrie überführt.

Führt man einen solchen Austauschprozess als Zweiphasenreaktion (Wasser und organisches Lösungsmittel) mit dem wasserlöslichen $\text{Au}_{25}(\text{SG})_{13}$ als Edukt durch, erfolgt ein Phasentransfer und die Bildung von $\text{Au}_{16}(2\text{-PET})_{14}$. Infrarotspektroskopie zeigte, dass die Liganden komplett ausgetauscht wurden, wohingegen Röntgenabsorptionsspektroskopie auf ähnliche Kerngeometrien der beiden Cluster hinwies. Bei $\text{Au}_{16}(2\text{-PET})_{14}$ handelt es sich um einen der kleinsten Thiolat-geschützten Goldnanocluster, die bisher in entsprechender Reinheit isoliert werden konnten. Das macht es zu einer interessanten Verbindung, um die strukturelle Evolution dieser Cluster zu untersuchen.

Zuletzt wurden auch Ligandeneffekte in der Katalyse untersucht. Hierfür wurde eine CO Oxidations-Modellreaktion mit Goldnanoclustern, die mit unterschiedlichen Arten von Liganden (Phosphine, Thiolate bzw. eine Mischung der beiden) in ihrer Struktur aufweisen, untersucht. Die geringere Umsetzung von CO mit den Clustern, die Phosphine in ihrer Ligandenschale aufweisen, im Vergleich zum Thiolat-geschützten Clusterkatalysator nach oxidativer Vorbehandlung bei 250 °C wurde auf die Ansammlung von Ligandenüberresten im Bereich der Schnittstelle zwischen Cluster und Trägermaterial zurückgeführt. Diese Positionen sind bei der CO Oxidation von großer Bedeutung. Im Gegensatz dazu konnte keine Abhängigkeit von der Verfügbarkeit freier Goldoberfläche oder der Clustergröße nachgewiesen werden. Das zeigt, dass die Liganden die Reaktivität von Clusterkatalysatoren beeinflussen, auch wenn sie bereits durch Vorbehandlung zersetzt wurden und muss daher beim Design des Katalysatorsystems berücksichtigt werden.

Abstract

Monolayer-protected gold nanoclusters show interesting catalytic activity, as well as electronic, geometric and chiral properties that are very different from inert bulk gold and therefore of interest for a number of applications. Furthermore, such clusters can be obtained as monodisperse samples, which allows to investigate structure–property relationships. One of the most important factors that influence for example the size and shape, but also the stability, reactivity or chirality in Au nanoclusters are the protecting ligands, for which already a subtle change in the hydrocarbon framework can result in significantly different properties of the cluster species. Understanding and selectively tuning the metal nanoclusters by ligand engineering has thus become an important objective in nanocluster chemistry. Within this thesis, three fields in which protecting ligands play a major role are investigated, namely (1) chirality, (2) synthesis strategies for Au nanoclusters and (3) heterogeneous catalysis.

Several species of gold nanoclusters exhibit intrinsic chiral properties, which can be due to chiral Au–ligand interfaces or chiral metal kernels. However, obtaining them as single enantiomers can be a daunting task since it requires specifically tailored separation techniques. Therefore, a direct synthesis approach with a chiral thiol ligand was employed to obtain two intrinsically chiral nanoclusters, Au₃₈ and Au₁₄₄, for which unusually high yields were achieved, whereas only moderate yields of an achiral Au₂₅ cluster were obtained. Comparison of the circular dichroism spectra to reported single enantiomer Au₃₈ and Au₁₄₄ spectra indicated that enantiopure samples had been obtained. These results demonstrate that synthesis with chiral ligands is a powerful tool to selectively afford chiral gold nanoclusters in high yield.

Furthermore, complementary density functional theory calculations of Au₂₅ and Au₃₈ were carried out to obtain suitable model structures for future investigation of their chiral properties.

Another approach for targeted cluster design are ligand exchange induced size/structure transformations, in which a precursor gold cluster is subjected to large amounts of thiolate ligands and thereby selectively converted to a new cluster species of different size and/or geometry. Applying such a two-phase LEIST process on the water-soluble Au₂₅(SG)₁₃ resulted in phase-transfer and formation of Au₁₆(2-PET)₁₄. Infrared spectroscopy confirmed complete replacement of the protecting ligands, whereas X-ray absorption spectroscopy indicated similar core structures of both clusters. Of note, Au₁₆(2-PET)₁₄ is among the

smallest thiolate-protected Au nanoclusters that have been isolated in significant purity, which makes it an interesting compound for studying structural evolution of gold nanoclusters.

Finally, also ligand effects in catalysis were investigated by studying CO oxidation as model reaction with Au nanoclusters protected by different types of ligands (phosphines, thiolates, mix of phosphines and thiolates). The lower conversion achieved by clusters with phosphines in the ligand shell compared to the thiolate-protected cluster after oxidative pretreatment at 250 °C was attributed to the accumulation of ligand residues at the cluster–support interface region. These sites are of great importance for the subsequent reaction. In contrast, no significant dependence on the availability of exposed Au surface or the cluster size was observed. This shows that the ligands influence the reactivity of cluster catalysts even after their decomposition, which must therefore be taken into account in the design of a catalytic system.

Acknowledgments

I want to thank my supervisor Prof. Günther Rupprechter for allowing me to conduct my PhD research in his research group. I am grateful for the valuable feedback on manuscripts and presentations, as well as the financial support I received to attend conferences/workshops and synchrotron measurements. I also want to thank my co-supervisor, Dr. Noelia Barrabés Rabanal, for all the input and scientific discussions, as well as for the support I received all along the way.

In addition, I am very grateful for having been able to work alongside my colleagues and friends Dr. Stephan Pollitt and Dr. Clara García. We had a great time in the lab, on beamtime nightshifts or at conferences. I would not have wanted to encounter this PhD journey without you!

I also want to thank the hard-working students at ClusCAT, who synthesized and studied gold nanoclusters with me: Rares Banu, Yukari Imai, Adea Loxha and Julia Rafetzeder. All of you contributed to deepen our understanding of these systems.

Furthermore, I want to acknowledge several people who have contributed to the work presented in this thesis: Hedda Drexler is acknowledged for conducting the ESI-MS measurements of our nanoclusters and Dr. Ernst Pittenauer for MALDI-MS. A big thank you also to Dr. Michael Stöger-Pollach (USTEM, TU Wien) for spending hours looking for our tiny gold particles in (S)TEM. Thank you to Pablo Ayala and Dr. Peter Kregsamer (ATI, TU Wien) for measuring XRF of our supported nanoclusters and to Sreejith P. Nandan for measuring fluorescence spectroscopy with me. The Negishi group (Tokyo University of Science) is acknowledged for their contribution to the CO oxidation project. Furthermore, I am grateful to the staff of ALBA synchrotron for the assistance during beamtimes.

Financial support through the doctoral school Solids4Fun (Building Solids for Function) of TU Wien is acknowledged. Participation in conferences was partially supported by a grant from the 'Funds for PhD students participating in conferences' (TU Wien) and by a FemChem travel grant (TU Wien).

Moreover, I acknowledge financial support by the Austrian Marshall Plan Foundation through a Marshall Plan Scholarship, which allowed me to perform DFT computations of my nanocluster systems during a three-month stay at Kansas State University (USA). I am very

grateful to Prof. Christine Aikens for all her support before and during my stay and all the help I received to get my calculations to run. A big thanks also to my fellow KSU colleagues, Shana Havenridge, Zhen Liu and Yuchen Wang. You were all so welcoming and helpful and made this research stay a really great experience for me (even with an ongoing pandemic)!

Thank you also to all my colleagues at TU Wien – for being great office partners, for watering my office plants, providing a regular stock of chocolate, all the social activities, all the relaxing coffee breaks and our regular board/card game rounds. I can truly say I had a great time working at the Institute of Materials Chemistry thanks to all of you!

Big thanks also go to my family: to Christian, for his support and patience when I came home late (again) because the experiments took three times as long as I thought; and to my parents, who always motivated me to pursue the studies and career I wanted.

Last but not least, I want to thank my chemistry teacher in High School, Wolfgang Liebhart, who first awakened my interest in chemistry and motivated me to study at TU Wien.

Contents

Contents	vii
1. Introduction	1
1.1. Structure and Electronic Properties of Au Nanoclusters	2
1.1.1. The Superatom Concept	2
1.1.2. Consequences of the Molecule-like Nature of Au Nanoclusters	4
1.2. Synthesis and Characterization	5
1.2.1. The Brust Synthesis Protocol	5
1.2.2. Separation Techniques for Au Nanoclusters	6
1.2.3. Characterization of Au Nanoclusters	6
1.3. Modification Possibilities	7
1.4. Protecting Ligands of Au Nanoclusters	9
1.4.1. Ligand Exchange and Ligand Exchange Induced Size/Structure Transformations (LEIST)	10
1.5. Chirality in Au Nanoclusters	12
1.5.1. Strategies Toward Chiral Au Nanoclusters	15
1.6. Au Nanoclusters in Heterogeneous Catalysis: Advantages and Influences	16
1.6.1. Nanocluster Size and Structure Effect	17
1.6.2. Doping	18
1.6.3. Support Material	18
1.6.4. Effect of the Protecting Ligands	19
1.6.5. Pretreatment Procedures and Fate of the Ligands	20
1.7. References	22
2. Motivation and Objectives	38
3. Inducing Chiral Properties to Au Nanoclusters by a Chiral Thiol Ligand	41
3.1. Chirality driven synthesis of intrinsically chiral cluster structures in high yield	42
3.1.1. Abstract	42
3.1.2. Introduction	42
3.1.3. Results	44
3.1.3.1. Chiral Nanocluster synthesis with 2-MeBuSH	44
3.1.3.2. Chiroptical properties	46
3.1.3.3. Temperature stability of the chiral clusters	48

3.1.3.4.	Discussion	49
3.1.3.5.	Methods	50
3.1.3.6.	Acknowledgements	50
3.1.3.7.	Author contributions	51
3.1.4.	Supplementary Information	52
3.1.4.1.	Synthetic Procedures	52
3.1.4.2.	NMR Spectra of the 2-MeBuSH Ligand	55
3.1.4.3.	Matrix-assisted Laser Desorption/Ionization (MALDI-MS) Spectra of the Au Nanoclusters	56
3.1.4.4.	Additional Circular Dichroism (CD) Spectra	58
3.1.4.5.	HPLC Separation of Au ₃₈ Nanoclusters	59
3.2.	Density Functional Theory Calculations of Au ₃₈ (2-MeBuS) ₂₄ and [Au ₂₅ (2-MeBuS) ₁₈] ⁻	60
3.2.1.	Au ₃₈ (2-MeBuS) ₂₄	60
3.2.1.1.	Comparison of the Crystal Structure and the JACS2010-based Structures of Au ₃₈ (2-MeBuS) ₂₄	60
3.2.1.2.	Comparison of the Different Staple Arrangements of Au ₃₈ (2-MeBuS) ₂₄	62
3.2.2.	[Au ₂₅ (2-MeBuS) ₁₈] ⁻	65
3.2.3.	Conclusions	66
3.2.4.	Computational Details	66
3.2.5.	Acknowledgments	67
3.2.6.	Supplementary Information	68
3.3.	References	73
4.	Selective Ligand Exchange Synthesis of Au₁₆(2-PET)₁₄ from Au₁₅(SG)₁₃	79
4.1.	Abstract	80
4.2.	Communication	80
4.3.	Acknowledgments	88
4.4.	Author Contributions	89
4.5.	Supplementary Information	90
4.5.1.	Materials and Methods	90
4.5.1.1.	Synthetic Procedures	90
4.5.1.2.	Characterization	92
4.5.2.	Additional UV-Vis Spectra of the Ligand Exchange Reactions	94
4.5.3.	Mass Spectra of the Au Nanoclusters	96
4.5.4.	Additional Photoluminescence Spectra	98
4.6.	References	99

5. Ligand Effect on the CO Oxidation Activity of CeO₂ Supported Gold Nanocluster Catalysts	103
5.1. Abstract	104
5.2. Introduction	104
5.3. Results and Discussion	107
5.3.1. Effect of the Pretreatment Temperature	107
5.3.2. Modifications by Oxidative Pretreatment	109
5.3.3. <i>Operando</i> Infrared Studies of CO Oxidation	114
5.3.4. Electron Microscopy of Used Catalysts	117
5.4. Materials and Methods	118
5.4.1. Catalyst Preparation	118
5.4.2. Catalytic CO Oxidation Experiments	118
5.4.3. <i>In situ/Operando</i> Transmission Infrared Studies	119
5.4.4. Transmission Electron Microscopy (TEM) and High-angle Annular Dark-field Scanning Transmission Electron Microscopy (HAADF-STEM)	119
5.4.5. Molecular Graphic Images	120
5.5. Conclusions	120
5.6. Author Contributions	120
5.7. Acknowledgments	121
5.8. Supplementary Information	122
5.8.1. Synthesis and Characterization of Au Nanoclusters	122
5.8.1.1. Au ₁₁ (PPh ₃) ₇ Cl ₃	123
5.8.1.2. [Au ₂₅ (PPh ₃) ₁₀ (SC ₂ H ₄ Ph) ₅ Cl ₂]Cl ₂	123
5.8.1.3. [Au ₂₅ (SC ₂ H ₄ Ph) ₁₈] ⁻ TOA ⁺	124
5.8.2. Preparation of Ceria Supported Au Nanocluster Catalysts	125
5.8.3. Thermogravimetric Analysis/Differential Scanning Calorimetry	125
5.8.4. Additional Kinetic Measurements	128
5.8.5. Additional Temperature Programmed Oxidation Spectra	129
5.8.6. Additional Spectra of <i>In Situ</i> Transmission Infrared Measurements	130
5.8.6.1. Catalytic CO Conversion	130
5.8.6.2. Additional Infrared Spectra of the Oxidative Pretreatment	131
5.8.6.3. Additional Spectra of the CO Oxidation	133
5.8.6.4. Infrared Spectra of Post-Reaction CO Adsorption	135
5.8.6.5. Additional Infrared Spectra at Different Steps of the Reaction	135
5.8.7. Additional High-angle Annular Dark-field Scanning Transmission Elec- tron Microscopy	137
5.9. References	138
6. Conclusions and Outlook	145
A. Further Publications During PhD Studies	148

B. Information on Images in Introduction and Chapter Title Pages	151
B.1. References	152
C. Coordinates of the Calculated Structures	154
List of Figures	169
List of Tables	178

Abbreviations

ADF Amsterdam Density Functional

S-Adm adamantanethiol

ATR-FTIR attenuated total reflection-Fourier transform infrared

bcc body-centered cubic

BINAP 2,2'-bis(diphenylphosphino)-1,1'-binaphthyl

BINAS 1,1'-binaphthyl-2,2'-dithiol

BP86 Becke Perdew exchange-correlation functional

HS-Bu butanethiol

S-But butanethiolate

CD circular dichroism

CID collision-induced dissociation

CPL circular polarized luminescence

Da Dalton

DFT density functional theory

DCM dichloromethane

DCTB *trans*-2-[3-(4-*tert*-butylphenyl)-2-methyl-2-propenylidene]malononitrile

DSC differential scanning calorimetry

DZP double zeta polarized basis set

ESI electrospray ionization

EtOAc ethylacetate

EXAFS extended X-ray absorption fine-structure

fcc face-centered cubic

- FIR** far-infrared
- FTIR** Fourier-transform infrared
- FWHM** full width half-maximum
- GGA** generalized gradient approximation
- GSH** L-glutathione
- GUM** grand unified model
- HAADF-STEM** high-angle annular dark-field scanning transmission electron microscopy
- HPLC** high-performance liquid chromatography
- HOMO** highest occupied molecular orbital
- IR** infrared
- LEIST** ligand-exchange-induced size/structure transformation
- LUMO** lowest unoccupied molecular orbital
- MALDI** matrix-assisted laser desorption/ionization
- m*-MBT** *meta*-methylbenzenethiol
- 2-MeBuS** (*S*)-2-methylbutanethiolate
- 2-MeBuSH** (*S*)-2-methylbutanethiol
- MeOH** methanol
- MIR** mid-infrared
- MS** mass spectrometry
- NHC** N-heterocyclic carbene
- NMR** nuclear magnetic resonance
- PAGE** polyacrylamide gel electrophoresis
- p*-BBT** *para*-bromobenzene thiol
- 2-PET** 2-phenylethanethiol
- PIC** particle-in-a-cylinder
- PL** photoluminescence

- p-MBA** *para*-mercaptobenzoic acid
- PP₃** *tris*(2-(diphenylphosphino)ethyl)phosphine
- PPT** 2-phenylpropanethiol
- RT** room temperature
- SEC** size exclusion chromatography
- SR** thiolate
- TBAB** borane *tert*-butylamine
- TBAC** tetrabutylammonium chloride
- TBBT** 4-*tert*-butylbenzenethiol
- TD-DFT** time dependent-density functional theory
- TD-DFT+TB** time dependent-density functional theory plus tight binding
- TEM** transmission electron microscopy
- THF** tetrahydrofuran
- TLC** thin-layer chromatography
- TMS** trimethylsilane
- TGA** thermogravimetric analysis
- TOAB** tetraoctylammonium bromide
- TOFMS** time of flight mass spectrometry
- TPO** temperature programmed oxidation
- TXRF** total X-ray fluorescence spectroscopy
- UV-Vis** Ultraviolet-visible
- VCD** vibrational circular dichroism
- X** halide
- XANES** X-ray absorption near edge structure
- XAS** x-ray absorption spectroscopy
- ZORA** zeroth-order regular approximation

1. Introduction

Ligand-protected metal nanoclusters can be considered as intermediate structures between molecules and nanoparticles/bulk,^[1,2] comprising both of their properties. In contrast to nanoparticles, which usually show a distribution of different sizes within a sample and diameters of several (tens of) nanometers,^[1,3] nanoclusters can be obtained as monodisperse structures of less than ~300 metal atoms or ~2 nm.^[4,5] Moreover, their electronic properties also differ significantly from those observed for nanoparticles and bulk metals. Instead of a quasicontinuous conduction band, the clusters show discrete energy levels and transitions, i.e. electronic structures which can be compared to those of molecules (see Figure 1.1).^[1,5,6] Au nanoclusters also show more diverse geometries than the typical face-centered cubic (fcc) structures of metallic gold (particles).^[1,4,6,7] Thus, significant interest has been sparked in their research and development.

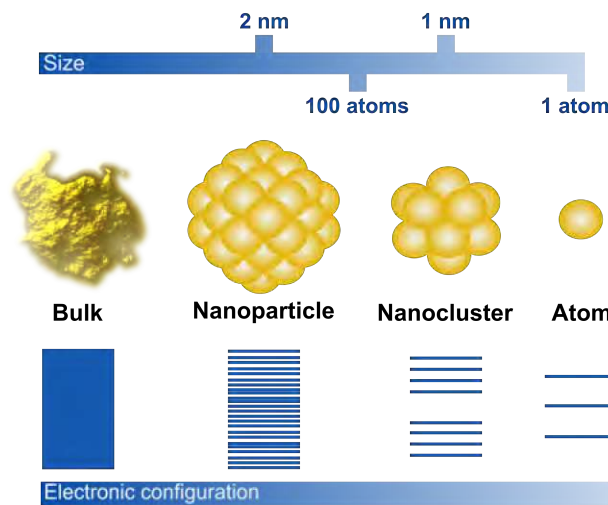


Figure 1.1.: Transition from bulk metal to a single atom and consequences for the electronic structure.

The earliest report of a Au nanocluster synthesis and characterization dates back to the 1960s^[8] and since then, significant progress has been made.^[2-4,7,9-14] Nowadays, numerous clusters can be selectively synthesized,^[2,4,7,9,15] have been crystallized,^[2,4,7,9] and/or applied for example in catalysis,^[3,4,7,10-13] photoluminescence^[13,16] or in biological areas.^[4,9,10,12,13] Within this chapter, the research on Au nanoclusters in the last decades will be briefly summarized, with special emphasis on the relevant aspects for the presented research in

Chapters 3, 4 and 5, namely chirality (Section 1.5), the ligands of Au nanoclusters (Section 1.4), and their use in heterogeneous catalysis (Section 1.6).

1.1. Structure and Electronic Properties of Au Nanoclusters

In general, the composition of Au nanoclusters follows the same principle, schematically depicted in Figure 1.2.^a Only the two most important classes of Au nanoclusters, namely phosphine-^[17,18] and thiolate-protected Au nanoclusters^[17] are presented, however, other ligands generally follow one of the schemes (see Section 1.4).

In both cases, the central element of the cluster is a Au_n kernel. Compared to small Au(I)-complexes, the essentially neutral Au atoms in the cluster core are able to form significant Au–Au bonding interactions.^[1] For phosphine-protected clusters (Figure 1.2a), each Au atom located on the core surface then usually binds to one phosphine or halide ligand. Instead of halides, also for example nitrates or SbF_6^- can be present.^[17,18] Thiolate-protected clusters, on the other hand (Figure 1.2b), show $-\text{S}(-\text{Au-S})_x-$ protecting motifs,^[1,17,19–21] which through binding to the Au core atoms form so-called ‘staples’.^[21] This concept was first proposed by Häkkinen and coworkers in 2006^[22] and provided an explanation to the different sizes and compositions observed for phosphine- and thiolate-protected Au nanoclusters. It was experimentally confirmed by the first crystal structure of a *para*-mercaptobenzoic acid (*p*-MBA)-protected $\text{Au}_{102}(\text{p-MBA})_{44}$ nanocluster shortly afterwards.^[21]

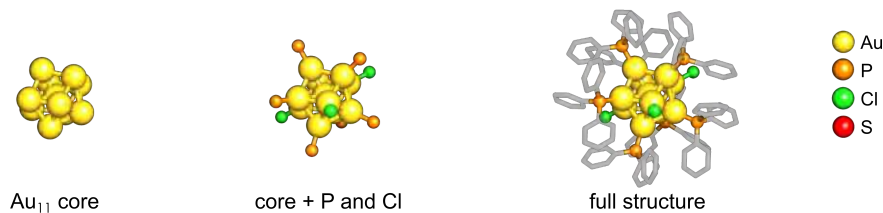
Even though early work on gold nanoclusters originally focused on phosphines as protecting ligands,^[8,17,18] in the last three decades, thiolates have emerged as the majorly employed ligands.^[1,4,10,12,13] The bond between Au and S is considerably stronger than the Au–P bond, which, in combination with the ability to form the above described staple units, ultimately results in much higher stability of thiolate-protected Au nanoclusters.^[22]

1.1.1. The Superatom Concept

The electronic structure of gold nanoclusters is often described by the superatom model.^[14,19,20] One can think of it as the gold atoms in a cluster delocalizing electrons across a positively charged spherical unit of space. This results in the formation of so-called superatomic orbitals and is able to explain both structural as well as electronic properties of metal nanoclusters. For example, pronounced highest occupied molecular orbital (HOMO)–lowest unoccupied molecular orbital (LUMO) gaps are formed and incorporation of other metal atoms results in significant alterations of the electronic structure. Notably, this concept also provides a universal approach towards prediction of stable structures independent of the nature of its ligands. The basis of the stability of a certain superatom is related to shell closing, which would give a series of magic numbers (Equation 1.1):

^aDetails on the molecular graphics presented in the Introduction can be found in the Appendix (Chapter B.)

(a) Phosphine-protected Au nanoclusters: $\text{Au}_{11}(\text{PPh}_3)_7\text{Cl}_3$



(b) Thiolate-protected Au nanoclusters: $\text{Au}_{25}(\text{SC}_2\text{H}_4\text{Ph})_{18}$

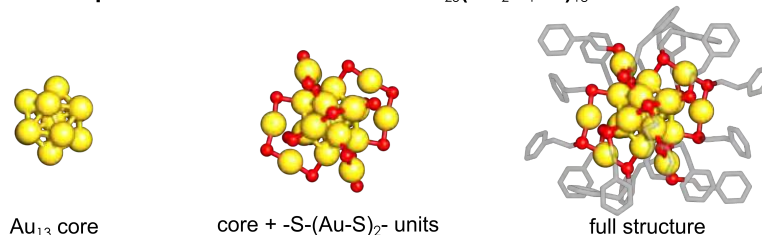


Figure 1.2.: Simplified representation of Au nanocluster structures: (a) $\text{Au}_{11}(\text{PPh}_3)_7\text{Cl}_3$ as an example for phosphine-protected Au nanoclusters and (b) $\text{Au}_{25}(\text{SC}_2\text{H}_4\text{Ph})_{18}$ as an example for thiolate-protected Au nanoclusters.

$$n^* = 2, 8, 18, 20, 34, 58, \dots \quad (1.1)$$

For Au nanoclusters, Equation 1.2 has been developed.^[19,20] Within it, each Au atom in a gold cluster (N Au atoms in total) bearing charge z contributes one electron, thus its effective valence $\nu_A = 1$. Anionic, electronegative substituents (total number M) such as thiolates or halides localize one electron each, whereas the neutral phosphines only interact weakly and are thus not to be considered in Equation 1.2.^[14,19,20] They are, however, necessary for complete passivation of the core.^[19,20]

$$n^* = N \cdot \nu_A - M - z \quad (1.2)$$

The superatom concept for example predicts the high stability of $\text{Au}_{11}(\text{PPh}_3)\text{X}_3$ (X = halide) and $[\text{Au}_{25}(\text{SR})_{18}]^-$ (SR = thiolate), which can both be considered as 8-electron systems (see Figure 1.3).^[19,20] In addition, it can also be used for clusters such as $[\text{Au}_{25}(\text{PPh}_3)_{10}(\text{SR})_5\text{X}_2]_2^+$, which is composed of structure of two vertex-fused Au_{13} icosahedra (structure depicted in Figure 1.3).^[23] Applying Equation 1.2 for it returns $n^* = 16$, i.e. a composition of two 8-electron superatoms.^[20]

Nevertheless, while the superatom concept can be used to explain the stability of several prominent cluster species, also a number of exceptions exist. Some notable examples are the neutral form of $\text{Au}_{25}(\text{SR})_{18}$,^[24] as well as $\text{Au}_{38}(\text{SR})_{24}$ (structure shown in 1.3).^[25,26] or

$\text{Au}_{144}(\text{SR})_{60}$ ^[27] It should thus only be considered as a guidance, rather than a strict rule, also considering that it has been developed for spherical particles.^[1,25]

Besides the superatom concept, other models have also been used to explain the stability and properties of gold nanoclusters, e.g. the grand unified model (GUM) model relying mainly on triangle and tetrahedron building blocks,^[28] the super valence bond model^[26] or the particle-in-a-cylinder (PIC) model for elongated, non-spherical systems.^[25]

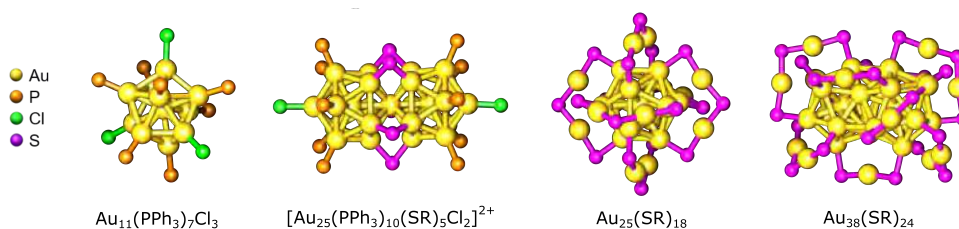


Figure 1.3.: Structures of selected Au nanoclusters. The organic ligand framework is omitted for clarity.

1.1.2. Consequences of the Molecule-like Nature of Au Nanoclusters

The molecule-like nature of metal nanoclusters results in a significant size-dependence^b of their properties.^[5] A difference of only a few atoms can drastically alter the electronic structure and is often reflected in pronounced changes in the optical absorption spectra.^[18,30,31] Moreover, in describing the electronic and geometric structures, as well as their magnetism, phenomena such as Jahn-Teller effect need to be taken into consideration. $\text{Au}_{25}(\text{SR})_{18}$, for example, which exists in charge states -1, 0 and +1, has been shown to exhibit significant levels of structural distortion in the neutral and positive form, which is also reflected by differences in the Ultraviolet-visible (UV-Vis) absorption spectra.^[24]

Another aspect would be the broad library of geometric structures that can be observed. Typical cluster kernel geometries feature e.g. icosahedral, decahedral, fcc or body-centered cubic (bcc) structures. In addition, some cluster structures are best described by combining several building blocks.^[4,32] One example would be the $\text{Au}_{38}(\text{SR})_{24}$ structure (see Figure 1.3), which Au_{23} core can be seen as a composite structure of two face-sharing Au_{13} icosahedra.^[4,33] As mentioned above, also the structure of $[\text{Au}_{25}(\text{PPh}_3)_{10}(\text{SR})_5\text{X}_2]_2^+$ (Figure 1.3) can be understood as a fusion of two icosahedra.^[23,32] Further examples include building cluster structures from Au_4 tetrahedra units^[4,32] or a shell-by-shell growth pattern, which can often be applied for several larger clusters with more than 100 Au atoms.^[4]

The number of Au nanocluster structures that have been discovered is still increasing nowadays. Within the last years, studies dedicated to understanding gold nanocluster growth

^bOf note, in metal nanocluster literature, the term *size* is sometimes used interchangeably with the number of metal atoms in a cluster (e.g.^[29]).

patterns have gained importance, aiming toward a more systematic approach in structure prediction and experimental studies.^[4,14,28,32,34–39]

1.2. Synthesis and Characterization

1.2.1. The Brust Synthesis Protocol

The synthesis for Au nanoclusters often follows procedures adapted from a protocol first published by Brust *et al.*^[40] In a typical Brust-type synthesis of thiolate-protected Au nanoclusters, first a gold precursor in form of a salt is dissolved in water and transferred to the organic phase, aided by a phase transfer catalyst. In some cases, it is also directly dissolved in polar organic solvents such as tetrahydrofuran (THF) or methanol (MeOH).^[9] Addition of the thiol ligand results in a first reduction and formation of Au(I) intermediate species. Their exact nature has been heavily debated in the community,^[9] with possible components being small Au(I) complexes^[41,42] or Au(I)-thiolate polymers.^[4,43] Note that for phosphine-protected nanoclusters, the synthesis procedures often start from Au(I)-phosphine compounds instead of Au(III) salts.^[18]

The Au nanoclusters are then formed by reduction, often initiated by addition of NaBH_4 ,^[9] though processes employing CO ,^[44,45] borane *tert*-butylamine (TBAB)^[46] or $\text{NaOH}/\text{NaBH}_4$ ^[47] mixtures in this step are also known. The nanoclusters formed in this step are initially polydisperse, but convert toward the most stable size(s) at the present conditions. This has become known as *size-focusing* and is a useful tool for obtaining highly monodisperse cluster samples.^[43] The whole synthesis process is also schematically depicted in Figure 1.4.

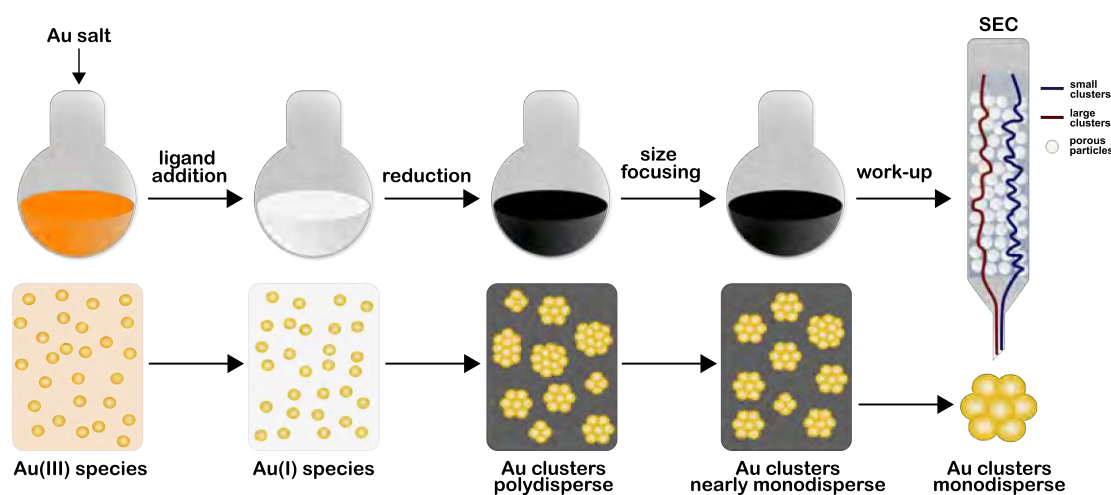


Figure 1.4.: Synthesis scheme of a classical Brust procedure followed by size-exclusion chromatography (SEC) and corresponding Au species present in each step. Note that the ligands are omitted in the illustration of the Au species for clarity.

Several parameters are known to influence the product (distribution) after synthesis, for example the solvent,^[43,48] the pH-value,^[44,46] the reaction temperature^[43,48,49] or the nature of the reducing agent,^[44–47] to name just a few. By fine-tuning and controlling them, a variety of different Au nanoclusters could already be obtained by direct synthesis.^[4]

1.2.2. Separation Techniques for Au Nanoclusters

The Au nanocluster samples obtained after synthesis are often already very pure, i.e., mainly a single size is present. If necessary, separation or washing steps can be performed to obtain a truly monodisperse product.^[50] One technique applied in Au nanocluster preparation is size exclusion chromatography (SEC), the principle of which is also depicted in Figure 1.4. It was first established in a preparative scale by Knoppe *et al.* in 2011^[51] and has been found to achieve good separation of Au nanoclusters even if the species are of very similar size (*cf.* Au₃₈ and Au₄₀). In addition, also chromatographic separation by thin-layer chromatography (TLC) can be employed.^[50,52] For water-soluble clusters, preparative polyacrylamide gel electrophoresis (PAGE) has been established,^[50] which has, for example, been successfully employed for the separation of several L-glutathione (GSH)-protected Au_n clusters of similar size ($n = 10-12, 15, 18, 22, 25, 29, 33, 39$).^[30,31]

For more complex scenarios, high-performance liquid chromatography (HPLC) can be useful.^[50,53] This includes, for example, the separation of mixtures of doped nanoclusters which only differ in the number and/or positions of substituted Au atoms^[50,53–55] or of product clusters after (incomplete) ligand exchange (i.e. same size but different ligand environment).^[50,53,56] In addition, chiral HPLC can be applied for the separation of enantiomeric pairs of Au nanoclusters (see Section 1.5).^[50,57,58]

1.2.3. Characterization of Au Nanoclusters

In order to fully understand the structure and properties of Au nanoclusters, usually several characterization techniques have to be employed, some of which – and the information one can gain for them – are summarized in 1.5.

One especially useful tool for characterization of gold nanoclusters is UV-Vis spectroscopy. Due their quantized electronic structure (see Section 1.1), the clusters exhibit several defined bands in their optical spectra, contrary to Au nanoparticles which show only a broad plasmonic band. For Au nanoclusters, these bands are related to discrete electronic transitions.^[5,9,59] As discussed before, they are, for example, depending on the number of metal atoms in a cluster^[18,30,31], but are also influenced by more subtle changes such as in the oxidation state^[24] or the ligand environment.^[60] Because of this, the optical spectra are often considered as a kind of ‘fingerprint’ for a respective cluster structure. Because of that, combined with the simplicity of the experimental method, UV-Vis spectroscopy has become an important tool in nanocluster characterization.

While the optical spectrum can be useful for assessment of the nature of a known cluster structure, identification of new species requires further investigation. In order to experi-

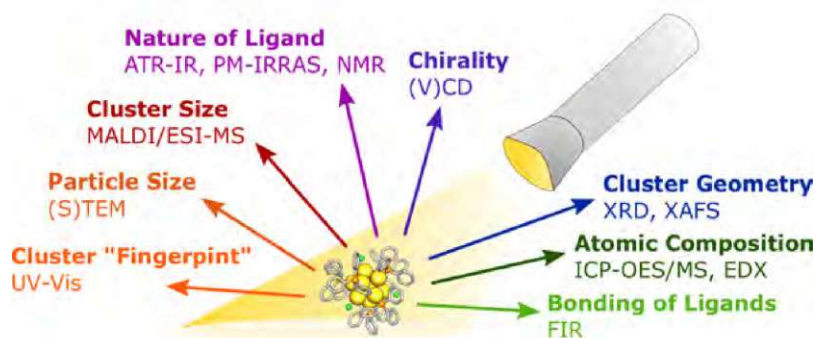


Figure 1.5.: Summary of characterization methods for Au nanoclusters and the provided information.

mentally elucidate the geometric structure, usually single crystal X-ray crystallography is necessary.^[4,9] However, obtaining such crystals in the required quality can be a considerable obstacle with Au nanoclusters, owing to their often limited stability in solution.^[9] Nevertheless, even if the full structure cannot be resolved, it is often possible to determine the composition of the cluster. This is generally performed by mass spectrometry (MS), predominantly using either electrospray ionization (ESI)^[9,61,62] or matrix-assisted laser desorption/ionization (MALDI) techniques.^[9,62,63] ESI-MS offers the advantage of being an especially soft ionization procedure, which can also be applied for less stable compounds, such as phosphine-protected nanoclusters.^[62] However, for bigger nanoclusters with masses of several 10k Da (Da = Dalton), usually MALDI-MS is used.^[62] Thereby, choice of a suitable matrix compound is crucial to observe intact cluster ions during spectrometry. In that regard, Dass *et al.* reported that the fragmentation could be significantly reduced by using *trans*-2-[3-(4-*tert*-butylphenyl)-2-methyl-2-propenylidene]malononitrile (DCTB) as matrix for the mass spectrometric characterization of Au₂₅ nanoclusters.^[63] Besides identification of reaction products and confirming their purity, MS has also been used to study the evolution of cluster structures during synthesis or ligand exchange procedures, contributing to the understanding of reaction mechanisms in nanocluster chemistry.^[61–63]

1.3. Modification Possibilities

One of the great advantages Au nanoclusters offer is that several different pathways exist to modify their properties, some of which are summarized in Figure 1.6 and will be briefly addressed in the following sections.

The origin and implications of the strong size-dependence of the properties of Au nanoclusters have already been discussed in Section 1.1. The influence of the protecting ligands will be addressed in Section 1.4, that of a potential support material in Section 1.6.

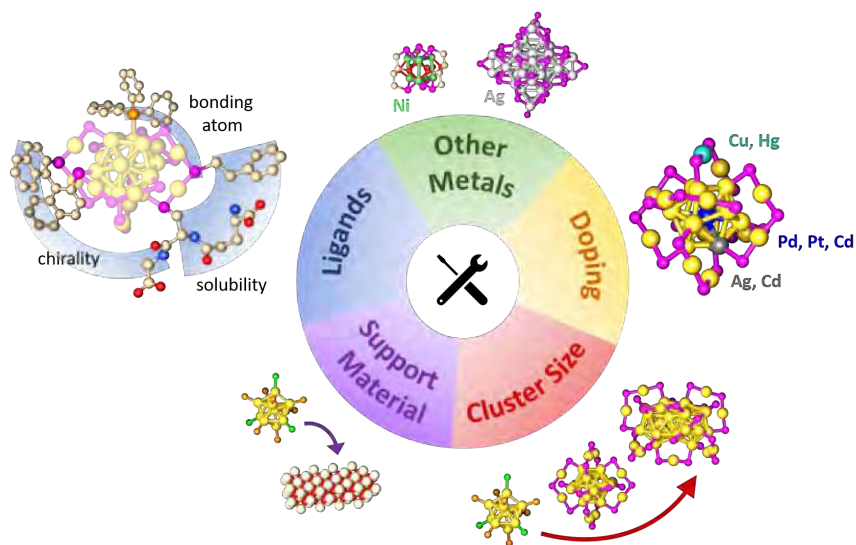


Figure 1.6.: Overview of the modification possibilities for metal nanoclusters.

Naturally, also a change of the metal making up the nanocluster has significant influence. Although gold nanoclusters have been studied intensively owing to their high stability,^[4,9,64,65] nowadays several other metals are used in nanocluster research, for example silver,^[4,9,64,65] nickel,^[65] platinum^[9] or palladium.^[9] However, even though several aspects discussed earlier in this chapter, such as the existence of molecule-like properties hold true for all of them, properties such as stability, electronic properties or reactivity can be vastly different.^[9,64] Since within this thesis only work on Au-based nanoclusters is presented, nanoclusters of other metals will not be further discussed.

Besides a complete change of the cluster element, also replacing single gold atoms in a certain structure is possible.^[4,12,15,66–68] This is usually done to alter certain properties of the nanocluster, such as its stability^[69–72] or electronic properties^[12,67,68,70,73–76] or for example to create another active site for reactions/catalysis.^[11,70] Introducing dopants into Au nanoclusters can be achieved during synthesis by adding another metal salt in the beginning (the so called co-reduction method) or through several post-synthetic modification protocols.^[2,12,67] The exact position and if only one or multiple replacements occur depend on both the dopant element and the Au nanocluster structure.^[67,68]

Taking the Au₂₅ nanocluster as an example, Pd and Pt dopants are known to replace the Au atom in the center of the cluster.^[66,68–71] Silver^[66,68,69,74,77] and cadmium,^[68,78] on the other hand, are usually located on the core surface (Cd also in the center^[79]) and can lead to several substitutions. The latter is also true for Cu^[66,68,77] and Hg,^[68,73,78] which prefer positions in the -(S(R)-Au)₂-S(R)- units. The different positions are schematically depicted in Figure 1.6. Of note, a study by Fei *et al.* employing nuclear magnetic resonance (NMR) spectroscopy

has come to different conclusions. Whereas the dopant position for Pd and Pt was confirmed to be at the core center, doping with a single Cd or Hg atom led to replacement at the core surface only, with no dopant atoms in the center or in the staple units.^[80]

In addition to monodoped clusters, also doping with multiple elements has already been achieved, resulting in tri-^[12,66,68,69,72,81] and even tetrametallic cluster species.^[66,68] Furthermore, controlling the number and positions of the substituting atoms to create monodisperse multimetallic clusters has become an important research focus in the last years,^[54,69,76,81] as have approaches for scale-up.^[82]

1.4. Protecting Ligands of Au Nanoclusters

The most prominent ligands for Au nanoclusters are thiolates^[1,4,10,13] and phosphines,^[4,17,18] however, selenolates,^[4,83,84] tellurolates,^[85] stibines,^[86,87] alkynyls^[4,88] and N-heterocyclic carbenes (NHCs).^[89–92] Their different binding motifs and the implication for the cluster structure have already been discussed in Section 1.1. Recapping briefly, thiolates lead to formation of $-S(-Au-S)_x-$ moieties that protect the Au kernel.^[1,17,19–21] Similar arrangements have also been observed for selenolates and tellurolates.^[83–85] Generally, the Au atoms located in the staple units of Au nanoclusters are positively charged due to electron-withdrawing properties of thiolates (or related) ligands, whereas the core Au atoms are not affected by this.^[19,20,22] Contrary to that, the neutral phosphine ligands can be considered as weak σ -donors that bind linearly.^[22] However, the anionic ligands usually also present for charge compensation (e.g. halides) mostly result in (partially) positively charged metal cores.^[22] Similar binding motifs are obtained with stibine ligands.^[86,87]

For terminal alkynyl-protected clusters, a more diverse structural library has been observed: (1) twofold $(R)C\equiv C-Au-C\equiv C(R)-Au-C\equiv C(R)$ units arranged in a V-type fashion, (2) linear monomeric $(R)C\equiv C-Au-C\equiv C(R)$ motifs and (3) monomeric $(R)C\equiv C-Au-C\equiv C(R)$ with the ligand frameworks oriented perpendicular to each other.^[88] Though this type of clusters forms protecting motifs reminiscent of the Au-thiolate staples, the nature of bonding is significantly different. In addition to the formation of σ -bonds between the terminal C-atom of the alkynyl ligand and a neighboring Au atom, also π -bonding between the Au and the triple bond is observed.^[88,93]

Recently, a new category of protecting ligands for Au nanoclusters has emerged: N-heterocyclic carbenes.^[89–92] Similar to phosphines, they are neutral ligands that bind in an end-on fashion. However, the Au–C bond was found to be significantly stronger than an Au–P bond in collision-induced dissociation (CID)-MS experiments and the NHC-stabilized clusters also exhibited higher stability in solution. However, only the monosubstituted product could be obtained as a monodisperse sample from undecagold precursor clusters so far.^[89] In addition, a biicosahedral Au_{25} cluster protected by only NHC-ligands and bromides could be obtained by direct synthesis. This cluster was also found to be highly stable in dissolved state at elevated temperatures, thus significantly outperforming its thiolate

and phosphine-thiolate isomers.^[90] Three NHC-protected Au₁₃ nanoclusters with different NHC ligands, ligand compositions and charge states were also recently synthesized and characterized. The specific ligand structures were revealed to have profound impact on the cluster properties, creating three very different nanocluster species, even though they are all of the same size.^[91] Furthermore, a Au₁₄₄ nanocluster protected by all NHCs, alkynyls and bromides was synthesized, which featured uncoordinated Au atoms on its core surface.^[92] These results clearly show the potential of NHCs as protecting ligands for Au nanoclusters, especially regarding the greatly enhanced stability.

The ligands in gold nanoclusters have profound influence on their properties. Effects on the geometries/sizes,^[13,94–97] stability,^[13,84,89–92,95,98–100] solubility/polarity,^[13,101] the optical properties,^[13,95,102,103] or chirality^[95,97,104,105] have been reported. Furthermore, they can also lead to different reactivities in catalysis, which is further discussed in Section 1.6.

1.4.1. Ligand Exchange and Ligand Exchange Induced Size/Structure Transformations (LEIST)

One possibility to alter the protecting ligand shell of Au nanoclusters is by ligand exchange procedures, which present an important tool for post-synthetic modification.^[106,107] It was first described by Murray and coworkers, who investigated the exchange dynamics and influence parameters of ligand exchange processes on Au nanoclusters.^[108–112] Since then, it has established itself as a possibility for directed structural modification, as well as a synthesis strategy,^[106,107] since it can be used to form cluster-ligand combinations which have not been obtained through a Brust-synthesis yet.^[13,113] However, a disadvantage of such ligand exchange processes is that in some cases, the exchange is not complete and thus mixed products are obtained, which subsequently have to be separated again.^[56,114–117]

The underlying mechanism of thiolate–thiolate exchange has been studied both experimentally and by employing density functional theory (DFT).^[118–121] By studying a partially exchanged Au₁₀₂(*p*-MBA)₄₀(*p*-BBT)₄ (with *para*-mercaptobenzoic acid = *p*-MBA and *para*-bromobenzene thiol = *p*-BBT) cluster, it was revealed that the ligand exchange process follows a S_N2 reaction pathway. In addition, existence of preferential ligand exchange sites was reported.^[118] Further investigations employing DFT by Aikens and coworkers showed that for Au₂₅(SR)₁₈ clusters, the most favorable site of exchange seems to be between the Au atom situated in the staple and a terminal thiolate.^[119] For Au₃₈(SR)₂₄, however, replacement at the site between a kernel Au atom and a terminal thiolate ligand in a monomeric staple unit was found to be lowest in energy.^[120] For both clusters replacement of the central thiolate ligand in the dimeric staple moiety resulted in the highest energy barriers.^[119,120] These calculations are consistent with experimental studies on Au₂₅(2-PET)₁₆(*p*-BBT)₂ that revealed that two symmetry-equivalent terminal thiolate ligands had been replaced.^[121] In principle, when speaking of ligand exchange, a distinction must be made between two different mechanisms: (1) ligand exchange procedures that proceed with retaining the

size and geometric structure of the cluster and (2) ligand-exchange-induced size/structure transformation (LEIST) processes.^[107,113] Examples for both are depicted in Figure 1.7.

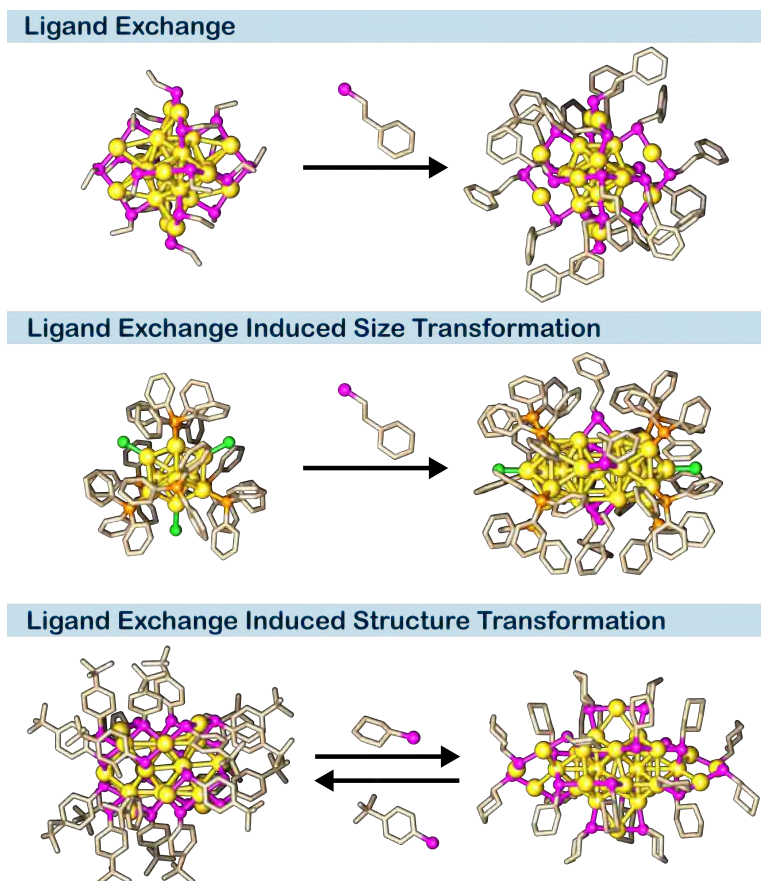


Figure 1.7.: Different ligand exchange processes on Au nanoclusters. Top: ligand exchange from $\text{Au}_{25}(\text{SC}_2\text{H}_5)_{18}$ to $\text{Au}_{25}(\text{2-PET})_{18}$, middle: ligand exchange induced size transformation from $\text{Au}_{11}(\text{PPh}_3)_7\text{Cl}_3$ to $\text{Au}_{25}(\text{PPh}_3)_{10}(\text{2-PET})_5\text{Cl}_2^{2+}$, bottom: reversible ligand exchange induced structure transformation between $\text{Au}_{28}(\text{TBBT})_{20}$ and $\text{Au}_{28}(\text{SC}_8\text{H}_{11})_{20}$. Color code: Au = gold, S = magenta, P = orange, Cl = green, C = beige.

Besides only replacing the protecting ligands of a nanocluster, exposure to exchange ligands can also result in more pronounced changes of the size and/or geometry of the cluster structure. This has become known as ligand-exchange-induced size/structure transformation (LEIST).^[107,113] Several such transformation reactions have already been reported and include all cluster growth, decreasing size or size maintenance but structural changes in the Au kernel.^[15,107] In addition, this phenomenon is not limited to thiolate–thiolate exchange only, but also phosphine–phosphine or phosphine–thiolate LEIST processes have been reported.^[15,107]

The question of why these more drastic changes occur in some systems but not in others has

naturally sparked the interest of researchers. In contrast to size-maintaining ligand exchange, a higher quantity of exchange ligand is usually needed, as well as elevated temperatures. Furthermore, the structural changes seem to be more pronounced if the original and the incoming ligand are also structurally different.^[113] Of note, exceptions also exist, for example the LEIST process from $\text{Au}_{25}(\text{2-PET})_{18}$ to $\text{Au}_{28}(\text{PPT})_{21}$, which proceeds without a large excess of exchange thiol (PPT = 2-phenylpropanethiol, which is in this case also structurally similar to the original one) and at room temperature.^[122]

For ligand exchange from phosphine to thiols, LEIST processes are especially common, which is related to the very different binding motif of these ligands.^[107] Two of the most studied examples are ligand exchanges of $\text{Au}_{11}(\text{PPh}_3)_7\text{Cl}_3$ with 2-phenylethanethiol (2-PET) and GSH. Both result in a significant increase in size and formation of Au_{25} clusters. However, the resulting structures are different: while GSH results in complete replacement of the phosphine ligands and formation of the well-known $\text{Au}_{25}(\text{SG})_{18}$ cluster,^[60,123] 2-PET only partially replaces the PPh_3 ligands and forms a biicosahedral $[\text{Au}_{25}(\text{PPh}_3)_{10}(\text{2-PET})_5\text{Cl}_2]^+$ structure.^[23] LEIST processes are usually highly selective and mainly produce a single product cluster, which can be an advantage over direct synthesis procedures that can produce a range of side products.^[113] In addition, it is also a pathway toward structures that are not easily accessible otherwise and has thus significantly contributed to enrich the structural library of Au nanoclusters.^[15,107,113] However, LEIST processes are strongly dependent on the nature of the exchange thiol and specific conditions used.^[107,113] For example, $\text{Au}_{25}(\text{SR})_{18}$ can undergo several different changes depending on the reaction conditions: (1) growth to $\text{Au}_{28}(\text{PPT})_{21}$,^[122] (2) growth to $\text{Au}_{28}(\text{TBBT})_{20}$ (with TBBT = 4-tert-butylbenzenethiol (TBBT)),^[124] (3) partial exchange and decrease in size to $\text{Au}_{22}(\text{2-PET})_4(\text{TBBT})_{14}$ ^[125] and (4) decrease in size to $\text{Au}_{20}(\text{TBBT})_{16}$.^[126] Furthermore, for $\text{Au}_{20}(\text{SR})_{20}$ nanoclusters, a change in the cluster geometry has been reported upon exchanging its surface ligands (TBBT *vs.* HS-*c*- C_6H_{11} with *c*- C_6H_{11} = cyclohexyl). Of note, the process was found to be reversible and did not result in a change of the cluster size.^[127] It is also represented in Figure 1.7

Another example for dependence on the protecting ligand has been reported by Li *et al.*,^[115] who found that the structure of Au_{38} is maintained if *ortho*-substituted aromatic thiolates were used, whereas conducting the ligand exchange with *para*-substituted aromatic thiolates or benzenethiol itself resulted in a size transformation to $\text{Au}_{36}(\text{SR})_{24}$, a known LEIST process that has been reported previously.^[128] For phosphine-protected Au nanoclusters, a similar steric effect has also been reported: whereas *meta* and *para*-substituted tri(tolyl)phosphines lead to exchange of the PPh_3 ligands on a Au_8 cluster, the *ortho*-substituted ligand did not.^[129]

1.5. Chirality in Au Nanoclusters

Chirality in inorganic nanomaterials has become a topic of interest in the last decade, since the connection with the versatile structures of such nanomaterials makes for an interesting

combination. Moreover, these materials usually show high anisotropy factors due to the evolution of the electronic structure as it approaches the nanoscale. Understanding and selectively modifying chirality in different nanomaterials is thus of great interest.^[130,131]

In gold nanoclusters, chirality can be present on several levels, which are represented in Figure 1.8. The first form involves the use of chiral protecting ligands. These can be chiral through asymmetric C atoms, as well as bidentate C_2 -symmetric ligands with a chiral axis.^[105] The first report of such a ‘ligand-chiral’ Au nanocluster was by Whetten and coworkers, who used the water soluble tripeptide GSH as ligand for their cluster synthesis.^[132] Since then, this concept has been extended to several other ligands and cluster structures.^[56,98,100,105,122,133–137] Especially 2,2’-bis(diphenylphosphino)-1,1’-binaphthyl (BINAP)-type ligands have been determined to induce strong chiral properties to the cluster structure.^[56,98,105,134–136]

Of note, induction of chiral ligands leads to chiral properties that can have an effect across the entire cluster structure. This can be confirmed by chiroptical spectroscopy in the form of circular dichroism (CD), since a chiral compound will absorb left and right-circularly polarized light to a different degree, resulting in non-zero parts in the difference spectrum.^[138] If now CD is performed with such modified clusters, they typically show signals that are clearly different from those of the free chiral ligand.^[104] Especially a red-shift in the on-set of the signal is known to be related to contribution of the Au kernel orbitals, even though the chiral center is located on the ligand.^[104,138–140]

In addition, several Au nanoclusters have also been confirmed to possess intrinsically chiral structures, i.e. possessing chiral properties even though the protecting ligands have no chiral center. This can be due to two different structural features: (1) a chiral cluster kernel or (2) chirality at the gold-thiolate interface.^[105] One prominent example of a cluster with a chiral core structure is $[Au_{20}(PP_3)_4]Cl_4$ ($PP_3 = tris(2-(diphenylphosphino)ethyl)phosphine$).^[141] Due to the different ligand binding motifs in thiolate and phosphine-protected Au nanoclusters, the latter do not usually exhibit intrinsic chirality, making this Au_{20} cluster a notable exception.^[104] In this case, the chirality is caused by one ligand binding to four gold atoms, resulting in a deformation of the nucleus.^[104,141] Indeed, analysis of its computed CD spectrum and the orbitals involved showed no significant contribution of ligand-to-metal charge transfer.^[105] The chiral kernel structure of $[Au_{20}(PP_3)_4]Cl_4$ is presented in Figure 1.8. For thiolate-protected Au nanoclusters, the more important origin of intrinsic chirality is the gold-sulfur interface.^[97,105] Several chiral clusters, such as $Au_{20}(SR)_{16}$,^[126] $Au_{28}(SR)_{20}$,^[124] $Au_{38}(SR)_{24}$,^[33] $Au_{40}(SR)_{24}$,^[142] $Au_{102}(SR)_{44}$,^[21] $Au_{133}(SR)_{52}$ ^[143] and $Au_{144}(SR)_{60}$ ^[144], among others^[97], have been found to possess a chiral Au-S environment. One of the most well-known examples is $Au_{38}(SR)_{24}$, for which the crystal structure was reported by Jin and coworkers in 2010.^[33] As also depicted in Figure 1.8, its monomeric and dimeric staple units are arranged in a counter-clockwise fashion (note that the clockwise-enantiomer is not shown), thus imposing chirality on the structure.

Furthermore, several cluster species are known to possess more than one chiral element, which has become known as hierarchical chirality.^[104,105] One example would be $Au_{133}(TBBT)_{52}$ (with TBBT = 4-tert-butylbenzenethiol), which exhibits a chiral kernel, a chiral arrangement

of its monomeric staple units forming a helical pattern, as well as several swirl-like formations of four ligand backbones each.^[104,143] Another example will be discussed in Chapter 3 and involves a combination of chiral protecting ligands (*S*)-2-methylbutanethiol (2-MeBuSH) on an intrinsically chiral cluster such as Au₃₈. Both examples are depicted in Figure 1.8. However, also several other examples of hierarchical chirality are known in metal nanocluster chemistry.^[104,105]

Of note, the influence of the ligands on both induced and intrinsic chirality is remarkable. As work by Jin and coworkers^[100,137] shows, the specific ligand used affects the positions, sign (i.e. positive or negative) and intensity of the CD bands of both achiral and chiral clusters. In addition, as discussed before, bidentate ligands such as 1,1'-binaphthyl-2,2'-dithiol (BINAS) often enhance the stability of Au nanoclusters and can thus also contribute to retain the chirality upon heating.^[98] Finally, the specific ligand used can also dictate if a certain cluster size will exhibit intrinsically chiral properties or not, related to its specific bonding motif, as well as steric effects.^[97]

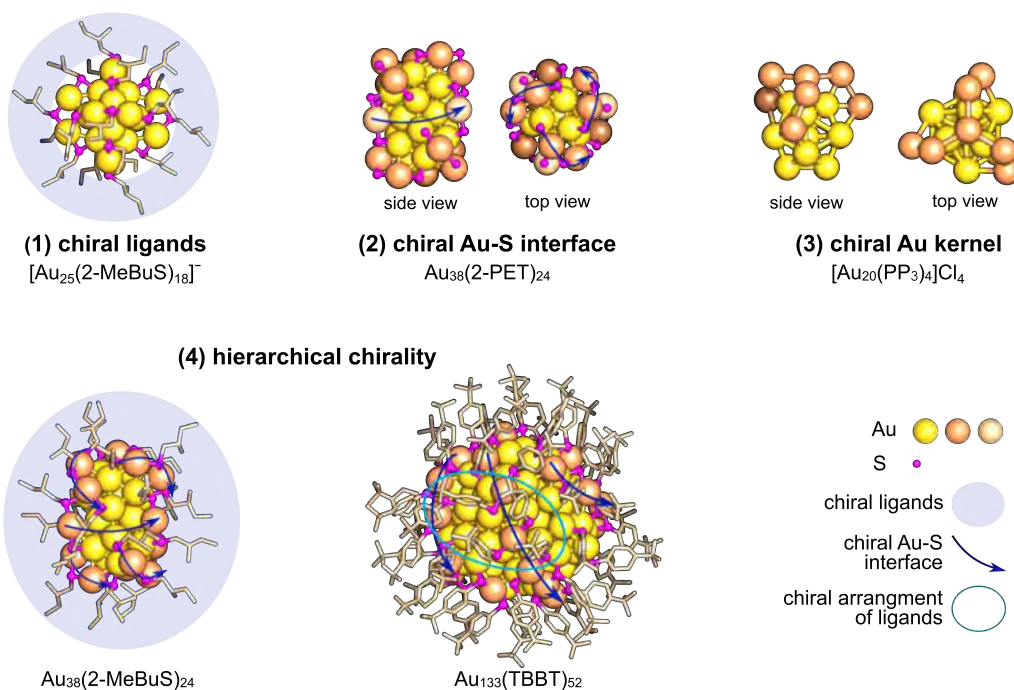


Figure 1.8.: Different forms of chirality in Au nanoclusters: (1) chiral ligands, (2) chiral Au-S interface, (3) chiral Au kernel and (4) hierarchical chirality by combining several different motifs. Note that for Au₃₈(2-PET)₂₄, the hydrocarbon backbone of the ligands is omitted for clarity. Similarly, for [Au(PP₃)₄]Cl₄, only the chiral core itself is depicted.

As already mentioned above, a useful tool for probing the chiral properties of Au nanoclusters is CD spectroscopy.^[105,138] Combined with DFT calculations, good understanding of the electronic structure of the chiral clusters can be obtained and the origin of the CD

signal evaluated.^[25,105,138–140,145,146] Besides CD, also vibrational circular dichroism (VCD) has been applied (again, mostly in combination with computations) to investigate the conformation of the chiral ligands on the Au core.^[105,147–149] In addition, also circular polarized luminescence (CPL) measurements^[105] or NMR spectroscopy^[150] are useful tools for studying chirality in Au nanoclusters.

1.5.1. Strategies Toward Chiral Au Nanoclusters

To obtain chiral Au nanoclusters, different approaches are possible. Both direct synthesis or ligand exchange strategies are useful for chiral induction,^[13,97,105,151] within their limitations described in Sections 1.2 and 1.4. Direct synthesis approaches are especially useful for selectively producing only a single form of intrinsically chiral cluster, as has already been achieved for Au₃₈(SR)₂₄.^[137] Ligand exchange followed by a heating step to allow for racemization has also already been reported for to lead to symmetry breaking of a mixture of Au₃₈(2-PET)₂₄ and Au₃₈(2-PET)₂₂*R*-BINAS.^[152] Nevertheless, such reports are still scarce and achieving yields high enough for practical applications still remains a challenge.^[97]

Another strategy toward enantiopure clusters is the separation of racemic mixtures of intrinsically chiral clusters. This has been done for several cluster mainly by employing chiral HPLC techniques. For example, Bürgi and coworkers succeeded to separate the Au₃₈(2-PET)₂₄ enantiomers and measured their circular dichroism spectra, which gave perfect mirror images.^[58] HPLC separation has also been applied to obtain enantiopure samples of several other clusters, e.g. Pd₂Au₃₆(SR)₂₄^[57] or Au₄₀(SR)₂₄.^[142]

However, one limiting aspect is that it is only suitable for small amounts of sample and large volumes of high purity solvents are needed. Furthermore, for each new cluster-ligand combination, a new method has to be developed. Thus, separation by chiral HPLC can be useful to obtain enantiopure clusters for investigating their chiral properties, however, different approaches are needed to be able to achieve sufficient sample for applications. Recently, Tang and coworkers have succeeded in separating the chiral [Au₂₀(PP₃)Cl₄] cluster by use of α -cyclodextrin.^[153] Briefly, both the Au₂₀ cluster and the α -cyclodextrin were dissolved and mixed together in a polar organic solvent. The benzene rings of the phosphine ligands on Au₂₀ were then found to interact with the hydrophobic cavity of α -cyclodextrin. Since the oligosaccharide adapts a chiral structure, also the hydrophobic binding site is chiral and thus, one enantiomer of Au₂₀ fits better in the pocket and is preferentially incorporated. Precipitating the Au₂₀-cyclodextrin composite out of the solution leaves mainly the other Au₂₀ enantiomer in the solution. Furthermore, Au₂₀ could also be extracted again from α -cyclodextrin by addition of tetrabutylammonium chloride (TBAC), which displaced the clusters in the binding pockets. For highly enantiopure samples, this procedure only had to be performed twice. This is a remarkable step toward separation of racemic mixtures of intrinsically chiral Au nanoclusters, considering that this simple strategy can be used for preparative amounts of nanoclusters.

1.6. Au Nanoclusters in Heterogeneous Catalysis: Advantages and Influences

Since the discovery that gold becomes very active when the particle size is in the nanometer regime in the 1980s,^[154,155] gold nanoparticles have been readily employed in heterogeneous catalysis, mainly for oxidation reactions.^[156–158] These Au nanoparticles show a distribution of sizes, which might be reduced to a few percent.^[3] However, when moving to ultrasmall scale, this might still result in significantly different properties and activities of the particles^[159] and thus prevent identification of structure–activity relations.^[11,160] Contrary to that, Au nanoclusters can be obtained monodisperse, making the catalytic systems more defined and therefore easier to understand.^[3,11,160] At this point, however, it should be pointed out that there is a pitfall associated with this: the system is only then monodisperse when the clusters retain their size and structure when immobilized and reacted, an assumption that has been shown not to hold for several systems already studied.^[3,161–165] Nevertheless, the complexity is significantly lower compared to industrial-grade catalysts, for which systematic approaches to identifying active systems still remain complicated.^[166]

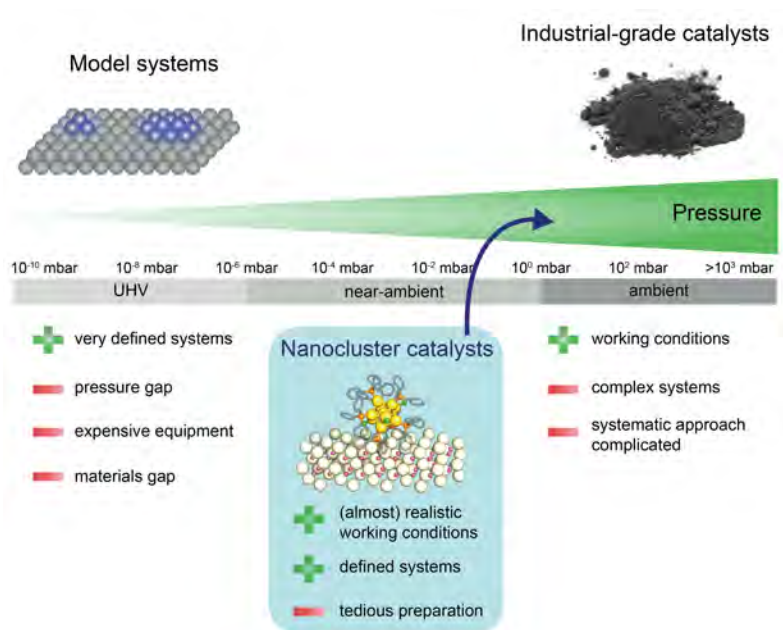


Figure 1.9.: Comparison of different catalyst systems.

On the other hand, comparing Au nanoclusters to surface science systems,^[167] cluster catalysts are obviously less defined, but can be used at ambient pressure (see also Figure

1.9). Thus, they constitute some kind of ‘intermediate materials’ between model systems and industrial-grade catalysts and can be employed to obtain critical information of catalytic systems under working conditions.^[3] As such, and because of the intriguing properties of Au nanoclusters described in previous sections, they have readily been employed in catalysis.^[3,4,10,11,13,15,160,168]

Due to the stabilization of the Au nanoclusters by a ligand monolayer, also application in homogeneous catalysis is possible,^[13] and the clusters have also been applied in electro- and photocatalysis.^[3,4,10,15,160] However, since the scope of the catalytic studies presented in this thesis was on heterogeneous systems, i.e. the clusters were immobilized on different metal oxide materials, homogeneous reactions will be no further discussed.

When employing gold nanoclusters as realistic model systems for structure–activity studies in heterogeneous catalysis, several influences on the behavior of the system have to be considered, such as the size and metal composition of the clusters, their ligand environment, the support material or the activation process applied. At the same time, these factors serve as parameters that can be used to control the catalytic activity in a targeted fashion.^[3,160] Examples of their influences will be discussed in the following.

1.6.1. Nanocluster Size and Structure Effect

In many cases, smaller particles are prone to exhibit higher catalytic activity than larger ones, related for example to changes in the adsorption energies or increased surface areas, making nanoclusters attractive for catalytic application^[3] Also within the typical size range of Au nanoclusters (which is up 2 nm or 300 atoms^[4,5]), the catalytic activity of Au nanoclusters has been proven to be dependent on the number of metal atoms in the cluster, but also factors such as the structure of the Au kernel can have an influence.^[3,168]

A so-called size-effect has been reported for several systems and reactions, for example in cyclohexane oxidation,^[169,170] benzyl alcohol oxidation,^[171] styrene oxidation,^[172] pyrrolidine oxidation,^[173] hydration of phenylacetylene^[174] or oxidation of methyl phenyl sulfide.^[175] A significant size effect was also found for phosphine-protected clusters on CeO₂ in CO oxidation.^[176]

When employing two clusters of similar size, Au₃₈(SR)₂₄ and Au₃₆(SR)₂₄, both supported on CeO₂, in CO oxidation, Jin and coworkers noticed that an optimum pretreatment temperature (see also Section 1.6.5) existed for Au₃₈, whereas the CO conversion of the Au₃₆ catalysts showed no such dependence. This was attributed to a difference in their kernel geometries (icosahedron *vs.* fcc).^[177] A comparison of two Au₂₅ clusters supported on CeO₂ in styrene oxidation and selective hydrogenation of α,β -unsaturated benzalacetone showed that Au₂₅(SC₂H₄Ph)₁₈ resulted in higher conversions than [Au₂₅(SC₂H₄Ph)₅(PPh₃)₁₀Cl₂]²⁺.^[178] Another example of structure-dependent activity was found for a Au₂₂ cluster protected by diphosphine ligands: Au sites on the core surface which were not directly bonded to the protecting ligands were found to be responsible for its high activity in CO oxidation even with a full ligand shell.^[179] Similar observations were also made for a triple NHC-alkynyl-

bromide-protected Au₄₄ nanocluster with uncoordinated Au atoms in the structure, which gave excellent yields in the catalytic hydration of alkynes.^[92]

1.6.2. Doping

One especially promising field of applications for bimetallic or multimetallic nanoclusters is catalysis. Several examples of the benefit of doping in terms of improved activity or selectivity have been reported.^[11,70,163,180] For instance, a single Pt dopant in a Au₂₅ nanocluster has been shown to greatly enhance their activity and selectivity in heterogeneous styrene oxidation,^[70] while a beneficial effect on the selectivity through Ag doping seems to be strongly linked to the presence of surface doped structures.^[181] Another example would be in heterogeneous CO oxidation, where Pd^[163] and Cu dopants^[180] have been shown to increase the conversion, whereas substitution with Ag led to either enhanced^[182] or reduced^[180] activity compared to the monometallic Au nanoclusters depending on the system under investigation.

1.6.3. Support Material

In the immense number of studies related to Au nanoparticle catalysis, several materials have been found to be active supports. Noteworthy examples are Fe_xO_y, which was first used by Haruta and coworkers when they reported the surprising activity of small Au particles in sub-room temperature CO oxidation,^[154] as well as TiO₂ and CeO₂.^[156,183] However, it seems that these observations are only partially transferable to the nanocluster counterparts. Taking CO oxidation as an example, studies by Jin and coworkers showed that Au₂₅(SR)₁₈ clusters were most active when supported on CeO₂, whereas significantly lower activity was observed for FeO₂-supported clusters.^[184] The same clusters immobilized on TiO₂ showed almost no CO conversion,^[184] an observation also confirmed by García *et al.*^[163] While CeO₂ was still the best support material for a phosphine-protected Au₂₂ cluster employed in CO oxidation, also immobilization on TiO₂ led to considerable conversion at slightly higher temperatures, whereas the Al₂O₃ catalyst was essentially inactive.^[179]

Support effects have also been reported for thiolate-protected Au nanoclusters in cyclohexane oxidation,^[170,185,186] pyrrolidine oxidation,^[173] Sonogashira cross-coupling^[187] or nitrobenzaldehyde hydrogenation.^[188] For cyclohexane oxidation, the pronounced differences in activity/selectivity were linked to differences in the stabilities of the Au nanoclusters on the used support materials: The supports that were able to preserve the small structures of the Au nanoclusters were also the ones giving better results in catalysis.^[170,185]

For phosphine-protected Au nanoclusters, a study by Longo *et al.*^[176] found that [Au₉(PPh₃)₈]³⁺ heated to 120 °C decomposed on supports such as SiO₂ or carbon, whereas stable and exposed Au₉ particles were obtained on CeO₂ and TiO₂. This was attributed to the different acid-base properties of the used support materials. For the same cluster species, Andersson *et al.*^[189] also reported phosphine migration and thus formation of bare Au particles on TiO₂, whereas they observed sintering to larger particles on SiO₂.

These varying results depending on the specific cluster species and reaction investigated are

already a clear indication that the parameters discussed in this section cannot be evaluated independently, but that a holistic approach is needed to understand the behavior of heterogeneous Au nanocluster catalysts. When choosing a specific support material, not only its suitability for a certain reaction, but also its ability to stabilize (partially) deprotected Au particles in small sizes has to be considered.^[160]

1.6.4. Effect of the Protecting Ligands

The presence of cluster ligands in heterogeneous systems is a controversially discussed topic. Nevertheless, while the ligand monolayer might be often hindering adsorption of reactants and thus inhibiting high activities,^[13,160] their presence can be also useful for tuning selectivity.^[3] For example, Tsukuda and coworkers reported that Au₂₅ nanoclusters on carbon nanosheets were most active for benzyl alcohol oxidation after removal of the ligand sphere. However, selectivity towards the desired product benzaldehyde was significantly increased with presence of thiolates in the system.^[190] The semihydrogenation of alkynes, in which un-pretreated Au₂₅/TiO₂ catalysts only reacted with terminal alkynes, whereas also internal alkynes were converted when the ligands are (partially) removed, is yet another example of the selectivity modification through the protecting ligands.^[191]

Furthermore, also influences of different ligand types or backbone structures have been reported.^[3,102,177,192–195] For example, studies on ceria supported Au₂₅ and Au₃₈ nanoclusters protected by different kinds of ligands in Ullmann heterocoupling showed that best conversion and selectivity could be achieved when the coordinating sulfur atom was directly bonded to a phenyl ring system.^[102,192] Jin and coworkers applied three Au nanoclusters (Au₂₅, Au₃₆ and Au₃₈) supported on CeO₂ in CO oxidation, which were also protected by several different thiolates (7 in total). They noticed a dependence of the activity on how strongly the ligand structure prevents adsorption of reactants at the cluster–ligand–support interfacial sites.^[177] In alkyne semihydrogenation of TiO₂ supported [Au₃₈(L)₂₀(Ph₃P)₄]²⁺ (with L being either PhC≡C or *meta*-methylbenzenethiol (*m*-MBT)), excellent conversion and selectivity was obtained with the alkynyl ligand, however, the thiolate-protected clusters were almost inactive.^[193] Mixed ligand biicosahedral Au₂₅ clusters both supported on activated carbon and protected by PPh₃, but by different thiolates (–SC₆H₁₃ *vs.* –SPh) exhibited distinctly different activities for glucose oxidation.^[194] Differences were also noticed for two Au₁₁/CeO₂ catalysts in 4-nitrobenzaldehyde hydrogenation: whereas Au₁₁(PPh₃)₇Cl₃ required presence of a base for catalytic activity, the reaction with Au₁₁(PPh₂Py)₇Br₃ (with PPh₂Py = diphenyl-2-pyridylphosphine) could proceed without due to the ligand being capable of hydrogen activation.^[195]

Besides the influence of intact ligands in catalytic systems, also the effect of their residues after potential activation procedures has to be considered, which is further discussed in Section 1.6.5.

1.6.5. Pretreatment Procedures and Fate of the Ligands

For most heterogeneous catalytic reactions with Au nanoclusters, pretreatment of the catalyst has been found necessary to achieve optimal activity.^[13] These treatments usually vary depending on the cluster species, support material or type of reaction. In many cases, thermal activation under oxidative atmosphere has been performed in an effort to remove part of the protecting ligand sphere and expose the bare Au surface for adsorption of reactants.^[11]

One of the most studied catalytic reactions with Au nanoclusters is CO oxidation, for which also several reports on pretreatment conditions exist: Nie *et al.* found that for Au₂₅/CeO₂ catalysts in CO oxidation, pretreatment under oxygen atmosphere at 150 °C for 1.5 h was sufficient for catalyst activation. Longer pretreatment times or at higher temperature (250 °C) did not increase the conversion any further. Combining oxygen with a reductive gas (H₂ or CO) and heating to 80 °C was found to be a suitable activation procedure for a Au₁₄₄/CeO₂ catalyst.^[196] Since these temperatures are not high enough for removal of the thiolate ligands from the system, in both cases, the fully-protected clusters were presumed to be the active catalysts.^[184,196] By testing a series of oxidative pretreatment temperatures between 100 and 250 °C for Au₃₈/CeO₂ in CO oxidation, optimal activity was observed after activation at 175 °C, which should correspond to partial deprotection of the Au core.^[197] Similar results were also obtained in a follow-up study on Au₂₅/CeO₂, which showed that a part of the protecting ligand sphere needs to be removed in order to obtain active catalysts.^[165]

Newer studies of Au₃₈ nanoclusters on CeO₂^[161,162,164] and Al₂O₃^[162] have indicated that the thiolate ligands are able to detach from the cluster core and migrate to the surface of the support. After oxidative pretreatment at 150 °C, the hydrocarbon structure of the ligands could be successfully removed, but residual sulfur atoms on the cluster prevented adsorption of reactants. After pretreatment at 250 °C, the remaining sulfur had relocated to the CeO₂ support, resulting in drastically increased CO conversion due to exposed Au surface. The structural dynamics continued throughout the reaction and ultimately, small Au⁺-S fragments formed in addition to the active Au particles.^[164] Residual sulfur in a Au₃₈/CeO₂ system after reductive treatment at 400 °C has also been reported.^[161] Ligand migration has also already been observed for phosphine-protected clusters (see also section 1.6.3).^[176,189]

These studies already clearly indicate that alternative protocols for nanocluster catalyst activation are required.^[13] One possible strategy could be oxidation of the ligands by peroxide species, which resulted in small and accessible Au particles in a study by Zhang *et al.*^[198] For Au₂₅ and Au₁₄₄ nanoclusters on functionalized SiO₂, a reductive ligand desorption method employing a NaBH₄ solution has been found to be beneficial for both the conversion and selectivity in styrene oxidation, while preserving the cluster sizes.^[199] However, a more thorough investigation of activation methods for Au nanoclusters other than calcination has yet to be conducted.

In summary, even though Au nanoclusters have the potential to reduce the complexity of catalytic systems and are thus appealing for catalytic model studies, there are still several factors influencing their catalytic activity. To better understand their behavior, *operando* studies have been of great help, since they allow to study the catalyst under working conditions.^[163,164,200] An application of such experiments is presented in Chapter 5.

1.7. References

- [1] Rongchao Jin, Yan Zhu, and Huifeng Qian. Quantum-Sized Gold Nanoclusters: Bridging the Gap between Organometallics and Nanocrystals. *Chemistry - A European Journal*, 17(24):6584–6593, may 2011. doi: 10.1002/chem.201002390.
- [2] Esmā Khatun and Thalappil Pradeep. New Routes for Multicomponent Atomically Precise Metal Nanoclusters. *ACS Omega*, 6(1):1–16, dec 2020. doi: 10.1021/acsomega.0c04832.
- [3] Rongchao Jin, Gao Li, Sachil Sharma, Yingwei Li, and Xiangsha Du. Toward Active-Site Tailoring in Heterogeneous Catalysis by Atomically Precise Metal Nanoclusters with Crystallographic Structures. *Chemical Reviews*, 121(2):567–648, sep 2020. doi: 10.1021/acs.chemrev.0c00495.
- [4] Rongchao Jin, Chenjie Zeng, Meng Zhou, and Yuxiang Chen. Atomically Precise Colloidal Metal Nanoclusters and Nanoparticles: Fundamentals and Opportunities. *Chemical Reviews*, 116(18):10346–10413, sep 2016. doi: 10.1021/acs.chemrev.5b00703.
- [5] Huifeng Qian, Manzhou Zhu, Zhikun Wu, and Rongchao Jin. Quantum sized gold nanoclusters with atomic precision. *Accounts of Chemical Research*, 45(9):1470–1479, jun 2012. doi: 10.1021/ar200331z.
- [6] Yuichi Negishi, Tafu Nakazaki, Sami Malola, Shinjiro Takano, Yoshiki Niihori, Wataru Kurashige, Seiji Yamazoe, Tatsuya Tsukuda, and Hannu Häkkinen. A critical size for emergence of nonbulk electronic and geometric structures in dodecanethiolate-protected au clusters. *Journal of the American Chemical Society*, 137(3):1206–1212, jan 2015. doi: 10.1021/ja5109968.
- [7] Jun Fang, Bin Zhang, Qiaofeng Yao, Yang Yang, Jianping Xie, and Ning Yan. Recent advances in the synthesis and catalytic applications of ligand-protected, atomically precise metal nanoclusters. *Coordination Chemistry Reviews*, 322:1–29, sep 2016. doi: 10.1016/j.ccr.2016.05.003.
- [8] Mary McPartlin, R. Mason, and L. Malatesta. Novel cluster complexes of gold(0)–gold(I). *J. Chem. Soc. D*, 0(7):334–334, 1969. doi: 10.1039/c29690000334.
- [9] Indranath Chakraborty and Thalappil Pradeep. Atomically Precise Clusters of Noble Metals: Emerging Link between Atoms and Nanoparticles. *Chemical Reviews*, 117(12):8208–8271, jun 2017. doi: 10.1021/acs.chemrev.6b00769.
- [10] Zhihe Liu, Zhennan Wu, Qiaofeng Yao, Yitao Cao, Osburg Jin Huang Chai, and Jianping Xie. Correlations between the fundamentals and applications of ultrasmall metal nanoclusters: Recent advances in catalysis and biomedical applications. *Nano Today*, 36:101053, feb 2021. doi: 10.1016/j.nantod.2020.101053.
- [11] Jianbo Zhao and Rongchao Jin. Heterogeneous catalysis by gold and gold-based bimetal nanoclusters. *Nano Today*, 18:86–102, feb 2018. doi: 10.1016/j.nantod.2017.12.009.
- [12] Xi Kang, Hanbao Chong, and Manzhou Zhu. Au₂₅SR₁₈: the captain of the great nanocluster ship. *Nanoscale*, 10(23):10758–10834, 2018. doi: 10.1039/c8nr02973c.
- [13] Ricca Rahman Nasaruddin, Tiankai Chen, Ning Yan, and Jianping Xie. Roles of thiolate ligands in the synthesis, properties and catalytic application of gold nanoclusters. *Coordination Chemistry Reviews*, 368:60–79, aug 2018. doi: 10.1016/j.ccr.2018.04.016.
- [14] Haru Hirai, Shun Ito, Shinjiro Takano, Kiichirou Koyasu, and Tatsuya Tsukuda. Ligand-protected gold/silver superatoms: current status and emerging trends. *Chemical Science*, 11(45):12233–12248, 2020. doi: 10.1039/d0sc04100a.

- [15] Tokuhisa Kawawaki, Ayano Ebina, Yasunaga Hosokawa, Shuhei Ozaki, Daiki Suzuki, Sakiat Hossain, and Yuichi Negishi. Thiolate-Protected Metal Nanoclusters: Recent Development in Synthesis, Understanding of Reaction, and Application in Energy and Environmental Field. *Small*, 17(27):2005328, feb 2021. doi: 10.1002/sml.202005328.
- [16] Xi Kang and Manzhou Zhu. Tailoring the photoluminescence of atomically precise nanoclusters. *Chemical Society Reviews*, 48(8):2422–2457, 2019. doi: 10.1039/c8cs00800k.
- [17] Yu Wang, Huayan Yang, and Nanfeng Zheng. Structural Engineering of Heterometallic Nanoclusters. In *Frontiers of Nanoscience*, pages 73–102. Elsevier, 2015. doi: 10.1016/b978-0-08-100086-1.00004-x.
- [18] Katsuaki Konishi. Phosphine-Coordinated Pure-Gold Clusters: Diverse Geometrical Structures and Unique Optical Properties/Responses. In *Structure and Bonding*, pages 49–86. Springer International Publishing, 2014. doi: 10.1007/430_2014_143.
- [19] Hannu Häkkinen. Atomic and electronic structure of gold clusters: understanding flakes, cages and superatoms from simple concepts. *Chemical Society Reviews*, 37(9):1847, 2008. doi: 10.1039/b717686b.
- [20] Michael Walter, Jaakko Akola, Olga Lopez-Acevedo, Pablo D. Jadzinsky, Guillermo Calero, Christopher J. Ackerson, Robert L. Whetten, Henrik Grönbeck, and Hannu Häkkinen. A unified view of ligand-protected gold clusters as superatom complexes. *Proceedings of the National Academy of Sciences*, 105(27):9157–9162, jul 2008. doi: 10.1073/pnas.0801001105.
- [21] Pablo D. Jadzinsky, Guillermo Calero, Christopher J. Ackerson, David A. Bushnell, and Roger D. Kornberg. Structure of a Thiol Monolayer-Protected Gold Nanoparticle at 1.1 Å Resolution. *Science*, 318(5849):430–433, oct 2007. doi: 10.1126/science.1148624.
- [22] Hannu Häkkinen, Michael Walter, and Henrik Grönbeck. Divide and Protect: Capping Gold Nanoclusters with Molecular Gold-Thiolate Rings. *The Journal of Physical Chemistry B*, 110(20):9927–9931, apr 2006. doi: 10.1021/jp0619787.
- [23] Yukatsu Shichibu, Yuichi Negishi, Takahito Watanabe, Nirmalya K. Chaki, Hiroyuki Kawaguchi, and Tatsuya Tsukuda. Biicosahedral Gold Clusters $[\text{Au}_{25}(\text{PPh}_3)_{10}(\text{SC}_n\text{H})_{(2n+1)5}\text{Cl}_2]^{2+}$ ($n = 2-18$): A Stepping Stone to Cluster-Assembled Materials. *The Journal of Physical Chemistry C*, 111(22):7845–7847, may 2007. doi: 10.1021/jp073101t.
- [24] Marcus A. Tofanelli, Kirsi Salorinne, Thomas W. Ni, Sami Malola, Brian Newell, Billy Phillips, Hannu Häkkinen, and Christopher J. Ackerson. Jahn-Teller effects in $\text{Au}_{25}(\text{SR})_{18}$. *Chemical Science*, 7(3):1882–1890, 2016. doi: 10.1039/c5sc02134k.
- [25] Olga Lopez-Acevedo, Hironori Tsunoyama, Tatsuya Tsukuda, Hannu Häkkinen, and Christine M. Aikens. Chirality and Electronic Structure of the Thiolate-Protected Au_{38} Nanocluster. *Journal of the American Chemical Society*, 132(23):8210–8218, may 2010. doi: 10.1021/ja102934q.
- [26] Longjiu Cheng, Changda Ren, Xiuzhen Zhang, and Jinlong Yang. New insight into the electronic shell of $\text{Au}_{38}(\text{SR})_{24}$: a superatomic molecule. *Nanoscale*, 5(4):1475, 2013. doi: 10.1039/c2nr32888g.
- [27] Olga Lopez-Acevedo, Jaakko Akola, Robert L. Whetten, Henrik Grönbeck, and Hannu Häkkinen. Structure and Bonding in the Ubiquitous Icosahedral Metallic Gold Cluster $\text{Au}_{144}(\text{SR})_{60}$. *The Journal of Physical Chemistry C*, 113(13):5035–5038, jan 2009. doi: 10.1021/jp8115098.
- [28] Wen Wu Xu, Xiao Cheng Zeng, and Yi Gao. Application of Electronic Counting Rules for Ligand-Protected Gold Nanoclusters. *Accounts of Chemical Research*, 51(11):2739–2747, oct 2018. doi: 10.1021/acs.accounts.8b00324.

- [29] Yan Zhu, Rongchao Jin, and Yuhan Sun. Atomically Monodisperse Gold Nanoclusters Catalysts with Precise Core-Shell Structure. *Catalysts*, 1(1):3–17, sep 2011. doi: 10.3390/catal1010003.
- [30] Yuichi Negishi, Yoshimitsu Takasugi, Seiichi Sato, Hiroshi Yao, Keisaku Kimura, and Tatsuya Tsukuda. Magic-Numbered Au_n Clusters Protected by Glutathione Monolayers (n = 18, 21, 25, 28, 32, 39): Isolation and Spectroscopic Characterization. *Journal of the American Chemical Society*, 126(21):6518–6519, may 2004. doi: 10.1021/ja0483589.
- [31] Yuichi Negishi, Katsuyuki Nobusada, and Tatsuya Tsukuda. Glutathione-Protected Gold Clusters Revisited: Bridging the Gap between Gold(I)-Thiolate Complexes and Thiolate-Protected Gold Nanocrystals. *Journal of the American Chemical Society*, 127(14):5261–5270, mar 2005. doi: 10.1021/ja042218h.
- [32] Xiangsha Du, Jinsong Chai, Sha Yang, Yingwei Li, Tatsuya Higaki, Site Li, and Rongchao Jin. Fusion growth patterns in atomically precise metal nanoclusters. *Nanoscale*, 11(41):19158–19165, 2019. doi: 10.1039/c9nr05789g.
- [33] Huifeng Qian, William T. Eckenhoff, Yan Zhu, Tomislav Pintauer, and Rongchao Jin. Total Structure Determination of Thiolate-Protected Au₃₈ Nanoparticles. *Journal of the American Chemical Society*, 132(24):8280–8281, jun 2010. doi: 10.1021/ja103592z.
- [34] Tiankai Chen, Qiaofeng Yao, Yitao Cao, and Jianping Xie. Studying the Growth of Gold Nanoclusters by Sub-stoichiometric Reduction. *Cell Reports Physical Science*, 1(9):100206, sep 2020. doi: 10.1016/j.xcrp.2020.100206.
- [35] Yong Pei, Pu Wang, Zhongyun Ma, and Lin Xiong. Growth-Rule-Guided Structural Exploration of Thiolate-Protected Gold Nanoclusters. *Accounts of Chemical Research*, 52(1):23–33, dec 2018. doi: 10.1021/acs.accounts.8b00385.
- [36] Qiaofeng Yao, Xun Yuan, Victor Fung, Yong Yu, David Tai Leong, De en Jiang, and Jianping Xie. Understanding seed-mediated growth of gold nanoclusters at molecular level. *Nature Communications*, 8(1), oct 2017. doi: 10.1038/s41467-017-00970-1.
- [37] Wen Wu Xu, Yadong Li, Yi Gao, and Xiao Cheng Zeng. Unraveling a generic growth pattern in structure evolution of thiolate-protected gold nanoclusters. *Nanoscale*, 8(14):7396–7401, 2016. doi: 10.1039/c6nr00272b.
- [38] Chenjie Zeng, Yuxiang Chen, Kenji Iida, Katsuyuki Nobusada, Kristin Kirschbaum, Kelly J. Lambright, and Rongchao Jin. Gold Quantum Boxes: On the Periodicities and the Quantum Confinement in the Au₂₈, Au₃₆, Au₄₄, and Au₅₂ Magic Series. *Journal of the American Chemical Society*, 138(12):3950–3953, mar 2016. doi: 10.1021/jacs.5b12747.
- [39] Zhentao Luo, Vairavan Nachammai, Bin Zhang, Ning Yan, David Tai Leong, De en Jiang, and Jianping Xie. Toward Understanding the Growth Mechanism: Tracing All Stable Intermediate Species from Reduction of Au(I)-Thiolate Complexes to Evolution of Au₂₅ Nanoclusters. *Journal of the American Chemical Society*, 136(30):10577–10580, jul 2014. doi: 10.1021/ja505429f.
- [40] Mathias Brust, Meryll Walker, Donald Bethell, David J. Schiffrin, and Robin Whyman. Synthesis of thiol-derivatised gold nanoparticles in a two-phase Liquid-Liquid system. *J. Chem. Soc., Chem. Commun.*, 0(7):801–802, 1994. doi: 10.1039/c39940000801.
- [41] Paul J. G. Goulet and R. Bruce Lennox. New Insights into Brust-Schiffrin Metal Nanoparticle Synthesis. *Journal of the American Chemical Society*, 132(28):9582–9584, jun 2010. doi: 10.1021/ja104011b.

- [42] Ying Li, Oksana Zaluzhna, Bolian Xu, Yuan Gao, Jacob M. Modest, and YuYe J. Tong. Mechanistic Insights into the Brust-Schiffrin Two-Phase Synthesis of Organo-chalcogenate-Protected Metal Nanoparticles. *Journal of the American Chemical Society*, 133(7):2092–2095, jan 2011. doi: 10.1021/ja1105078.
- [43] Rongchao Jin, Huifeng Qian, Zhikun Wu, Yan Zhu, Manzhou Zhu, Ashok Mohanty, and Niti Garg. Size Focusing: A Methodology for Synthesizing Atomically Precise Gold Nanoclusters. *The Journal of Physical Chemistry Letters*, 1(19):2903–2910, sep 2010. doi: 10.1021/jz100944k.
- [44] Yong Yu, Xi Chen, Qiaofeng Yao, Yue Yu, Ning Yan, and Jianping Xie. Scalable and Precise Synthesis of Thiolated Au_{10–12}, Au₁₅, Au₁₈, and Au₂₅ Nanoclusters via pH Controlled CO Reduction. *Chemistry of Materials*, 25(6):946–952, mar 2013. doi: 10.1021/cm304098x.
- [45] Yong Yu, Zhentao Luo, Yue Yu, Jim Yang Lee, and Jianping Xie. Observation of Cluster Size Growth in CO-Directed Synthesis of Au₂₅(SR)₁₈ Nanoclusters. *ACS Nano*, 6(9):7920–7927, aug 2012. doi: 10.1021/nn3023206.
- [46] Qiaofeng Yao, Yong Yu, Xun Yuan, Yue Yu, Jianping Xie, and Jim Yang Lee. Two-Phase Synthesis of Small Thiolate-Protected Au₁₅ and Au₁₈ Nanoclusters. *Small*, 9(16):2696–2701, feb 2013. doi: 10.1002/sml.201203112.
- [47] Xun Yuan, Bin Zhang, Zhentao Luo, Qiaofeng Yao, David Tai Leong, Ning Yan, and Jianping Xie. Balancing the Rate of Cluster Growth and Etching for Gram-Scale Synthesis of Thiolate-Protected Au₂₅ Nanoclusters with Atomic Precision. *Angewandte Chemie International Edition*, 53(18):4623–4627, mar 2014. doi: 10.1002/anie.201311177.
- [48] Huifeng Qian, Yan Zhu, and Rongchao Jin. Size-Focusing Synthesis, Optical and Electrochemical Properties of Monodisperse Au₃₈(SC₂H₄Ph)₂₄ Nanoclusters. *ACS Nano*, 3(11):3795–3803, oct 2009. doi: 10.1021/nn901137h.
- [49] Huifeng Qian and Rongchao Jin. Controlling Nanoparticles with Atomic Precision: The Case of Au₁₄₄(SCH₂CH₂Ph)₆₀. *Nano Letters*, 9(12):4083–4087, sep 2009. doi: 10.1021/nl902300y.
- [50] Yuichi Negishi, Sayaka Hashimoto, Ayano Ebina, Kota Hamada, Sakiat Hossain, and Tokuhisa Kawawaki. Atomic-level separation of thiolate-protected metal clusters. *Nanoscale*, 12(15):8017–8039, 2020. doi: 10.1039/d0nr00824a.
- [51] Stefan Knoppe, Julien Boudon, Igor Dolamic, Amala Dass, and Thomas Bürgi. Size Exclusion Chromatography for Semipreparative Scale Separation of Au₃₈(SR)₂₄ and Au₄₀(SR)₂₄ and Larger Clusters. *Analytical Chemistry*, 83(13):5056–5061, jun 2011. doi: 10.1021/ac200789v.
- [52] Lakshmi V. Nair, Sakiat Hossain, Shunjiro Takagi, Yukari Imai, Guoxiang Hu, Shota Wakayama, Bharat Kumar, Wataru Kurashige, De en Jiang, and Yuichi Negishi. Hetero-biicosahedral [Au₂₄Pd(PPh₃)₁₀(SC₂H₄Ph)₅Cl₂]²⁺ nanocluster: selective synthesis and optical and electrochemical properties. *Nanoscale*, 10(40):18969–18979, 2018. doi: 10.1039/c8nr04078h.
- [53] Yoshiki Niihori, Kana Yoshida, Sakiat Hossain, Wataru Kurashige, and Yuichi Negishi. Deepening the Understanding of Thiolate-Protected Metal Clusters Using High-Performance Liquid Chromatography. *Bulletin of the Chemical Society of Japan*, 92(3):664–695, mar 2019. doi: 10.1246/bcsj.20180357.
- [54] Yoshiki Niihori, Yuki Koyama, Seiichiro Watanabe, Sayaka Hashimoto, Sakiat Hossain, Lakshmi V. Nair, Bharat Kumar, Wataru Kurashige, and Yuichi Negishi. Atomic and Isomeric Separation of Thiolate-Protected Alloy Clusters. *The Journal of Physical Chemistry Letters*, 9(17):4930–4934, aug 2018. doi: 10.1021/acs.jpcclett.8b02211.

- [55] Yoshiki Niihori, Sayaka Hashimoto, Yuki Koyama, Sakiat Hossain, Wataru Kurashige, and Yuichi Negishi. Dynamic Behavior of Thiolate-Protected Gold-Silver 38-Atom Alloy Clusters in Solution. *The Journal of Physical Chemistry C*, 123(21):13324–13329, apr 2019. doi: 10.1021/acs.jpcc.9b02644.
- [56] Annelies Sels, Noelia Barrabés, Stefan Knoppe, and Thomas Bürgi. Isolation of atomically precise mixed ligand shell PdAu₂₄ clusters. *Nanoscale*, 8(21):11130–11135, 2016. doi: 10.1039/c6nr00931j.
- [57] Noelia Barrabés, Bei Zhang, and Thomas Bürgi. Racemization of Chiral Pd₂Au₃₆(SC₂H₄Ph)₂₄: Doping Increases the Flexibility of the Cluster Surface. *Journal of the American Chemical Society*, 136(41):14361–14364, sep 2014. doi: 10.1021/ja507189v.
- [58] Igor Dolamic, Stefan Knoppe, Amala Dass, and Thomas Bürgi. First enantioseparation and circular dichroism spectra of Au₃₈ clusters protected by achiral ligands. *Nature Communications*, 3(1), jan 2012. doi: 10.1038/ncomms1802.
- [59] Manzhou Zhu, Christine M. Aikens, Frederick J. Hollander, George C. Schatz, and Rongchao Jin. Correlating the Crystal Structure of A Thiol-Protected Au₂₅ Cluster and Optical Properties. *Journal of the American Chemical Society*, 130(18):5883–5885, apr 2008. doi: 10.1021/ja801173r.
- [60] Lallie C. McKenzie, Tatiana O. Zaikova, and James E. Hutchison. Structurally Similar Triphenylphosphine-Stabilized Undecagolds, Au₁₁(PPh₃)₇Cl₃ and [Au₁₁(PPh₃)₈Cl₂]Cl, Exhibit Distinct Ligand Exchange Pathways with Glutathione. *Journal of the American Chemical Society*, 136(38):13426–13435, sep 2014. doi: 10.1021/ja5075689.
- [61] Tiankai Chen, Qiaofeng Yao, Ricca Rahman Nasaruddin, and Jianping Xie. Electrospray Ionization Mass Spectrometry: A Powerful Platform for Noble-Metal Nanocluster Analysis. *Angewandte Chemie International Edition*, 58(35):11967–11977, aug 2019. doi: 10.1002/anie.201901970.
- [62] Yizhong Lu and Wei Chen. Application of Mass Spectrometry in the Synthesis and Characterization of Metal Nanoclusters. *Analytical Chemistry*, 87(21):10659–10667, jul 2015. doi: 10.1021/acs.analchem.5b00848.
- [63] Amala Dass, Anthony Stevenson, George R. Dubay, Joseph B. Tracy, and Royce W. Murray. Nanoparticle MALDI-TOF Mass Spectrometry without Fragmentation: Au₂₅(SCH₂CH₂Ph)₁₈ and Mixed Monolayer Au₂₅(SCH₂CH₂Ph)_{18-x}(L)_x. *Journal of the American Chemical Society*, 130(18):5940–5946, apr 2008. doi: 10.1021/ja710323t.
- [64] Yun-Peng Xie, Yang-Lin Shen, Guang-Xiong Duan, Jun Han, Lai-Ping Zhang, and Xing Lu. Silver nanoclusters: synthesis, structures and photoluminescence. *Materials Chemistry Frontiers*, 4(8):2205–2222, 2020. doi: 10.1039/d0qm00117a.
- [65] Srestha Basu, Anumita Paul, and Rodolphe Antoine. Controlling the Chemistry of Nanoclusters: From Atomic Precision to Controlled Assembly. *Nanomaterials*, 12(1):62, dec 2021. doi: 10.3390/nano12010062.
- [66] Sakiat Hossain, Yoshiki Niihori, Lakshmi V. Nair, Bharat Kumar, Wataru Kurashige, and Yuichi Negishi. Alloy Clusters: Precise Synthesis and Mixing Effects. *Accounts of Chemical Research*, 51(12):3114–3124, nov 2018. doi: 10.1021/acs.accounts.8b00453.
- [67] Tokuhisa Kawawaki, Yukari Imai, Daiki Suzuki, Shun Kato, Ibuki Kobayashi, Taiyo Suzuki, Ryo Kaneko, Sakiat Hossain, and Yuichi Negishi. Atomically Precise Alloy Nanoclusters. *Chemistry – A European Journal*, 26(69):16150–16193, oct 2020. doi: 10.1002/chem.202001877.

- [68] Sachil Sharma, Seiji Yamazoe, Tasuku Ono, Wataru Kurashige, Yoshiki Niihori, Katsuyuki Nobusada, Tatsuya Tsukuda, and Yuichi Negishi. Tuning the electronic structure of thiolate-protected 25-atom clusters by co-substitution with metals having different preferential sites. *Dalton Transactions*, 45(45): 18064–18068, 2016. doi: 10.1039/c6dt03214a.
- [69] Sakiat Hossain, Tasuku Ono, Mahiro Yoshioka, Guoxiang Hu, Mai Hosoi, Zhaoheng Chen, Lakshmi V. Nair, Yoshiki Niihori, Wataru Kurashige, De en Jiang, and Yuichi Negishi. Thiolate-Protected Trimetallic Au₂₀Ag₄Pd and Au₂₀Ag₄Pt Alloy Clusters with Controlled Chemical Composition and Metal Positions. *The Journal of Physical Chemistry Letters*, 9(10):2590–2594, apr 2018. doi: 10.1021/acs.jpcllett.8b00910.
- [70] Huifeng Qian, De en Jiang, Gao Li, Chakicherla Gayathri, Anindita Das, Roberto R. Gil, and Rongchao Jin. Monoplatinum Doping of Gold Nanoclusters and Catalytic Application. *Journal of the American Chemical Society*, 134(39):16159–16162, sep 2012. doi: 10.1021/ja307657a.
- [71] Yuichi Negishi, Wataru Kurashige, Yoshiki Niihori, Takeshi Iwasa, and Katsuyuki Nobusada. Isolation, structure, and stability of a dodecanethiolate-protected Pd₁Au₂₄ cluster. *Physical Chemistry Chemical Physics*, 12(23):6219, 2010. doi: 10.1039/b927175a.
- [72] Sachil Sharma, Wataru Kurashige, Katsuyuki Nobusada, and Yuichi Negishi. Effect of trimetallization in thiolate-protected Au_{24-n}Cu_nPd clusters. *Nanoscale*, 7(24):10606–10612, 2015. doi: 10.1039/c5nr01491c.
- [73] Lingwen Liao, Shiming Zhou, Yafei Dai, Liren Liu, Chuanhao Yao, Cenfeng Fu, Jinlong Yang, and Zhikun Wu. Mono-Mercury Doping of Au₂₅ and the HOMO/LUMO Energies Evaluation Employing Differential Pulse Voltammetry. *Journal of the American Chemical Society*, 137(30):9511–9514, jul 2015. doi: 10.1021/jacs.5b03483.
- [74] Douglas R. Kauffman, Dominic Alfonso, Christopher Matranga, Huifeng Qian, and Rongchao Jin. A Quantum Alloy: The Ligand-Protected Au_{25-x}Ag_x(SR)₁₈ Cluster. *The Journal of Physical Chemistry C*, 117(15):7914–7923, apr 2013. doi: 10.1021/jp4013224.
- [75] Yuichi Negishi, Takeyuki Iwai, and Mao Ide. Continuous modulation of electronic structure of stable thiolate-protected Au₂₅ cluster by Ag doping. *Chemical Communications*, 46(26):4713, 2010. doi: 10.1039/c0cc01021a.
- [76] Megumi Suyama, Shinjiro Takano, and Tatsuya Tsukuda. Synergistic Effects of Pt and Cd Codoping to Icosahedral Au₁₃ Superatoms. *The Journal of Physical Chemistry C*, 124(43):23923–23929, oct 2020. doi: 10.1021/acs.jpcc.0c06765.
- [77] Seiji Yamazoe, Wataru Kurashige, Katsuyuki Nobusada, Yuichi Negishi, and Tatsuya Tsukuda. Preferential Location of Coinage Metal Dopants (M = Ag or Cu) in [Au_{25-x}M_x(SC₂H₄Ph)₁₈]⁻ (x ~ 1) As Determined by Extended X-ray Absorption Fine Structure and Density Functional Theory Calculations. *The Journal of Physical Chemistry C*, 118(43):25284–25290, oct 2014. doi: 10.1021/jp5085372.
- [78] Chuanhao Yao, Yue jian Lin, Jinyun Yuan, Lingwen Liao, Min Zhu, Lin hong Weng, Jinlong Yang, and Zhikun Wu. Mono-cadmium vs Mono-mercury Doping of Au₂₅ Nanoclusters. *Journal of the American Chemical Society*, 137(49):15350–15353, dec 2015. doi: 10.1021/jacs.5b09627.
- [79] Shuxin Wang, Yongbo Song, Shan Jin, Xia Liu, Jun Zhang, Yong Pei, Xiangming Meng, Man Chen, Peng Li, and Manzhou Zhu. Metal Exchange Method Using Au₂₅ Nanoclusters as Templates for Alloy Nanoclusters with Atomic Precision. *Journal of the American Chemical Society*, 137(12):4018–4021, mar 2015. doi: 10.1021/ja511635g.
- [80] Wenwen Fei, Sabrina Antonello, Tiziano Dainese, Alessandro Dolmella, Manu Lahtinen, Kari Rissanen, Alfonso Venzo, and Flavio Maran. Metal Doping of Au₂₅(SR)₁₈⁻ Clusters: Insights and Hindsight. *Journal of the American Chemical Society*, 141(40):16033–16045, sep 2019. doi: 10.1021/jacs.9b08228.

- [81] Haru Hirai, Shinjiro Takano, and Tatsuya Tsukuda. Synthesis of Trimetallic (HPd@M₂Au₈)³⁺ Superatoms (M = Ag, Cu) via Hydride-Mediated Regioselective Doping to (Pd@Au₈)²⁺. *ACS Omega*, 4(4): 7070–7075, apr 2019. doi: 10.1021/acsomega.9b00575.
- [82] Shinjiro Takano, Shun Ito, and Tatsuya Tsukuda. Efficient and Selective Conversion of Phosphine-Protected (MAu₈)²⁺ (M = Pd, Pt) Superatoms to Thiolate-Protected (MAu₁₂)⁶⁺ or Alkynyl-Protected (MAu₁₂)⁴⁺ Superatoms via Hydride Doping. *Journal of the American Chemical Society*, 141(40):15994–16002, sep 2019. doi: 10.1021/jacs.9b08055.
- [83] Xi Kang and Manzhou Zhu. Metal Nanoclusters Stabilized by Selenol Ligands. *Small*, 15(43):1902703, sep 2019. doi: 10.1002/smll.201902703.
- [84] Wataru Kurashige, Masaki Yamaguchi, Katsuyuki Nobusada, and Yuichi Negishi. Ligand-Induced Stability of Gold Nanoclusters: Thiolate versus Selenolate. *The Journal of Physical Chemistry Letters*, 3(18):2649–2652, sep 2012. doi: 10.1021/jz301191t.
- [85] Wataru Kurashige, Seiji Yamazoe, Masaki Yamaguchi, Keisuke Nishido, Katsuyuki Nobusada, Tatsuya Tsukuda, and Yuichi Negishi. Au₂₅ Clusters Containing Unoxidized Tellurolates in the Ligand Shell. *The Journal of Physical Chemistry Letters*, 5(12):2072–2076, may 2014. doi: 10.1021/jz500901f.
- [86] Ying-Zhou Li, Rakesh Ganguly, Kar Yiu Hong, Yongxin Li, Malcolm Eugene Tessensohn, Richard Webster, and Weng Kee Leong. Stibine-protected Au₁₃ nanoclusters: syntheses, properties and facile conversion to GSH-protected Au₂₅ nanocluster. *Chemical Science*, 9(46):8723–8730, 2018. doi: 10.1039/c8sc03132k.
- [87] Justin B. Patty, Shana Havenridge, Dylan Tietje-Mckinney, Maxime A. Siegler, Kundan K. Singh, Roumina Hajy Hosseini, Mohamed Ghabin, Christine M. Aikens, and Anindita Das. Crystal Structure and Optical Properties of a Chiral Mixed Thiolate/Stibine-Protected Au₁₈ Cluster. *Journal of the American Chemical Society*, 144(1):478–484, dec 2021. doi: 10.1021/jacs.1c10778.
- [88] Zhen Lei, Xian-Kai Wan, Shang-Fu Yuan, Jia-Qi Wang, and Quan-Ming Wang. Alkynyl-protected gold and gold-silver nanoclusters. *Dalton Transactions*, 46(11):3427–3434, 2017. doi: 10.1039/c6dt04763g.
- [89] Mina R. Narouz, Kimberly M. Osten, Phillip J. Unsworth, Renee W. Y. Man, Kirsi Salorinne, Shinjiro Takano, Ryohei Tomihara, Sami Kaappa, Sami Malola, Cao-Thang Dinh, J. Daniel Padmos, Kennedy Ayoo, Patrick J. Garrett, Masakazu Nambo, J. Hugh Horton, Edward H. Sargent, Hannu Häkkinen, Tatsuya Tsukuda, and Cathleen M. Crudden. N-heterocyclic carbene-functionalized magic-number gold nanoclusters. *Nature Chemistry*, 11(5):419–425, apr 2019. doi: 10.1038/s41557-019-0246-5.
- [90] Hui Shen, Guocheng Deng, Sami Kaappa, Tongde Tan, Ying-Zi Han, Sami Malola, Shui-Chao Lin, Boon K. Teo, Hannu Häkkinen, and Nanfeng Zheng. Highly Robust but Surface-Active: An N-Heterocyclic Carbene-Stabilized Au₂₅ Nanocluster. *Angewandte Chemie International Edition*, 58(49): 17731–17735, dec 2019. doi: 10.1002/anie.201908983.
- [91] Hui Shen, Sijin Xiang, Zhen Xu, Chen Liu, Xihua Li, Cunfa Sun, Shuichao Lin, Boon K. Teo, and Nanfeng Zheng. Superatomic Au₁₃ clusters ligated by different N-heterocyclic carbenes and their ligand-dependent catalysis, photoluminescence, and proton sensitivity. *Nano Research*, 13(7):1908–1911, feb 2020. doi: 10.1007/s12274-020-2685-0.
- [92] Hui Shen, Zhen Xu, Maryam Sabooni Asre Hazer, Qingyuan Wu, Jian Peng, Ruixuan Qin, Sami Malola, Boon K. Teo, Hannu Häkkinen, and Nanfeng Zheng. Surface Coordination of Multiple Ligands Endows N-Heterocyclic Carbene-Stabilized Gold Nanoclusters with High Robustness and Surface Reactivity. *Angewandte Chemie International Edition*, 60(7):3752–3758, dec 2020. doi: 10.1002/anie.202013718.

- [93] Qing Tang and De en Jiang. Insights into the PhC≡C/Au Interface. *The Journal of Physical Chemistry C*, 119(20):10804–10810, oct 2014. doi: 10.1021/jp508883v.
- [94] Yuxiang Chen, Chenjie Zeng, Douglas R. Kauffman, and Rongchao Jin. Tuning the Magic Size of Atomically Precise Gold Nanoclusters via Isomeric Methylbenzenethiols. *Nano Letters*, 15(5):3603–3609, apr 2015. doi: 10.1021/acs.nanolett.5b01122.
- [95] Bihan Zhang, Jishi Chen, Yitao Cao, Osburg Jin Huang Chai, and Jianping Xie. Ligand Design in Ligand-Protected Gold Nanoclusters. *Small*, 17(27):2004381, jan 2021. doi: 10.1002/smll.202004381.
- [96] Milan Rambukwella, Naga Arjun Sakthivel, Jared H. Delcamp, Luca Sementa, Alessandro Fortunelli, and Amala Dass. Ligand Structure Determines Nanoparticles’ Atomic Structure, Metal-Ligand Interface and Properties. *Frontiers in Chemistry*, 6, aug 2018. doi: 10.3389/fchem.2018.00330.
- [97] Yingwei Li, Tatsuya Higaki, Xiangsha Du, and Rongchao Jin. Chirality and Surface Bonding Correlation in Atomically Precise Metal Nanoclusters. *Advanced Materials*, 32(41):1905488, mar 2020. doi: 10.1002/adma.201905488.
- [98] Stefan Knoppe, Sophie Michalet, and Thomas Bürgi. Stabilization of Thiolate-Protected Gold Clusters Against Thermal Inversion: Diastereomeric Au₃₈(SCH₂CH₂Ph)_{24-2x}(R-BINAS)_x. *The Journal of Physical Chemistry C*, 117(29):15354–15361, jul 2013. doi: 10.1021/jp4040908.
- [99] Xun Yuan, Nirmal Goswami, Ivan Mathews, Yong Yu, and Jianping Xie. Enhancing stability through ligand-shell engineering: A case study with Au₂₅(SR)₁₈ nanoclusters. *Nano Research*, 8(11):3488–3495, sep 2015. doi: 10.1007/s12274-015-0847-2.
- [100] Santosh Kumar and Rongchao Jin. Water-soluble Au₂₅(Capt)₁₈ nanoclusters: synthesis, thermal stability, and optical properties. *Nanoscale*, 4(14):4222, 2012. doi: 10.1039/c2nr30833a.
- [101] Qiaofeng Yao, Xun Yuan, Yong Yu, Yue Yu, Jianping Xie, and Jim Yang Lee. Introducing Amphiphilicity to Noble Metal Nanoclusters via Phase-Transfer Driven Ion-Pairing Reaction. *Journal of the American Chemical Society*, 137(5):2128–2136, jan 2015. doi: 10.1021/jacs.5b00090.
- [102] Gao Li, Hadi Abroshan, Chong Liu, Shuo Zhuo, Zhimin Li, Yan Xie, Hyung J. Kim, Nathaniel L. Rosi, and Rongchao Jin. Tailoring the Electronic and Catalytic Properties of Au₂₅ Nanoclusters via Ligand Engineering. *ACS Nano*, 10(8):7998–8005, jul 2016. doi: 10.1021/acsnano.6b03964.
- [103] Xun Yuan, Nirmal Goswami, Weiliang Chen, Qiaofeng Yao, and Jianping Xie. Insights into the effect of surface ligands on the optical properties of thiolated Au₂₅ nanoclusters. *Chemical Communications*, 52(30):5234–5237, 2016. doi: 10.1039/c6cc00857g.
- [104] Chenjie Zeng and Rongchao Jin. Chiral Gold Nanoclusters: Atomic Level Origins of Chirality. *Chemistry – An Asian Journal*, 12(15):1839–1850, jun 2017. doi: 10.1002/asia.201700023.
- [105] Yanfei Zhu, Jun Guo, Xueying Qiu, Shenlong Zhao, and Zhiyong Tang. Optical Activity of Chiral Metal Nanoclusters. *Accounts of Materials Research*, 2(1):21–35, dec 2020. doi: 10.1021/accountsmr.0c00057.
- [106] Yanan Wang and Thomas Bürgi. Ligand exchange reactions on thiolate-protected gold nanoclusters. *Nanoscale Advances*, 3(10):2710–2727, 2021. doi: 10.1039/d1na00178g.
- [107] Xi Kang and Manzhou Zhu. Transformation of Atomically Precise Nanoclusters by Ligand-Exchange. *Chemistry of Materials*, 31(24):9939–9969, nov 2019. doi: 10.1021/acs.chemmater.9b03674.
- [108] Michael J. Hostetler, Allen C. Templeton, and Royce W. Murray. Dynamics of Place-Exchange Reactions on Monolayer-Protected Gold Cluster Molecules. *Langmuir*, 15(11):3782–3789, apr 1999. doi: 10.1021/la981598f.

- [109] Yang Song and Royce W. Murray. Dynamics and Extent of Ligand Exchange Depend on Electronic Charge of Metal Nanoparticles. *Journal of the American Chemical Society*, 124(24):7096–7102, may 2002. doi: 10.1021/ja0174985.
- [110] Yang Song, Tao Huang, and Royce W. Murray. Heterophase Ligand Exchange and Metal Transfer between Monolayer Protected Clusters. *Journal of the American Chemical Society*, 125(38):11694–11701, aug 2003. doi: 10.1021/ja0355731.
- [111] Robert L. Donkers, Yang Song, and Royce W. Murray. Substituent Effects on the Exchange Dynamics of Ligands on 1.6 nm Diameter Gold Nanoparticles. *Langmuir*, 20(11):4703–4707, apr 2004. doi: 10.1021/la0497494.
- [112] Rui Guo, Yang Song, Gangli Wang, and Royce W. Murray. Does Core Size Matter in the Kinetics of Ligand Exchanges of Monolayer-Protected Au Clusters? *Journal of the American Chemical Society*, 127(8):2752–2757, feb 2005. doi: 10.1021/ja044638c.
- [113] Chenjie Zeng, Yuxiang Chen, Anindita Das, and Rongchao Jin. Transformation Chemistry of Gold Nanoclusters: From One Stable Size to Another. *The Journal of Physical Chemistry Letters*, 6(15):2976–2986, jul 2015. doi: 10.1021/acs.jpcclett.5b01150.
- [114] Yoshiki Niihori, Miku Matsuzaki, Thalappil Pradeep, and Yuichi Negishi. Separation of Precise Compositions of Noble Metal Clusters Protected with Mixed Ligands. *Journal of the American Chemical Society*, 135(13):4946–4949, mar 2013. doi: 10.1021/ja4009369.
- [115] Yingwei Li, Rosalba Juarez-Mosqueda, Yongbo Song, Yuzhuo Zhang, Jinsong Chai, Giannis Mpourmpakis, and Rongchao Jin. Ligand exchange on Au₃₈(SR)₂₄: substituent site effects of aromatic thiols. *Nanoscale*, 12(17):9423–9429, 2020. doi: 10.1039/d0nr01430c.
- [116] Marshall R. Ligare, J. Ulises Reveles, Niranjana Govind, Grant E. Johnson, and Julia Laskin. Influence of Interligand Interactions and Core-Charge Distribution on Gold Cluster Stability: Enthalpy Versus Entropy. *The Journal of Physical Chemistry C*, 123(40):24899–24911, sep 2019. doi: 10.1021/acs.jpcc.9b06597.
- [117] Annelies Sels, Giovanni Salassa, Stephan Pollitt, Clara Guglieri, Günther Rupprechter, Noelia Barrabés, and Thomas Bürgi. Structural Investigation of the Ligand Exchange Reaction with Rigid Dithiol on Doped (Pt, Pd) Au₂₅ Clusters. *The Journal of Physical Chemistry C*, 121(20):10919–10926, feb 2017. doi: 10.1021/acs.jpcc.6b12066.
- [118] Christine L. Heinecke, Thomas W. Ni, Sami Malola, Ville Mäkinen, O. Andrea Wong, Hannu Häkkinen, and Christopher J. Ackerson. Structural and Theoretical Basis for Ligand Exchange on Thiolate Monolayer Protected Gold Nanoclusters. *Journal of the American Chemical Society*, 134(32):13316–13322, aug 2012. doi: 10.1021/ja3032339.
- [119] Amendra Fernando and Christine M. Aikens. Ligand Exchange Mechanism on Thiolate Monolayer Protected Au₂₅(SR)₁₈ Nanoclusters. *The Journal of Physical Chemistry C*, 119(34):20179–20187, aug 2015. doi: 10.1021/acs.jpcc.5b06833.
- [120] Amendra Fernando and Christine M. Aikens. Deciphering the Ligand Exchange Process on Thiolate Monolayer Protected Au₃₈(SR)₂₄ Nanoclusters. *The Journal of Physical Chemistry C*, 120(27):14948–14961, jun 2016. doi: 10.1021/acs.jpcc.6b04516.
- [121] Thomas W. Ni, Marcus A. Tofanelli, Billy D. Phillips, and Christopher J. Ackerson. Structural Basis for Ligand Exchange on Au₂₅(SR)₁₈. *Inorganic Chemistry*, 53(13):6500–6502, jun 2014. doi: 10.1021/ic5010819.

- [122] Yanan Wang, Belén Nieto-Ortega, and Thomas Bürgi. Transformation from $[\text{Au}_{25}(\text{SCH}_2\text{CH}_2\text{CH}_2\text{CH}_3)_{18}]^0$ to $\text{Au}_{28}(\text{SCH}_2\text{CH}(\text{CH}_3)\text{Ph})_{21}$ gold nanoclusters: gentle conditions is enough. *Chemical Communications*, 55(99):14914–14917, 2019. doi: 10.1039/c9cc08872e.
- [123] Yukatsu Shichibu, Yuichi Negishi, Tatsuya Tsukuda, and Toshiharu Teranishi. Large-Scale Synthesis of Thiolated Au_{25} Clusters via Ligand Exchange Reactions of Phosphine-Stabilized Au_{11} Clusters. *Journal of the American Chemical Society*, 127(39):13464–13465, sep 2005. doi: 10.1021/ja053915s.
- [124] Chenjie Zeng, Tao Li, Anindita Das, Nathaniel L. Rosi, and Rongchao Jin. Chiral Structure of Thiolate-Protected 28-Gold-Atom Nanocluster Determined by X-ray Crystallography. *Journal of the American Chemical Society*, 135(27):10011–10013, jul 2013. doi: 10.1021/ja404058q.
- [125] Anu George, Anusree Sundar, Akhil S. Nair, Manju P. Maman, Biswarup Pathak, Nitya Ramanan, and Sukhendu Mandal. Identification of Intermediate $\text{Au}_{22}(\text{SR})_4(\text{SR}')_{14}$ Cluster on Ligand-Induced Transformation of $\text{Au}_{25}(\text{SR})_{18}$ Nanocluster. *The Journal of Physical Chemistry Letters*, 10(16):4571–4576, jul 2019. doi: 10.1021/acs.jpcclett.9b01856.
- [126] Chenjie Zeng, Chong Liu, Yuxiang Chen, Nathaniel L. Rosi, and Rongchao Jin. Gold–Thiolate Ring as a Protecting Motif in the $\text{Au}_{20}(\text{SR})_{16}$ Nanocluster and Implications. *Journal of the American Chemical Society*, 136(34):11922–11925, aug 2014. doi: 10.1021/ja506802n.
- [127] Yuxiang Chen, Chong Liu, Qing Tang, Chenjie Zeng, Tatsuya Higaki, Anindita Das, De en Jiang, Nathaniel L. Rosi, and Rongchao Jin. Isomerism in $\text{Au}_{28}(\text{SR})_{20}$ Nanocluster and Stable Structures. *Journal of the American Chemical Society*, 138(5):1482–1485, jan 2016. doi: 10.1021/jacs.5b12094.
- [128] Chenjie Zeng, Chunyan Liu, Yong Pei, and Rongchao Jin. Thiol Ligand-Induced Transformation of $\text{Au}_{38}(\text{SC}_2\text{H}_4\text{Ph})_{24}$ to $\text{Au}_{36}(\text{SPh}-t\text{-Bu})_{24}$. *ACS Nano*, 7(7):6138–6145, jun 2013. doi: 10.1021/nm401971g.
- [129] Katherine A. Parrish, Mary King, Marshall R. Ligare, Grant E. Johnson, and Heriberto Hernández. Role of sterics in phosphine-ligated gold clusters. *Physical Chemistry Chemical Physics*, 21(4):1689–1699, 2019. doi: 10.1039/c8cp04961k.
- [130] Wei Ma, Liguang Xu, André F. de Moura, Xiaoling Wu, Hua Kuang, Chuanlai Xu, and Nicholas A. Kotov. Chiral Inorganic Nanostructures. *Chemical Reviews*, 117(12):8041–8093, apr 2017. doi: 10.1021/acs.chemrev.6b00755.
- [131] Prakash Chandra Mondal, Deepak Asthana, Ranjeev Kumar Parashar, and Sakshi Jadhav. Imprinting chirality in inorganic nanomaterials for optoelectronic and bio-applications: strategies, challenges, and opportunities. *Materials Advances*, 2(23):7620–7637, 2021. doi: 10.1039/d1ma00846c.
- [132] T. Gregory Schaaff, Grady Knight, Marat N. Shafgullin, Raymond F. Borkman, and Robert L. Whetten. Isolation and Selected Properties of a 10.4 kDa Gold:Glutathione Cluster Compound. *The Journal of Physical Chemistry B*, 102(52):10643–10646, dec 1998. doi: 10.1021/jp9830528.
- [133] Manzhou Zhu, Huifeng Qian, Xiangming Meng, Shenshen Jin, Zhikun Wu, and Rongchao Jin. Chiral Au_{25} Nanospheres and Nanorods: Synthesis and Insight into the Origin of Chirality. *Nano Letters*, 11(9):3963–3969, aug 2011. doi: 10.1021/nl202288j.
- [134] Shinjiro Takano and Tatsuya Tsukuda. Amplification of the Optical Activity of Gold Clusters by the Proximity of BINAP. *The Journal of Physical Chemistry Letters*, 7(22):4509–4513, nov 2016. doi: 10.1021/acs.jpcclett.6b02294.

- [135] Takumi Nashimoto and Hiroshi Yao. Strong chiroptical activity in Au₂₅ clusters protected by mixed ligands of chiral phosphine and achiral thiolate. *Physical Chemistry Chemical Physics*, 22(27):15288–15294, 2020. doi: 10.1039/d0cp02543g.
- [136] Satyabrata Si, Cyrille Gautier, Julien Boudon, Rossana Taras, Serafino Gladiali, and Thomas Bürgi. Ligand Exchange on Au₂₅ Cluster with Chiral Thiols. *The Journal of Physical Chemistry C*, 113(30):12966–12969, jul 2009. doi: 10.1021/jp9044385.
- [137] Qian Xu, Santosh Kumar, Shenshen Jin, Huifeng Qian, Manzhou Zhu, and Rongchao Jin. Chiral 38-Gold-Atom Nanoclusters: Synthesis and Chiroptical Properties. *Small*, 10(5):1008–1014, oct 2013. doi: 10.1002/smll.201302279.
- [138] Hiroshi Yao. Chiral ligand-protected gold nanoclusters: Considering the optical activity from a viewpoint of ligand dissymmetric field. *Progress in Natural Science: Materials International*, 26(5):428–439, oct 2016. doi: 10.1016/j.pnsc.2016.08.006.
- [139] Makenzie R. Provorse and Christine M. Aikens. Origin of Intense Chiroptical Effects in Undecagold Subnanometer Particles. *Journal of the American Chemical Society*, 132(4):1302–1310, feb 2010. doi: 10.1021/ja906884m.
- [140] Michael-Rock Goldsmith, Christopher B. George, Gérard Zuber, Ron Naaman, David H. Waldeck, Peter Wipf, and David N. Beratan. The chiroptical signature of achiral metal clusters induced by dissymmetric adsorbates. *Phys. Chem. Chem. Phys.*, 8(1):63–67, 2006. doi: 10.1039/b511563a.
- [141] Xian-Kai Wan, Shang-Fu Yuan, Zhi-Wei Lin, and Quan-Ming Wang. A Chiral Gold Nanocluster Au₂₀ Protected by Tetradentate Phosphine Ligands. *Angewandte Chemie International Edition*, 53(11):2923–2926, feb 2014. doi: 10.1002/anie.201308599.
- [142] Stefan Knoppe, Igor Dolamic, Amala Dass, and Thomas Bürgi. Separation of Enantiomers and CD Spectra of Au₄₀(SCH₂CH₂Ph)₂₄: Spectroscopic Evidence for Intrinsic Chirality. *Angewandte Chemie International Edition*, 51(30):7589–7591, jun 2012. doi: 10.1002/anie.201202369.
- [143] Chenjie Zeng, Yuxiang Chen, Kristin Kirschbaum, Kannatassen Appavoo, Matthew Y. Sfeir, and Rongchao Jin. Structural patterns at all scales in a nonmetallic chiral Au₁₃₃(SR)₅₂ nanoparticle. *Science Advances*, 1(2), mar 2015. doi: 10.1126/sciadv.1500045.
- [144] Nan Yan, Nan Xia, Lingwen Liao, Min Zhu, Fengming Jin, Rongchao Jin, and Zhikun Wu. Unraveling the long-pursued Au₁₄₄ structure by X-ray crystallography. *Science Advances*, 4(10), oct 2018. doi: 10.1126/sciadv.aat7259.
- [145] Sami Malola, Sami Kaappa, and Hannu Häkkinen. Role of Nanocrystal Symmetry in the Crossover Region from Molecular to Metallic Gold Nanoparticles. *The Journal of Physical Chemistry C*, 123(33):20655–20663, jul 2019. doi: 10.1021/acs.jpcc.9b05863.
- [146] Sami Malola and Hannu Häkkinen. Chiral footprint of the ligand layer in the all-alkynyl-protected gold nanocluster Au₁₄₄(CCPhF)₆₀. *Chemical Communications*, 55(64):9460–9462, 2019. doi: 10.1039/c9cc04914b.
- [147] Cyrille Gautier and Thomas Bürgi. Vibrational circular dichroism of N-acetyl-l-cysteine protected gold nanoparticles. *Chemical Communications*, (43):5393, 2005. doi: 10.1039/b509346e.
- [148] Annelies Sels, Raymond Azoulay, Wybren Jan Buma, Mark A. J. Koenis, Valentin Paul Nicu, and Thomas Bürgi. Vibrational Circular Dichroism of Thiolate-Protected Au₂₅ Clusters: Accurate Prediction of Spectra and Chirality Transfer within the Mixed Ligand Shell. *The Journal of Physical Chemistry C*, 123(36):22586–22594, aug 2019. doi: 10.1021/acs.jpcc.9b05638.

- [149] Igor Dolamic, Birte Varnholt, and Thomas Bürgi. Chirality transfer from gold nanocluster to adsorbate evidenced by vibrational circular dichroism. *Nature Communications*, 6(1), may 2015. doi: 10.1038/ncomms8117.
- [150] Huifeng Qian, Manzhou Zhu, Chakicherla Gayathri, Roberto R. Gil, and Rongchao Jin. Chirality in Gold Nanoclusters Probed by NMR Spectroscopy. *ACS Nano*, 5(11):8935–8942, oct 2011. doi: 10.1021/nn203113j.
- [151] Stefan Knoppe and Thomas Bürgi. Chirality in Thiolate-Protected Gold Clusters. *Accounts of Chemical Research*, 47(4):1318–1326, mar 2014. doi: 10.1021/ar400295d.
- [152] Yanan Wang, Belén Nieto-Ortega, and Thomas Bürgi. Amplification of enantiomeric excess by dynamic inversion of enantiomers in deracemization of Au₃₈ clusters. *Nature Communications*, 11(1), sep 2020. doi: 10.1038/s41467-020-18357-0.
- [153] Yanfei Zhu, Hui Wang, Kaiwei Wan, Jun Guo, Chunting He, Yue Yu, Luyang Zhao, Yin Zhang, Jiawei Lv, Lin Shi, Renxi Jin, Xinxiang Zhang, Xinghua Shi, and Zhiyong Tang. Enantioseparation of Au₂₀(PP₃)₄Cl₄ Clusters with Intrinsically Chiral Cores. *Angewandte Chemie*, 130(29):9197–9201, jun 2018. doi: 10.1002/ange.201805695.
- [154] Masatake Haruta, Tetsuhiko Kobayashi, Hiroshi Sano, and Nobumasa Yamada. Novel Gold Catalysts for the Oxidation of Carbon Monoxide at a Temperature far Below 0 °C. *Chemistry Letters*, 16(2):405–408, feb 1987. doi: 10.1246/cl.1987.405.
- [155] Graham J. Hutchings. Vapor phase hydrochlorination of acetylene: Correlation of catalytic activity of supported metal chloride catalysts. *Journal of Catalysis*, 96(1):292–295, nov 1985. doi: 10.1016/0021-9517(85)90383-5.
- [156] Graham J. Hutchings and Jennifer K. Edwards. Application of Gold Nanoparticles in Catalysis. In *Metal Nanoparticles and Nanoalloys*, pages 249–293. Elsevier, 2012. doi: 10.1016/b978-0-08-096357-0.00001-7.
- [157] Manolis Stratakis and Hermenegildo Garcia. Catalysis by Supported Gold Nanoparticles: Beyond Aerobic Oxidative Processes. *Chemical Reviews*, 112(8):4469–4506, jun 2012. doi: 10.1021/cr3000785.
- [158] Lichen Liu and Avelino Corma. Metal Catalysts for Heterogeneous Catalysis: From Single Atoms to Nanoclusters and Nanoparticles. *Chemical Reviews*, 118(10):4981–5079, apr 2018. doi: 10.1021/acs.chemrev.7b00776.
- [159] Tamao Ishida, Toru Murayama, Ayako Taketoshi, and Masatake Haruta. Importance of Size and Contact Structure of Gold Nanoparticles for the Genesis of Unique Catalytic Processes. *Chemical Reviews*, 120(2):464–525, dec 2019. doi: 10.1021/acs.chemrev.9b00551.
- [160] Tokuhisa Kawawaki, Yuki Kataoka, Momoko Hirata, Yuki Iwamatsu, Sakiat Hossain, and Yuichi Negishi. Toward the creation of high-performance heterogeneous catalysts by controlled ligand desorption from atomically precise metal nanoclusters. *Nanoscale Horizons*, 6(6):409–448, 2021. doi: 10.1039/d1nh00046b.
- [161] Sarthak Gaur, Jeffrey T. Miller, Daniel Stellwagen, Ashwin Sanampudi, Challa S. S. R. Kumar, and James J. Spivey. Synthesis, characterization, and testing of supported Au catalysts prepared from atomically-tailored Au₃₈(SC₁₂H₂₅)₂₄ clusters. *Phys. Chem. Chem. Phys.*, 14(5):1627–1634, 2012. doi: 10.1039/c1cp22438g.

- [162] Bei Zhang, Annelies Sels, Giovanni Salassa, Stephan Pollitt, Vera Truttmann, Christoph Rameshan, Jordi Llorca, Wojciech Olszewski, Günther Rupprechter, Thomas Bürgi, and Noelia Barrabés. Ligand Migration from Cluster to Support: A Crucial Factor for Catalysis by Thiolate-protected Gold Clusters. *ChemCatChem*, 10(23):5372–5376, nov 2018. doi: 10.1002/cctc.201801474.
- [163] Clara Garcia, Vera Truttmann, Irene Lopez, Thomas Haunold, Carlo Marini, Christoph Rameshan, Ernst Pittenauer, Peter Kregsamer, Klaus Dobrezberger, Michael Stöger-Pollach, Noelia Barrabés, and Günther Rupprechter. Dynamics of Pd Dopant Atoms inside Au Nanoclusters during Catalytic CO Oxidation. *The Journal of Physical Chemistry C*, 124(43):23626–23636, oct 2020. doi: 10.1021/acs.jpcc.0c05735.
- [164] Stephan Pollitt, Vera Truttmann, Thomas Haunold, Clara Garcia, Wojciech Olszewski, Jordi Llorca, Noelia Barrabés, and Günther Rupprechter. The Dynamic Structure of Au₃₈(SR)₂₄ Nanoclusters Supported on CeO₂ upon Pretreatment and CO Oxidation. *ACS Catalysis*, 10(11):6144–6148, may 2020. doi: 10.1021/acscatal.0c01621.
- [165] Zili Wu, De en Jiang, Amanda K. P. Mann, David R. Mullins, Zhen-An Qiao, Lawrence F. Allard, Chenjie Zeng, Rongchao Jin, and Steven H. Overbury. Thiolate Ligands as a Double-Edged Sword for CO Oxidation on CeO₂ Supported Au₂₅(SCH₂CH₂Ph)₁₈ Nanoclusters. *Journal of the American Chemical Society*, 136(16):6111–6122, apr 2014. doi: 10.1021/ja5018706.
- [166] Rongchao Jin. The impacts of nanotechnology on catalysis by precious metal nanoparticles. *Nanotechnology Reviews*, 1(1):31–56, jan 2012. doi: 10.1515/ntrev-2011-0003.
- [167] H.-J. Freund, N. Ernst, M. Bäumer, G. Rupprechter, J. Libuda, H. Kuhlenbeck, T. Risse, W. Drachsel, K. Al-Shamery, and H. Hamann. Model Systems for Heterogeneous Catalysis: Quo Vadis Surface Science? In *Surface Chemistry and Catalysis*, pages 103–145. Springer US, 2002. doi: 10.1007/978-1-4757-6637-0_6.
- [168] Tatsuya Higaki, Yingwei Li, Shuo Zhao, Qi Li, Site Li, Xiang-Sha Du, Sha Yang, Jinsong Chai, and Rongchao Jin. Atomically Tailored Gold Nanoclusters for Catalytic Application. *Angewandte Chemie International Edition*, 58(25):8291–8302, mar 2019. doi: 10.1002/anie.201814156.
- [169] Yongmei Liu, Hironori Tsunoyama, Tomoki Akita, Songhai Xie, and Tatsuya Tsukuda. Aerobic Oxidation of Cyclohexane Catalyzed by Size-Controlled Au Clusters on Hydroxyapatite: Size Effect in the Sub-2 nm Regime. *ACS Catalysis*, 1(1):2–6, dec 2010. doi: 10.1021/cs100043j.
- [170] Clara García, Stephan Pollitt, Marte van der Linden, Vera Truttmann, Christoph Rameshan, Rafael Rameshan, Ernst Pittenauer, Günter Allmaier, Peter Kregsamer, Michael Stöger-Pollach, Noelia Barrabés, and Günther Rupprechter. Support effect on the reactivity and stability of Au₂₅(SR)₁₈ and Au₁₄₄(SR)₆₀ nanoclusters in liquid phase cyclohexane oxidation. *Catalysis Today*, 336:174–185, oct 2019. doi: 10.1016/j.cattod.2018.12.013.
- [171] Seiji Yamazoe, Tatchamapan Yoskamtorn, Shinjiro Takano, Sudarat Yadnum, Jumras Limtrakul, and Tatsuya Tsukuda. Controlled Synthesis of Carbon-Supported Gold Clusters for Rational Catalyst Design. *The Chemical Record*, 16(5):2338–2348, aug 2016. doi: 10.1002/tcr.201600074.
- [172] Yan Zhu, Huifeng Qian, and Rongchao Jin. An Atomic-Level Strategy for Unraveling Gold Nanocatalysis from the Perspective of Au_n(SR)_m Nanoclusters. *Chemistry - A European Journal*, 16(37):11455–11462, aug 2010. doi: 10.1002/chem.201001086.
- [173] Dan Yang and Yan Zhu. Evolution of catalytic activity driven by structural fusion of icosahedral gold cluster cores. *Chinese Journal of Catalysis*, 42(2):245–250, feb 2021. doi: 10.1016/s1872-2067(20)63659-2.

- [174] Yongnan Sun, Endong Wang, Yujing Ren, Kang Xiao, Xu Liu, Dan Yang, Yi Gao, Weiping Ding, and Yan Zhu. The Evolution in Catalytic Activity Driven by Periodic Transformation in the Inner Sites of Gold Clusters. *Advanced Functional Materials*, 29(38):1904242, jul 2019. doi: 10.1002/adfm.201904242.
- [175] Chao Liu, Chunyang Yan, Jizhi Lin, Changlin Yu, Jiahui Huang, and Gao Li. One-pot synthesis of Au₁₄₄(SCH₂Ph)₆₀ nanoclusters and their catalytic application. *Journal of Materials Chemistry A*, 3(40):20167–20173, 2015. doi: 10.1039/c5ta05747g.
- [176] Alessandro Longo, Ewoud J. J. Boed, Nisha Mammen, Marte Linden, Karoliina Honkala, Hannu Häkkinen, Petra E. Jongh, and Baira Donoeva. Towards Atomically Precise Supported Catalysts from Monolayer-Protected Clusters: The Critical Role of the Support. *Chemistry – A European Journal*, 26(31):7051–7058, apr 2020. doi: 10.1002/chem.202000637.
- [177] Yingwei Li, Yuxiang Chen, Stephen D. House, Shuo Zhao, Zahid Wahab, Judith C. Yang, and Rongchao Jin. Interface Engineering of Gold Nanoclusters for CO Oxidation Catalysis. *ACS Applied Materials & Interfaces*, 10(35):29425–29434, aug 2018. doi: 10.1021/acsami.8b07552.
- [178] Yan ZHU, Huifeng QIAN, Anindita DAS, and Rongchao JIN. Comparison of the Catalytic Properties of 25-Atom Gold Nanospheres and Nanorods. *Chinese Journal of Catalysis*, 32(6-8):1149–1155, jan 2011. doi: 10.1016/s1872-2067(10)60238-0.
- [179] Zili Wu, Guoxiang Hu, De en Jiang, David R. Mullins, Qian-Fan Zhang, Lawrence F. Allard, Lai-Sheng Wang, and Steven H. Overbury. Diphosphine-Protected Au₂₂ Nanoclusters on Oxide Supports Are Active for Gas-Phase Catalysis without Ligand Removal. *Nano Letters*, 16(10):6560–6567, oct 2016. doi: 10.1021/acs.nanolett.6b03221.
- [180] Weili Li, Chao Liu, Hadi Abroshan, Qingjie Ge, Xiujuan Yang, Hengyong Xu, and Gao Li. Catalytic CO Oxidation Using Bimetallic M_xAu_{25-x} Clusters: A Combined Experimental and Computational Study on Doping Effects. *The Journal of Physical Chemistry C*, 120(19):10261–10267, may 2016. doi: 10.1021/acs.jpcc.6b00793.
- [181] Shuxin Wang, Shan Jin, Sha Yang, Shuang Chen, Yongbo Song, Jun Zhang, and Manzhou Zhu. Total structure determination of surface doping [Ag₄₆Au₂₄(SR)₃₂](BPh₄)₂ nanocluster and its structure-related catalytic property. *Science Advances*, 1(7), aug 2015. doi: 10.1126/sciadv.1500441.
- [182] Irene López-Hernández, Vera Truttman, Clara Garcia, Christian Wittee Lopes, Christoph Rameshan, Michael Stöger-Pollach, Noelia Barrabés, Günther Rupprechter, Fernando Rey, and A. Eduardo Palomares. AgAu nanoclusters supported on zeolites: Structural dynamics during CO oxidation. *Catalysis Today*, 384-386:166–176, feb 2022. doi: 10.1016/j.cattod.2021.04.016.
- [183] Meenakshisundaram Sankar, Qian He, Rebecca V. Engel, Mala A. Sainna, Andrew J. Logsdail, Alberto Roldan, David J. Willock, Nishtha Agarwal, Christopher J. Kiely, and Graham J. Hutchings. Role of the Support in Gold-Containing Nanoparticles as Heterogeneous Catalysts. *Chemical Reviews*, 120(8):3890–3938, mar 2020. doi: 10.1021/acs.chemrev.9b00662.
- [184] Xiaotao Nie, Huifeng Qian, Qingjie Ge, Hengyong Xu, and Rongchao Jin. CO Oxidation Catalyzed by Oxide-Supported Au₂₅(SR)₁₈ Nanoclusters and Identification of Perimeter Sites as Active Centers. *ACS Nano*, 6(7):6014–6022, jun 2012. doi: 10.1021/nm301019f.
- [185] Bei Zhang, Clara García, Annelies Sels, Giovanni Salassa, Christoph Rameshan, Jordi Llorca, Klaudia Hradil, Günther Rupprechter, Noelia Barrabés, and Thomas Bürgi. Ligand and support effects on the reactivity and stability of Au₃₈(SR)₂₄ catalysts in oxidation reactions. *Catalysis Communications*, 130:105768, oct 2019. doi: 10.1016/j.catcom.2019.105768.

- [186] B. Zhang, S. Kaziz, H. Li, M. G. Hevia, D. Wodka, C. Mazet, T. Bürgi, and N. Barrabés. Modulation of Active Sites in Supported $\text{Au}_{38}(\text{SC}_2\text{H}_4\text{Ph})_{24}$ Cluster Catalysts: Effect of Atmosphere and Support Material. *The Journal of Physical Chemistry C*, 119(20):11193–11199, mar 2015. doi: 10.1021/jp512022v.
- [187] Gao Li, De en Jiang, Chao Liu, Changlin Yu, and Rongchao Jin. Oxide-supported atomically precise gold nanocluster for catalyzing Sonogashira cross-coupling. *Journal of Catalysis*, 306:177–183, oct 2013. doi: 10.1016/j.jcat.2013.06.017.
- [188] Gao Li, Chenjie Zeng, and Rongchao Jin. Thermally Robust $\text{Au}_{99}(\text{SPh})_{42}$ Nanoclusters for Chemoselective Hydrogenation of Nitrobenzaldehyde Derivatives in Water. *Journal of the American Chemical Society*, 136(9):3673–3679, feb 2014. doi: 10.1021/ja500121v.
- [189] Gunther G. Andersson, Vladimir B. Golovko, Jason F. Alvino, Trystan Bennett, Oliver Wrede, Sol M. Mejia, Hassan S. Al Qahtani, Rohul Adnan, Nathaniel Gunby, David P. Anderson, and Gregory F. Mehta. Phosphine-stabilised Au_9 clusters interacting with titania and silica surfaces: The first evidence for the density of states signature of the support-immobilised cluster. *The Journal of Chemical Physics*, 141(1):014702, jul 2014. doi: 10.1063/1.4884642.
- [190] Tatchamapan Yoskamtorn, Seiji Yamazoe, Ryo Takahata, Jun-ichi Nishigaki, Anawat Thivasasith, Jumras Limtrakul, and Tatsuya Tsukuda. Thiolate-Mediated Selectivity Control in Aerobic Alcohol Oxidation by Porous Carbon-Supported Au_{25} Clusters. *ACS Catalysis*, 4(10):3696–3700, sep 2014. doi: 10.1021/cs501010x.
- [191] Gao Li and Rongchao Jin. Gold Nanocluster-Catalyzed Semihydrogenation: A Unique Activation Pathway for Terminal Alkynes. *Journal of the American Chemical Society*, 136(32):11347–11354, jul 2014. doi: 10.1021/ja503724j.
- [192] Quanquan Shi, Zhaoxian Qin, Changlin Yu, Shuang Liu, Hui Xu, and Gao Li. Pyridine as a trigger in transformation chemistry from $\text{Au}_{144}(\text{SR})_{60}$ to aromatic thiolate-ligated gold clusters. *Nanoscale*, 12(8):4982–4987, 2020. doi: 10.1039/c9nr10522k.
- [193] Xian-Kai Wan, Jia-Qi Wang, Zi-Ang Nan, and Quan-Ming Wang. Ligand effects in catalysis by atomically precise gold nanoclusters. *Science Advances*, 3(10), oct 2017. doi: 10.1126/sciadv.1701823.
- [194] Kai Zheng, Jiangwei Zhang, Dan Zhao, Yong Yang, Zhimin Li, and Gao Li. Motif-mediated $\text{Au}_{25}(\text{SPh})_5(\text{PPh}_3)_{10}\text{X}_2$ nanorods with conjugated electron delocalization. *Nano Research*, 12(3):501–507, aug 2018. doi: 10.1007/s12274-018-2147-0.
- [195] Chao Liu, Hadi Abroshan, Chunyang Yan, Gao Li, and Masatake Haruta. One-Pot Synthesis of $\text{Au}_{11}(\text{PPH}_2\text{Py})_7\text{Br}_3$ for the Highly Chemoselective Hydrogenation of Nitrobenzaldehyde. *ACS Catalysis*, 6(1):92–99, dec 2015. doi: 10.1021/acscatal.5b02116.
- [196] Weili Li, Qingjie Ge, Xiangang Ma, Yuxiang Chen, Manzhou Zhu, Hengyong Xu, and Rongchao Jin. Mild activation of CeO_2 -supported gold nanoclusters and insight into the catalytic behavior in CO oxidation. *Nanoscale*, 8(4):2378–2385, 2016. doi: 10.1039/c5nr07498c.
- [197] Xiaotao Nie, Chenjie Zeng, Xiangang Ma, Huifeng Qian, Qingjie Ge, Hengyong Xu, and Rongchao Jin. CeO_2 -supported $\text{Au}_{38}(\text{SR})_{24}$ nanocluster catalysts for CO oxidation: a comparison of ligand-on and -off catalysts. *Nanoscale*, 5(13):5912, 2013. doi: 10.1039/c3nr00970j.
- [198] Bin Zhang, Jun Fang, Jingguo Li, Jun Jie Lau, Davide Mattia, Ziyi Zhong, Jianping Xie, and Ning Yan. Soft, Oxidative Stripping of Alkyl Thiolate Ligands from Hydroxyapatite-Supported Gold Nanoclusters for Oxidation Reactions. *Chemistry - An Asian Journal*, 11(4):532–539, dec 2015. doi: 10.1002/asia.201501074.

- [199] Sayantani Das, Anandarup Goswami, Mahdi Hesari, Jafar F. Al-Sharab, Eliška Mikmeková, Flavio Maran, and Tewodros Asefa. Reductive Deprotection of Monolayer Protected Nanoclusters: An Efficient Route to Supported Ultrasmall Au Nanocatalysts for Selective Oxidation. *Small*, 10(8):1473–1478, jan 2014. doi: 10.1002/sml.201302854.
- [200] Günther Rupprechter. Operando Surface Spectroscopy and Microscopy during Catalytic Reactions: From Clusters via Nanoparticles to Meso-Scale Aggregates. *Small*, 17(27):2004289, mar 2021. doi: 10.1002/sml.202004289.

2. Motivation and Objectives

Within this thesis, the influence of the ligand shell of Au nanoclusters is investigated. As outlined in Chapter 1, the ligands can have profound impact on several properties of the clusters, including solubility, stability, geometric structure, chirality or reactivity. In view of potential applications of these nanoclusters in fields like asymmetric or heterogeneous catalysis, the presented work mainly focuses on: (1) possibilities to modify cluster properties (with emphasis on chirality) of gold nanoclusters, as well as to obtain novel cluster structures by ligand engineering in solution phase and (2) on the influence of different protecting ligands in heterogeneous ligand-cluster-support systems.

Since the intrinsic chirality of certain Au nanoclusters, as well as the possibility of chirality induction by the protecting ligands, are among the most promising properties of these clusters in view of potential applications, one main focus was to selectively obtain enantiopure chiral nanoclusters. Furthermore, understanding their chiral properties, as well as their stability will be required for employing Au nanoclusters as functional chiral nanomaterials. Combining ligand-induced chirality with different core structures and intrinsic chirality of Au nanoclusters opens a broad variety of chiral structures to be explored. Thus, within the framework of this thesis, the **(chiral) properties of a test set of Au nanoclusters with a chiral thiol ligand** were investigated. Therefore, both intrinsically achiral (Au_{25}) and chiral (Au_{38} and Au_{144}) clusters were chosen.

For further investigation of such systems, including the influence of chiral ligands on the electronic structure and chiroptical spectroscopy (e.g. circular dichroism (CD) and vibrational circular dichroism (VCD) spectroscopy), complementary density functional theory (DFT) calculations can be useful. Thus, two selected systems were optimized and their optical and CD spectra simulated, aiming to create a suitable model for future experimental and computational studies.

Furthermore, Au nanoclusters can be obtained by different approaches, as further discussed in the Introduction (Chapter 1). A specific cluster structure obtained by direct synthesis or post-synthetic reactions is known to strongly depend on the specific conditions. Better understanding of these processes is therefore crucial to enable optimization of the synthesis procedures of Au nanoclusters, ultimately allowing more systematic approaches. Thus, focus was also placed on exploring different **synthesis strategies for Au nanoclusters**. The examples on this presented in the following Chapters 3 and 4 include a high-yield protocol toward chiral cluster structures employing a chiral thiolate as protecting ligand and the design

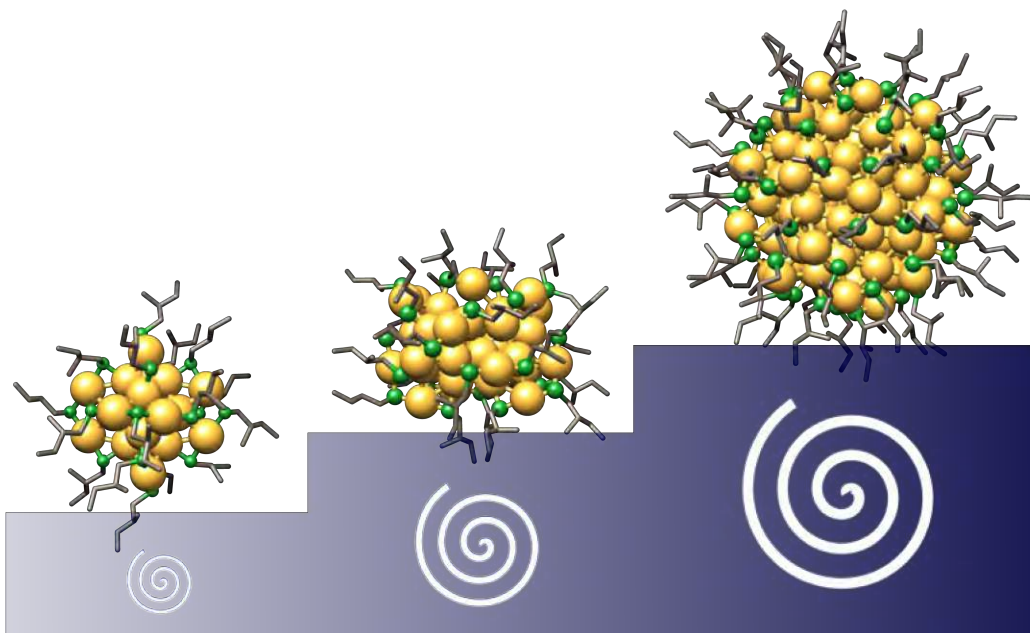
of a selective synthesis of Au₁₆ nanoclusters through a two-phase ligand-exchange-induced size/structure transformation (LEIST) process.

Moving to Au nanoclusters employed in heterogeneous catalytic reactions, the fate of their protecting ligands after supporting and activation treatments has often been neglected. However, in recent years, this subject has received more attention, owing to the influence these ligands can have on the activity and the structures of active sites present in the system. Broadening this knowledge is essential for the future design of tailored cluster catalysts for heterogeneous reactions. A third research question has therefore dealt with the **influence of protecting ligands on immobilized Au nanocluster catalysts**. Indeed, the influence of phosphine *versus* thiolate ligand in catalytic CO oxidation with CeO₂ supported Au nanoclusters was evaluated.

Interesting reaction! But what does it mean?!

Jack Skellington in *The Nightmare before Christmas*,
1993 movie by Henry Selick and Tim Burton

3. Inducing Chiral Properties to Au Nanoclusters by a Chiral Thiol Ligand



3.1. Chirality driven synthesis of intrinsically chiral cluster structures in high yield

Vera Truttmann, Adea Loxha, Rares Banu, Ernst Pittenauer, Noelia Barrabés

The content of this section has been submitted for publication in the current form.

3.1.1. Abstract

Chiral Au nanoclusters capable of holding chirality at different levels are not only of particular interest to study chirality at a fundamental level, but are also promising nanomaterials for sensing or catalysis. However, the low yield and the tedious necessary separation of their intrinsic enantiomeric forms still prevents their extended use. Herein, we applied the chiral ligand (2-MeBuSH) in the synthesis of Au₂₅, Au₃₈ and Au₁₄₄ nanoclusters. Preferential formation of intrinsically chiral clusters was observed, leading to outstanding yields of the chiral Au₃₈ and Au₁₄₄ nanoclusters. For Au₃₈, comparison of the chiral properties probed by circular dichroism spectroscopy with previously reported spectra of separated enantiomers with achiral ligands confirmed only one enantiomeric form of the cluster was present. The chiral properties are mostly preserved up to a temperature of 80 °C, with differences observed depending on the cluster structures, in consistence with previously reported experimental and theoretical studies. This demonstrates the critical effect of the chiral ligand in directing the chirality of Au nanoclusters and the importance of careful ligand design in the preparation of intrinsically chiral species.

3.1.2. Introduction

Compounds featuring chiral properties are omnipresent in nature and have attracted significant interest in science since their discovery in the 19th century.^[1] Especially in the production of pharmaceuticals, single enantiomers nowadays play a key role due to the potentially different behaviour of a pair of enantiomers.^[2] The development of chiral nanomaterials plays an important role in various fields, such as catalysis, sensing or medicine.^[3,4] However, transferring chirality from the molecular scale to the nanoscale requires the use of well-defined chiral nanomaterials. This would allow to study their chiral properties while gaining an understanding of chirality at the molecular level.

Chiral ligand protected metal nanoclusters are an emerging class of atomically precise nanomaterials that presents molecular like properties, resolved structures and can hold chirality at different levels.^[5-8] They consist of a Au core stabilized by a ligand monolayer often composed of thiolates,^[5,6,9,10] although other types of ligands^[5,10] are known. In general, imparting chirality to the nanocluster is possible by introducing chiral protecting ligands,^[11,12] which was first observed by Whetten *et al.* with L-glutathione (GSH) protected gold nanoclusters 20 years ago.^[13] Moreover, several different Au nanoclusters also exhibit chiral properties even

when protected by only achiral ligands, which has become known as intrinsic chirality and was first discovered for the crystal structures of $\text{Au}_{102}(\text{SR})_{44}$ and $\text{Au}_{38}(\text{SR})_{24}$.^[14,15] The number of intrinsically chiral $\text{Au}_n(\text{SR})_m$ nanoclusters is increasing nowadays: $\text{Au}_{20}(\text{SR})_{16}$, $\text{Au}_{28}(\text{SR})_{20}$, $\text{Au}_{38}(\text{SR})_{24}$, $\text{Au}_{102}(\text{SR})_{44}$, $\text{Au}_{133}(\text{SR})_{52}$ and $\text{Au}_{144}(\text{SR})_{60}$ are all proven to be chiral, despite all their thiolate ligands SR being achiral.^[5,8,14–19]

Taking a close look to the structure of thiolate-protected gold nanoclusters structure reveals that it is composed of Au cores protected by short $-(\text{S}(\text{R})-\text{Au})_x-\text{S}(\text{R})-$ units of different length ($x = 1, 2, 3, \dots$), often called staples.^[6] Therefore, the intrinsic chirality in thiolate-protected gold clusters can have different origins, such as a chiral Au-S interface or a chiral Au kernel.^[5,7,11,12,20] In addition, a chiral arrangement of ligands can be detected in several structures, although it has never been identified as the sole origin of intrinsic chirality. Combinations of more than one chiral element in a nanocluster structure has become known as hierarchical chirality.^[11,12] An extended and detailed study on the different chiral nanoclusters by Jin's group suggested that the bonding of the ligands on the Au surface (metal-ligand interface) can be considered the main origin of intrinsic chirality in thiolate protected Au nanoclusters.^[7] It should be noted that when achiral ligands are used to synthesize intrinsically chiral Au nanoclusters, a racemic mixture is obtained.^[11,21]

In order to obtain enantiopure forms of chiral nanoclusters, three main approaches are possible: i) direct synthesis approach with chiral ligands, ii) post-synthetic introduction of chiral ligands by ligand exchange reactions or iii) separation of racemic mixtures of intrinsically chiral clusters.^[11] The latter was first achieved by Bürgi and coworkers, who achieved enantioseparation of $\text{Au}_{38}(\text{2-PET})_{24}$ (2-PET: 2-phenylethanethiol) by using chiral high-performance liquid chromatography (HPLC).^[21] $\text{Au}_{38}(\text{2-PET})_{24}$ displayed strong signals in circular dichroism (CD) spectroscopy, which is due to the chiral arrangement of the $-(\text{S-Au})_2-\text{S}-$ staple units on both sides of the biicosahedral Au_{23} kernel.^[8,15,22] The CD spectra of each enantiomeric form lead to perfect mirror images,^[21] in good agreement with density functional theory (DFT) predictions^[23] and enabled the assignment of the right- and left-handed enantiomers. However, in general, individual methods for chromatographic separation need to be developed for each chiral nanocluster composition, which can be a time-consuming and complex process.

Upon comparing direct synthesis and ligand exchange, it is worth noting that both approaches can be used to either induce chirality to achiral clusters or to enhance the intrinsic chiral properties.^[9] The use of ligand exchange is more versatile in terms of steric^[6,9] and solubility^[9] of the ligands. One example would be the introduction of bidentate chiral thiol ligands, 1,1'-binaphthyl-2,2'-dithiol (BINAS), to Au_{25} ^[23–26] and Au_{38} ^[27] nanoclusters. In addition, change in the intrinsic chiral properties and thus symmetry breaking of an originally racemic $\text{Au}_{38}(\text{2-PET})_{24}$ mixture after ligand exchange with BINAS has been reported recently.^[28] However, inhomogeneous ligand compositions in the cluster sample after exchange are common,^[6,9,24,29,30] as are size and/or structure transformations of the Au nanoclusters.^[5,9,31–33]

These complications can be avoided by applying the chiral ligand directly in the synthesis process. For thiolate-protected Au nanoclusters, adapted Brust procedures are mostly ap-

plied.^[5,10,34,35] Several factors are known to influence the outcome of a synthesis, including the solvent,^[5,10] the type of ligand,^[5,6,10,34] the kinetics of the $Au_x(SR)_y$ formation^[5,6,34,36] or the size focusing step after reduction.^[5,6,34,36] By optimizing these factors, a number of chiral nanoclusters can be obtained almost monodisperse nowadays.^[5,10] Nevertheless, the preparation of Au nanoclusters typically suffers from relatively low yields, making the practical applicability of these materials difficult.^[37,38] Thus, several attempts have been made in the last years to develop high-yield Au nanocluster synthesis protocols.^[37–40]

Direct synthesis of chiral Au nanoclusters with induced chirality has, for example, been reported for $Au_{25}(2\text{-PPT})_{18}$ and biicosahedral $[Au_{25}(2\text{-PPT})_5(PPh_3)_{10}Cl_2]^{2+}$ (2-PPT: 2-phenylpropanethiol).^[41] Both clusters exhibited CD signals up to at least 500 nm, which can be ascribed to mixing of orbitals of the chiral protecting ligands with those of the achiral Au kernel.^[41,42] If the synthesis is carried out with an intrinsically chiral cluster instead, one enantiomeric form of the cluster can be obtained, thus avoiding post-synthetic separation by chiral chromatography. This has been demonstrated by Jin and coworkers for $Au_{38}(SR)_{24}$ nanoclusters protected by 2-PPT, captotril and L-glutathione. They further reported a strong influence of the chiral ligand on the CD signal, which illustrates the importance of considering all levels of chirality in Au nanocluster systems.^[43] The significant effect of different chiral ligands on the chiral properties of Au nanoclusters has also been reported for Au_{11} ^[44,45] and Au_{125} ^[46]. Although several studies have shown the critical influence of ligands and the different approaches to obtain chiral nanoclusters, in terms of practical applications, high yields in combination with strong chiroptical activity have still not been achieved.^[7]

In this study, highly pure chiral Au_{25} , Au_{38} and Au_{144} nanoclusters were prepared using the chiral thiol ligand, (*S*)-2-methylbutanethiol (2-MeBuSH). The yield of the intrinsically chiral clusters Au_{38} and Au_{144} was significantly higher compared to the analogous synthesis using butanethiol (HS-Bu) or 2-phenylethanethiol (2-PET) as ligands. The formation of the enantiomers was confirmed by comparing the circular dichroism (CD) spectra of the $Au_{38}(2\text{-MeBuS})_{24}$ and $Au_{144}(2\text{-MeBuS})_{60}$ with data reported by other authors.^[21,23,47,48] Moreover, the chiral properties are mostly preserved upon heating to 80 °C without a drastic decrease in the CD signal, confirming that this ligand preferentially produces stable chiral clusters in high yield.

3.1.3. Results

3.1.3.1. Chiral Nanocluster synthesis with 2-MeBuSH

Two cluster sizes known to be intrinsically chiral, $Au_{38}(2\text{-MeBuS})_{24}$ and $Au_{144}(2\text{-MeBuS})_{60}$ were prepared, following published direct synthesis protocols using the chiral (*S*)-2-MeBuSH ligand (see Section 3.1.4.1.1 and 3.1.4.1.2).^[49,50] In addition, $[Au_{25}(2\text{-MeBuS})_{18}]TOA$, which does not exhibit intrinsically chiral features, was prepared for comparison.^[51] The clusters were characterized by UV-Vis spectroscopy (see Figure 3.1) and matrix-assisted laser desorption-ionization (MALDI) mass spectrometry (Figure 3.7 - 3.9).

The first unexpected observation was the substantially increased yield of pure chiral clusters

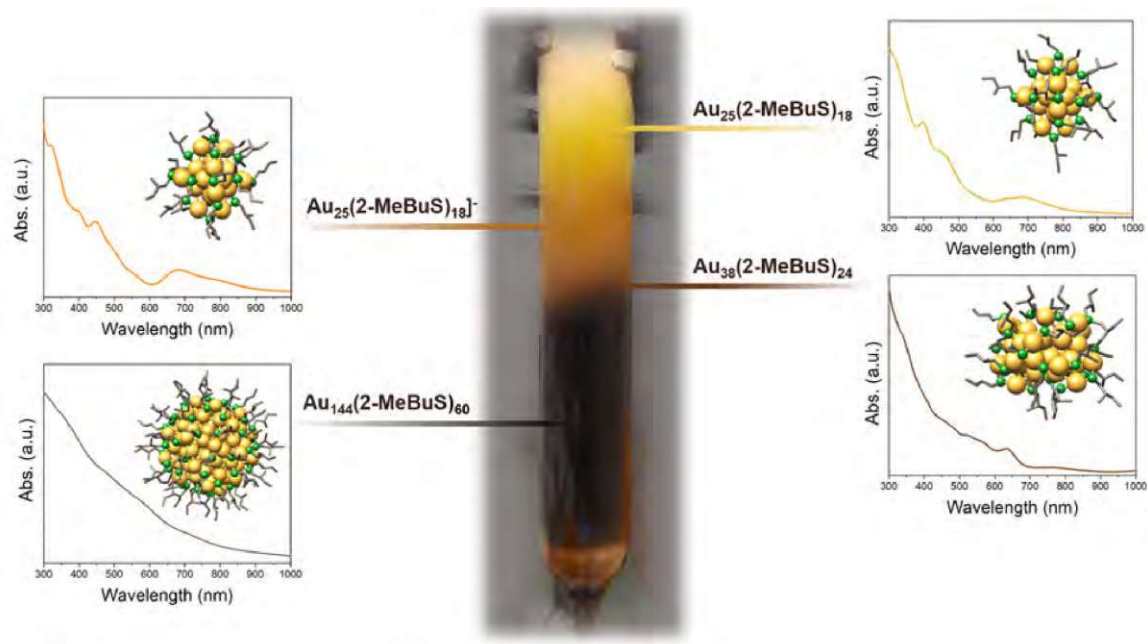


Figure 3.1.: Exemplary picture of a size exclusion separation after a $\text{Au}_{144}(\text{2-MeBuS})_{60}$ synthesis and corresponding UV-Vis spectra of the isolated products. The in-sets show exemplary structures of the (*S*)-2-MeBuS protected Au nanoclusters. Note that the enantiomers chosen in the representation of $\text{Au}_{38}(\text{2-MeBuS})_{24}$ and $\text{Au}_{144}(\text{2-MeBuS})_{60}$ are not necessarily the enantiomers formed during synthesis.

in the synthesis of both Au_{38} and Au_{144} , compared to the reported yields obtained with similar achiral ligands.^[37,38,49] In the case of Au_{38} , a yield of 78 % was achieved using 2-MeBuSH as opposed to 26 % with HS-Bu (which differs from 2-MeBuSH only in the absence of the methyl group on the β -carbon atom). Similarly, for Au_{144} , a yield of 73 % was obtained with 2-MeBuSH versus 34 % with HS-Bu. However, this trend was not observed for the achiral Au_{25} cluster, of which similar quantities were obtained for both ligands (25 % for 2-MeBuSH and 23 % for HS-Bu). Therefore, the preferential formation of intrinsically chiral clusters due to the chiral environment provided by the new chiral ligand is observed, resulting in high yields of enantiopure clusters. This seems to be related to differences in the arrangement of the two enantiomers of the chiral ligands on the surface of the Au core.^[52]

A common by-product in the synthesis of Au_{144} is Au_{25} , which was previously reported by Qian and coauthors^[49] and which was also observed in our study using 2-PET or HS-Bu as ligands. However, performing the synthesis with the chiral ligand 2-MeBuSH, the intrinsically chiral Au_{38} cluster is also formed in addition. Figure 3.1 shows the size exclusion chromatography of the crude product obtained after the Au_{144} synthesis with 2-MeBuSH as ligand. As is evident, the main fraction obtained corresponds to Au_{144} , with smaller amounts of Au_{38} , as well as both neutral and anionic Au_{25} eluting afterwards. The characteristic UV-Vis spectra of each cluster, together with the MALDI-MS analysis (Figure 3.7 - 3.9),

confirmed the purity of each fraction. An unexpected product distribution was also observed in the synthesis of Au₂₅ using 2-MeBuSH, where a considerable amount of Au₁₄₄ was obtained as a side product, whereas no Au₁₄₄ was formed using HS-Bu as ligand. Furthermore, even though the anionic form of Au₂₅ was still the main product, an increased amount of the neutral species was obtained compared to conventional synthesis.

Thus, the preferential formation of intrinsically chiral Au nanocluster using 2-MeBuSH as chiral ligand in the synthesis is disclosed. This could be related to the effect of one chiral center influencing another, which is commonly observed in chemistry and biology but, to the best of our knowledge, has not yet been observed with Au nanoclusters to this extent (i.e. increased yield and shift toward intrinsically chiral clusters).

3.1.3.2. Chiroptical properties

The chiral properties of the 2-MeBuSH protected Au nanoclusters were studied by CD spectroscopy (see Figure 3.2a). The spectra are very different from those of the chiral 2-MeBuSH ligand (Figure 3.11), confirming that the structural chirality is not only located in the ligand backbone. Both Au₃₈(2-MeBuS)₂₄ and Au₁₄₄(2-MeBuS)₆₀ showed low-energy signals above 500 nm, consistent with the CD signal being majorly influenced by the Au kernel orbitals.^[42] This was also observed for [Au₂₅(2-MeBuS)₁₈]⁻, however, of significantly lower intensity compared to the intrinsically chiral clusters. Nevertheless, a contribution from the core orbitals also seems likely for this intrinsically achiral cluster, since the signals appear significantly red-shifted with respect to those of the free ligand (Figure 3.11).^[41]

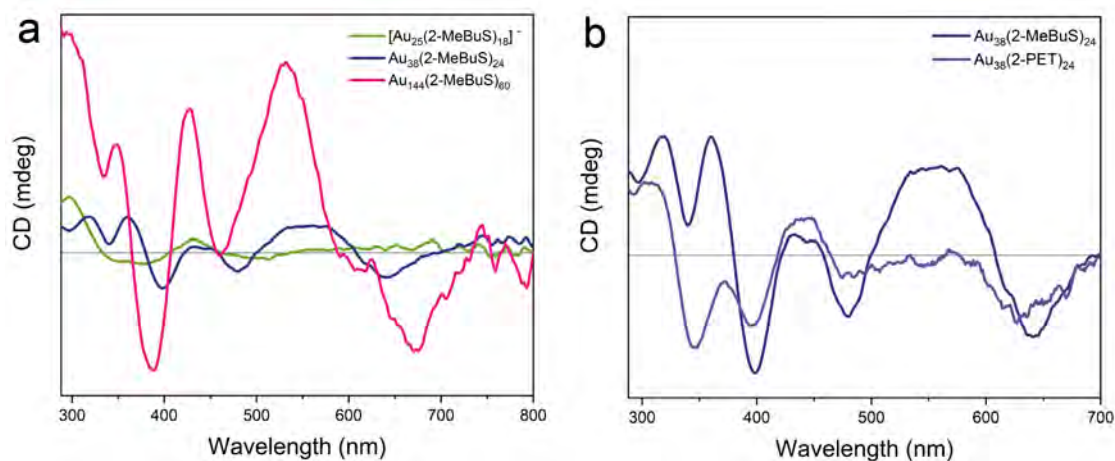


Figure 3.2.: *a*: Normalized CD spectra of the [Au₂₅(2-MeBuS)₁₈]⁻, Au₃₈(S-MeBuS)₂₄ and Au₁₄₄(S-MeBuS)₆₀ nanoclusters at RT; *b*: comparison of the CD spectra of Au₃₈(2-MeBuS)₂₄ and the enantiomer of Au₃₈(2-PET)₂₄ eluting first during a HPLC separation following the procedure by Dolamic *et al.*^[21]

The relative intensity of the normalized CD signals of the three clusters is compared in Figure 3.2a. The Au₁₄₄(2-MeBuS)₆₀ cluster clearly exhibits the strongest signal, followed by

the one of $\text{Au}_{38}(\text{2-MeBuS})_{24}$ and lastly $[\text{Au}_{25}(\text{2-MeBuS})_{18}]^-$. Taking the intrinsically chiral nature of the Au_{144} and Au_{38} clusters into account, this can be attributed to a cooperative effect between ligand and core/staple arrangement.^[15,21,23]

In the case of Au_{38} , its chiral properties mainly originate from the Au-S interface where the staple motifs $-(\text{S}(\text{R})-\text{Au})_2-\text{S}(\text{R})-$ are self-assembled into chiral patterns.^[12,15,23] Similarly, Au_{144} shows five rings of monomeric staple units, the orientation of which imparts chirality to the structure.^[19,53,54] The strong chiral properties of Au_{144} were predicted by DFT calculations by Malola and Häkkinen,^[47,48,55] showing that even the core itself already leads to a noticeable CD signal.^[48] Their reported theoretical relative intensities of Au_{144} and Au_{38} are in agreement with the ones observed experimentally for $\text{Au}_{144}(\text{2-MeBuS})_{60}$ and $\text{Au}_{38}(\text{2-MeBuS})_{24}$. The stronger signal of Au_{144} is attributed to the chiral arrangement of the 30 staple units on the core surface, which amplify the already strong chirality from the core itself.^[48]

In addition, compared to Au_{38} , Au_{144} has been predicted to be significantly more stable against rearrangement procedures resulting in inversion of chirality (and thus potential racemization of enantiopure cluster samples).^[55]

Furthermore, for both intrinsically chiral clusters, one can presume that only one chiral cluster enantiomer is formed, which would indicate the chiral ligand directing the chirality of the Au-ligand interface. To clarify this, the CD spectrum of $\text{Au}_{38}(\text{2-MeBuS})_{24}$ was compared to those of the two enantiomers of $\text{Au}_{38}(\text{2-PET})_{24}$ separated by chiral HPLC (Figure 3.10).^[21] As can be seen from Figure 3.2b, the enantiomer first eluting during the HPLC separation exhibits strong similarities to the one of $\text{Au}_{38}(\text{2-MeBuS})_{24}$, thus suggesting that this isomer was preferentially obtained by the synthesis with (*S*)-2-MeBuSH.

This is further confirmed when performing a chiral HPLC separation of $\text{Au}_{38}(\text{2-MeBuS})_{24}$, employing the published method for the separation $\text{Au}_{38}(\text{2-PET})_{24}$.^[21] The corresponding chromatograms of both separations are presented in Figure 3.12. Only one major peak can be observed at a retention of 2 min, whereas the racemic $\text{Au}_{38}(\text{2-PET})_{24}$ exhibits two peaks at 11.3 min and 23.2 min. The differences in retention time between the $\text{Au}_{38}(\text{2-MeBuS})_{24}$ and the first $\text{Au}_{38}(\text{2-PET})_{24}$ enantiomer is attributed to the influence of the ligand present.

For Au_{144} , the question if only one enantiomer is formed during synthesis cannot currently be addressed due to the lack of experimental spectra of separated Au_{144} enantiomers from racemic mixtures. The separation of the enantiomeric forms of Au_{144} has not yet been achieved, so the only possible reference is the calculated CD spectra. The comparison at the lower energy part of the spectrum (> 500 nm) where the influence of the chiral ligand should be negligible with calculated spectra by Häkkinen and coworkers^[47,48] could indicate preferential formation of the right-handed enantiomer. However, it should be noted that deviations from the computed and experimentally measured spectrum, especially in the near UV and UV-region, render a definite assignment impossible. Presence of both forms in the sample cannot be excluded either at this point.

3.1.3.3. Temperature stability of the chiral clusters

An important aspect when dealing with intrinsically chiral Au nanoclusters is their stability against racemization, i.e. structural reorganization processes in the core-ligand interface.^[20,55,56] This will usually affect their circular dichroism spectra, resulting in diminished features and ultimately loss of chiroptical activity.^[20,56] Thus, the temperature stability of the clusters was tested by *in situ* CD measurements at elevated temperatures. Therefore, the clusters were dissolved in toluene and heated to 80 °C *in situ*, with CD spectra measured every 10 °C.

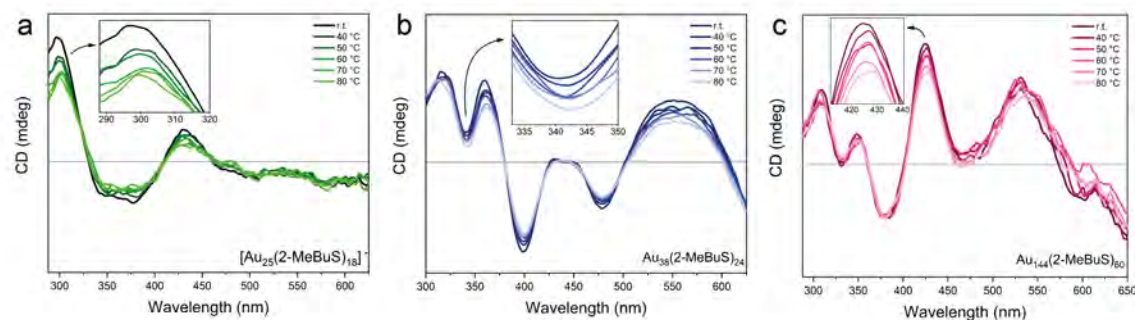


Figure 3.3.: Evolution of the CD spectra with increasing temperature (RT to 80 °C): $[\text{Au}_{25}(\text{2-MeBuS})_{18}]^-$ (a), $\text{Au}_{38}(\text{2-MeBuS})_{24}$ (b) and $\text{Au}_{144}(\text{2-MeBuS})_{60}$ (c)

For Au_{38} , the CD spectra measured at the different temperatures are displayed in Figure 3.3. The band at 341 nm was chosen for quantification of the relative decrease in CD signal. At 40 °C a decrease to 88 % of the original intensity was observed, at 50 °C and 60 °C to 72 %, and at 70 °C to 70 % relative to the original signal. Comparing this to the study performed by Bürgi's group,^[56] it can be deduced that the stability against racemization of the $\text{Au}_{38}(\text{2-MeBuS})_{24}$ cluster is higher than that of a single enantiomer of $\text{Au}_{38}(\text{2-PET})_{24}$. By analyzing the relative intensities of the band at 345 nm, relative intensities of 97 % for 40 °C, 92 % for 50 °C, 65 % for 60 °C, and 23 % for 70 °C were calculated.

It should be noted that at low temperatures (40 °C and 50 °C) the 2-PET cluster shows slightly higher stability, whereas at higher temperatures (60 °C and 70 °C), the 2-MeBuS-cluster retains a significantly higher CD signal as compared to the 2-PET cluster. The different behavior depending on the temperature suggests that the racemization process is dependent on multiple factors. The higher stability of the 2-PET cluster could be attributed to the larger size of the 2-PET as compared to the 2-MeBuSH, which could offer a slight steric advantage for the 2-PET cluster, resulting in the higher retainment of the CD signal. However, the drastic decrease of the 2-PET cluster at higher temperatures, and the stability of the 2-MeBuS-cluster, imply a second factor responsible for the retainment of chirality. The addition of a second chiral level through the optically active 2-MeBuSH seems to increase the nanocluster's stability against racemization processes at higher temperatures, when the steric

protection offered by bulkier ligands is not sufficient anymore.

The CD spectra of Au₂₅ and Au₁₄₄ at different temperatures can be found in Figure 3.3a and Figure 3.3c. Regarding the stability of the Au₁₄₄ nanocluster, the band at 425 nm was considered for the relative decrease in the CD signal. A percentual decrease to 82 % of the original intensity was observed at 70 °C, which is lower than that of the Au₃₈, indicating a higher stability of the Au₁₄₄ cluster. This is in accordance with the calculations performed by Malola *et al.*,^[55] who state that the energy barrier for the inversion of Au₃₈ should lie lower than the one of Au₁₄₄. Of note, the thermal energy brought to the system by heating to 70 °C should be significantly lower than their estimated activation energies.

3.1.3.4. Discussion

Summarizing, a chiral thiol ligand has been prepared, with which chiral Au nanoclusters can be synthesized in unprecedentedly high yield. This chiral thiol can be used to drive the synthesis of gold nanoclusters toward intrinsically chiral, monodisperse products. By employing 2-MeBuSH in the preparation of Au₁₄₄ and Au₃₈ nanoclusters, the yield could be drastically increased (by about 350 %), as compared to previous accounts.^[49,57] Furthermore, a shift in the product distribution of the nanocluster syntheses was observed in the syntheses of Au₁₄₄ and Au₂₅, which delivered noteworthy amounts of Au₃₈ and Au₁₄₄ respectively. This indicates that by employing chiral thiols in Brust type protocols, the synthesis can be driven toward formation of chiral products, a phenomenon that might become of interest for the high-yield synthesis of chiral Au nanocluster structures.

Furthermore, by comparing the CD spectra and chiral HPLC chromatograms of Au₃₈(S-2-MeBuS)₂₄ and the separated enantiomers of Au₃₈(2-PET)₂₄, only one cluster enantiomer of Au₃₈(S-2-MeBuS)₂₄ could be observed (as opposed to the formation of a pair of diastereomers). This is of great importance since it can eliminate the tedious separation^[21] usually needed to obtain the pure enantiomer.

Regarding the relative intensity of the CD signals of the different clusters, it was observed that the Au₁₄₄ nanocluster presented significantly more intense signals than the Au₃₈ cluster, thus confirming the DFT calculations of the Häkkinen group.^[48]

Regarding the thermal stability of the synthesized clusters, it was found that through the addition of a further level of chirality by the optically active (*S*)-2-MeBuSH, the stability of the clusters against racemization at high temperatures could be significantly improved. This could open new pathways for chiral nanoclusters to be used in a wider range of applications, due to an increased ability to withstand elevated temperatures.

In conclusion, we report a first important step in developing a new approach for the preparation of chiral Au nanoclusters, providing a solution to one of the biggest problems in the field, the generally unsatisfactory yield of the cluster syntheses. By combining a drastic increase in yield with the preferential formation of intrinsically chiral and enantiopure nanoclusters, (*S*)-MeBuSH might become an important tool for the synthesis of chiral Au nanoclusters, given that similar effects can also be observed for further chiral cluster structures.

3.1.3.5. Methods

3.1.3.5.1. Synthetic procedures

The (*S*)-enantiomer chiral thiol ligand used in the nanocluster synthesis was obtained from the corresponding (*S*)-alcohol in a two-step process adapted from Jin and coworkers.^[41] The detailed procedure is described in Section 3.1.4.1.1.

All nanocluster syntheses were performed following modified Brust procedures reported previously.^[49–51,58] The detailed individual procedures are described in Section 3.1.4.1.2.

3.1.3.5.2. Characterization techniques

Ultraviolet-visible (UV-Vis) spectroscopy was performed on a UV-1600PC spectrometer using cuvettes of 1 cm pathlength. Different solvents (DCM, toluene, THF) were used to dissolve the Au nanoclusters depending on the specific reaction step.

Circular dichroism (CD) spectra were obtained using a JASCO J-810 spectropolarimeter equipped with a Peltier temperature controller. Quartz glass cuvettes with a path length of 0.2 cm were used. The samples were dissolved in DCM or toluene for measurement.

Matrix-assisted laser desorption/ionization mass spectrometry (MALDI-MS) was conducted on a Bruker Ultraflex extreme MALDI-TOF instrument equipped with a Nd:YAG laser in linear mode. Each spectrum was obtained by averaging 5000 single shots (split in packets of 500 shots). Spectra were obtained at 10 % (Au₂₅ and Au₃₈) or 30 % (Au₁₄₄) laser power. *trans*-2-[3-(4-*tert*-butylphenyl)-2-methyl-2-propenylidene]-malononitrile (DCTB) was used as matrix. Sample and matrix solutions were prepared in toluene.

High-performance liquid chromatography (HPLC) separation experiments of the Au₃₈ nanocluster stereoisomers were performed on a Shimadzu Lab Solution LC-20 A system, following a published protocol.^[21] The instrument was equipped with a chiral 5 μ m Lux Cellulose-1 (250 x 4.6 mm, company Phenomenex) column. The nanoclusters were dissolved in toluene and a mobile phase of 80:20 n-hexane:isopropanol at 2 ml/min was chosen for separation. The elution of the nanocluster fractions was observed by UV-Vis detection at 380 nm.

Nuclear magnetic resonance (NMR) spectroscopy was measured on a Bruker Avance 400 MHz NMR spectrometer. Samples were dissolved in CDCl₃ and the solvent signal was used as internal reference. Chemical shifts relative to trimethylsilane (TMS) are reported.

3.1.3.5.3. Nanocluster Graphics

Au nanocluster images were created with UCSF Chimera, developed by the Resource for Biocomputing, Visualization, and Informatics at the University of California, San Francisco.^[59] The presented structures were adapted from published coordinates.^[15,19,60,61]

3.1.3.6. Acknowledgements

The authors thank Alberto Tampieri for his input and helpful discussions. CD spectroscopy was supported by an Innovative Project (RAKI-MINT) granted by TU Wien to Astrid R.

Mach-Aigner. N.B. acknowledges support by the Austrian Science Fund (FWF) via grant Elise Richter (V831-N).

3.1.3.7. Author contributions

V.T. and N.B. designed the experiments. The syntheses, purification and characterization of the nanoclusters was carried out by V.T., A.L., R.B. and N.B. MALDI-MS was measured by E.P. Data evaluation was performed by V.T., A.L., R.B. and N.B. The manuscript was prepared by V.T., A.L., R.B. and N.B. with contributions from all authors.

3.1.4. Supplementary Information

The Supplementary Information contains information on the synthesis of the chiral thiol ligand (Section 3.1.4.1.1), synthesis of the Au nanoclusters (Section 3.1.4.1.2), NMR spectra of the chiral thiol (Figures 3.5 - 3.6), MALDI-MS spectra of the Au nanoclusters (Figures 3.7 - 3.9), additional CD spectra (Figures 3.10 - 3.11), HPLC chromatograms (Figure 3.12).

3.1.4.1. Synthetic Procedures

The reagents, solvents and other consumables used in the preparation of both ligands and nanoclusters were obtained from commercial suppliers. Any steps involving aqueous solutions were performed using ultrapure Milli-Q H₂O (18.6 MΩ·cm at 25 °C).

3.1.4.1.1. Supplementary Note 1: (*S*)-2-Methylpropane-1-thiol (2-MeBuSH)

The synthesis of 2-MeBuSH was performed according to Figure 3.4, by adapting a procedure presented by Zhu and co-workers.^[41]

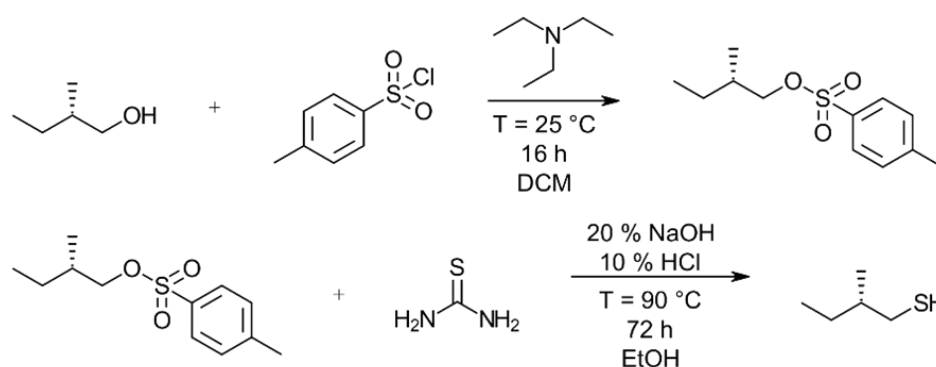


Figure 3.4.: Synthesis of 2-MeBuSH.

To begin with, 7 g (79.5 mmol) (*S*)-2-methylbutan-1-ol and 16.34 g (85.7 mmol) 4-toluenesulfonyl chloride were dissolved in 60 ml of dichloromethane (DCM). Slow addition of 27.49 ml (197.8 mmol) of triethylamine to the ice-cooled mixture resulted in formation of a white precipitate. After stirring at room temperature for 16 h, the white precipitate was removed and the solution was washed with diluted HCl and water. After extraction of the aqueous phase with DCM, the combined organic phases were dried over Na₂SO₄. Removal of DCM by rotary evaporation yielded a clear oil, which was purified by silica column chromatography in 1:3 hexane:EtOAc (EtOAc = ethylacetate).

The intermediate (14.50 g, 59.9 mmol) and 4.56 g (59.9 mmol) of thiourea were dissolved in 85 ml of ethanol (EtOH). After refluxing at 80 °C for 72 h, 60 ml of 20 % NaOH were added and the reaction mixture kept at 80 °C for another 60 min. The solution was subsequently cooled to room temperature and acidified with 100 ml of 10 % HCl. The organic phase was extracted with hexane and dried over Na₂SO₄. Removal of the solvent and impurities was achieved by

distillation at 40 °C. The product, which was obtained as a clear oil, was characterized by nuclear magnetic resonance spectroscopy (NMR; see Figures 3.5 - 3.6).

3.1.4.1.2. Supplementary Note 2: Nanocluster Syntheses

[Au₂₅(2-MeBuS)₁₈][TOA] and Au₂₅(2-MeBuS)₁₈

[Au₂₅(2-MeBuS)₁₈][TOA] and Au₂₅(2-MeBuS)₁₈ were synthesized following a protocol by Shihare *et al.*^[51] To a 10 ml tetrahydrofuran (THF) solution of 100 mg (0.25 mmol) HAuCl₄·3H₂O and 167 mg (0.31 mmol) tetraoctylammonium bromide (TOAB) 156 µl (1.27 mmol) of 2-MeBuSH were added, which resulted in the original orange color of the solution to slowly fading out over the course of an hour. The reaction mixture was subsequently reduced by addition of 96 mg (2.54 mmol) NaBH₄ in 2 µl ice-cold water. Stirring at room temperature was continued for 2 days, after which the solvent was removed by rotary evaporation and the residue washed with 1:1 H₂O:methanol (MeOH) and purified by size-exclusion chromatography (SEC; THF/Bio-Beads S-X1 support). After elution of a black fraction (which was identified as Au₁₄₄(2-MeBuS)₆₀), a reddish-brown fraction of [Au₂₅(2-MeBuS)₁₈][TOA] and a greenish fraction containing Au₂₅(2-MeBuS)₁₈ could be isolated. Approximate yields of 25 % ([Au₂₅(2-MeBuS)₁₈][TOA]), 6 % (Au₂₅(2-MeBuS)₁₈) and 8 % (Au₁₄₄(2-MeBuS)₆₀) were obtained.

[Au₂₅(S-Bu)₁₈][TOA] and Au₂₅(S-Bu)₁₈

The synthesis protocol was identical to the one used for [Au₂₅(2-MeBuS)₁₈][TOA] and Au₂₅(2-MeBuS)₁₈, except for the addition of 136 µl (1.26 mmol) of butanethiol (SH-Bu) instead of 2-MeBuSH. No Au₁₄₄(S-Bu)₆₀ was isolated in this synthesis and the approximate yields of [Au₂₅(2-MeBuS)₁₈][TOA] and Au₂₅(S-Bu)₁₈ were 23 % and 4 % respectively.

Au₃₈(2-MeBuS)₂₄

Au₃₈(2-MeBuS)₂₄ was synthesized by adapting the protocol reported by Stellwagen and co-workers.^[50] 50 mg (0.15 mmol) HAuCl₄·3H₂O and 155 mg (0.5 mmol) of L-glutathione (GSH) were dissolved in 8 µl MeOH and 3.5 µl H₂O, yielding a white suspension. After cooling the mixture to 0 °C, 47 mg (1.2 mmol) NaBH₄ suspended in 2.4 µl ice-cold water were added, which resulted in the formation of a black precipitate. The reaction was stirred at 0 °C for 1 h. After separating the black precipitate by centrifugation, the solid was dissolved in 2.4 µl H₂O, 1.5 µl acetone and 2 µl (15.6 mmol) 2-MeBuSH. The reaction was continued at 80 °C for 16 h. The phases were separated and the aqueous phase washed with DCM. The organic phase was dried and the resulting black precipitate washed with ethanol for purification (yield with respect to HAuCl₄·3H₂O was 78 %).

Au₃₈(2-PET)₂₄

Au₃₈(2-PET)₂₄ was prepared by following the procedure published by Pollitt and co-workers.^[58] First, 1 g (2.9 mmol) HAuCl₄·3H₂O and 3.17 g (10.3 mmol) GSH were dissolved

in 100 μl acetone, giving a yellow suspension, which was stirred at 0 $^{\circ}\text{C}$ for 30 min. Next, an ice-cold solution of 30 μl H_2O and 0.98 g (25.9 mmol) NaBH_4 was poured in carefully, resulting in the formation of a black precipitate. After decanting the solvent and drying the solid, 6 μl EtOH, 10 μl toluene, 30 μl water and 10 μl (74.7 mmol) 2-PET were added. The mixture was stirred at 80 $^{\circ}\text{C}$ for 4 h and subsequently cooled to room temperature. 50 μl hexane were added and the black precipitate removed by filtration. After washing several times with MeOH, the crude product was redissolved in DCM and dried by rotary evaporation at 30 $^{\circ}\text{C}$. For purification of the crude product, SEC (THF, Bio-Beads SX-1 support) was performed (yield of final product was 6 % with respect to $\text{HAuCl}_4 \cdot 3\text{H}_2\text{O}$).

$\text{Au}_{38}(\text{S-Bu})_{24}$

The synthesis was performed in an analogous fashion to the procedure presented for $\text{Au}_{38}(\text{2-MeBuS})_{24}$, with the difference that 20 ml (185.6 mmol) of SH-Bu were added instead of the 2-MeBuSH. Furthermore, after stirring at 80 $^{\circ}\text{C}$ for 16 h, the cluster was precipitated with 88 μl of a 1:10 $\text{H}_2\text{O}:\text{MeOH}$ solution. The black/violet solid was then filtered, washed with EtOH, and subsequently extracted with toluene and dried. Yield with respect to $\text{HAuCl}_4 \cdot 3\text{H}_2\text{O}$ was 26 %.

$\text{Au}_{144}(\text{2-MeBuS})_{60}$

$\text{Au}_{144}(\text{2-MeBuS})_{60}$ nanoclusters were prepared by modifying the procedure presented by Qian *et al.* [49] 236 mg (0.6 mmol) $\text{HAuCl}_4 \cdot 3\text{H}_2\text{O}$ were mixed with 380 mg (0.7 mmol) TOAB and dissolved in 30 μl MeOH. The red solution was stirred for 15 minutes at room temperature, after which 394 μl (3.18 mmol) 2-MeBuSH were added, giving a white suspension. After stirring for 15 min at room temperature, the polymer suspension was reduced using a cooled solution of 227 mg (6 mmol) NaBH_4 dissolved in 12 μl water, yielding a black precipitate. The black solution was stirred for another 5 h at room temperature. Subsequently, the black precipitate was separated by centrifugation and washed several times with methanol. The crude product was purified by SEC (THF, Bio-Beads S-X1 support). $\text{Au}_{144}(\text{2-MeBuS})_{60}$ eluted as the first fraction (black), followed by another black fraction (identified as $\text{Au}_{38}(\text{2-MeBuS})_{24}$) and $\text{Au}_{25}(\text{2-MeBuS})_{18}$ in anionic (reddish-brown) and neutral (greenish) charge state. The yield of $\text{Au}_{144}(\text{2-MeBuS})_{60}$ with respect to $\text{HAuCl}_4 \cdot 3\text{H}_2\text{O}$ was 73 %.

$\text{Au}_{144}(\text{2-Bu})_{60}$

The synthesis protocol was analogous to the one described for $\text{Au}_{144}(\text{2-MeBuS})_{60}$, except for the addition of 343 μl (3.18 mmol) HS-Bu instead of 2-MeBuSH. The yield of $\text{Au}_{144}(\text{2-Bu})_{60}$ with respect to $\text{HAuCl}_4 \cdot 3\text{H}_2\text{O}$ was 38 %.

3.1.4.2. NMR Spectra of the 2-MeBuSH Ligand

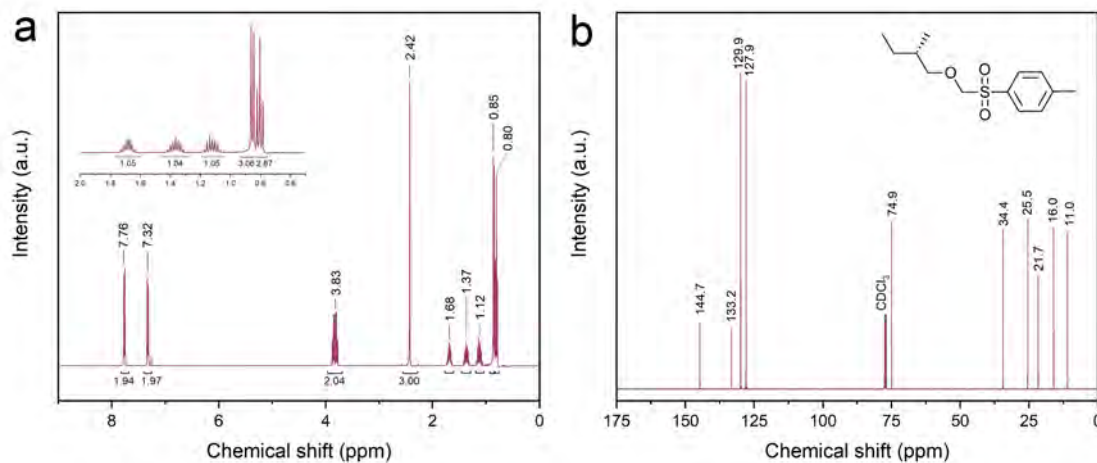


Figure 3.5.: ^1H (a) and ^{13}C -NMR spectrum (b) of (*S*)-2-methylbutyl 4-methylbenzenesulfonate.

^1H -NMR (400 MHz, CDCl_3 , TMS): $\delta = 0.80$ (t, 3H, CH_2CH_3); 0.85 (d, 3H, CHCH_3); 1.12 (m, 1H, CHCH_2CH_3); 1.37 (m, 1H, CHCH_2CH_3); 1.68 (m, 1H, CH); 2.42 (s, 3H, Ar- CH_3); 3.83 (m, 2H, O- CH_2); 7.32 (d, 2H, Ar-H); 7.76 (d, 2H, Ar-H).

$^{13}\text{C}\{^1\text{H}\}$ -NMR (101 MHz, CDCl_3 , TMS): $\delta = 11.0$ (s); 16.0 (s); 21.7 (s); 25.5 (s); 34.4 (s); 74.9 (s); 127.9 (s); 129.9 (s); 133.2 (s); 144.7 (s).

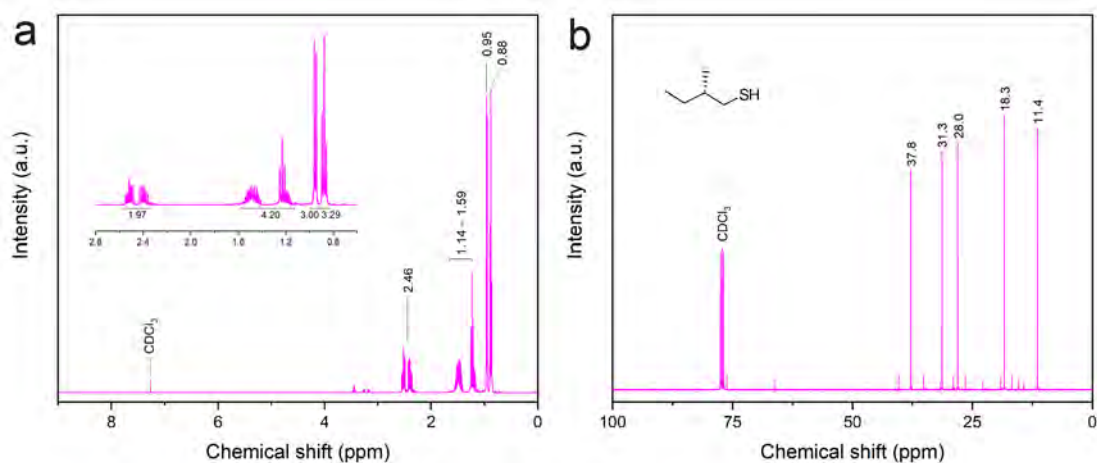


Figure 3.6.: ^1H (a) and ^{13}C -NMR spectrum (b) of (*S*)-2-methylbutanethiol.

^1H -NMR (400 MHz, CDCl_3 , TMS): $\delta = 0.88$ (t, 3H, CH_2CH_3); 0.95 (d, 3H, CHCH_3); 1.14-1.59 (m, 4H, CHCH_2CH_3 , SH); 2.46 (m, 2H, S- CH_2).

$^{13}\text{C}\{^1\text{H}\}$ -NMR (101 MHz, CDCl_3 , TMS): $\delta = 11.4$ (s); 18.3 (s); 28.0 (s); 31.3 (s); 37.8 (s).

A small amount ($< 5\%$) of impurities could not be removed by distillation and was still present in the final product. These correspond to traces of solvents (hexane), and presumably also to formed disulfides. Note that this has no influence on the nanocluster synthesis.

3.1.4.3. Matrix-assisted Laser Desorption/Ionization (MALDI-MS) Spectra of the Au Nanoclusters

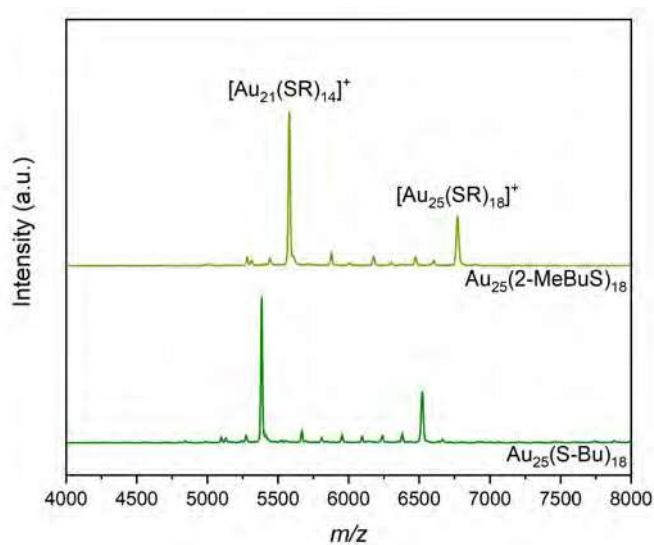


Figure 3.7.: MALDI-MS spectra of $[\text{Au}_{25}(2\text{-MeBuS})_{18}]^-$ (top) and $[\text{Au}_{25}(\text{S-Bu})_{18}]^-$ (bottom). Note that the counterion cannot be identified due to measuring in positive mode.

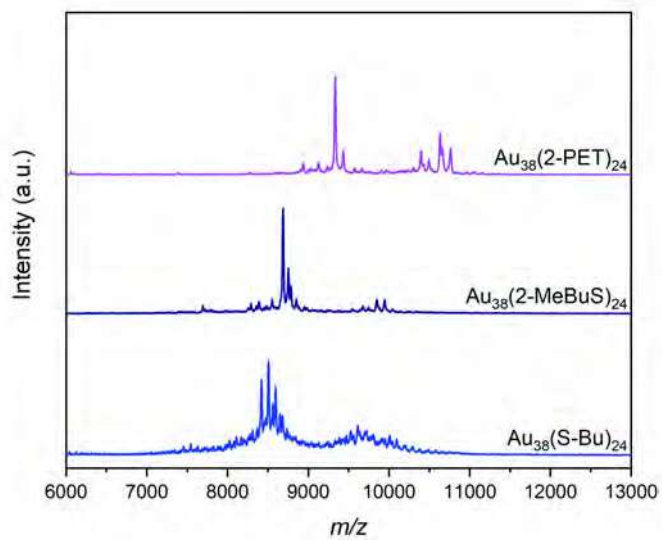


Figure 3.8.: MALDI-MS spectra of $\text{Au}_{38}(\text{2-PET})_{24}$ (top), $\text{Au}_{38}(\text{2-MeBuS})_{24}$ (middle) and $\text{Au}_{38}(\text{S-Bu})_{24}$ (bottom).

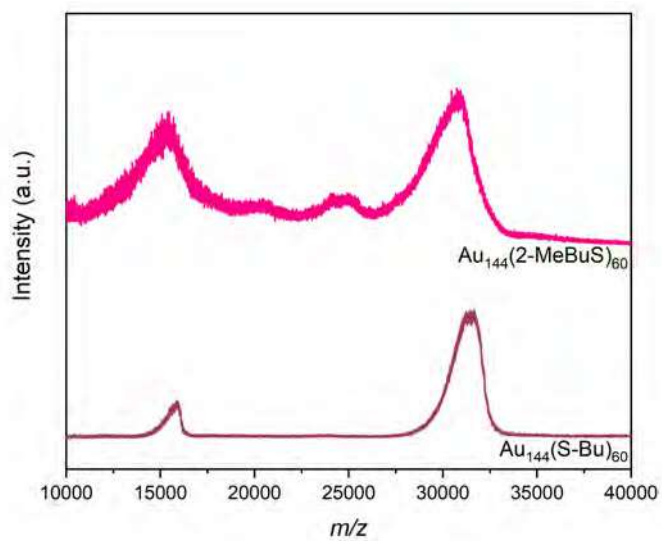


Figure 3.9.: MALDI-MS spectra of $\text{Au}_{144}(\text{2-MeBuS})_{60}$ (top) and $\text{Au}_{144}(\text{S-Bu})_{60}$ (bottom).

3.1.4.4. Additional Circular Dichroism (CD) Spectra

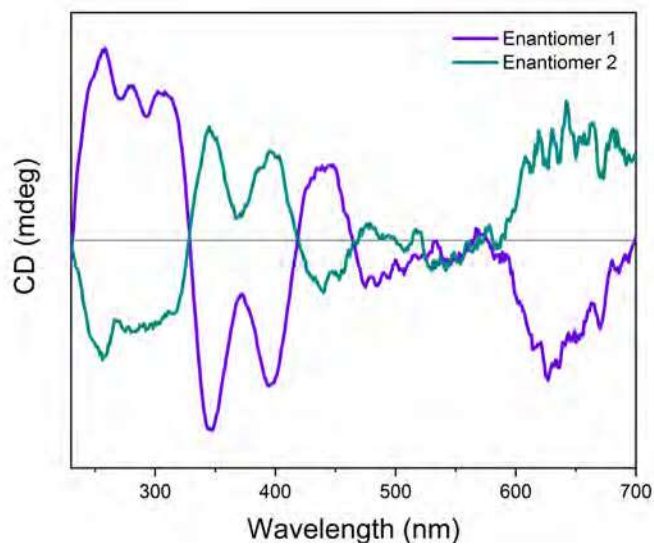


Figure 3.10.: CD spectra of two enantiomers of $\text{Au}_{38}(\text{2-PET})_{24}$

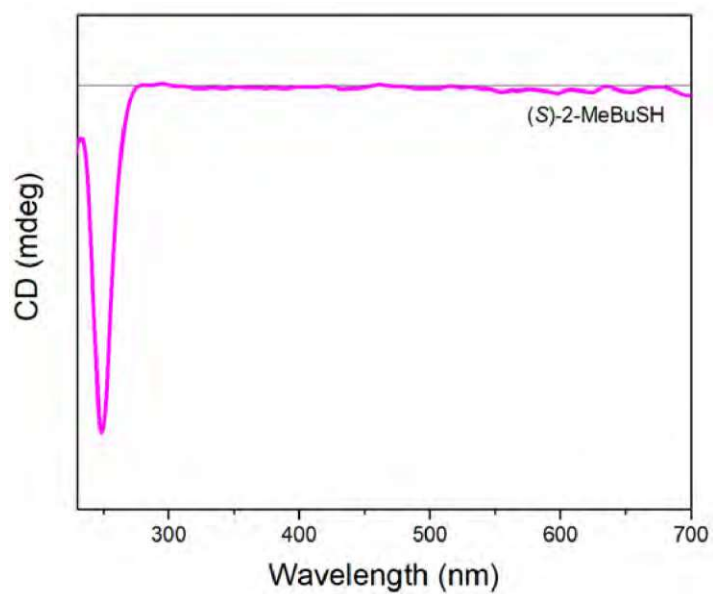


Figure 3.11.: CD spectrum of the (S) -2-methylbutanethiol ligand.

3.1.4.5. HPLC Separation of Au₃₈ Nanoclusters

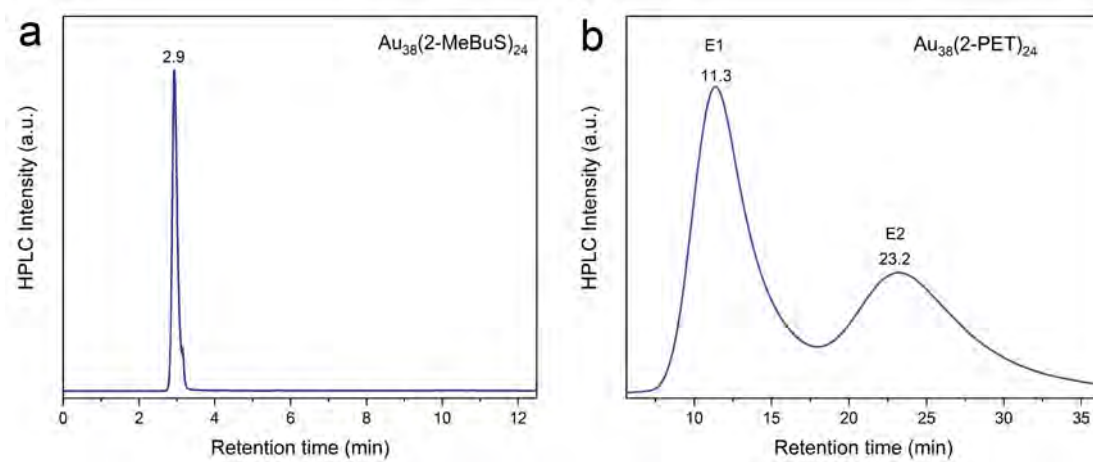


Figure 3.12.: HPLC chromatograms of Au₃₈(2-MeBuS)₂₄ (a) and Au₃₈(2-PET)₂₄ (b)

3.2. Density Functional Theory Calculations of $\text{Au}_{38}(\text{2-MeBuS})_{24}$ and $[\text{Au}_{25}(\text{2-MeBuS})_{18}]^-$

To be able to study the chiral properties of the synthesized clusters protected by 2-MeBuSH, density functional theory (DFT) calculations were carried out. The main objective thereby was to develop an adequate model of the clusters for use in future studies. However, another interest was to confirm which enantiomer of Au_{38} was present after synthesis (i.e. clockwise or counter-clockwise arrangement of the staple units). Due to its size, no DFT calculations were carried out for Au_{144} .

3.2.1. $\text{Au}_{38}(\text{2-MeBuS})_{24}$

Four different model structures of $\text{Au}_{38}(\text{2-MeBuS})_{24}$ were made, based on both the $\text{Au}_{38}(\text{2-PET})_{24}$ crystal structure^[15] (isomer 1), as well as on the lowest energy structure of $\text{Au}_{38}(\text{SCH}_3)_{24}$ found by Lopez-Acevedo *et al.* (isomer 2), namely structure 1 in their work.^[23] To avoid confusion, this structure 1 will be referenced to as *JACS2010* structure in the following. For both structures investigated in the framework of this thesis (isomer 1 and isomer 2), both an anti-clockwise (denoted by an appendix *a*) and a clockwise (denoted by an appendix *b*) conformer was created and optimized. Further refinements of each substructure produced the lowest energy isomers isomers 1a, 1b, 2a and 2b, the energy of which is compared in Table 3.1. The energies of all calculated isomers can also be found in Table 3.2.

Table 3.1.: Relative energies of the lowest energy structures of each subcategory. A = anti-clockwise and C = clockwise staple rotation. Isomers 1 are crystal structure^[15] based and isomers 2 were obtained starting from the calculated structure by Lopez-Acevedo *et al.*^[23] The energies of all calculated isomers can be found in Table 3.2.

Enantiomer	Structure	Relative Energy(kJ/mol)	
		Enantiomer	Overall
A	isomer 1a	30.8	46.5
A	isomer 2a	0	15.7
C	isomer 1b	7.4	7.4
C	isomer 2b	0	0

3.2.1.1. Comparison of the Crystal Structure and the JACS2010-based Structures of $\text{Au}_{38}(\text{2-MeBuS})_{24}$

As can already be seen from Table 3.1, the isomers based on the crystal structure (isomers 1a and 1b) tend to be higher in energy than the JACS2010 ones. This might be explained by the slightly different arrangements of the ligands for the two structures.^[15,23] Figure 3.13 shows a comparison of the two different anti-clockwise isomers 1a and 2a. For isomer 1a, the ligands

in the monomeric staple units (see side view in (a)) are mostly facing outwards, whereas the ones of isomer 2a are also a slightly tilted up- and downwards, respectively. This is due to the different orientation of the $-S(R)-Au-S(R)-$ units, which restricts the orientation of the hydrocarbon framework of the 2-MeBuSH ligand in isomer 1a. Furthermore, the top view of the nine ligands in the upper dimeric staple units show that isomer 2a has a very symmetric arrangement of these nine ligands, with each subset (i.e. the three top, middle and bottom ligands in light of sight) mostly following the idealized D_3 symmetry of the cluster. For isomer 1a, the same nine ligands are arranged in a much less symmetric fashion. Whereas the bottom three ligands still take symmetrical positions with respect to each other, the topmost ones as well as the ones in the middle of the staple units do not. This implies that the symmetry of isomer 1a is reduced as compared to 2a, which might be related with higher energy. However, besides symmetry, other structural factors (for example the different arrangement of the monomeric staples and its implication for the orientation of the surrounding ligands) will affect that as well.

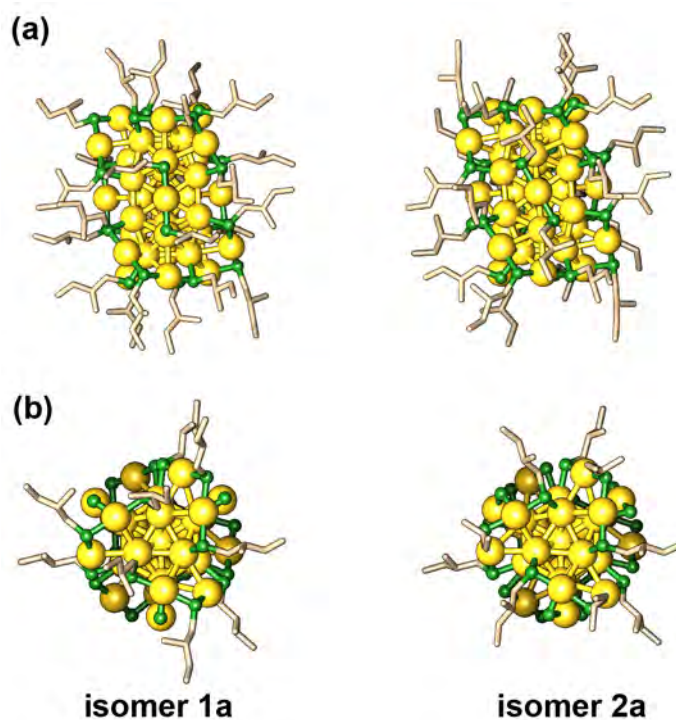


Figure 3.13.: Structures of isomer 1a and 2a: (a) side view and (b) top view. Note that in (b), the hydrocarbon framework of all but the 9 ligands in the dimeric staples on top is not shown to allow for better visualization.

For both isomers, the optical absorption as well as the CD spectrum were calculated using time dependent-density functional theory plus tight binding (TD-DFT+TB). Their comparison is shown in Figure 3.14. As is evident, besides small shifts in the positions of the UV-Vis and CD bands (especially at lower energy), the spectra are not affected much by these struc-

tural differences. This could be expected considering that these transitions are not usually sensitive to the ligand conformation.^[11] Interestingly enough, isomer 2a shows a significant CD signal at 1295 nm, which is completely absent in isomer 1a.

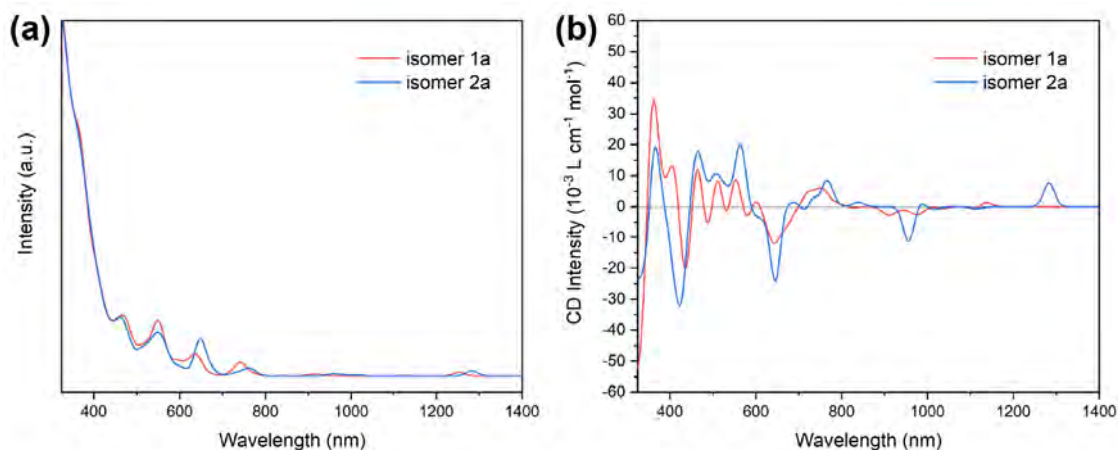


Figure 3.14.: Theoretical UV-Vis (a) and CD spectra (b) of isomers 1a (crystal structure) and 2a (JACS2010) in gas phase.

3.2.1.2. Comparison of the Different Staple Arrangements of $\text{Au}_{38}(\text{2-MeBuS})_{24}$

As previously discussed, $\text{Au}_{38}(\text{SR})_{24}$ can have two different orientations of its staple units, i.e. clockwise (C) or anti-clockwise (A) rotatory arrangement. The comparison of both structures is shown in Figure 3.15 and the comparison of the computed spectra in Figure 3.16. Since the differences between the isomers obtained starting from the crystal structure *vs.* the JACS2010 structure were deemed to be minor (especially compared to the deviations one usually observes between experiment and calculations), only the lowest energy anti-clockwise and clockwise isomers, namely 2a and 2b, were used for the following comparison.

As seen from Figure 3.16a, both clusters exhibit a very similar UV-Vis profile and only negligible differences are noted. Since the signal in the CD spectra of $\text{Au}_{38}(\text{2-MeBuS})_{24}$ is expected to be mainly due to the chiral Au-S interface,^[23] their CD spectra compare to mirror-images (see Figure 3.16b), even though these two clusters are diastereomers (as opposed to a pair of enantiomers). Note that above 800 nm (1.55 eV), the spectra appear to deviate more, which will have to be investigated further in the future. In this energy range, also the deviations between the time dependent-density functional theory (TD-DFT) and the TD-DFT+TB CD spectra of isomer 2b were most pronounced, as shown in Figure 3.20.

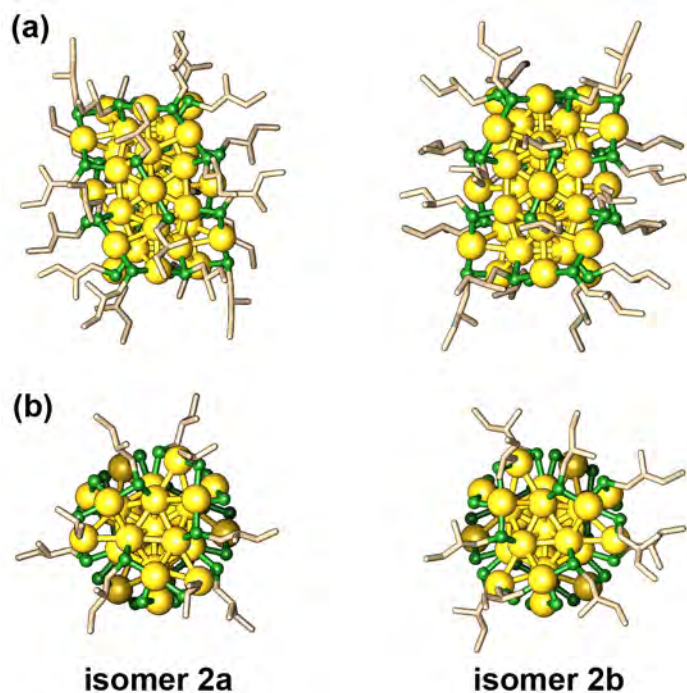


Figure 3.15.: Structures of isomer 2a and 2b: (a) side view and (b) top view. Note that in (b), the hydrocarbon framework of all but the 9 ligands in the dimeric staples on top is not shown to allow for better visualization.

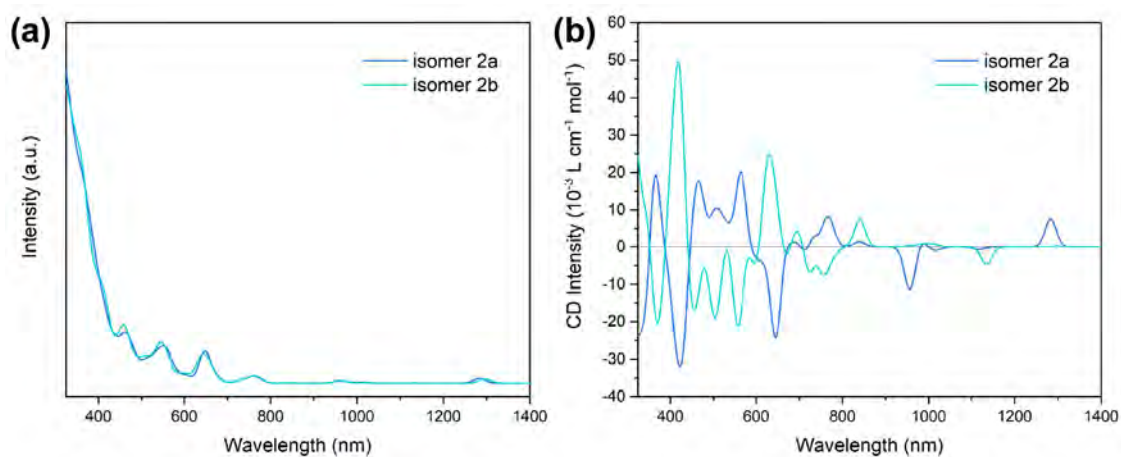


Figure 3.16.: Theoretical UV-Vis (a) and CD spectra (b) of isomers 2a and 2b in gas phase.

It is also worth comparing the spectra of isomer 2b to the JACS2010 structure studied by Lopez-Acevedo *et al.*^[23] For both the UV-Vis and the CD spectrum, the shape and positions of the bands are found to be very similar. The lowest energy bands of isomer 2b are located at approximately 1295 nm/0.95 eV, 960 nm/1.29 eV, 765 nm/1.62 eV and 645 nm/1.92 eV

and thus compare well to those observed by Lopez-Acevedo *et al.*^[23] The nature of the transitions causing the bands was also studied by them. Summarizing very briefly, the band at 1295 nm is due to the HOMO→LUMO transition, whereas the ones at 960 nm, 765 nm and 645 nm correspond to HOMO→LUMO+2, a mixture of mainly HOMO–1→LUMO and HOMO–2→LUMO and a mixture of several transitions, respectively.^[23] Furthermore, also the CD bands of isomer 2b are very similar to the one of the JACS2010 structure (within the energy range that can be compared), except for said absent excitation at around 1295 nm/0.95 eV in isomer 2b. This indicates that the 2-MeBuSH ligand does not induce significant changes to the cluster kernel and staple geometry, which was expected owing to its small size.

To investigate which enantiomer is preferentially formed in a synthesis with (*S*)-2-MeBuSH, the experimental spectra of Au₃₈(2-MeBuS)₂₄ were compared to the calculated ones. This comparison is depicted in Figure 3.17. As can be seen in Figure 3.17a, the calculated optical absorption spectra are in good agreement with the experimental one. Note that no offset on the energy axis had to be applied in this case. Furthermore, the experimental CD spectrum mainly follows the same trend as the one of isomer 2b (see 3.17b), strongly indicating that this enantiomer has been formed during synthesis.

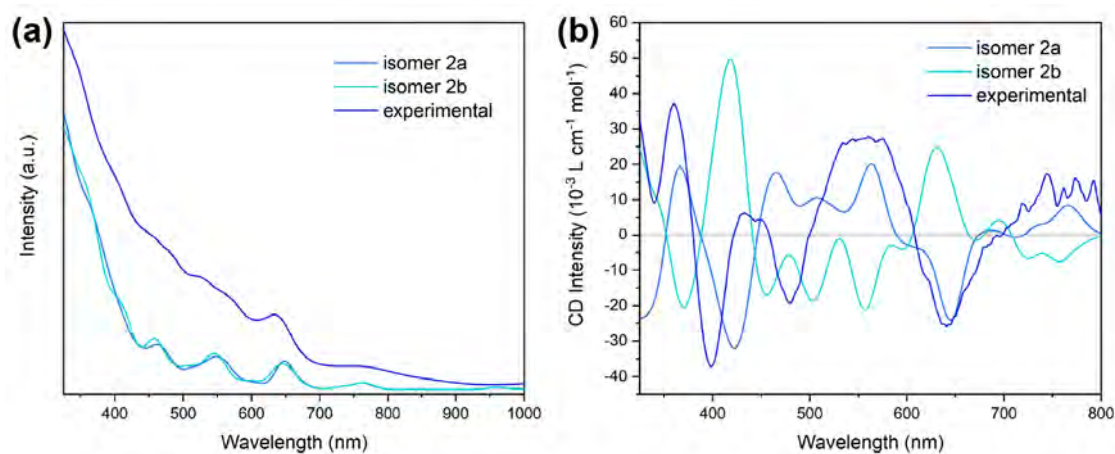


Figure 3.17.: Theoretical spectra of isomers 2a and 2b in gas phase and experimental spectrum of Au₃₈(2-MeBuS)₂₄: (a) UV-Vis and (b) CD spectra. Note that the experimental UV-Vis spectrum is offset on the intensity axis from the theoretical ones to allow for better visualization.

Interestingly, the isomers with the anti-clockwise staple unit arrangement (isomers 1a and 2a) are higher in energy than their clockwise counterparts at the level of theory used (see Table 3.1). Nevertheless, the comparison with experiment shows that this enantiomer is preferentially obtained when using (*S*)-2-MeBuSH as protecting ligand. As of yet, it is unclear if the same energy trend would also be observed at a different level of theory. Furthermore, it might also be possible that kinetic effects during the formation and size focusing of the

clusters during the synthesis are responsible for the directed chirality observed in this case.

3.2.2. $[\text{Au}_{25}(\text{2-MeBuS})_{18}]^-$

The structure of $[\text{Au}_{25}(\text{2-MeBuS})_{18}]^-$ obtained after optimization at BP86/DZP level of theory is depicted in Figure 3.18. This cluster has an achiral arrangement of its dimeric staple units, thus, its chiral properties are solely due to induction by the chiral (*S*)-2-MeBuSH ligand. The theoretical optical absorption and the CD spectrum of $[\text{Au}_{25}(\text{2-MeBuS})_{18}]^-$ are presented in Figure 3.19 and compared to the experimental spectra. As can be seen, the energies of the optical absorption bands are significantly underestimated by TD-DFT+TB at this level of theory. This has been reported for Au_{25} calculated with the BP86 functional before.^[62,63] For better visualization, the theoretical spectrum was shifted by +0.48 eV and then shows acceptable agreement with the experimental spectrum, especially considering the shape of the bands.

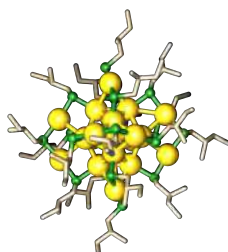


Figure 3.18.: Calculated structure of $[\text{Au}_{25}(\text{2-MeBuS})_{18}]^-$.

However, for the CD spectra, significant deviations are noticed as well, which cannot be corrected by a shift of the energy axis only. This shows that the current cluster model is not sufficient for comparison to the experiment. Further refinement, for example at a different level of theory, would be required.

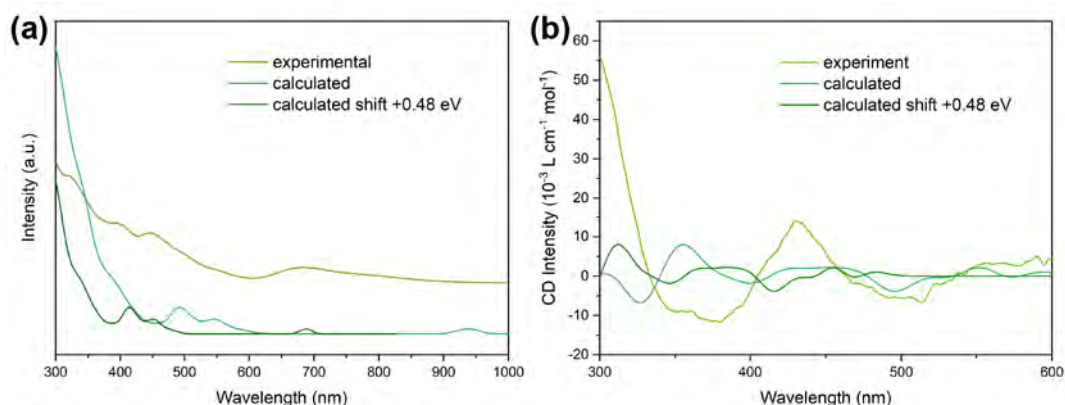


Figure 3.19.: Theoretical spectra of $[\text{Au}_{25}(\text{2-MeBuS})_{18}]^-$ in gas phase and experimental spectrum: (a) UV-Vis and (b) CD spectra. Note that the experimental UV-Vis spectrum is offset on the intensity axis from the theoretical ones to allow for better visualization.

3.2.3. Conclusions

Both $[\text{Au}_{25}(\text{2-MeBuS})_{18}]^-$ and $\text{Au}_{38}(\text{2-MeBuS})_{24}$ were optimized employing DFT at the BP86/DZP level of theory. For Au_{25} , the energies of the transitions were significantly red-shifted compared to the experiment, which has been reported for this cluster species before. The comparison of the theoretical and experimental CD spectra shows that the computational model structure still has to be improved. For Au_{38} , the simulated optical absorption spectrum is in good agreement with the experimental one. Four different substructures were generated based on the published crystal structure and a calculated one (JACS2010). The isomers obtained starting from the crystal structure coordinates were found to be higher in energy, which was attributed to structural differences and lowering of symmetry. Comparison of the experimental CD spectrum with the calculated ones using TD-DFT+TB indicated that the structure with anti-clockwise rotary arrangement of the staples is preferentially formed. However, these isomers (1a and 2a) were found to be higher in energy than the clockwise ones. Further calculations are required to determine if the same trend is also observed at a different level of theory.

3.2.4. Computational Details

All DFT calculations carried out using the Amsterdam Density Functional (ADF) 2021.1 package.^[64] The initial structures before optimization were based on previously reported structures^[15,23,61] and the ligands were replaced with a gas-phase optimized structure of 2-MeBuSH. All geometry optimizations of the clusters were done in gas-phase, using a generalized gradient approximation (GGA) Becke Perdew exchange-correlation functional (BP86).^[65,66] A double zeta polarized basis set (DZP) was used.^[67] The zeroth-order regular approximation (ZORA) was used to account for scalar relativistic effects.^[68,69] The gradient convergence was set to 10^{-3} and the energy convergence to 10^{-4} . For Au_{38} , after a first optimization, further isomers of each structure were created by editing of the ligand positions using the MacMolPlt software.^[70]

Optical absorption and circular dichroism (CD) spectra were obtained after a linear response TD-DFT+TB^[71] calculation and subsequent convolution of the excitation energies into a spectrum by applying a Gaussian fit with a full width half-maximum (FWHM) of 30 nm. The CD spectrum of the (*S*)-2-MeBuSH ligand was obtained by employing a Gaussian fit with a FWHM of 15 nm. Refer to the literature for details on the fitting procedure.^[45,72] The energy axis was converted to wavelength units to be able to compare them to the experimental spectra. To confirm that TD-DFT+TB was applicable for the calculations of the nanoclusters in question, some spectra were also simulated employing time dependent-density functional theory (TD-DFT) (see Figure 3.20).^[73]

3.2.5. Acknowledgments

The results presented in this section were acquired during a research stay at Kansas State University, financially supported through a Marshall Plan Scholarship of the Austrian Marshall Plan Foundation. The computing for this work was performed on the Beocat Research Cluster at Kansas State University, which is funded, in part, by the NSF (Grant Nos. CHE-1726332, CNS-1006860, EPS-1006860, and EPS-0919443).

3.2.6. Supplementary Information

This section contains a comparison of the UV-Vis and CD spectra obtained from the same structure by a TD-DFT *vs.* a TD-DFT+TB calculation (Figure 3.20), as well as the individual representations of the UV-Vis and CD spectra of the Au₃₈ isomers, of Au₂₅, and of the 2-MeBuSH ligand including the plots of the calculated linear response TD-DFT+TB oscillator/rotatory strength (Figures 3.21, 3.22, 3.23, 3.24, 3.25 and 3.26), and the relative energies of all calculated Au₃₈ isomers (Table 3.2). The coordinates of the Au₂₅ structure as well as of the Au₃₈ isomers 1a, 1b, 2a and 2b can be found in Chapter C.

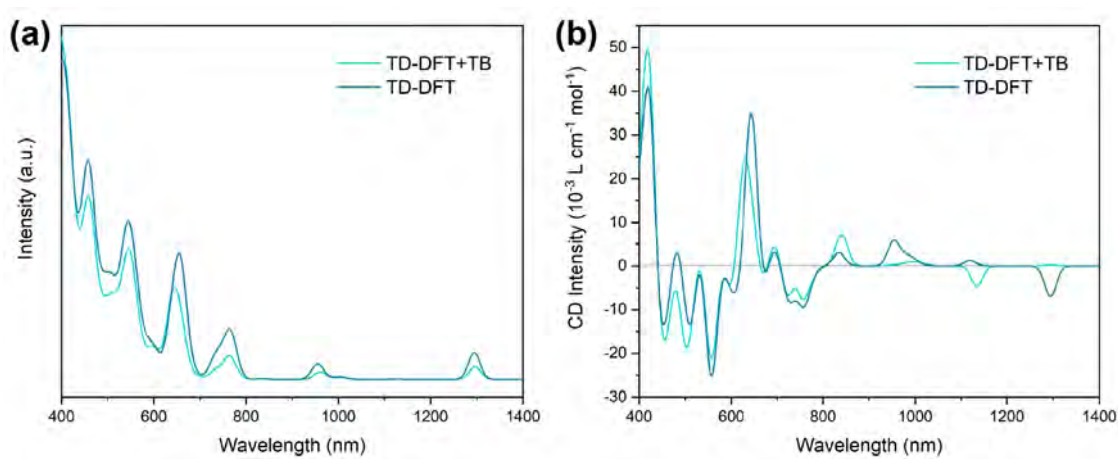


Figure 3.20.: Comparison of the UV-Vis (a) and CD spectra (b) of Au₃₈(2-MeBuS)₂₄ isomer 2b obtained by TD-DFT and TD-DFT+TB.

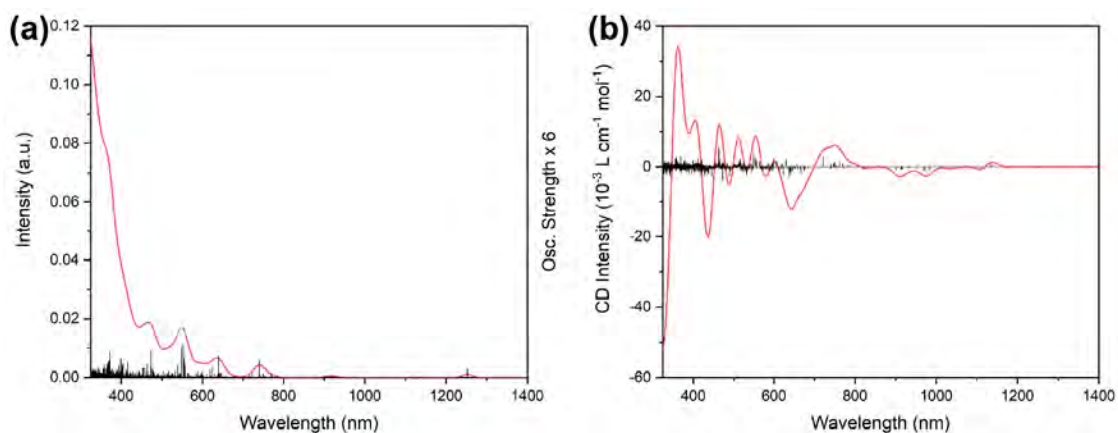


Figure 3.21.: Calculated linear response TD-DFT+TB spectra of isomer 1a: (a) oscillator strength and optical absorption spectrum and (b) rotatory strength and CD spectrum.

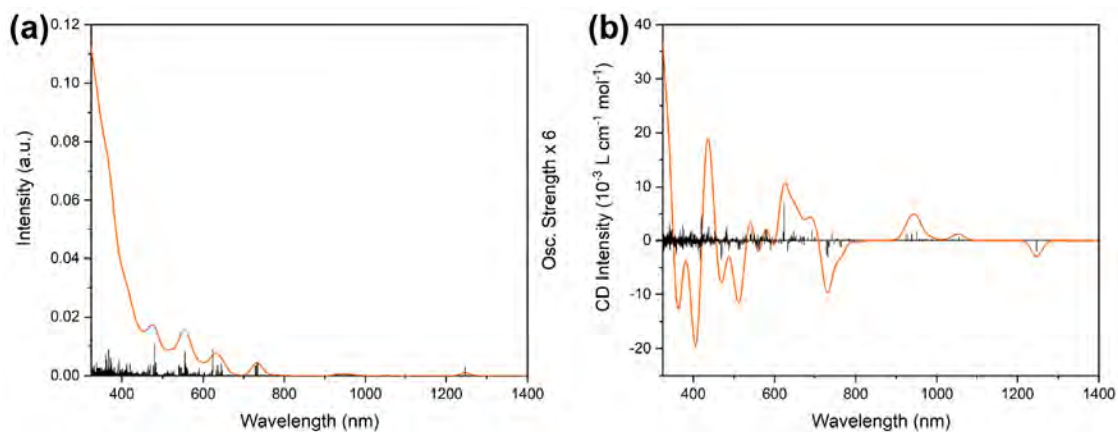


Figure 3.22.: Calculated linear response TD-DFT+TB spectra of isomer 1b: (a) oscillator strength and optical absorption spectrum and (b) rotatory strength and CD spectrum.

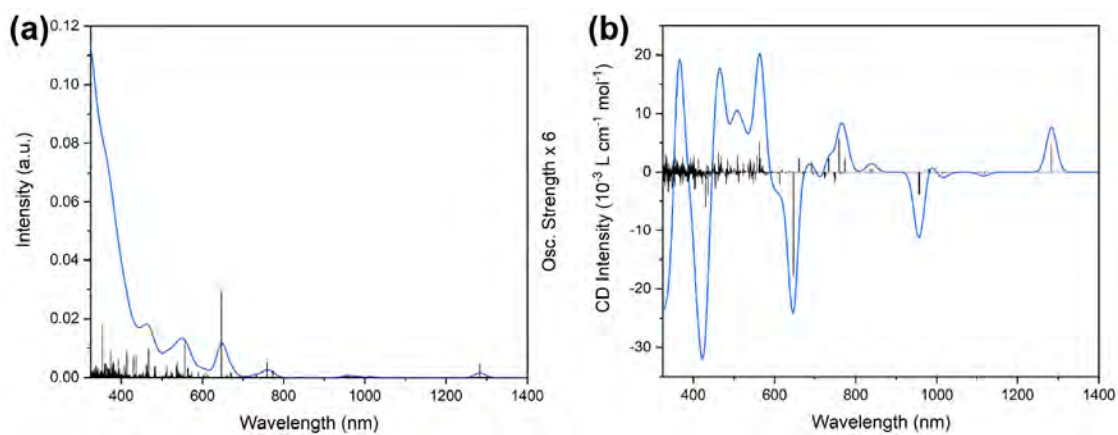


Figure 3.23.: Calculated linear response TD-DFT+TB spectra of isomer 2a: (a) oscillator strength and optical absorption spectrum and (b) rotatory strength and CD spectrum.

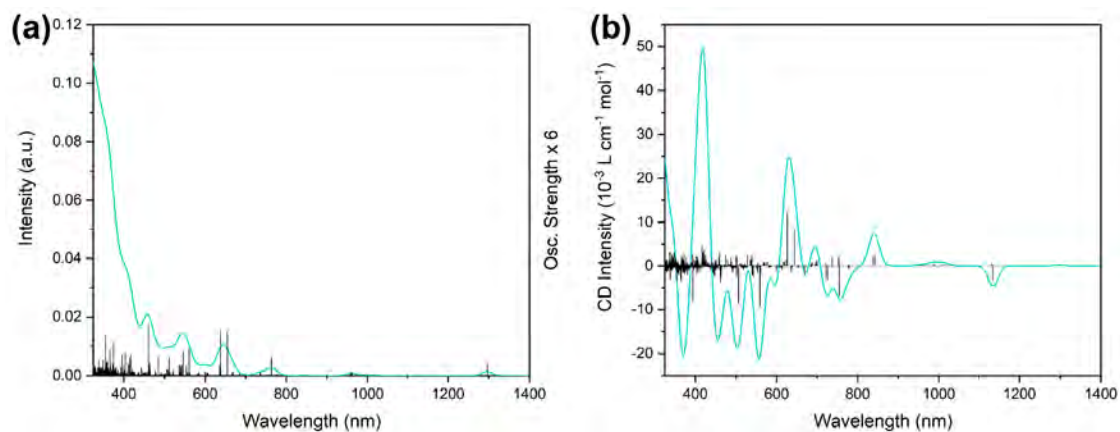


Figure 3.24.: Calculated linear response TD-DFT+TB spectra of isomer 2b: (a) oscillator strength and optical absorption spectrum and (b) rotatory strength and CD spectrum.

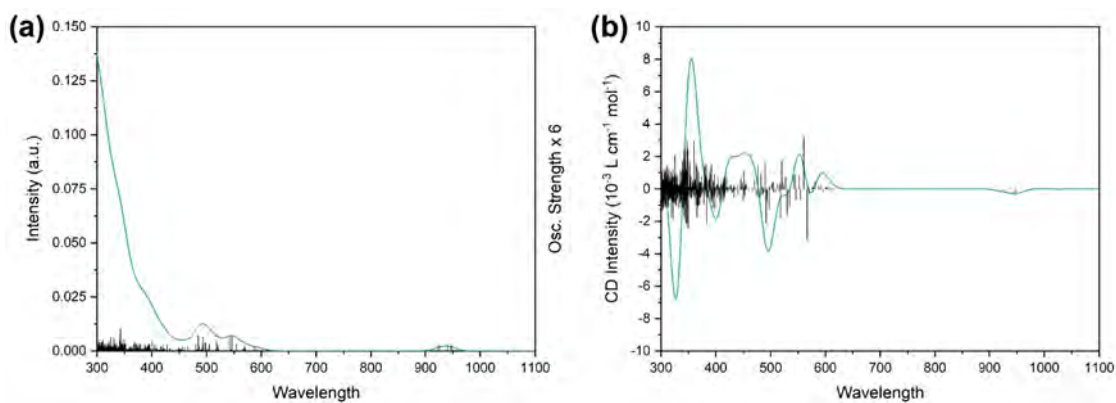


Figure 3.25.: Calculated linear response TD-DFT+TB spectra of $[\text{Au}_{25}(\text{2-MeBuS})_{18}]^-$: (a) oscillator strength and optical absorption spectrum and (b) rotatory strength and CD spectrum.

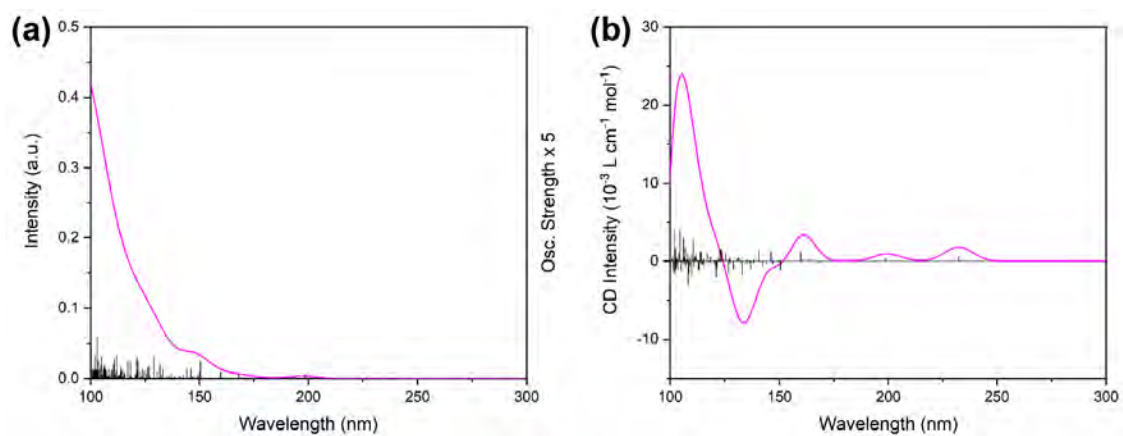


Figure 3.26.: Calculated linear response TD-DFT+TB spectra of (*S*)-2-MeBuSH: (a) oscillator strength and optical absorption spectrum and (b) rotatory strength and CD spectrum.

Table 3.2.: Relative energies of all calculated $\text{Au}_{38}(\text{2-MeBuS})_{24}$ isomers. A = anti-clockwise and C = clockwise staple rotation. Isomers 1 are crystal structure^[15] based and isomers 2 were obtained starting from the calculated structure by Lopez-Acevedo *et al.*^[23]

Cluster isomer	Structure	Relative Energy (kJ/mol)		
		group	enantiomer	overall
A	isomer 1a	0.0	30.8	46.5
A	isomer 1a-2	11.4		
A	isomer 1a-3	33.8		
A	isomer 1a-4	33.9		
A	isomer 2a	0.0	0.0	15.7
A	isomer 2a-2	0.1		
A	isomer 2a-3	0.5		
A	isomer 2a-4	1.1		
A	isomer 2a-5	2.1		
A	isomer 2a-6	4.0		
A	isomer 2a-7	5.7		
A	isomer 2a-8	5.9		
C	isomer 1b	0.0	7.4	7.4
C	isomer 1b-2	7.8		
C	isomer 1b-3	8.1		
C	isomer 1b-4	8.5		
C	isomer 1b-5	13.0		
C	isomer 2b	0.0	0.0	0.0
C	isomer 2b-2	0.2		
C	isomer 2b-3	5.0		
C	isomer 2b-4	25.1		
C	isomer 2b-5	45.1		

3.3. References

- [1] Prakash Chandra Mondal, Deepak Asthana, Ranjeev Kumar Parashar, and Sakshi Jadhav. Imprinting chirality in inorganic nanomaterials for optoelectronic and bio-applications: strategies, challenges, and opportunities. *Materials Advances*, 2(23):7620–7637, 2021. doi: 10.1039/d1ma00846c.
- [2] Andrea Calcaterra and Ilaria D’Acquarica. The market of chiral drugs: Chiral switches versus de novo enantiomerically pure compounds. *Journal of Pharmaceutical and Biomedical Analysis*, 147:323–340, jan 2018. doi: 10.1016/j.jpba.2017.07.008.
- [3] Wei Ma, Liguang Xu, André F. de Moura, Xiaoling Wu, Hua Kuang, Chuanlai Xu, and Nicholas A. Kotov. Chiral Inorganic Nanostructures. *Chemical Reviews*, 117(12):8041–8093, apr 2017. doi: 10.1021/acs.chemrev.6b00755.
- [4] Muhammad Shajih Zafar and Andrea Ragusa. Chirality at the Nanoparticle Surface: Functionalization and Applications. *Applied Sciences*, 10(15):5357, aug 2020. doi: 10.3390/app10155357.
- [5] Rongchao Jin, Chenjie Zeng, Meng Zhou, and Yuxiang Chen. Atomically Precise Colloidal Metal Nanoclusters and Nanoparticles: Fundamentals and Opportunities. *Chemical Reviews*, 116(18):10346–10413, sep 2016. doi: 10.1021/acs.chemrev.5b00703.
- [6] Ricca Rahman Nasaruddin, Tiankai Chen, Ning Yan, and Jianping Xie. Roles of thiolate ligands in the synthesis, properties and catalytic application of gold nanoclusters. *Coordination Chemistry Reviews*, 368:60–79, aug 2018. doi: 10.1016/j.ccr.2018.04.016.
- [7] Yingwei Li, Tatsuya Higaki, Xiangsha Du, and Rongchao Jin. Chirality and Surface Bonding Correlation in Atomically Precise Metal Nanoclusters. *Advanced Materials*, 32(41):1905488, mar 2020. doi: 10.1002/adma.201905488.
- [8] Stefan Knoppe and Thomas Bürgi. Chirality in Thiolate-Protected Gold Clusters. *Accounts of Chemical Research*, 47(4):1318–1326, mar 2014. doi: 10.1021/ar400295d.
- [9] Yanan Wang and Thomas Bürgi. Ligand exchange reactions on thiolate-protected gold nanoclusters. *Nanoscale Advances*, 3(10):2710–2727, 2021. doi: 10.1039/d1na00178g.
- [10] Bihan Zhang, Jishi Chen, Yitao Cao, Osburg Jin Huang Chai, and Jianping Xie. Ligand Design in Ligand-Protected Gold Nanoclusters. *Small*, 17(27):2004381, jan 2021. doi: 10.1002/smll.202004381.
- [11] Yanfei Zhu, Jun Guo, Xueying Qiu, Shenlong Zhao, and Zhiyong Tang. Optical Activity of Chiral Metal Nanoclusters. *Accounts of Materials Research*, 2(1):21–35, dec 2020. doi: 10.1021/accountsmr.0c00057.
- [12] Chenjie Zeng and Rongchao Jin. Chiral Gold Nanoclusters: Atomic Level Origins of Chirality. *Chemistry – An Asian Journal*, 12(15):1839–1850, jun 2017. doi: 10.1002/asia.201700023.
- [13] T. Gregory Schaaff, Grady Knight, Marat N. Shafigullin, Raymond F. Borkman, and Robert L. Whetten. Isolation and Selected Properties of a 10.4 kDa Gold:Glutathione Cluster Compound. *The Journal of Physical Chemistry B*, 102(52):10643–10646, dec 1998. doi: 10.1021/jp9830528.
- [14] Pablo D. Jadzinsky, Guillermo Calero, Christopher J. Ackerson, David A. Bushnell, and Roger D. Kornberg. Structure of a Thiol Monolayer-Protected Gold Nanoparticle at 1.1 Å Resolution. *Science*, 318(5849):430–433, oct 2007. doi: 10.1126/science.1148624.
- [15] Huifeng Qian, William T. Eckenhoff, Yan Zhu, Tomislav Pintauer, and Rongchao Jin. Total Structure Determination of Thiolate-Protected Au₃₈ Nanoparticles. *Journal of the American Chemical Society*, 132(24):8280–8281, jun 2010. doi: 10.1021/ja103592z.

- [16] Chenjie Zeng, Chong Liu, Yuxiang Chen, Nathaniel L. Rosi, and Rongchao Jin. Gold–Thiolate Ring as a Protecting Motif in the Au₂₀(SR)₁₆ Nanocluster and Implications. *Journal of the American Chemical Society*, 136(34):11922–11925, aug 2014. doi: 10.1021/ja506802n.
- [17] Chenjie Zeng, Tao Li, Anindita Das, Nathaniel L. Rosi, and Rongchao Jin. Chiral Structure of Thiolate-Protected 28-Gold-Atom Nanocluster Determined by X-ray Crystallography. *Journal of the American Chemical Society*, 135(27):10011–10013, jul 2013. doi: 10.1021/ja404058q.
- [18] Chenjie Zeng, Yuxiang Chen, Kristin Kirschbaum, Kannatassen Appavoo, Matthew Y. Sfeir, and Rongchao Jin. Structural patterns at all scales in a nonmetallic chiral Au₁₃₃(SR)₅₂ nanoparticle. *Science Advances*, 1(2), mar 2015. doi: 10.1126/sciadv.1500045.
- [19] Nan Yan, Nan Xia, Lingwen Liao, Min Zhu, Fengming Jin, Rongchao Jin, and Zhikun Wu. Unraveling the long-pursued Au₁₄₄ structure by X-ray crystallography. *Science Advances*, 4(10), oct 2018. doi: 10.1126/sciadv.aat7259.
- [20] Noelia Barrabés, Bei Zhang, and Thomas Bürgi. Racemization of Chiral Pd₂Au₃₆(SC₂H₄Ph)₂₄: Doping Increases the Flexibility of the Cluster Surface. *Journal of the American Chemical Society*, 136(41):14361–14364, sep 2014. doi: 10.1021/ja507189v.
- [21] Igor Dolamic, Stefan Knoppe, Amala Dass, and Thomas Bürgi. First enantioseparation and circular dichroism spectra of Au₃₈ clusters protected by achiral ligands. *Nature Communications*, 3(1), jan 2012. doi: 10.1038/ncomms1802.
- [22] Igor Dolamic, Birte Varnholt, and Thomas Bürgi. Chirality transfer from gold nanocluster to adsorbate evidenced by vibrational circular dichroism. *Nature Communications*, 6(1), may 2015. doi: 10.1038/ncomms8117.
- [23] Olga Lopez-Acevedo, Hironori Tsunoyama, Tatsuya Tsukuda, Hannu Häkkinen, and Christine M. Aikens. Chirality and Electronic Structure of the Thiolate-Protected Au₃₈ Nanocluster. *Journal of the American Chemical Society*, 132(23):8210–8218, may 2010. doi: 10.1021/ja102934q.
- [24] Stefan Knoppe and Thomas Bürgi. The fate of Au₂₅(SR)₁₈ clusters upon ligand exchange with binaphthyl-dithiol: interstaple binding vs. decomposition. *Physical Chemistry Chemical Physics*, 15(38):15816, 2013. doi: 10.1039/c3cp52634h.
- [25] Satyabrata Si, Cyrille Gautier, Julien Boudon, Rossana Taras, Serafino Gladiali, and Thomas Bürgi. Ligand Exchange on Au₂₅ Cluster with Chiral Thiols. *The Journal of Physical Chemistry C*, 113(30):12966–12969, jul 2009. doi: 10.1021/jp9044385.
- [26] Annelies Sels, Noelia Barrabés, Stefan Knoppe, and Thomas Bürgi. Isolation of atomically precise mixed ligand shell PdAu₂₄ clusters. *Nanoscale*, 8(21):11130–11135, 2016. doi: 10.1039/c6nr00931j.
- [27] Stefan Knoppe, Asantha C. Dharmaratne, Ella Schreiner, Amala Dass, and Thomas Bürgi. Ligand Exchange Reactions on Au₃₈ and Au₄₀ Clusters: A Combined Circular Dichroism and Mass Spectrometry Study. *Journal of the American Chemical Society*, 132(47):16783–16789, nov 2010. doi: 10.1021/ja104641x.
- [28] Yanan Wang, Belén Nieto-Ortega, and Thomas Bürgi. Amplification of enantiomeric excess by dynamic inversion of enantiomers in deracemization of Au₃₈ clusters. *Nature Communications*, 11(1), sep 2020. doi: 10.1038/s41467-020-18357-0.
- [29] Yoshiki Niihori, Miku Matsuzaki, Thalappil Pradeep, and Yuichi Negishi. Separation of Precise Compositions of Noble Metal Clusters Protected with Mixed Ligands. *Journal of the American Chemical Society*, 135(13):4946–4949, mar 2013. doi: 10.1021/ja4009369.

- [30] Thomas W. Ni, Marcus A. Tofaneli, Billy D. Phillips, and Christopher J. Ackerson. Structural Basis for Ligand Exchange on $\text{Au}_{25}(\text{SR})_{18}$. *Inorganic Chemistry*, 53(13):6500–6502, jun 2014. doi: 10.1021/ic5010819.
- [31] Chenjie Zeng, Yuxiang Chen, Anindita Das, and Rongchao Jin. Transformation Chemistry of Gold Nanoclusters: From One Stable Size to Another. *The Journal of Physical Chemistry Letters*, 6(15):2976–2986, jul 2015. doi: 10.1021/acs.jpcllett.5b01150.
- [32] Tokuhisa Kawawaki, Ayano Ebina, Yasunaga Hosokawa, Shuhei Ozaki, Daiki Suzuki, Sakiat Hossain, and Yuichi Negishi. Thiolate-Protected Metal Nanoclusters: Recent Development in Synthesis, Understanding of Reaction, and Application in Energy and Environmental Field. *Small*, 17(27):2005328, feb 2021. doi: 10.1002/sml.202005328.
- [33] Xi Kang and Manzhou Zhu. Transformation of Atomically Precise Nanoclusters by Ligand-Exchange. *Chemistry of Materials*, 31(24):9939–9969, nov 2019. doi: 10.1021/acs.chemmater.9b03674.
- [34] Qiaofeng Yao, Tiankai Chen, Xun Yuan, and Jianping Xie. Toward Total Synthesis of Thiolate-Protected Metal Nanoclusters. *Accounts of Chemical Research*, 51(6):1338–1348, may 2018. doi: 10.1021/acs.accounts.8b00065.
- [35] Mathias Brust, Merryl Walker, Donald Bethell, David J. Schiffrin, and Robin Whyman. Synthesis of thiol-derivatised gold nanoparticles in a two-phase Liquid–Liquid system. *J. Chem. Soc., Chem. Commun.*, 0(7):801–802, 1994. doi: 10.1039/c39940000801.
- [36] Rongchao Jin, Huifeng Qian, Zhikun Wu, Yan Zhu, Manzhou Zhu, Ashok Mohanty, and Niti Garg. Size Focusing: A Methodology for Synthesizing Atomically Precise Gold Nanoclusters. *The Journal of Physical Chemistry Letters*, 1(19):2903–2910, sep 2010. doi: 10.1021/jz100944k.
- [37] Michael Galchenko, Raphael Schuster, Andres Black, Maria Riedner, and Christian Klinke. Preparation of high-yield and ultra-pure Au_{25} nanoclusters: towards their implementation in real-world applications. *Nanoscale*, 11(4):1988–1994, 2019. doi: 10.1039/c8nr08200f.
- [38] Zhen Lei, Jiao-Jiao Li, Zi-Ang Nan, Zhan-Guo Jiang, and Quan-Ming Wang. Cluster From Cluster: A Quantitative Approach to Magic Gold Nanoclusters [$\text{Au}_{25}(\text{SR})_{18}$]. *Angewandte Chemie International Edition*, 60(26):14415–14419, may 2021. doi: 10.1002/anie.202103290.
- [39] Shinjiro Takano, Shun Ito, and Tatsuya Tsukuda. Efficient and Selective Conversion of Phosphine-Protected $(\text{MAu}_8)^{2+}$ ($M = \text{Pd}, \text{Pt}$) Superatoms to Thiolate-Protected $(\text{MAu}_{12})^{6+}$ or Alkynyl-Protected $(\text{MAu}_{12})^{4+}$ Superatoms via Hydride Doping. *Journal of the American Chemical Society*, 141(40):15994–16002, sep 2019. doi: 10.1021/jacs.9b08055.
- [40] Xun Yuan, Bin Zhang, Zhentao Luo, Qiaofeng Yao, David Tai Leong, Ning Yan, and Jianping Xie. Balancing the Rate of Cluster Growth and Etching for Gram-Scale Synthesis of Thiolate-Protected Au_{25} Nanoclusters with Atomic Precision. *Angewandte Chemie International Edition*, 53(18):4623–4627, mar 2014. doi: 10.1002/anie.201311177.
- [41] Manzhou Zhu, Huifeng Qian, Xiangming Meng, Shenshen Jin, Zhikun Wu, and Rongchao Jin. Chiral Au_{25} Nanospheres and Nanorods: Synthesis and Insight into the Origin of Chirality. *Nano Letters*, 11(9):3963–3969, aug 2011. doi: 10.1021/nl202288j.
- [42] Hiroshi Yao. Chiral ligand-protected gold nanoclusters: Considering the optical activity from a viewpoint of ligand dissymmetric field. *Progress in Natural Science: Materials International*, 26(5):428–439, oct 2016. doi: 10.1016/j.pnsc.2016.08.006.

- [43] Qian Xu, Santosh Kumar, Shenshen Jin, Huifeng Qian, Manzhou Zhu, and Rongchao Jin. Chiral 38-Gold-Atom Nanoclusters: Synthesis and Chiroptical Properties. *Small*, 10(5):1008–1014, oct 2013. doi: 10.1002/sml.201302279.
- [44] Makenzie R. Provorse and Christine M. Aikens. Origin of Intense Chiroptical Effects in Undecagold Subnanometer Particles. *Journal of the American Chemical Society*, 132(4):1302–1310, feb 2010. doi: 10.1021/ja906884m.
- [45] Natalia V. Karimova and Christine M. Aikens. Chiroptical Activity in BINAP- and DIOP-Stabilized Octa- and Undecagold Clusters. *The Journal of Physical Chemistry C*, 122(20):11051–11065, apr 2018. doi: 10.1021/acs.jpcc.7b12264.
- [46] Santosh Kumar and Rongchao Jin. Water-soluble Au₂₅(Capt)₁₈ nanoclusters: synthesis, thermal stability, and optical properties. *Nanoscale*, 4(14):4222, 2012. doi: 10.1039/c2nr30833a.
- [47] Sami Malola, Sami Kaappa, and Hannu Häkkinen. Role of Nanocrystal Symmetry in the Crossover Region from Molecular to Metallic Gold Nanoparticles. *The Journal of Physical Chemistry C*, 123(33):20655–20663, jul 2019. doi: 10.1021/acs.jpcc.9b05863.
- [48] Sami Malola and Hannu Häkkinen. Chiral footprint of the ligand layer in the all-alkynyl-protected gold nanocluster Au₁₄₄(CCPhF)₆₀. *Chemical Communications*, 55(64):9460–9462, 2019. doi: 10.1039/c9cc04914b.
- [49] Huifeng Qian and Rongchao Jin. Ambient Synthesis of Au₁₄₄(SR)₆₀ Nanoclusters in Methanol. *Chemistry of Materials*, 23(8):2209–2217, mar 2011. doi: 10.1021/cm200143s.
- [50] Daniel Stellwagen, Andrew Weber, Gudrun Lisa Bovenkamp, Rongchao Jin, J. H. Bitter, and Challa S. S. R. Kumar. Ligand control in thiol stabilized Au₃₈ clusters. *RSC Advances*, 2(6):2276, 2012. doi: 10.1039/c2ra00747a.
- [51] Atal Shivhare, Stephen J. Ambrose, Haixia Zhang, Randy W. Purves, and Robert W. J. Scott. Stable and recyclable Au₂₅ clusters for the reduction of 4-nitrophenol. *Chem. Commun.*, 49(3):276–278, 2013. doi: 10.1039/c2cc37205c.
- [52] Rui Hong, Joseph M. Fernández, Hiroshi Nakade, Rochelle Arvizo, Todd Emrick, and Vincent M. Rotello. In situ observation of place exchange reactions of gold nanoparticles. Correlation of monolayer structure and stability. *Chem. Commun.*, (22):2347–2349, 2006. doi: 10.1039/b603988j.
- [53] J. Jesús Pelayo, Robert L. Whetten, and Ignacio L. Garzón. Geometric Quantification of Chirality in Ligand-Protected Metal Clusters. *The Journal of Physical Chemistry C*, 119(51):28666–28678, dec 2015. doi: 10.1021/acs.jpcc.5b10235.
- [54] Olga Lopez-Acevedo, Jaakko Akola, Robert L. Whetten, Henrik Grönbeck, and Hannu Häkkinen. Structure and Bonding in the Ubiquitous Icosahedral Metallic Gold Cluster Au₁₄₄(SR)₆₀. *The Journal of Physical Chemistry C*, 113(13):5035–5038, jan 2009. doi: 10.1021/jp8115098.
- [55] Sami Malola and Hannu Häkkinen. Chiral Inversion of Thiolate-Protected Gold Nanoclusters via Core Reconstruction without Breaking a Au–S Bond. *Journal of the American Chemical Society*, 141(14):6006–6012, mar 2019. doi: 10.1021/jacs.9b01204.
- [56] Stefan Knoppe, Igor Dolamic, and Thomas Bürgi. Racemization of a Chiral Nanoparticle Evidences the Flexibility of the Gold–Thiolate Interface. *Journal of the American Chemical Society*, 134(31):13114–13120, jul 2012. doi: 10.1021/ja3053865.

- [57] Huifeng Qian, Yan Zhu, and Rongchao Jin. Size-Focusing Synthesis, Optical and Electrochemical Properties of Monodisperse $\text{Au}_{38}(\text{SC}_2\text{H}_4\text{Ph})_{24}$ Nanoclusters. *ACS Nano*, 3(11):3795–3803, oct 2009. doi: 10.1021/nm901137h.
- [58] Stephan Pollitt, Vera Truttmann, Thomas Haunold, Clara Garcia, Wojciech Olszewski, Jordi Llorca, Noelia Barrabés, and Günther Rupprechter. The Dynamic Structure of $\text{Au}_{38}(\text{SR})_{24}$ Nanoclusters Supported on CeO_2 upon Pretreatment and CO Oxidation. *ACS Catalysis*, 10(11):6144–6148, may 2020. doi: 10.1021/acscatal.0c01621.
- [59] Eric F. Pettersen, Thomas D. Goddard, Conrad C. Huang, Gregory S. Couch, Daniel M. Greenblatt, Elaine C. Meng, and Thomas E. Ferrin. UCSF Chimera – A visualization system for exploratory research and analysis. *Journal of Computational Chemistry*, 25(13):1605–1612, 2004. doi: 10.1002/jcc.20084.
- [60] Marcus A. Tofaneli, Kirsi Salorinne, Thomas W. Ni, Sami Malola, Brian Newell, Billy Phillips, Hannu Häkkinen, and Christopher J. Ackerson. Jahn-Teller effects in $\text{Au}_{25}(\text{SR})_{18}$. *Chemical Science*, 7(3):1882–1890, 2016. doi: 10.1039/c5sc02134k.
- [61] Michael W. Heaven, Amala Dass, Peter S. White, Kennedy M. Holt, and Royce W. Murray. Crystal Structure of the Gold Nanoparticle $[\text{N}(\text{C}_8\text{H}_{17})_4][\text{Au}_{25}(\text{SCH}_2\text{CH}_2\text{Ph})_{18}]$. *Journal of the American Chemical Society*, 130(12):3754–3755, mar 2008. doi: 10.1021/ja800561b.
- [62] Christine M. Aikens. Effects of core distances, solvent, ligand, and level of theory on the TDDFT optical absorption spectrum of the thiolate-protected Au_{25} nanoparticle. *The Journal of Physical Chemistry A*, 113(40):10811–10817, sep 2009. doi: 10.1021/jp9051853.
- [63] Manzhou Zhu, Christine M. Aikens, Frederick J. Hollander, George C. Schatz, and Rongchao Jin. Correlating the Crystal Structure of A Thiol-Protected Au_{25} Cluster and Optical Properties. *Journal of the American Chemical Society*, 130(18):5883–5885, apr 2008. doi: 10.1021/ja801173r.
- [64] G. te Velde, F. M. Bickelhaupt, E. J. Baerends, C. Fonseca Guerra, S. J. A. van Gisbergen, J. G. Snijders, and T. Ziegler. Chemistry with ADF. *Journal of Computational Chemistry*, 22(9):931–967, 2001. doi: 10.1002/jcc.1056.
- [65] A. D. Becke. Density-functional exchange-energy approximation with correct asymptotic behavior. *Physical Review A*, 38(6):3098–3100, sep 1988. doi: 10.1103/physreva.38.3098.
- [66] John P. Perdew. Density-functional approximation for the correlation energy of the inhomogeneous electron gas. *Physical Review B*, 33(12):8822–8824, jun 1986. doi: 10.1103/physrevb.33.8822.
- [67] E. Van Lenthe and E. J. Baerends. Optimized Slater-type basis sets for the elements 1-118. *Journal of Computational Chemistry*, 24(9):1142–1156, may 2003. doi: 10.1002/jcc.10255.
- [68] E. van Lenthe, E. J. Baerends, and J. G. Snijders. Relativistic regular two-component Hamiltonians. *The Journal of Chemical Physics*, 99(6):4597–4610, sep 1993. doi: 10.1063/1.466059.
- [69] Erik van Lenthe, Andreas Ehlers, and Evert-Jan Baerends. Geometry optimizations in the zero order regular approximation for relativistic effects. *The Journal of Chemical Physics*, 110(18):8943–8953, may 1999. doi: 10.1063/1.478813.
- [70] Brett M. Bode and Mark S. Gordon. MacMolPlt: a graphical user interface for GAMESS. *Journal of Molecular Graphics and Modelling*, 16(3):133–138, jun 1998. doi: 10.1016/s1093-3263(99)00002-9.
- [71] Robert Rüger, Erik van Lenthe, Thomas Heine, and Lucas Visscher. Tight-binding approximations to time-dependent density functional theory – A fast approach for the calculation of electronically excited states. *The Journal of Chemical Physics*, 144(18):184103, may 2016. doi: 10.1063/1.4948647.

- [72] Jochen Autschbach. Computing chiroptical properties with first-principles theoretical methods: Background and illustrative examples. *Chirality*, 21(1E):E116–E152, 2009. doi: 10.1002/chir.20789.
- [73] S.J.A. van Gisbergen, J.G. Snijders, and E.J. Baerends. Implementation of time-dependent density functional response equations. *Computer Physics Communications*, 118(2-3):119–138, may 1999. doi: 10.1016/s0010-4655(99)00187-3.

4. Selective Ligand Exchange Synthesis of $\text{Au}_{16}(\text{2-PET})_{14}$ from $\text{Au}_{15}(\text{SG})_{13}$

Vera Truttmann, Stephan Pollitt, Hedda Drexler, Sreejith P. Nandan, Dominik Eder, Noelia Barrabés, and Günther Rupprechter



The content of this chapter has been published in *J. Chem. Phys.*, 155, 161102 (2021)
<https://doi.org/10.1063/5.0062534>

4.1. Abstract

Replacement of protecting ligands of gold nanoclusters by ligand exchange has become an established post-synthetic tool for selectively modifying the nanoclusters' properties. Several Au nanoclusters are known to additionally undergo size transformations upon ligand exchange, enabling access to cluster structures that are difficult to obtain by direct synthesis. This work reports on the selective size transformation of Au₁₅(SG)₁₃ (SG: glutathione) nanoclusters to Au₁₆(2-PET)₁₄ (2-PET: 2-phenylethanethiol) nanoclusters through a two-phase ligand exchange process at room temperature. Among several parameters evaluated, the addition of a large excess of exchange thiol (2-PET) to the organic phase was identified as the key factor for the structure conversion. After exchange, the nature of the clusters was determined by UV-Vis, electrospray ionization-time of flight mass spectrometry, attenuated total reflection-Fourier transform infrared, and extended x-ray absorption fine-structure spectroscopy. The obtained Au₁₆(2-PET)₁₄ clusters proved to be exceptionally stable in solution, showing only slightly diminished UV-Vis absorption features after 3 days, even when exposed to an excess of thiol ligands.

4.2. Communication

Thiolate protected gold (Au) nanoclusters have received widespread attention in the recent years, owing to their size-selective and tunable properties.^[1,2] They consist of a small gold core stabilized by thiolate ligands (SR⁻), which surround the inner metal atoms by forming -SR-(Au-SR-)_x staple units.^[3] A series of magic-number clusters was predicted by Häkkinen and co-workers, exhibiting extraordinary stability due to their closed electron shells.^[4] Several candidates of this series have been synthesized and characterized, including Au₂₅(SR)₁₈⁻,^[5] Au₁₀₂(SR)₄₄,^[6] and Au₁₄₄(SR)₆₀.^[7]

However, ultrasmall thiolate protected Au nanoclusters with 20 or less atoms have only scarcely been studied so far. This is related to their limited stability in the size-focusing processes taking place during synthesis,^[8] following modified Brust procedures.^[9] Typically, a gold salt precursor is dissolved and partially reduced by addition of thiols. This step is then followed by a second reduction to yield Au nanoclusters.^[2] The clusters are initially polydisperse but can be focused to predominantly one size by reacting for a defined time interval under reducing conditions in which unstable sizes will eventually convert to more stable ones.^[10,11]

Several ultrasmall nanoclusters were obtained by Negishi *et al.*, employing the water soluble tripeptide, L-glutathione (GSH), as a ligand.^[12] However, the presented synthesis method yielded a size dispersion of structures consisting of between 10 and 39 Au atoms. Monodisperse samples were only accessible by polyacrylamide gel electrophoresis (PAGE) separation. Significant progress in selective production of small Au nanoclusters protected by water soluble thiolates was later made by Xie and co-workers, establishing selective protocols toward Au₁₅(SG)₁₃ and Au₁₈(SG)₁₄.^[13,14] Nevertheless, even though these ultrasmall nanoclusters

can be obtained with significant yield and purity, their reactivity has remained widely unexplored.

Over the last decade, fueled by the isolation and identification of a variety of different gold nanoclusters, understanding the structural transformations in Au nanocluster formation and reactions has become a major research focus in metal nanocluster chemistry. An emerging field is related to cluster growth schemes from simple kernel building blocks to superatom structures.^[15–17] So-called ligand-exchange-induced size/structure transformations (LEISTs) are currently also intensively studied, since they present synthetic approaches toward novel cluster compositions and structures while avoiding post-synthetic separation steps.^[16,18–22] During exchange reactions of thiolate-protected Au nanoclusters with thiolate ligands, Au-SR is transformed to Au-SR', i.e., the interaction between the protecting ligand sphere and the Au kernel should remain mostly unaltered.^[18] However, structural transformations of the Au nanoclusters are known to occur because of differences in the properties or structures of the original and the exchange ligand.^[18–21] These processes usually require the addition of a large excess of exchange ligands as well as elevated temperatures,^[19] though exceptions are known.^[21] Several clusters obtained by the LEIST strategy have been reported so far.^[18,21]

The degree of changes imposed to the cluster structure is known to depend on the specific exchange conditions and may vary significantly. For example, reacting the glutathione-protecting Au₁₈(SG)₁₄ with cyclohexanethiol led to a simple structural rearrangement of the cluster core while maintaining its size.^[23] This seems to be related to the interplay of the cluster, ligand, and solvent, clearly showing that the whole ligand exchange system has to be taken into account.^[24] However, the number of Au atoms may also be altered upon thiol-to-thiol ligand exchange, e.g., in the growth of Au₂₅(S-But)₁₈ to Au₂₈(PPT)₂₁ (S-But: butanethiol, PPT: 2-phenylpropanethiol)^[25] or from Au₁₅(SG)₁₃ to Au₁₆(S-Adm)₁₂ (S-Adm: adamantanethiol).^[26] Reductions in cluster size are also common, for example, in the reaction of Au₂₅(2-PET)₁₈ with TBBT, yielding Au₂₂(2-PET)₄(TBBT)₁₄ (2-PET: 2-phenylethanethiol, TBBT: 4-tert-butylbenzenethiol).^[27] Au₂₀(TBBT)₁₆ has also already been obtained from Au₂₅(2-PET)₁₈[−],^[28] as well as Au₃₆(TBBT)₂₄ from Au₃₈(2-PET)₂₄. Overall, a range of cluster species can be accessed through selective ligand exchange transformations, some of which are challenging to obtain by direct synthesis.^[19] This confirms the use of LEIST post-synthetic modifications as a synthesis tool toward novel cluster structures.

In this work, the ligand exchange of Au₁₅(SG)₁₃ precursor clusters with 2-phenylethanethiol ligands was explored, selectively yielding Au₁₆(2-PET)₁₄ clusters. The reaction was found to proceed only when a large excess (as compared to conventional ligand exchange processes) of the organic thiol was added. Moreover, a dependence on the purity of the water-soluble precursor clusters could be noted. The unexpected formation of Au₁₆(2-PET)₁₄ in this exchange is explained by its high stability against thiolate etching. The selective ligand exchange synthesis of Au₁₆(2-PET)₁₄ is yet another application of the LEIST approach, enriching the library of nanocluster transformation reactions.

To obtain the $\text{Au}_{16}(\text{2-PET})_{14}$ clusters, a simple two-phase ligand exchange procedure is used, which is described in the supplementary material, see Chapter 4.5, in more detail. First, a solution of $\text{Au}_{15}(\text{SG})_{13}$ in H_2O is prepared. After addition of a solution of 2-PET (>500 eq. compared to mol precursor cluster) in dichloromethane (DCM), the mixture is stirred vigorously at room temperature. Over a few hours, the yellow color of the aqueous phase gradually vanishes, whereas the shade of orange in the previously colorless organic phase darkens (see photographs in Figure 4.10). This is accompanied by a change in the UV-Vis absorption profile of the organic phase, which starts to show defined bands at 365, 420, and 485 nm [Figure 4.2(b)]. Size exclusion chromatography of the ligand exchange product in the organic phase then yields mainly $\text{Au}_{16}(\text{2-PET})_{14}$, with only very small amounts of smaller polydisperse clusters eluting at the end.

The nature of the exchange product was evaluated by ESI-TOFMS (electrospray ionization-time of flight mass spectrometry). As can be seen from Figure 4.1, a sharp peak is observed at 4933 Da, which could be identified as $[\text{Au}_{16}(\text{2-PET})_{13}]^+$, as a comparison of the experimental isotope pattern with a simulated one shows. The spectrum further shows cluster fragments obtained by the loss of several (Au-2-PET) units from $[\text{Au}_{16}(\text{2-PET})_{13}]^+$, as well as further in-source fragmentation and gas phase chemistry products. It is worth noting that this might be the result of the relatively high concentration of the sample used for this specific measurement (as compared to the other ESI-MS measurements in this Communication) to ensure a signal-to-noise ratio sufficient for the comparison with isotope pattern fits, as only by that a definitive assignment of the nature of the exchange product was possible. The top graphic of Figure 4.1 shows an enlarged view of the patterns associated with $[\text{Au}_{16}(\text{2-PET})_{14}]^+$ (Me: Na, K, Cu). A comparison with their isotope pattern fits can be found in Fig. S7. A low intensity $[\text{Au}_{16}(\text{2-PET})_{14}]^+$ peak could be identified as well in Figure 4.1. This indicates formation of a neutral $\text{Au}_{16}(\text{2-PET})_{14}$ cluster species upon ligand exchange.

It should be noted that the formation of $\text{Au}_{20}(\text{2-PET})_{16}$ was assumed in the beginning, since the UV-Vis spectrum obtained after the exchange showed close similarities with a reported spectrum.^[29] However, no significant signals associated with $[\text{Au}_{20}(\text{2-PET})_{15}]^+$ (5995 Da) or $[\text{Au}_{20}(\text{2-PET})_{16}\text{-Me}]^+$ adducts (6150-6200 Da) could be identified. Moreover, while $\text{Au}_{16}(\text{S-Adm})_{12}$ has been reported and has even been crystallized before,^[26,30] reports on a Au_{16} cluster with 14 protecting units are scarce. Formation of $\text{Au}_{16}(\text{SG})_{14}$ in their syntheses was, however, observed by Hamouda *et al.* with ESI-MS in negative mode, and it was determined to be of neutral charge.^[31]

This selective transformation of $\text{Au}_{15}(\text{SG})_{13}$ toward $\text{Au}_{16}(\text{2-PET})_{14}$ was also unexpected because the relatively small 2-phenylethanethiol does not usually induce a change in the cluster size, even though size transformations regularly happen upon exchange with bulky exchange ligands.^[20] Moreover, $\text{Au}_{15}(\text{SG})_{13}$ is known to react with adamantaneethiol to give $\text{Au}_{16}(\text{S-Adm})_{12}$.^[26] This cluster possesses the same number of Au atoms but has only 12 instead of 14 protecting ligands. The reaction proceeds via a twophase ligand exchange process comparable to the one described in this manuscript, also employing DCM as the organic solvent. However, the attempt of Zhu and co-workers of conducting the exchange with

2-PET instead of S-Adm resulted in a featureless UV-Vis absorption spectrum, indicating decomposition of the sample.^[26]

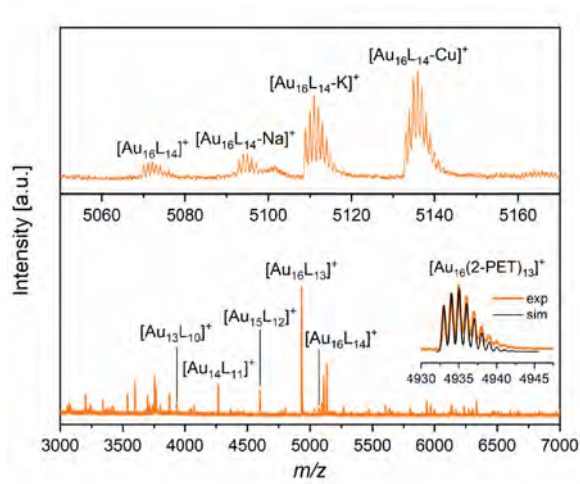


Figure 4.1.: ESI-time of flight mass spectrometry (TOFMS) spectrum of the product clusters after the ligand exchange reaction (L: 2-phenylethanethiolate). The top graphic shows an enlarged view of the m/z 5050–5170 area. The comparison of the measured accurate mass (exp) and the calculated exact mass (sim) of the $[\text{Au}_{16}(2\text{-PET})_{13}]^+$ species is shown in the inset.

Therefore, to investigate the origin of this unexpected size transformation and to optimize the procedure, several parameters of the protocol were altered. Thereby, the amount of excess 2-PET added to the reaction mixture was found to have the biggest influence. Whereas the reaction proceeded within a few hours if 500 or more equivalents of 2-PET with respect to the moles of $\text{Au}_{15}(\text{SG})_{13}$ were added to the reaction mixture, no reaction was observed if less than 300 equivalents were used. This was indicated by the organic phase still being completely colorless after a few days of stirring, whereas a significant amount of white precipitate had formed at the interface.

It should be noted that even though ligand exchange processes require an excess of exchange thiol to be added to the reaction, the 500-1000 eq. used for this reaction can be considered a large excess for a conventional ligand exchange maintaining the kernel size. However, this has been found to promote size transformation reactions also by other authors.^[19,28,32] $\text{Au}_{16}(2\text{-PET})_{14}$ was indeed found to be very stable in the presence of free thiol ligands. As shown in Figure 4.6, even after stirring in an excess thiol solution for 3 days, the UV-Vis profile of $\text{Au}_{16}(2\text{-PET})_{14}$ shows only minor weakening of the absorption features. It is therefore assumed that the selective formation of $\text{Au}_{16}(2\text{-PET})_{14}$ originates from its exceptional stability in the presence of free thiols. This also explains why no $\text{Au}_{16}(2\text{-PET})_{14}$ was found by Zhu and co-workers, since significantly less thiol was used in their experiments.^[26] Moreover, adamantanethiol, the exchange ligand used in that case, is significantly more bulky than 2-

phenylethanethiol, which can likely result in different cluster structures and might explain the different Au/ligand ratios observed of the product Au_{16} clusters.

To obtain a crude understanding of the reaction kinetics, the ligand exchange was followed by UV-Vis spectroscopy [Figures 4.2(a) and 4.2(b)] and ESI-TOFMS [Figures 4.13(a) and 4.13(b)]. As can be seen, the characteristic absorption features of $\text{Au}_{15}(\text{SG})_{13}$ at 380 and 420 nm^[13] disappeared quickly and mostly featureless spectra were obtained from then on. This was accompanied by formation of a white dispersion in the H_2O phase shortly after the start of the reaction, which disappeared again after some hours. The disappearance of the $\text{Au}_{15}(\text{SG})_{13}$ clusters within the first 6 h of the reaction was also evident in the ESI mass spectra [Figure 4.13(a)]. The DCM phase was originally colorless and did not show significant UV-Vis absorption. However, after 6 h, the bands associated with $\text{Au}_{16}(2\text{-PET})_{14}$ were already observed, even though the solution was still almost colorless. The ESI mass spectrum of the DCM reaction phase also already showed a prominent $[\text{Au}_{16}(2\text{-PET})_{13}]^+$ peak [Figure 4.13(b)]. The features then intensified up to 15 h, after which no major change could be observed anymore. The H_2O phase was completely colorless at this point of the reaction. In addition, formation of a yellow precipitate at the interface was noted, which did not disappear anymore in the subsequent hours of stirring.

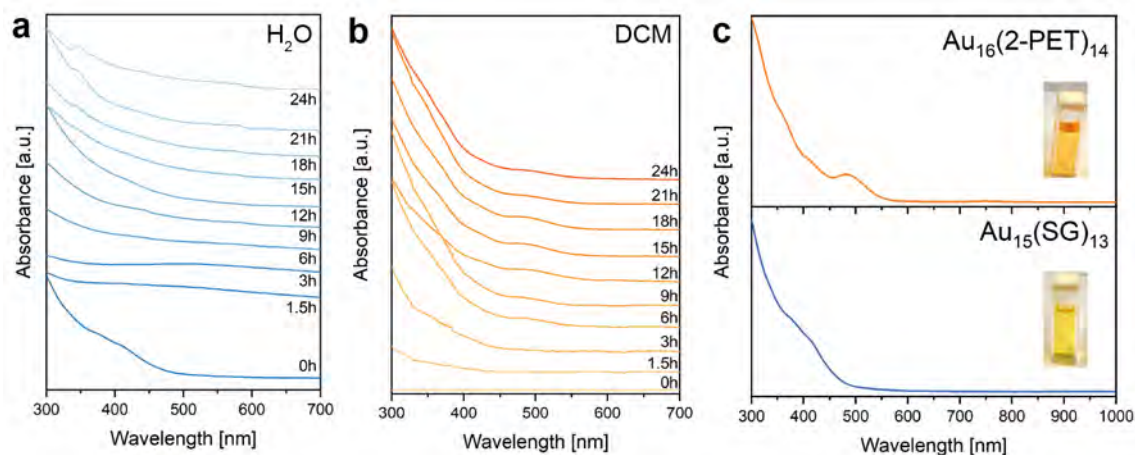


Figure 4.2.: UV-Vis absorption spectra of the ligand exchange reaction of $\text{Au}_{15}(\text{SG})_{13}$ with 2-PET at defined time intervals: (a) aqueous phase and (b) DCM phase. The optical absorption spectra of the purified clusters before (bottom) and after (top) the ligand exchange are shown in (c). The insets show photographs of the respective cluster solutions.

It is therefore assumed that the product cluster $\text{Au}_{16}(2\text{-PET})_{14}$ had already been formed upon transition of the cluster from the aqueous to the DCM phase, since no indication of a polydisperse reaction mixture could be seen from the UV-Vis spectra of the organic phase. The size transformation and focusing process thus seems to occur at the reaction interface. This is in agreement with the general understanding of LEIST processes of Au nanoclusters,

which suggests a reconstruction mechanism rather than decomposition and subsequent reforming of cluster species.^[13,32] However, further studies would be required to elucidate the exact nature of the structural modifications, which are beyond the scope of this Communication.

To elucidate the role of $\text{Au}_{15}(\text{SG})_{13}$ in this reaction, the ligand exchange was also attempted with a polydisperse mixture of water-soluble $\text{Au}_x(\text{SG})_y$ nanoclusters. However, even though a color transfer to the DCM phase was noticed, the UV-Vis spectrum showed no sign of the formation of $\text{Au}_{16}(\text{2-PET})_{14}$ [Figure 4.8]. This indicates that the structural transformation might originate from the building blocks already present in the $\text{Au}_{15}(\text{SG})_{13}$ structure.

Moreover, also a "one-pot ligand exchange synthesis" approach was tested, for which the $\text{Au}_{15}(\text{SG})_{13}$ was not isolated first and then only subsequently subjected to the ligand exchange reaction. Therefore, the $\text{Au}_{15}(\text{SG})_{13}$ was set up in H_2O and toluene as described by Yao *et al.*,^[13] and after the reduction process was completed, 2-PET was directly added to the toluene phase and the stirring continued until complete color transfer to the organic phase was observed [Figure 4.7(a)]. However, even though some $\text{Au}_{16}(\text{2-PET})_{14}$ could be isolated after size exclusion chromatography, also polydisperse clusters were found [Figure 4.7(b)]. Compared to the ligand exchange starting from isolated $\text{Au}_{15}(\text{SG})_{13}$, the yield was significantly lower and the process less selective.

Further attempts were made by adjusting the solvent mixture by addition of methanol (MeOH) to tune the polarity. The influence of the pH of the aqueous phase was also investigated, since it plays a crucial role in the synthesis of $\text{Au}_{15}(\text{SG})_{13}$.^[13] Therefore, the mixture was acidified to $\text{pH} = 2.0$ by the addition of 1 N HNO_3 (pH was ≈ 4.2 before). However, neither of these seemed to have a significant influence on the reaction dynamics.

Complementary structural information of the clusters was obtained by attenuated total reflection-Fourier transform infrared (ATR-FTIR) spectroscopy by probing the characteristic vibrations of the ligands at mid- (MIR) and the Au-S vibrations at far-infrared (FIR). The spectra of the clusters before and after the ligand exchange are shown in Figure 4.3. The initial glutathione ligand of $\text{Au}_{15}(\text{SG})_{13}$ features intense bands in the amide I and II regions and a broad band centered at 3300 cm^{-1} related to OH and NH_3^+ stretching vibrations [Figure 4.3, blue line].^[33,34] The broadness of the bands can be explained by the presence of residual H_2O due to the hygroscopic nature of the clusters. In contrast, after the ligand exchange ($\text{Au}_{16}(\text{2-PET})_{14}$), only vibrations associated with the 2-PET ligand were detected, i.e., vibrations of the aromatic ring ($1600\text{--}1450\text{ cm}^{-1}$).^[35] This confirms that all original GSH ligands were replaced by 2-PET. The absence of a band associated with the S-H stretch (2500 cm^{-1})^[35] confirmed that no free ligands were present in the sample.

The two distinctly different ligands before and after ligand exchange also exhibit different vibrations in the far-infrared energy range [Figure 4.3(b)]. In this region, Au-S vibrations related to different staple configurations can be observed, based on previous experimental and theoretical studies.^[36–38] Depending on the nature of the Au-S vibration (tangential or radial), $\text{Au}_{\text{core}}\text{-S}_{\text{staple}}$ or $\text{Au}_{\text{staple}}\text{-S}_{\text{staple}}$ vibrations can be distinguished,^[36,37] in some cases even the length of the staple motif.^[39] The range below 110 cm^{-1} is associated with weak

Au–S–Au bending modes and bands above 300 cm^{-1} may be assigned to vibrations of Au and S both located inside the staple, whereas bands between 200 and 300 cm^{-1} may originate from $\text{Au}_{\text{core}}\text{--S}_{\text{staple}}$.^[36]

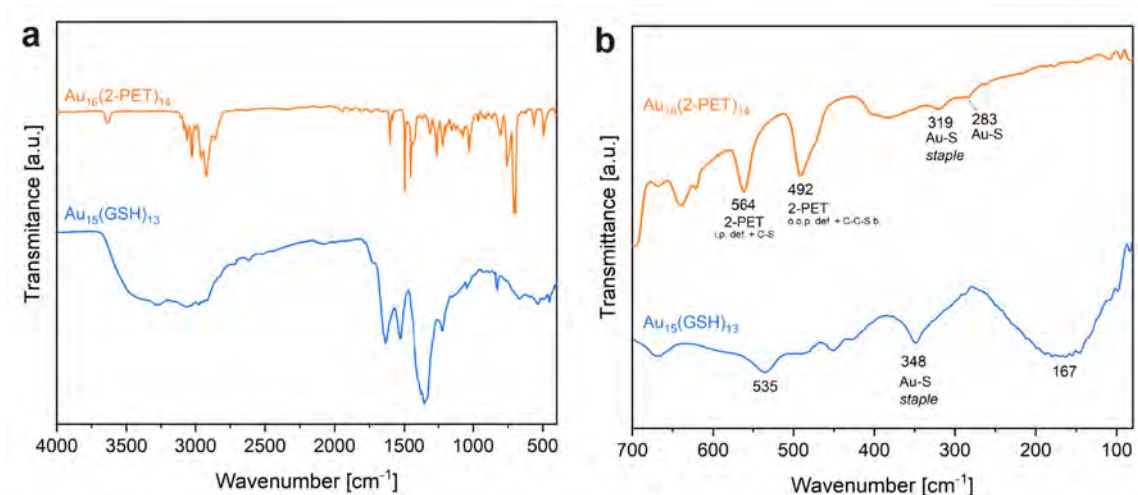


Figure 4.3.: Attenuated total reflection-Fourier transform infrared spectra of the clusters before and after ligand exchange: (a) mid-infrared and (b) far-infrared regions.

The two clusters investigated in this work, $\text{Au}_{15}(\text{SG})_{13}$ and $\text{Au}_{16}(2\text{-PET})_{14}$ [Figure 4.3(b)], showed quite different spectra, denoting the structural evolution. The precursor nanocluster $\text{Au}_{15}(\text{SG})_{13}$ with GSH ligands showed an intense band at 348 cm^{-1} , which could be due to $\text{Au}_{\text{staple}}\text{--S}_{\text{staple}}$ vibrations. Below 300 cm^{-1} , a broad band centered at 167 cm^{-1} prevents further identification of potential Au–S modes. Overall, the spectrum matches the one of $\text{Au}_{25}(\text{SG})_{18}$ clusters reported by Valušová *et al.*^[33] After the ligand exchange, characteristic FIR vibrations of the 2-PET ligand are observed at 564 and 492 cm^{-1} .^[37] Moreover, a band appeared at 319 cm^{-1} , associated with Au–S vibrations of both atoms inside a staple. A weak band at 283 cm^{-1} can also be identified, which can be assigned to tangential or radial Au–S vibrations.^[37]

Furthermore, extended X-ray absorption fine-structure (EXAFS) studies were performed to inspect the structural differences from the starting $\text{Au}_{15}(\text{GSH})_{13}$ cluster to the one obtained after ligand exchanged $\text{Au}_{16}(2\text{-PET})_{14}$. The X-ray absorption near edge structure (XANES) spectrum of $\text{Au}_{16}(2\text{-PET})_{14}$ shows a small increase in white line intensity (most prominent at $11\,923\text{ eV}$) compared to $\text{Au}_{15}(\text{GSH})_{13}$ [Figure 4.4(a)], which is usually related to a difference in the valence electron occupancy.^[40] This would indicate an increase in the valence state from Au_{15} to Au_{16} , as the higher Au/S ratio leads to more unoccupied d orbitals to which electrons can be excited, resulting in higher white line intensity. However, Yamazoe and co-workers reported that the change in white line intensity can also be related to differences in the nature of the Au–S bonds as well as due to different types of ligands.^[40] This is also

denoted in the R space spectrum [Figure 4.4(b)], which shows a small increase in the intensity of the scattering peak at 2 Å (Au–S bond). The following peak at around 2.5 Å originating from the Au–Au bonds was also increasing, which could denote the increase of the Au cluster kernel.^[41] Au₁₅(SG)₁₃ has been predicted to possess a Au₄ kernel,^[42,43] whereas the resolved crystal structure of Au₁₆(S–Adm)₁₂ showed a Au₇ kernel.^[26] However, it should be noted that it is unclear if the Au₁₆(2-PET)₁₄ obtained in this study would possess the same kernel structure, considering that it has two additional protecting thiolate ligands. Similar cluster kernels before and after exchange would explain the similarity of their EXAFS spectra.

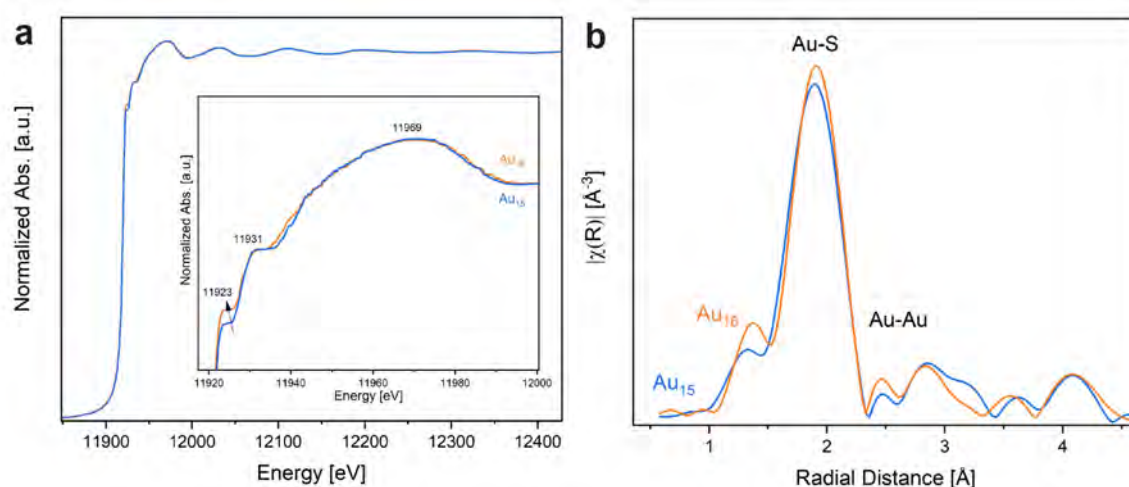


Figure 4.4.: Au L₃-edge (a) XANES and (b) FT-EXAFS spectra of the Au₁₅(SG)₁₃ and Au₁₆(2-PET)₁₄ nanoclusters.

Both clusters, Au₁₅(SG)₁₃ and Au₁₆(2-PET)₁₄, also show photoluminescence (PL) in the near-infrared region, as can be seen in Figure 4.5. The discrete energy levels, which are characteristic of the nanoclusters, result in molecular-like optical properties and enable luminescence, though usually with bands in the red wavelength region.^[44] To further characterize the properties of the obtained Au₁₆(2-PET)₁₄ nanoclusters and to compare them to those of the initial Au₁₅(SG)₁₃, a photoluminescence analysis was performed. The PL spectra of both Au₁₅(SG)₁₃ and Au₁₆(2-PET)₁₄ shown in Figure 4.5 exhibit a broad band centered at around 670 nm and another maximum above 800 nm, in agreement with published spectra.^[13,30,45] The dual fluorescence profile of both clusters indicates electron donation from the ligands when excited, as determined by previous studies.^[46] Slight differences were noticed when measuring the emission decay (probed at 650 and 700 nm; see Figure 4.14) after excitation at 375 nm: The lifetimes found for the Au₁₅(SG)₁₃ nanoclusters were a bit longer at both emission wavelengths (12.2 vs 9.6 ns at 650 nm and 14.5 vs 11.3 ns at 700 nm), which seems to be related to the electronegative substituents of the GSH ligand.^[46] This further confirms the influence of the protecting ligand on the cluster

properties and the importance of selective ligand engineering, for example, by ligand exchange.

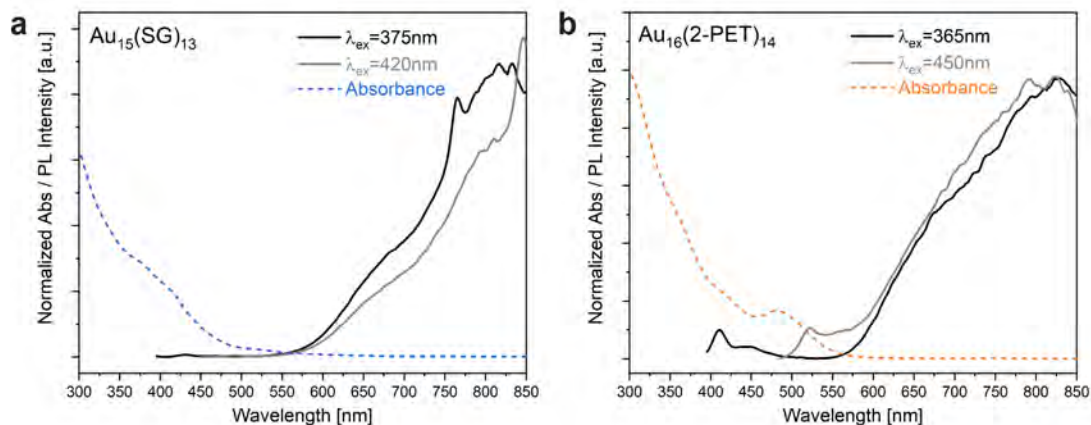


Figure 4.5.: Absorbance and photoluminescence spectra of (a) $\text{Au}_{15}(\text{SG})_{13}$ and (b) $\text{Au}_{16}(\text{2-PET})_{14}$. The sharp features in the emission spectra at 750 and 840 nm in (a), which are due to 2nd order diffraction from the excitation wavelength, and the ones at 410 and 525 nm in (b) also appear in the PL spectra of the pure solvents and do not originate from the Au nanoclusters (see solvent PL spectra in Figure 4.15).

In summary, this work reports on the synthesis of $\text{Au}_{16}(\text{2-PET})_{14}$ by ligand exchange from $\text{Au}_{15}(\text{SG})_{13}$. The selective size transformation occurred only upon addition of a sufficiently large excess of 2-phenylethanethiol. The obtained $\text{Au}_{16}(\text{2-PET})_{14}$ is exceptionally stable in the presence of free thiols in solution, preserving its optical absorption features even after days of exposure. Complete replacement of the protecting ligand sphere was confirmed by ESI-TOFMS and ATR-FTIR, whereas EXFAS measurements showed that both clusters seem to bear structural and electronic similarities. Moreover, they both show photoemission in the near-infrared region. Overall, this application of the LEIST methodology presents a feasible synthesis approach toward $\text{Au}_{16}(\text{2-PET})_{14}$, one of the smallest thiolate-protected nanoclusters isolated so far.

4.3. Acknowledgments

The staff of CLAESS beamline at ALBA synchrotron, especially Dr. Wojciech Olszewski and Dr. Carlo Marini, are thanked for help in acquiring the EXFAS spectra reported in this manuscript (Proposal No. 2017092492). EQ VIBT GmbH and the BOKU Core Facility Mass Spectrometry are acknowledged for providing mass spectrometry instrumentation. We acknowledge support from the Austrian Science Fund (FWF) via grants Single Atom Catalysis (Grant No. I 4434-N) and Elise Richter (Grant No. V831-N). The authors acknowledge TU Wien Bibliothek for financial support through its Open Access Funding Programme.

4.4. Author Contributions

The synthesis of the Au nanoclusters and the exchange reactions as well as characterization were performed by V.T. and S.P. ESI-MS was measured by H.D. Photoluminescence measurements were conducted by S.P.N. and D.E. Data evaluation and manuscript preparation were performed by V.T. and N.B., with contributions from all authors. Funding was acquired by N.B. and G.R.

4.5. Supplementary Information

The supplementary material contains all experimental details, additional UV-Vis of the ligand exchanges, and photographs showing the phase transfer of the clusters through the reaction, as well as MS and additional PL spectra.

4.5.1. Materials and Methods

All chemicals mentioned in the following were obtained from commercial suppliers and were used as received, unless stated otherwise. Ultrapure Milli-Q H₂O (18.6 MΩcm at 25 °C) was used for all steps involving water.

4.5.1.1. Synthetic Procedures

4.5.1.1.1. Synthesis of Au₁₅(SG)₁₃

Au₁₅(SG)₁₃ was synthesized following the procedure by Yao *et al.*^[13] Therefore, 100 mg HAuCl₄ · 3 H₂O (0.25 mmol, 1 eq. and 234.1 mg L-glutathione (GSH; 0.76 mmol, 3 eq.) were dissolved in 184 ml Milli-Q H₂O. The pH of the aqueous solution was adjusted to 2.0 by careful addition of 1 N HNO₃. This led to a slight color change from light yellow to murky white. After 5 minutes, a solution of 220.8 mg borane tert-butylamine (TBAB; 2.54 mmol, 10 eq.) in 250 ml toluene was added and the reaction mixture stirred at room temperature overnight. During that time, the color of the aqueous phase gradually changed from white to light orange. After phase separation, the precipitate in the aqueous phase was removed by centrifugation (4500 rpm, 5 min). The solution was then concentrated to 5-10 ml by evaporation at reduced pressure and the clusters then precipitated by addition of methanol (MeOH). After centrifugation, the clusters were redissolved in 5 ml H₂O and precipitated once more by addition of methanol, yielding Au₁₅(SG)₁₃ nanoclusters, as confirmed by the characteristic UV-Vis absorption bands at 380 and 420 nm and the Au₁₅(SG)₁₃^{x+} ions (x= 3, 4, 5) observed in the mass spectrum (Figure 4.11).

4.5.1.1.2. Synthesis of Au₁₆(SC₂H₄Ph)₁₄ by Ligand Exchange from Au₁₅(SG)₁₃ with 2-PET

10 mg Au₁₅(SG)₁₃ were dissolved in 20 ml H₂O, resulting in an intense yellow color of the solution. To this, 134.5 µl 2-phenylethanethiol (2-PET) in 20 ml dichloromethane (DCM) were added. The mixture was stirred vigorously at room temperature for 24 h. The reaction was followed by UV-Vis spectroscopy (see Figure 4.2 in the main text) and ESI-TOFMS (Figure 4.13). The aqueous phase got murky within the first few hours. However, no color was observed in the organic phase until after 6 h.

After 15 h, the organic phase exhibited an intense orange color and some orange precipitate had formed at the interface. No major change was observed anymore from that point on. After 24 h, the DCM phase was separated and dried. The crude product was loaded on a size

exclusion chromatography (SEC) column (Biobeads SX-1 support, Bio-Rad) in tetrahydrofuran (THF). 3.3 mg (48% theoretical yield) of pure $\text{Au}_{16}(\text{2-PET})_{14}$ were obtained. The cluster was identified by the $[\text{Au}_{16}(\text{2-PET})_{13}]^+$ and the $[\text{Au}_{16}(\text{2-PET})_{14}\text{-Me}]^+$ (Me: Na, K, Cu) ions observed in the mass spectrum (Figure 4.1 in the main text).

The same ligand exchange procedure was conducted with the aqueous phase adjusted with 1 N HNO_3 to pH 2.0, since this had been found to be the optimal pH for formation of $\text{Au}_{15}(\text{SG})_{13}$ by Yao *et al.*^[13] The UV-Vis spectra of this exchange are shown in Figure 4.6.

4.5.1.1.3. One-pot Synthesis of $\text{Au}_{16}(\text{2-PET})_{14}$ from $\text{HAuCl}_4 \cdot 3 \text{H}_2\text{O}$

In a first step, the synthesis of $\text{Au}_{15}(\text{SG})_{13}$ starting from 50 mg $\text{HAuCl}_4 \cdot 3 \text{H}_2\text{O}$ (0.13 mmol, 1 eq.) was set up as described in Section 4.5.1.1.1. After stirring overnight after the addition of 10 eq. TBAB, 566.3 μl of 2-PET (4.23 mmol, 33.3 eq.) were added to the toluene phase (the beige precipitate was not removed). The light orange color of the aqueous phase faded out within the next few hours and formation of a yellow precipitate was noticed; however, no color transfer to the toluene phase was observed at that time. The reaction was continued for 3 days until the color transfer to the organic phase seemed complete. No yellow precipitate was noticed anymore at the end of the reaction, only the same white solids at the interface that were also found after the standard ligand exchange procedures (Section 4.5.1.1.2). UV-Vis spectra of this approach are shown in Figure 4.7(a).

The organic phase was then isolated and the solvent was removed at reduced pressure. The crude product was loaded onto a SEC column (Biobeads SX-1 support, Bio-Rad) in tetrahydrofuran. 2.4 mg (6% theoretical yield) of $\text{Au}_{16}(\text{2-PET})_{14}$ could be isolated (Figure 4.7(b), top line). Compared to the ligand exchange procedure described in Section 4.5.1.1.2, also a pre-fraction was isolated, which exhibited a quite featureless absorption profile (Figure 4.7(b), bottom line).

4.5.1.1.4. Attempted Ligand Exchange Towards $\text{Au}_{16}(\text{2-PET})_{14}$ from a Polydisperse $\text{Au}_x(\text{SG})_y$ Nanocluster Mixture

The polydisperse nanocluster mixture was obtained by adapting the synthesis of $\text{Au}_{15}(\text{SG})_{13}$ as described by Yao *et al.*^[13] 200 mg $\text{HAuCl}_4 \cdot 3 \text{H}_2\text{O}$ (0.51 mmol, 1 eq.) and 473.2 mg L-glutathione (GSH; 1.54 mmol, 3 eq.) were dissolved in 350 ml Milli-Q H_2O . The pH of the aqueous solution was adjusted to 2.0 with 1 N HNO_3 and 439.6 mg borane *tert*-butylamine (TBAB); 5.05 mmol, 10 eq.) in 300 ml toluene was added. The reaction was continued overnight and then the precipitate removed by centrifugation (4500 rpm, 5 min). The solvent was then removed at reduced pressure and the sample redissolved in 20 ml H_2O (precipitation with MeOH was not successful in this case). The mixture was filtered to remove the significant amount of white precipitate that had formed. The featureless UV-Vis spectrum of the aqueous phase (Figure 4.8, top line) confirmed the polydispersity of the sample.

A solution of 1 ml 2-PET (7.47 mmol, 14.6 eq.) in 35 ml DCM was added to the sample in 20 ml H_2O . The mixture was stirred for a day until the orange color had completely transferred to the organic phase. After phase separation and removal of DCM, the product was loaded

onto a SEC column (Biobeads SX-1 support, Bio-Rad) in tetrahydrofuran. However, the UV-Vis profile did not indicate formation of $\text{Au}_{16}(\text{2-PET})_{14}$ (Figure 4.8, bottom line).

4.5.1.1.5. Stability Tests of $\text{Au}_{16}(\text{2-PET})_{14}$

To test the stability of the synthesized $\text{Au}_{16}(\text{2-PET})_{14}$, two different experiments were conducted: In a first test, 0.9 mg $\text{Au}_{16}(\text{2-PET})_{14}$ were dissolved in 3 ml toluene and the sample left in a closed vial at room temperature for several days. Every 24 h, a UV-Vis spectrum of the solution was recorded (see Figure 4.9).

Further, also the stability of the $\text{Au}_{16}(\text{2-PET})_{14}$ clusters in a solution containing a large excess (approx. 1000 eq. thiols per cluster) of 2-PET ligands was tested. Therefore, a typical ligand exchange experiment as described in Section 4.5.1.1.2 was continued for 3 d. The sample still showed the typical absorption pattern of Au_{16} , though the features were slightly reduced (Figure 4.6, top line). It should be noted that in this specific case, the pH of the aqueous phase was set to 2.0 at the beginning of the exchange. However, as discussed in the main text, this was not found to have a major influence on the exchange.

4.5.1.2. Characterization

Ultraviolet-visible (UV-Vis) spectra were recorded on a UV-1600PC spectrometer (VWR) or a Perkin Elmer Lambda 35 spectrometer. The clusters were dissolved in an appropriate solvent (H_2O for $\text{Au}_{15}(\text{SG})_{13}$ and DCM, THF or toluene for $\text{Au}_{16}(\text{2-PET})_{14}$ and placed in 1 cm cuvettes for measurement.

ATR-FTIR spectra of the solid nanoclusters were recorded on a Perkin Elmer Spectrum 400 instrument equipped with a mid- (MIR) and far-infrared (FIR) detector.

Mass spectrometric analysis of $\text{Au}_{15}(\text{SG})_{13}$ and $\text{Au}_{16}(\text{2-PET})_{14}$ was performed by electrospray ionization-time of flight mass spectrometry (ESI-TOFMS). Therefore, the H_2O soluble samples were dissolved in 100 % LC-MS grade water. All other samples were first dissolved in 100 % toluene and further diluted in 100 % acetonitrile (ACN) to a ratio of 1:1 (v/v) and filtered (0.2 μm PTFE filter, Ref: 4552T, Pall Corporation) prior to analysis to obtain an approximate sample concentration of 100-200 $\mu\text{g}/\text{ml}$ (with the exception of the $\text{Au}_{16}(\text{2-PET})_{14}$ after SEC, for which a higher concentration was used). A flow injection method was applied (1290 Infinity II UPLC, Agilent Technologies) using 5 μl of the sample. The flow rate was 100 $\mu\text{l}/\text{min}$ with an eluent composition of 75:25 (99.9 % H_2O , 0.1 % formic acid: 99.9 % ACN, 0.1 % formic acid) for the water-soluble samples; for the rest an eluent composition of 10:90 (99.9 % H_2O , 0.1 % formic acid: 99.9 % ACN, 0.1 % formic acid) was used. The measurements were performed on a Time of Flight instrument (6230 B, Agilent Technologies) in the 1 GHz mode (m/z range: 100 - 20000). The settings for the ion source and the TOF can be found in Table 4.1. Before the analysis the instrument was tuned in positive mode (mass calibration up to m/z 2722), and during the analysis the reference masses were enabled, allowing for a mass accuracy of ± 1 ppm within the calibrated range. Data evaluation was performed with the Agilent MassHunter Qualitative Analysis Software (B.10.00). For the measured

molecules, single to quintuple charges could be observed. Isotope patterns were simulated using enviPat.^[47]

Table 4.1.: Instrument settings for the ESI-TOFMS analysis

Ion source settings		TOFMS settings	
Source type	dual AJS ESI	m/z range	100 - 20000
Ionisation mode	positive	Scan rate	2.00
Gas Temp./ °C	200	Accuracy/ resolution	± 1 ppm / 10000 (m/z 322)
Gas flow/ 1 min ⁻¹	10	Data storage	profile
Nebulizer/ psig	35	Reference mass	enabled
Sheath Gas Temp./ °C	350	Fragmentor/ V	180
Sheath Gas Flow/ 1 min ⁻¹	11	Capillary/ V	3500

Photoluminescence (PL) measurements of the Au nanoclusters dissolved in H₂O Au₁₅(SG)₁₃ or toluene Au₁₆(2-PET)₁₄ were carried out on a Picoquant FluoTime 300 spectrophotometer equipped with a PMA Hybrid 07 detector. A Xe arc lamp was used as excitation source. The excitation wavelengths of the steady state measurements were chosen according to the absorption features of the respective Au nanoclusters. Different longpass filters were used depending on the excitation wavelength: a 385 nm filter for excitation at 365 nm and 375 nm, a 435 nm filter for excitation at 420 nm and a 475 nm filter for excitation at 450 nm. Emission decay times after excitation at 375 nm laser wavelength were acquired at emission wavelengths of 700 nm and 650 nm for both samples. Fitting of the emission decay was performed using EasyTau2 software.

Extended X-ray absorption fine-structure spectroscopy was measured at CLAESS beamline of ALBA synchrotron (Au-L₃ edge). The clusters were dissolved in a minimum amount of H₂O (Au₁₅(SG)₁₃) or DCM (Au₁₆(2-PET)₁₄) and dropcasted onto Kapton tape. After complete solvent evaporation, EXAFS measurements of the solid samples were performed. Data evaluation was performed using the Artemis software package.^[48]

4.5.2. Additional UV-Vis Spectra of the Ligand Exchange Reactions

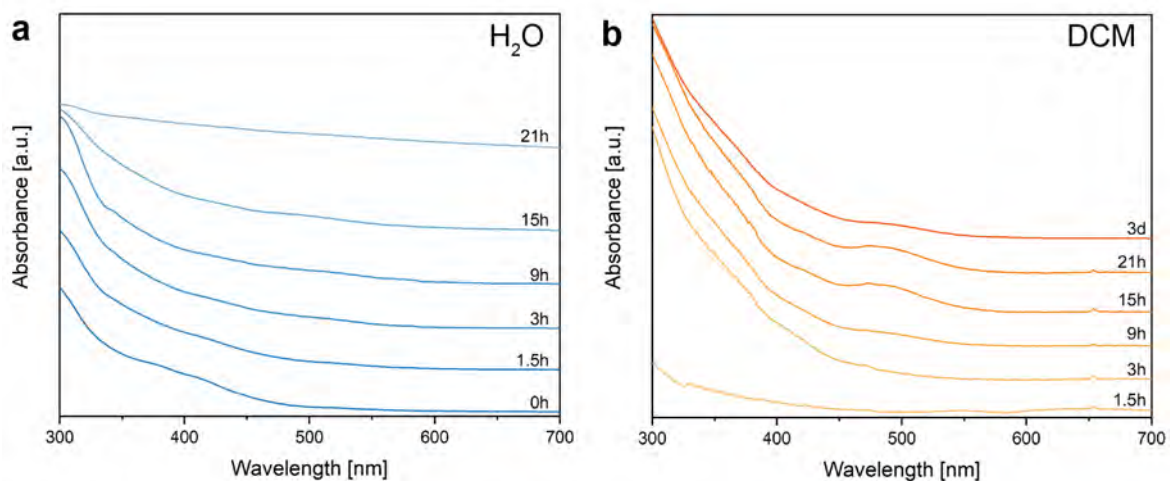


Figure 4.6.: UV-Vis absorbance of samples of the aqueous phase (a) and dichloromethane phase (b) at defined time intervals of the ligand exchange. The pH of the aqueous phase was adjusted to 2.0 before addition of 2-PET by acidifying with 1 N HNO₃.

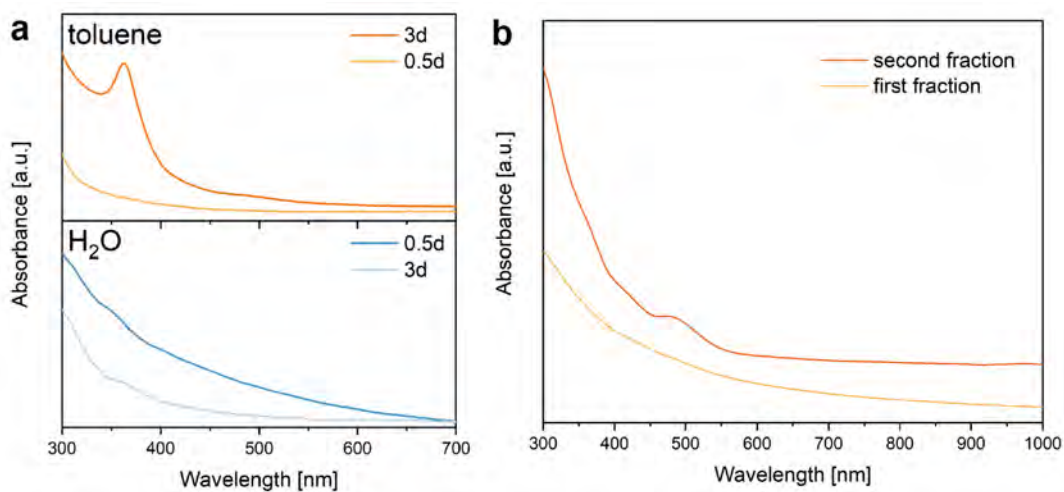


Figure 4.7.: (a) UV-Vis absorbance of samples of the toluene and aqueous phase of the one-pot ligand exchange synthesis attempt (Section 4.5.1.1.3): 0.5 days and 3 days days after addition of the exchange thiol 2-PET. (b) Fractions obtained after size exclusion chromatography of the toluene phase.

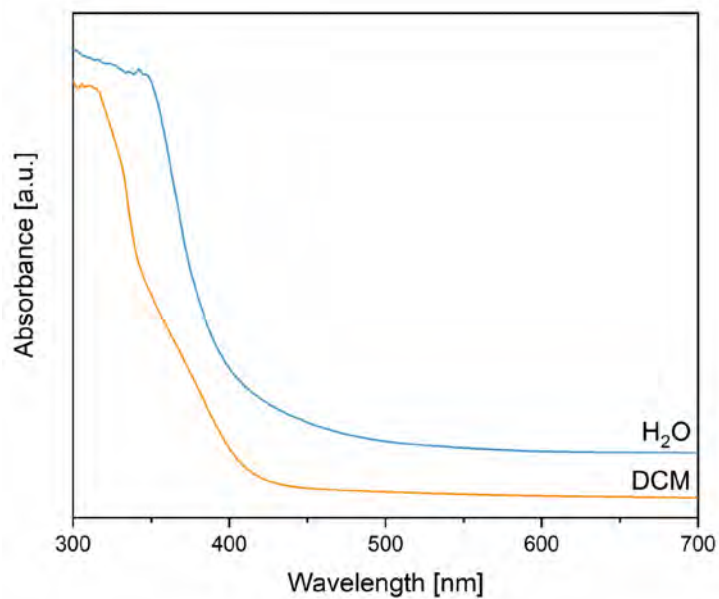


Figure 4.8.: UV-Vis absorbance of samples of the H₂O phase before and the dichloromethane phase after a ligand exchange attempt with 2-PET (24 h). Color transfer to the organic phase was complete at the time of measurement.

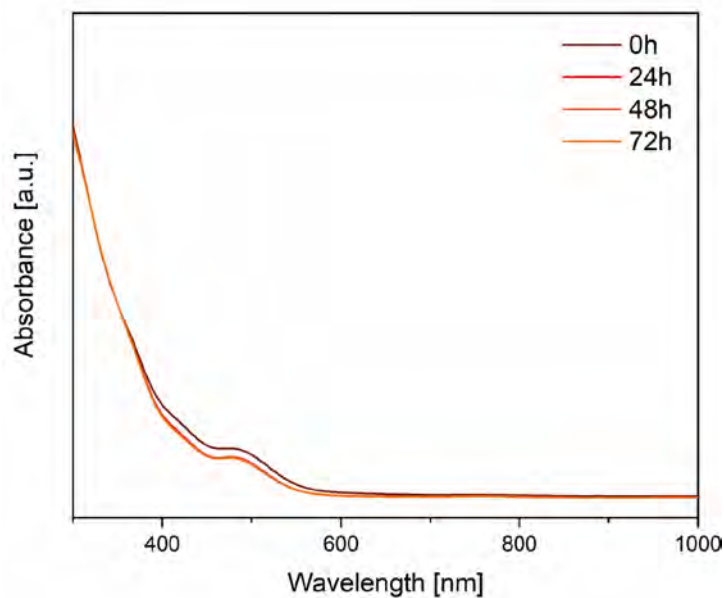


Figure 4.9.: UV-Vis absorbance of Au₁₆(2-PET)₁₄ dissolved in toluene at defined time intervals. The sample was stored at room temperature.

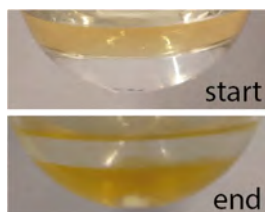


Figure 4.10.: Photographs of the ligand exchange batch.

4.5.3. Mass Spectra of the Au Nanoclusters

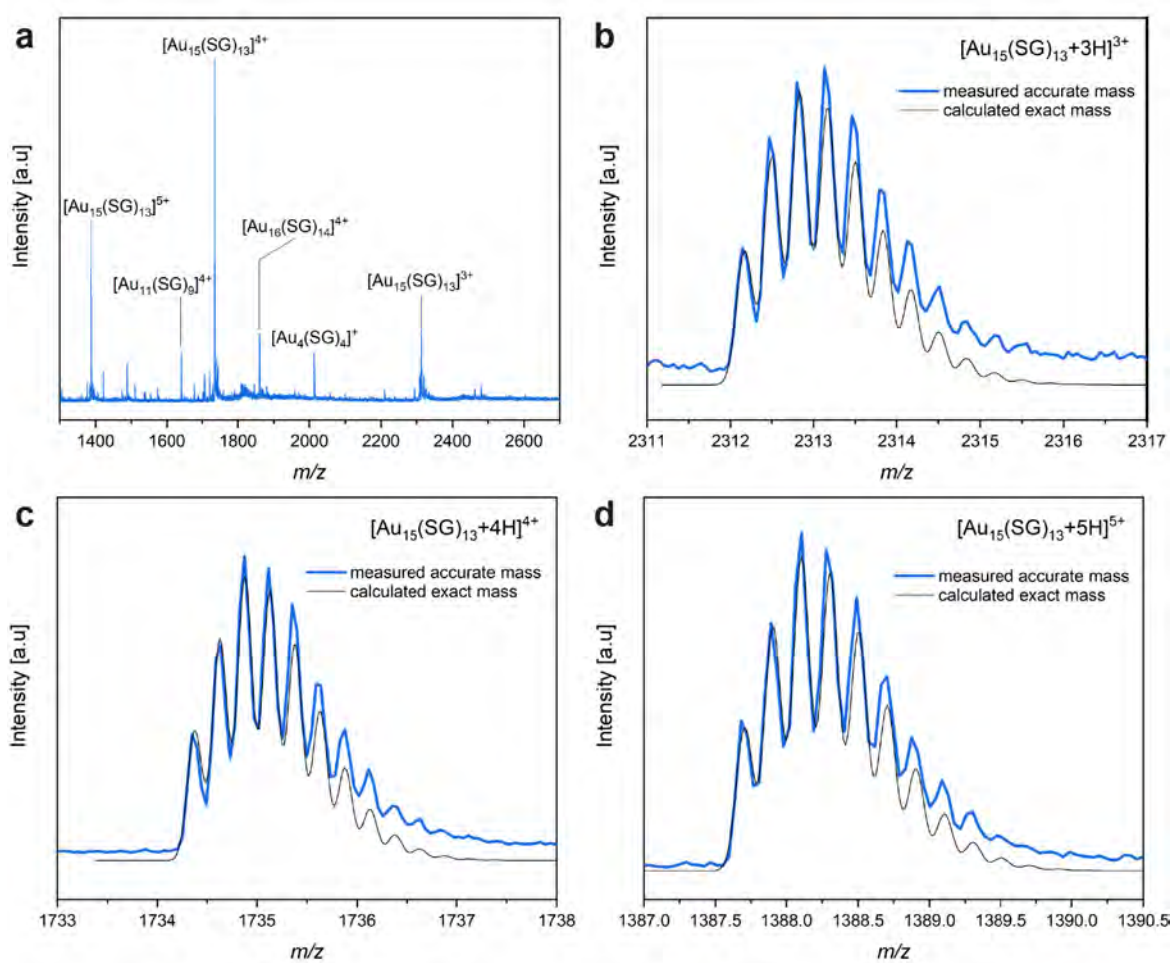


Figure 4.11.: ESI-TOF mass spectrum of $\text{Au}_{15}(\text{SG})_{13}$: m/z range 1300-2700 Dalton (a) and comparison of experimental and simulated isotope patterns of the multiple charged $\text{Au}_{15}(\text{SG})_{13}$ ions (b)-(d).

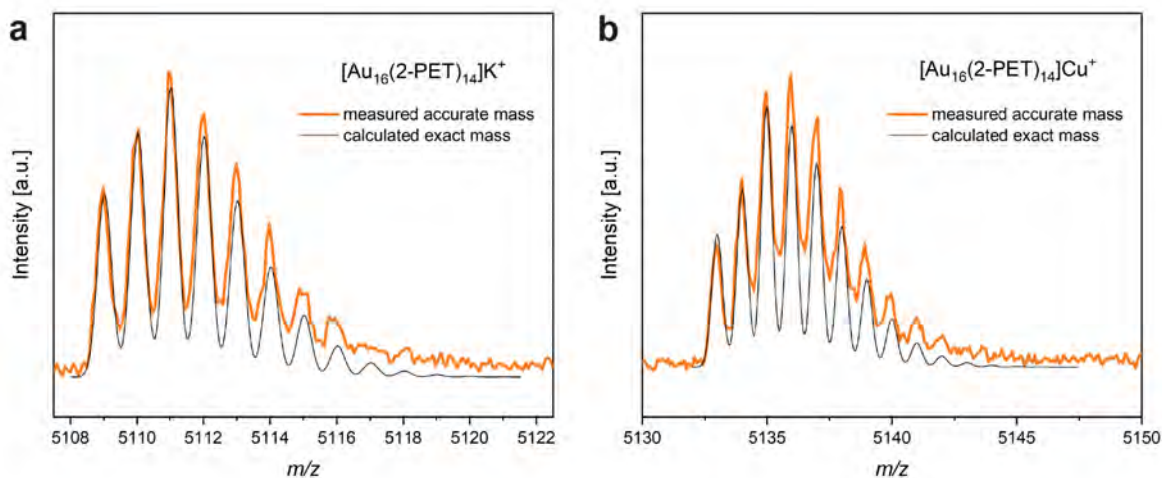


Figure 4.12.: Comparison of experimental and simulated isotope patterns of the $[\text{Au}_{16}(\text{SG})_{14}\text{-K}]^+$ (a) and $[\text{Au}_{16}(\text{SG})_{14}\text{-Cu}]^+$ ions (b). For $[\text{Au}_{16}(2\text{-PET})_{14}]^+$ and $[\text{Au}_{16}(\text{SG})_{14}\text{-Na}]^+$, the intensity of the peaks was not sufficient for a definite comparison.

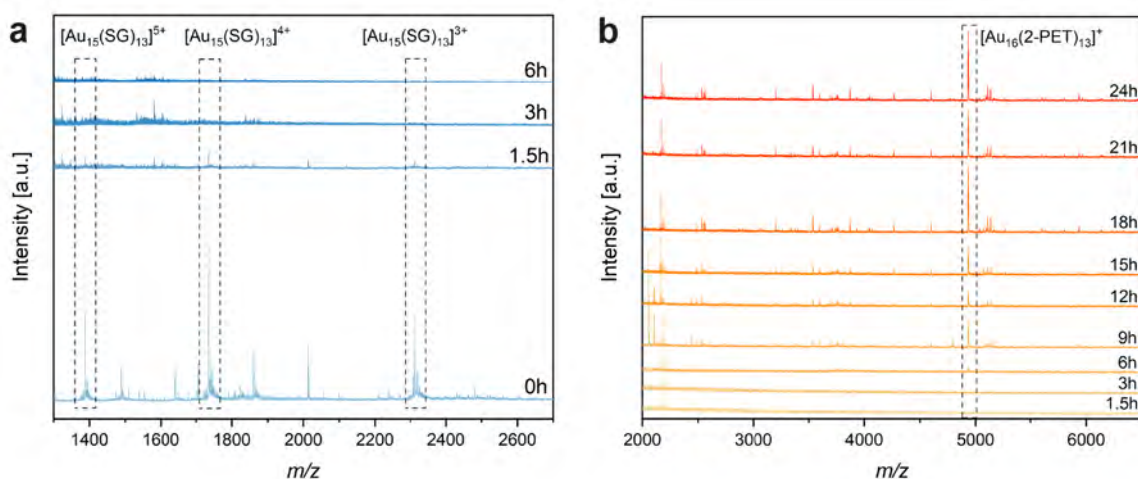


Figure 4.13.: ESI-TOF mass spectra of the samples taken during the ligand exchange process (Section 4.5.1.1.1): (a) H_2O phase and (b) DCM phase.

4.5.4. Additional Photoluminescence Spectra

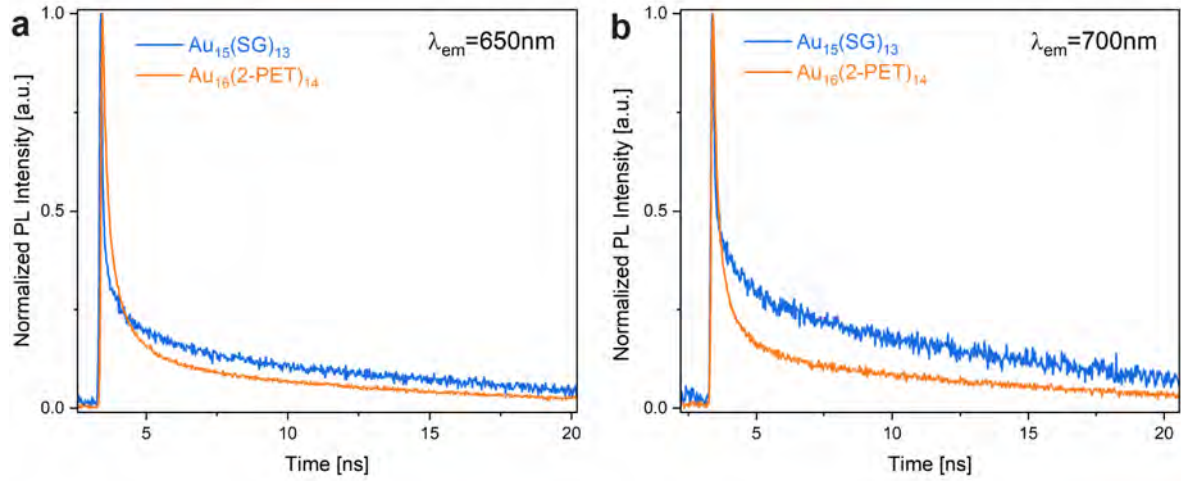


Figure 4.14.: Emission decay of the nanocluster samples at 650 nm (a) and at 700 nm (b) after excitation at 375 nm.

Table 4.2.: Emission lifetimes of the nanocluster samples after excitation at 375 nm

Cluster	$\lambda_{em} = 650 \text{ nm}$	$\lambda_{em} = 700 \text{ nm}$
$\text{Au}_{15}(\text{SG})_{13}$	$12.2 \pm 3.4 \text{ ns}$	$14.5 \pm 2.3 \text{ ns}$
$\text{Au}_{16}(\text{2-PET})_{14}$	$9.6 \pm 0.4 \text{ ns}$	$11.3 \pm 1.9 \text{ ns}$

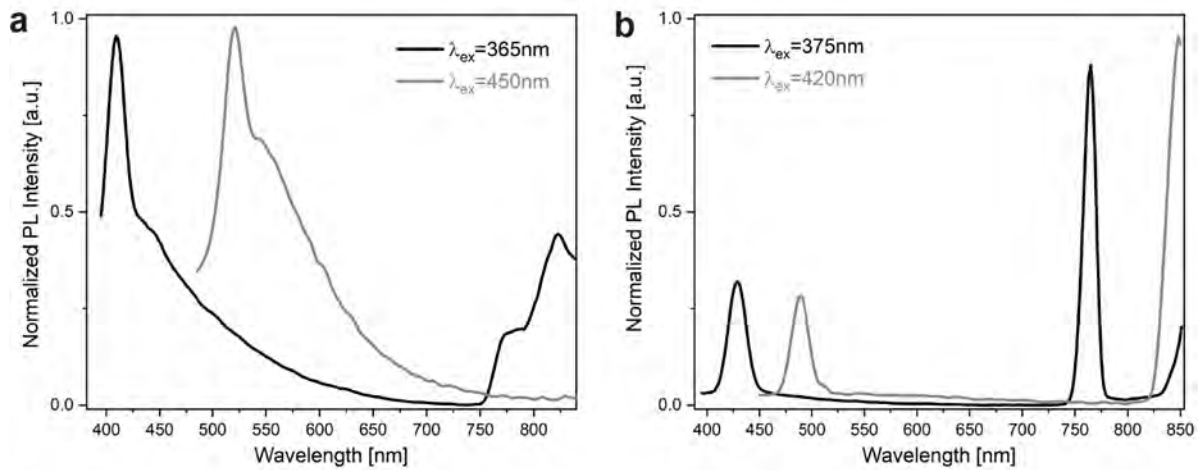


Figure 4.15.: Photoluminescence spectra of toluene (a) and H_2O (b) after excitation at different wavelengths.

4.6. References

- [1] Indranath Chakraborty and Thalappil Pradeep. Atomically Precise Clusters of Noble Metals: Emerging Link between Atoms and Nanoparticles. *Chemical Reviews*, 117(12):8208–8271, jun 2017. doi: 10.1021/acs.chemrev.6b00769.
- [2] Rongchao Jin, Chenjie Zeng, Meng Zhou, and Yuxiang Chen. Atomically Precise Colloidal Metal Nanoclusters and Nanoparticles: Fundamentals and Opportunities. *Chemical Reviews*, 116(18):10346–10413, sep 2016. doi: 10.1021/acs.chemrev.5b00703.
- [3] Thomas Bürgi. Properties of the gold–sulphur interface: from self-assembled monolayers to clusters. *Nanoscale*, 7(38):15553–15567, 2015. doi: 10.1039/c5nr03497c.
- [4] Michael Walter, Jaakko Akola, Olga Lopez-Acevedo, Pablo D. Jadzinsky, Guillermo Calero, Christopher J. Ackerson, Robert L. Whetten, Henrik Gronbeck, and Hannu Häkkinen. A unified view of ligand-protected gold clusters as superatom complexes. *Proceedings of the National Academy of Sciences*, 105(27):9157–9162, jul 2008. doi: 10.1073/pnas.0801001105.
- [5] Xi Kang, Hanbao Chong, and Manzhou Zhu. Au₂₅SR₁₈: the captain of the great nanocluster ship. *Nanoscale*, 10(23):10758–10834, 2018. doi: 10.1039/c8nr02973c.
- [6] Evgueni G. Mednikov and Lawrence F. Dahl. Crystallographically Proven Nanometer-Sized Gold Thiolate Cluster Au₁₀₂(SR)₄₄: Its Unexpected Molecular Anatomy and Resulting Stereochemical and Bonding Consequences. *Small*, 4(5):534–537, may 2008. doi: 10.1002/sml.200800051.
- [7] Nan Yan, Nan Xia, Lingwen Liao, Min Zhu, Fengming Jin, Rongchao Jin, and Zhikun Wu. Unraveling the long-pursued Au₁₄₄ structure by X-ray crystallography. *Science Advances*, 4(10), oct 2018. doi: 10.1126/sciadv.aat7259.
- [8] Yukatsu Shichibu, Yuichi Negishi, Hironori Tsunoyama, Masayuki Kanehara, Toshiharu Teranishi, and Tatsuya Tsukuda. Extremely High Stability of Glutathione-Protected Au₂₅ Clusters Against Core Etching. *Small*, 3(5):835–839, may 2007. doi: 10.1002/sml.200600611.
- [9] Mathias Brust, Merryll Walker, Donald Bethell, David J. Schiffrin, and Robin Whyman. Synthesis of thiol-derivatised gold nanoparticles in a two-phase Liquid–Liquid system. *J. Chem. Soc., Chem. Commun.*, 0(7):801–802, 1994. doi: 10.1039/c39940000801.
- [10] Shinjiro Takano and Tatsuya Tsukuda. Controlled Synthesis. In *Frontiers of Nanoscience*, pages 9–38. Elsevier, 2015. doi: 10.1016/b978-0-08-100086-1.00002-6.
- [11] Rongchao Jin, Huifeng Qian, Zhikun Wu, Yan Zhu, Manzhou Zhu, Ashok Mohanty, and Niti Garg. Size Focusing: A Methodology for Synthesizing Atomically Precise Gold Nanoclusters. *The Journal of Physical Chemistry Letters*, 1(19):2903–2910, sep 2010. doi: 10.1021/jz100944k.
- [12] Yuichi Negishi, Katsuyuki Nobusada, and Tatsuya Tsukuda. Glutathione-Protected Gold Clusters Revisited: Bridging the Gap between Gold(I)-Thiolate Complexes and Thiolate-Protected Gold Nanocrystals. *Journal of the American Chemical Society*, 127(14):5261–5270, mar 2005. doi: 10.1021/ja042218h.
- [13] Qiaofeng Yao, Yong Yu, Xun Yuan, Yue Yu, Jianping Xie, and Jim Yang Lee. Two-Phase Synthesis of Small Thiolate-Protected Au₁₅ and Au₁₈ Nanoclusters. *Small*, 9(16):2696–2701, feb 2013. doi: 10.1002/sml.201203112.
- [14] Yong Yu, Xi Chen, Qiaofeng Yao, Yue Yu, Ning Yan, and Jianping Xie. Scalable and Precise Synthesis of Thiolated Au_{10–12}, Au₁₅, Au₁₈, and Au₂₅ Nanoclusters via pH Controlled CO Reduction. *Chemistry of Materials*, 25(6):946–952, mar 2013. doi: 10.1021/cm304098x.

- [15] Xiangsha Du, Jinsong Chai, Sha Yang, Yingwei Li, Tatsuya Higaki, Site Li, and Rongchao Jin. Fusion growth patterns in atomically precise metal nanoclusters. *Nanoscale*, 11(41):19158–19165, 2019. doi: 10.1039/c9nr05789g.
- [16] Haru Hirai, Shun Ito, Shinjiro Takano, Kiichirou Koyasu, and Tatsuya Tsukuda. Ligand-protected gold/silver superatoms: current status and emerging trends. *Chemical Science*, 11(45):12233–12248, 2020. doi: 10.1039/d0sc04100a.
- [17] Zhentao Luo, Vairavan Nachammai, Bin Zhang, Ning Yan, David Tai Leong, De en Jiang, and Jianping Xie. Toward Understanding the Growth Mechanism: Tracing All Stable Intermediate Species from Reduction of Au(I)–Thiolate Complexes to Evolution of Au₂₅ Nanoclusters. *Journal of the American Chemical Society*, 136(30):10577–10580, jul 2014. doi: 10.1021/ja505429f.
- [18] Xi Kang and Manzhou Zhu. Transformation of Atomically Precise Nanoclusters by Ligand-Exchange. *Chemistry of Materials*, 31(24):9939–9969, nov 2019. doi: 10.1021/acs.chemmater.9b03674.
- [19] Chenjie Zeng, Yuxiang Chen, Anindita Das, and Rongchao Jin. Transformation Chemistry of Gold Nanoclusters: From One Stable Size to Another. *The Journal of Physical Chemistry Letters*, 6(15):2976–2986, jul 2015. doi: 10.1021/acs.jpcclett.5b01150.
- [20] Yoshiki Niihori, Sakiat Hossain, Sachil Sharma, Bharat Kumar, Wataru Kurashige, and Yuichi Negishi. Understanding and Practical Use of Ligand and Metal Exchange Reactions in Thiolate-Protected Metal Clusters to Synthesize Controlled Metal Clusters. *The Chemical Record*, 17(5):473–484, mar 2017. doi: 10.1002/tcr.201700002.
- [21] Yanan Wang and Thomas Bürgi. Ligand exchange reactions on thiolate-protected gold nanoclusters. *Nanoscale Advances*, 3(10):2710–2727, 2021. doi: 10.1039/d1na00178g.
- [22] Tokuhisa Kawawaki, Ayano Ebina, Yasunaga Hosokawa, Shuhei Ozaki, Daiki Suzuki, Sakiat Hossain, and Yuichi Negishi. Thiolate-Protected Metal Nanoclusters: Recent Development in Synthesis, Understanding of Reaction, and Application in Energy and Environmental Field. *Small*, 17(27):2005328, feb 2021. doi: 10.1002/sml.202005328.
- [23] Shuang Chen, Shuxin Wang, Juan Zhong, Yongbo Song, Jun Zhang, Hongting Sheng, Yong Pei, and Manzhou Zhu. The Structure and Optical Properties of the [Au₁₈(SR)₁₄] Nanocluster. *Angewandte Chemie International Edition*, 54(10):3145–3149, jan 2015. doi: 10.1002/anie.201410295.
- [24] Daniel M. Chevrier, Lluís Raich, Carme Rovira, Anindita Das, Zhentao Luo, Qiaofeng Yao, Amares Chatt, Jianping Xie, Rongchao Jin, Jaakko Akola, and Peng Zhang. Molecular-Scale Ligand Effects in Small Gold–Thiolate Nanoclusters. *Journal of the American Chemical Society*, 140(45):15430–15436, oct 2018. doi: 10.1021/jacs.8b09440.
- [25] Yanan Wang, Belén Nieto-Ortega, and Thomas Bürgi. Transformation from [Au₂₅(SCH₂CH₂CH₂CH₃)₁₈]⁰ to Au₂₈(SCH₂CH(CH₃)Ph)₂₁ gold nanoclusters: gentle conditions is enough. *Chemical Communications*, 55(99):14914–14917, 2019. doi: 10.1039/c9cc08872e.
- [26] Sha Yang, Shuang Chen, Lin Xiong, Chong Liu, Haizhu Yu, Shuxin Wang, Nathaniel L. Rosi, Yong Pei, and Manzhou Zhu. Total Structure Determination of Au₁₆(S–Adm)₁₂ and Cd₁Au₁₄(StBu)₁₂ and Implications for the Structure of Au₁₅(SR)₁₃. *Journal of the American Chemical Society*, 140(35):10988–10994, aug 2018. doi: 10.1021/jacs.8b04257.
- [27] Anu George, Anusree Sundar, Akhil S. Nair, Manju P. Maman, Biswarup Pathak, Nitya Ramanan, and Sukhendu Mandal. Identification of Intermediate Au₂₂(SR)₄(SR')₁₄ Cluster on Ligand-Induced Transformation of Au₂₅(SR)₁₈ Nanocluster. *The Journal of Physical Chemistry Letters*, 10(16):4571–4576, jul 2019. doi: 10.1021/acs.jpcclett.9b01856.

- [28] Chenjie Zeng, Chong Liu, Yuxiang Chen, Nathaniel L. Rosi, and Rongchao Jin. Gold–Thiolate Ring as a Protecting Motif in the $\text{Au}_{20}(\text{SR})_{16}$ Nanocluster and Implications. *Journal of the American Chemical Society*, 136(34):11922–11925, aug 2014. doi: 10.1021/ja506802n.
- [29] Manzhou Zhu, Huifeng Qian, and Rongchao Jin. Thiolate-Protected Au_{20} Clusters with a Large Energy Gap of 2.1 eV. *Journal of the American Chemical Society*, 131(21):7220–7221, may 2009. doi: 10.1021/ja902208h.
- [30] Wan Jiang, Yuyuan Bai, Qinzhen Li, Xiean Yao, Hui Zhang, Yongbo Song, Xiangming Meng, Haizhu Yu, and Manzhou Zhu. Steric and Electrostatic Control of the pH-Regulated Interconversion of $\text{Au}_{16}(\text{SR})_{12}$ and $\text{Au}_{18}(\text{SR})_{14}$ (SR: Deprotonated Captopril). *Inorganic Chemistry*, 59(8):5394–5404, feb 2020. doi: 10.1021/acs.inorgchem.9b03694.
- [31] Ramzi Hamouda, Franck Bertorelle, Driss Rayane, Rodolphe Antoine, Michel Broyer, and Philippe Dugourd. Glutathione capped gold $\text{Au}_N(\text{SG})_M$ clusters studied by isotope-resolved mass spectrometry. *International Journal of Mass Spectrometry*, 335:1–6, feb 2013. doi: 10.1016/j.ijms.2012.10.008.
- [32] Chenjie Zeng, Chunyan Liu, Yong Pei, and Rongchao Jin. Thiol Ligand-Induced Transformation of $\text{Au}_{38}(\text{SC}_2\text{H}_4\text{Ph})_{24}$ to $\text{Au}_{36}(\text{SPh}-t-\text{Bu})_{24}$. *ACS Nano*, 7(7):6138–6145, jun 2013. doi: 10.1021/nn401971g.
- [33] Eva Valušová, Mária Kaňuchová, Tomáš Baše, Viktor Víglaský, and Marián Antalík. The $\text{Au}_{25}(\text{SR})_{18}$ cluster carrying icosahedral dodecaborate and glutathione ligands: A spectroscopic view. *Journal of Physics and Chemistry of Solids*, 150:109838, mar 2021. doi: 10.1016/j.jpcc.2020.109838.
- [34] Michel Picquart, Lydie Grajcar, Marie Helene Baron, and Zohreh Abedinzadeh. Vibrational spectroscopic study of glutathione complexation in aqueous solutions. *Biospectroscopy*, 5(6): 328–337, 1999. doi: [https://doi.org/10.1002/\(SICI\)1520-6343\(1999\)5:6<328::AID-BSPY2>3.0.CO;2-J](https://doi.org/10.1002/(SICI)1520-6343(1999)5:6<328::AID-BSPY2>3.0.CO;2-J). URL <https://onlinelibrary.wiley.com/doi/abs/10.1002/%28SICI%291520-6343%281999%295%3A6%3C328%3A%3AAID-BSPY2%3E3.0.CO%3B2-J>.
- [35] Mostafa Farrag, Martin Tschurl, Amala Dass, and Ulrich Heiz. Infra-red spectroscopy of size selected Au_{25} , Au_{38} and Au_{144} ligand protected gold clusters. *Physical Chemistry Chemical Physics*, 15(30):12539, 2013. doi: 10.1039/c3cp51406d.
- [36] Alfredo Tlahuice-Flores, Robert L. Whetten, and Miguel Jose-Yacaman. Vibrational Normal Modes of Small Thiolate-Protected Gold Clusters. *The Journal of Physical Chemistry C*, 117(23):12191–12198, may 2013. doi: 10.1021/jp4033063.
- [37] Igor Dolamic, Birte Varnholt, and Thomas Bürgi. Far-infrared spectra of well-defined thiolate-protected gold clusters. *Physical Chemistry Chemical Physics*, 15(45):19561, 2013. doi: 10.1039/c3cp53845a.
- [38] Belén Nieto-Ortega and Thomas Bürgi. Vibrational Properties of Thiolate-Protected Gold Nanoclusters. *Accounts of Chemical Research*, 51(11):2811–2819, nov 2018. doi: 10.1021/acs.accounts.8b00376.
- [39] Birte Varnholt, Patric Oulevey, Sandra Luber, Chanaka Kumara, Amala Dass, and Thomas Bürgi. Structural Information on the Au–S Interface of Thiolate-Protected Gold Clusters: A Raman Spectroscopy Study. *The Journal of Physical Chemistry C*, 118(18):9604–9611, apr 2014. doi: 10.1021/jp502453q.
- [40] Tomoki Matsuyama, Jun Hirayama, Yu Fujiki, Soichi Kikkawa, Wataru Kurashige, Hiroyuki Asakura, Naomi Kawamura, Yuichi Negishi, Naoki Nakatani, Keisuke Hatada, Fukiko Ota, and Seiji Yamazoe. Effect of Ligand on the Electronic State of Gold in Ligand-Protected Gold Clusters Elucidated by X-ray Absorption Spectroscopy. *The Journal of Physical Chemistry C*, 125(5):3143–3149, jan 2021. doi: 10.1021/acs.jpcc.0c09369.

- [41] Rui Yang, Daniel M. Chevrier, and Peng Zhang. Structure and Bonding Properties of a 20-Gold-Atom Nanocluster Studied by Theoretical X-ray Absorption Spectroscopy. *MRS Proceedings*, 1802:33–39, 2015. doi: 10.1557/opl.2015.516.
- [42] Alfredo Tlahuice-Flores, Miguel Jose-Yacamán, and Robert L. Whetten. On the structure of the thiolated Au₁₅ cluster. *Physical Chemistry Chemical Physics*, 15(45):19557, 2013. doi: 10.1039/c3cp53837k.
- [43] De en Jiang, Steven H. Overbury, and Sheng Dai. Structure of Au₁₅(SR)₁₃ and Its Implication for the Origin of the Nucleus in Thiolated Gold Nanoclusters. *Journal of the American Chemical Society*, 135(24):8786–8789, jun 2013. doi: 10.1021/ja402680c.
- [44] Xi Kang and Manzhou Zhu. Tailoring the photoluminescence of atomically precise nanoclusters. *Chemical Society Reviews*, 48(8):2422–2457, 2019. doi: 10.1039/c8cs00800k.
- [45] Guillaume F. Combes, Hussein Fakhouri, Christophe Moulin, Marion Girod, Franck Bertorelle, Srestha Basu, Romain Ladouce, Martina Perić Bakulić, Željka Sanader Maršić, Isabelle Russier-Antoine, Pierre-François Brevet, Philippe Dugourd, Anita Krisko, Katarina Trajković, Miroslav Radman, Vlasta Bonačić-Koutecký, and Rodolphe Antoine. Functionalized Au₁₅ nanoclusters as luminescent probes for protein carbonylation detection. *Communications Chemistry*, 4(1), may 2021. doi: 10.1038/s42004-021-00497-z.
- [46] Zhikun Wu and Rongchao Jin. On the Ligand’s Role in the Fluorescence of Gold Nanoclusters. *Nano Letters*, 10(7):2568–2573, jun 2010. doi: 10.1021/nl101225f.
- [47] Martin Loos, Christian Gerber, Francesco Corona, Juliane Hollender, and Heinz Singer. Accelerated Isotope Fine Structure Calculation Using Pruned Transition Trees. *Analytical Chemistry*, 87(11):5738–5744, may 2015. doi: 10.1021/acs.analchem.5b00941.
- [48] B. Ravel and M. Newville. ATHENA, ARTEMIS, HEPHAESTUS: data analysis for x-ray absorption spectroscopy using IFEFFIT. *Journal of Synchrotron Radiation*, 12(4):537–541, jun 2005. doi: 10.1107/s0909049505012719.

5. Ligand Effect on the CO Oxidation Activity of CeO₂ Supported Gold Nanocluster Catalysts

Vera Truttmann, Daiki Suzuki, Michael Stöger-Pollach, Hedda Drexler, Yuichi Negishi, Noelia Barrabés, and Günther Rupprechter

The content of this chapter is to be submitted for publication in the current form.

5.1. Abstract

Monolayer protected Au nanocluster catalysts are known to undergo structural changes during catalytic reactions, including dissociation and migration of ligands onto the support, which strongly affects their activity and stability. To better understand how the nature of ligands influences the catalytic activity of such catalysts, three types of ceria supported Au nanoclusters with different kinds of ligands (thiolates, phosphines and a mixture thereof) have been studied, employing CO oxidation as model reaction. The thiolate-protected Au₂₅/CeO₂ showed significantly higher CO conversion after activation at 250 °C than the cluster catalysts possessing phosphine ligands. TPO and *in situ* infrared spectroscopy revealed that while the phosphine ligands seemed to decompose and free Au surface was exposed, temperatures higher than 250 °C are required to efficiently remove them from the whole catalyst system. Moreover, the presence of residues on the support seemed to have much greater influence on the reactivity than the gold particle size.

5.2. Introduction

Heterogeneous catalysis employing nanomaterials is a well-established field, often featuring metal nanoparticles supported on oxides.^[1] Among them, Au nanoparticles have been frequently used,^[1–3] especially since Haruta and coworkers reported their high activity in low-temperature CO oxidation.^[4] As bulk gold is unreactive, the difference in activity was attributed to the small size and electronic structure of these nanoparticles.^[2,5–7]

More recently, ligand protected Au nanoclusters immobilized on various supports have also been applied in heterogeneous catalysis.^[8–13] Unlike their nanoparticle counterparts, Au nanoclusters can be readily prepared monodisperse, i.e. possessing a uniform size and structure.^[9,11–15] Their molecule-like properties are influenced by a variety of factors, for example the number of metal atoms and their arrangement,^[14,15] the presence of dopant atoms^[14,16] or their protecting ligands.^[17,18] For the latter, different classes can be employed,^[8,15] including for example thiolates^[8,15,17] or phosphines.^[8,19] The ligands directly influence parameters such as cluster stability or polarity^[8,15,17,20] and have therefore profound effect on the overall structural properties or catalytic activity.^[8,10,11,17,20–24] Modifying or replacing them by ligand exchange has become a useful tool for optimizing cluster properties.^[14,25]

Combining versatility and high activity, Au nanoclusters can be used to catalyze different kinds of heterogeneous reactions,^[8,9,11,13] among which oxidations are the most studied.^[26] Due to their monodisperse nature and defined structure, they can be used as model systems, obtaining molecular level insight in the catalytic reaction.^[8,9,11–13,26]

A variety of factors influence the performance of Au nanocluster catalysts in heterogeneous reactions: Probably the most evident is the number of metal atoms in the cluster, determining the structure. A size dependence of the catalytic activity – sometimes even of only a few atoms – has been reported for different types of reactions, for example, for CO,^[21,27] cyclohexane^[28,29] or styrene oxidation.^[30] Furthermore, the catalytic behavior is influenced

by the geometry^[10,21,31,32] and heteroatom doping creating bimetallic nanoclusters.^[13,33–37]

Previous work showed a strong effect of the support on the reactivity and stability of the cluster catalysts for various pretreatment conditions. For example, SiO₂ supported Au nanoclusters showed higher activity in cyclohexane oxidation, whereas better selectivity was obtained using TiO₂ as support material.^[28] For CO oxidation, CeO₂ supported Au nanoclusters were found to be significantly more active than those supported on Fe₂O₃,^[38] TiO₂^[34,38,39] or Al₂O₃,^[39] related to ceria aiding the transfer of oxygen to CO adsorbed on Au sites.^[40] The support material is also known influence the stability of nanocluster catalysts.^[27,28,41–43]

To obtain optimal catalytic activity with cluster catalysts, the removal of ligands is essential to create accessible Au sites on the cluster surface.^[44,45] Oxidative pretreatment was found to significantly enhance the activity of a Au₂₅/CeO₂ in CO oxidation by Jin and coworkers.^[38,44] Thereby, highest conversion was found for the sample pretreated at 250 °C for 1 h.^[44] Similarly, Au₃₈/CeO₂ could be activated by oxidative thermal treatment at 175 °C for 2 h, while further increase of the pretreatment temperature resulted in reduced CO oxidation activity.^[46] However, combined oxidative and reductive treatment of Au₁₄₄/CeO₂ enhanced the catalytic performance, ascribed to the production of active oxygen species on the ceria support.^[47] Theoretical investigations of a Au₂₀(SCH₃)₁₆ cluster on CeO₂ showed that optimal cluster-support interaction and O₂ adsorption are achieved by partial ligand removal.^[48] All this clearly indicates the importance of catalyst activation by ligand removal from Au nanocluster catalysts.

Our recent studies of Au₃₈/CeO₂ catalysts by X-ray absorption spectroscopy (XAS) revealed that the temperature induced rearrangements of the cluster structure during activation cannot be solely explained by detachment of thiolate ligands.^[49,50] While the ligands start to disintegrate already at 150 °C, the cluster surface is still covered by Au⁺-S units which can only be removed at higher temperature.^[49] However, sulfur moieties remain in the system even after oxidative treatment at 250 °C.^[49–51]

Comparing the influence of different thiolate ligands on the CO oxidation activity of Au_x/CeO₂ catalysts (x = 25, 36, 38), it was found that they determine the steric hindrance on the perimeter sites crucial for CO adsorption.^[21] A distinct influence of the type of protecting thiolate ligand on the reactivity was also found for Au₂₈(SR)₂₀/CeO₂ catalysts (R = cyclohexyl and 4-tert-butylphenyl).^[23] The CO oxidation activity is therefore apparently influenced by the nature of the protecting ligands of a cluster catalyst as well.^[21,49,50]

Nevertheless, the investigation of the ‘ligand effect’ in Au nanocluster CO oxidation catalysis has so far mainly been focused on thiolates as protecting ligands. Phosphine-protected Au nanoclusters have only rarely been employed as catalysts for this reaction. Wu *et al.* reported a highly active Au₂₂(1,8-bis(diphenylphosphino)octane)₆ catalyst, where uncoordinated gold atoms were identified as the active sites.^[39] For a series of PPh₃-protected Au_n species (n = 1, 8, 9, 101), mild thermal treatment (up to 120 °C) was found to alter the structure depending on the nature of the support material: Whereas fragmentation into small (Au–PPh₃)⁺ units was observed on supports with mainly Brønsted acid sites such as SiO₂, immobilizing Au clusters on Lewis acidic supports such as CeO₂ resulted in exposure of the bare Au_n cores

due to migration of the phosphine ligands. When testing the pretreated CeO_2 supported Au_n catalysts in CO oxidation, activity was found to be strongly size-dependent, with the larger clusters being more active.^[27] All these studies support the hypothesis that the ligands of the Au nanoclusters play a significant role for catalysis.

Thus, herein the influence of the clusters' initial ligand shell on the performance of Au nanoclusters in CO oxidation was studied. Three differently sized gold nanoclusters protected by different kinds of ligands were chosen as heterogeneous catalysts: phosphine-protected Au_{11} , thiolate-protected Au_{25} , and biicosahedral Au_{25} with a mixed phosphine/thiolate ligand shell. The cluster structures are illustrated in Figure 5.1. All three clusters, $\text{Au}_{11}(\text{PPh}_3)_7\text{Cl}_3$, $[\text{Au}_{25}(\text{SC}_2\text{H}_4\text{Ph})_5(\text{PPh}_3)_{10}\text{Cl}_2]^{2+}$ and the anionic $[\text{Au}_{25}(\text{SC}_2\text{H}_4\text{Ph})_{18}]^-$, belong to the so-called 'magic number series', indicating that they are very stable because of having closed electron shells.^[52,53] Furthermore, they can be considered 'standard clusters' in their respective class.^[19,53,54] The biicosahedral cluster $[\text{Au}_{25}(\text{SC}_2\text{H}_4\text{Ph})_5(\text{PPh}_3)_{10}\text{Cl}_2]^{2+}$ is straightforwardly prepared by treating $\text{Au}_{11}(\text{PPh}_3)_7\text{Cl}_3$ with an excess of 2-phenylethanthiol in solution and represents an intermediate between fully phosphine or thiolate protected clusters.^[55,56] Motivated by previous studies, CeO_2 was used as support material since it leads to high CO oxidation activity while stabilizing the cluster structure at elevated temperatures.^[27,38]

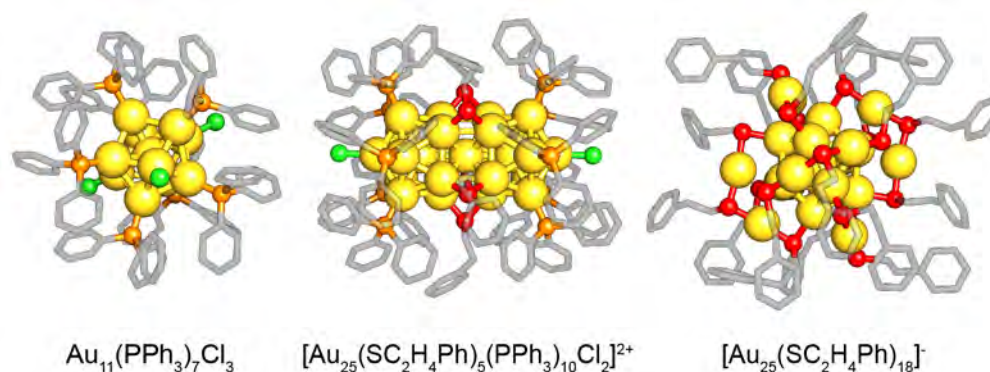


Figure 5.1.: Structures of the three Au nanoclusters employed in this study: (a) $\text{Au}_{11}(\text{PPh}_3)_7\text{Cl}_3$, (b) $[\text{Au}_{25}(\text{SR})_5(\text{PPh}_3)_{10}\text{Cl}_2]^{2+}$ and (c) $[\text{Au}_{25}(\text{SC}_2\text{H}_4\text{Ph})_{18}]^-$. Color code: Au = yellow, P = orange, Cl = green, S = red, C = grey. The images are based on structures determined by X-ray crystallography.^[54,56,57]

Pretreatment studies showed that heating to 250 °C under oxidative atmosphere is sufficient for activation of $\text{Au}_{25}/\text{CeO}_2$, while 300 °C are required for $\text{Au}_{11}/\text{CeO}_2$ and Biico Au_{25} . This appears to be related to the process of ligand removal, necessary to produce accessible Au surface for heterogeneous catalysis. Furthermore, *in situ* infrared measurements of the Au_x/CeO_2 catalysts were performed, allowing to obtain an understanding of ligand behavior upon pretreatment and reaction. IR bands of the thiolate and/or phosphine ligands clearly decreased during oxidative pretreatment, whereas several bands related to adsorbed species were formed. CO adsorption experiments after pretreatment showed that the activation pro-

cess yielded exposed Au surfaces for all three cluster catalysts. Reduction of Au⁺ species was observed during reaction, which was more efficient for Au₂₅/CeO₂ compared to the other catalysts. Thus, the significant differences in catalytic activity might be related to ligand residues located on the support rather than on the Au particles, potentially blocking crucial interfacial sites.

5.3. Results and Discussion

The three types of gold nanoclusters were prepared and purified as described in Section 5.8. Characterization of the unsupported clusters was performed by Ultraviolet-visible spectroscopy (UV-Vis), attenuated total reflection infrared spectroscopy (ATR-IR), and matrix-assisted laser desorption/ionization (MALDI) or electrospray ionization mass spectrometry (ESI-MS), confirming the purity of the samples. The supported catalysts were prepared by wet impregnation of ceria, yielding a Au loading of 1.2 wt%. Refer to the Supplementary Material in Section 5.8 for further details.

5.3.1. Effect of the Pretreatment Temperature

Catalyst activation, prior to CO oxidation, is closely linked to (partial) removal of the respective ligand monolayer from the nanoclusters.^[8,44,45,49] The optimal conditions were thus determined for each cluster-ligand configuration. Based on previous work,^[28,49] thermal oxidative pretreatment (5 % O₂ in Ar) was chosen for this step, with the maximum temperature varied from 150 °C to 300 °C and held for 30 minutes.

As seen in Figure 5.2a-c, none of the samples showed significant activity after pretreatment at 150 °C. Similarly, only minor CO conversion above 150 °C was achieved with a 200 °C pretreatment. After pretreatment at 250 °C, Au₂₅/CeO₂ showed a sudden onset in activity, forming CO₂ already at room temperature and reaching 100 % conversion above 200 °C (Figure 5.2c). Because Au₂₅/CeO₂ showed such a high activity, the Au loading was reduced to 0.3 wt% for all catalysts by further dilution with ceria. This enabled more meaningful measurements of the temperature-dependent activity.

A similar pretreatment effect was observed for Au₃₈/CeO₂ previously, which showed significantly higher activity when activated at 250 °C than at 150 °C.^[49] In contrast, Nie *et al.*^[38] observed that oxidative pretreatment at 150 °C for 1.5 h seemed to be optimal, considering that no further increase in CO conversion could be achieved at a pretreatment temperature to 250 °C. The same study reported that the duration of the pretreatment plays a significant role: 30 minutes pretreatment at 150 °C was considerably less effective for catalyst activation than 1.5 h. This might explain this difference.

An increase in activity after 250 °C pretreatment was also noted for Au₁₁/CeO₂ (Figure 5.2a) and Biico Au₂₅/CeO₂ (Figure 5.2b). However, as Figure 5.2d shows, these two cluster catalysts showed significantly lower CO conversion than the Au₂₅/CeO₂ sample pretreated at the same temperature. When the maximum temperature of the oxidative pretreatment was

raised to 300 °C, all three catalysts had high activity in CO oxidation. Moreover, even though there were differences in conversion levels of the three catalysts, these were less pronounced as after pretreatment at 250 °C (see Figure 5.17c), indicating that the activation of the Au nanoclusters strongly depends on their specific ligand. It seems that phosphine ligands hinder catalyst activation at and below 250 °C. Since the greatest difference in catalytic activity of the cluster catalysts was observed at 250 °C, it was chosen as pretreatment and reaction temperature for all further studies.

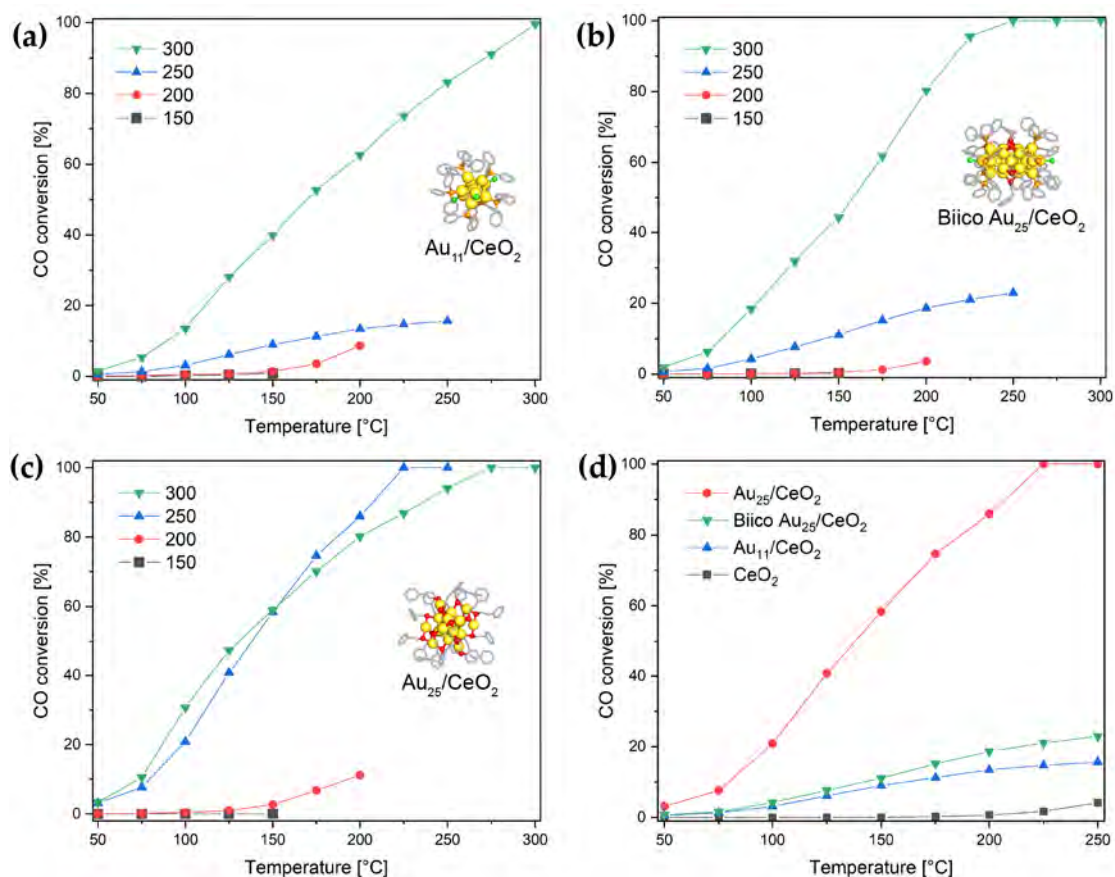


Figure 5.2.: Catalytic activity of Au nanoclusters on CeO₂ (0.3 wt% Au loading, 15 mg catalyst) in CO oxidation depending on the temperature of oxidative pretreatment: (a) Au₁₁/CeO₂; (b) Biico Au₂₅/CeO₂; (c) Au₂₅/CeO₂. Comparison of the catalytic activity of the different nanocluster catalysts pretreated at 250 °C (d).

Potential catalyst deactivation after pretreatment at 250 °C was studied by performing three consecutive runs with each sample. A sample was cooled to room temperature in inert gas atmosphere after reaching 250 °C reaction temperature and then the reaction was carried out two more times (without further pretreatment). As Figure 5.3 shows, each catalyst only showed minor signs of deactivation or activation

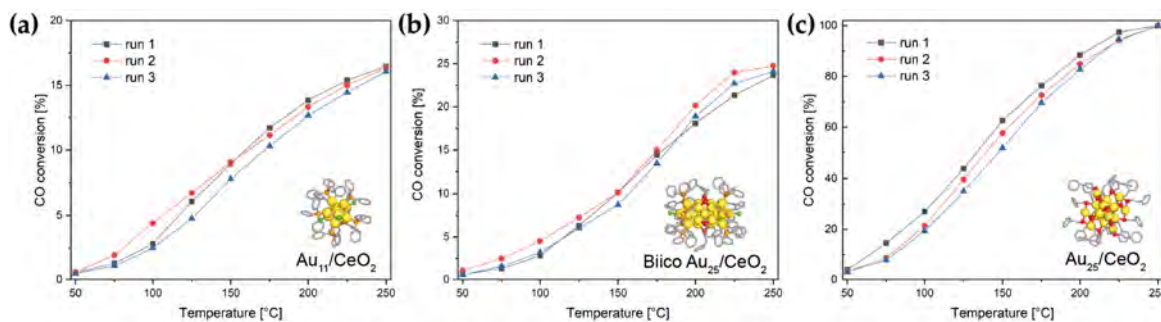


Figure 5.3.: CO conversion of the same catalyst sample (0.3 wt% Au loading, 15 mg catalyst) in 3 consecutive CO oxidation runs after pretreatment at 250 °C: (a) Au₁₁/CeO₂, (b) Biico Au₂₅/CeO₂ and (c) Au₂₅/CeO₂.

5.3.2. Modifications by Oxidative Pretreatment

Changes of the cluster catalysts imposed by oxidative pretreatment were further studied by temperature programmed oxidation (TPO), thermogravimetric analysis (TGA)/differential scanning calorimetry (DSC) and *in situ* transmission infrared measurements. Based on their similar conversion levels after pretreatment at 250 °C, 1.2 wt% Au₁₁/CeO₂ and 1.2 wt%, BiicoAu₂₅/CeO₂ were compared to 0.3 wt% Au₂₅/CeO₂.

In a first step, the approximate ligand decomposition/desorption temperature was estimated by studying the CO₂ generation and O₂ consumption mass spectra (Figure 5.4) during pretreatment (performed in the *in situ* infrared cell). The relatively low intensity of the Au₂₅/CeO₂ signals in Figure 5.4 is due to the lower Au content. This was done to ensure that the activity of all three cluster catalysts was in a similar range for the *operando* infrared experiments (Section 5.3.3).

As shown in Figure 5.4a, low-temperature generation of CO₂ was observed from ≈60 °C onwards for all catalysts including pure CeO₂, which is due to desorption of CO₂ adsorbed on ceria at room temperature.^[38] Interestingly, the on-set of ligand decomposition/desorption from the catalyst (marked by O₂ consumption and CO₂ evolution) varies significantly for the three clusters: For Au₂₅/CeO₂, CO₂ generation and O₂ consumption started at 150-155 °C, with a maximum at approximately 235 °C, which is in good agreement with Nie *et al.*^[38] Biico Au₂₅/CeO₂ and Au₁₁/CeO₂ showed evolution of CO₂ only above 185 °C. For the latter two, the maximum CO₂ formation was observed during the holding period at 250 °C. The pure ceria support showed a minor CO₂ signal above ≈200 °C. For all three cluster catalysts, CO₂ generation and O₂ consumption were observed in the same temperature range, clearly indicating oxidative removal of the organic protecting ligands.

To investigate whether the ligand removal was complete at 250 °C, a second temperature programmed oxidation experiment was performed until 300 °C (see Figure 5.19). Thereby, continued ligand removal was observed for all three cluster species. Moreover, the maximum CO₂ formation for Au₁₁/CeO₂ and Biico Au₂₅/CeO₂ was found to be between 250 °C and

300 °C, whereas Au₂₅/CeO₂ still featured a maximum just below 250 °C. TGA and DSC of the unsupported nanocluster samples (Figures 5.15-5.15) further showed that while all three clusters exhibited mass loss up to at least 300 °C, Au₂₅ was the only cluster with DSC features just below 250 °C, likely indicating that potential structural changes are already completed at 250 °C. However, it is unclear if the same changes also happen for supported clusters or if they would adapt different geometries upon supporting.

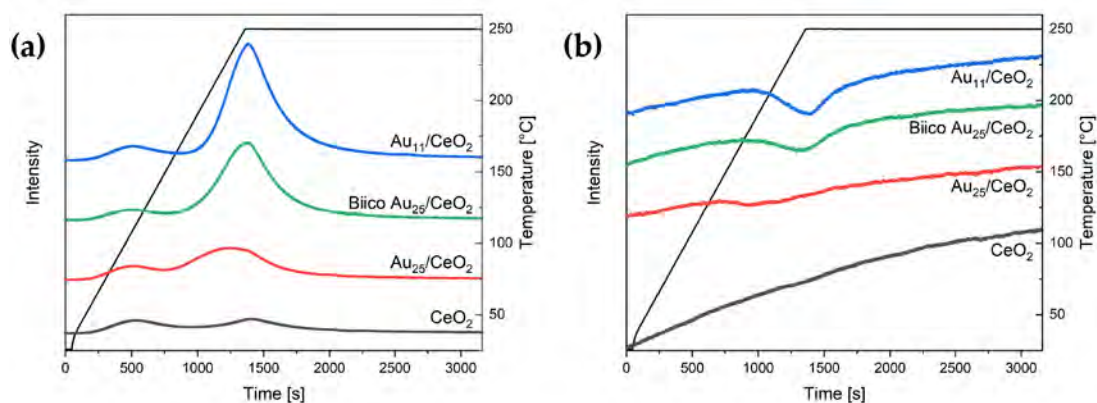


Figure 5.4.: CO₂ generation (a) and O₂ consumption spectra (b) of the different catalysts during oxidative pretreatment until 250 °C. Au content in catalyst: Au₁₁ and BiicoAu₂₅/CeO₂: 1.2 wt%, Au₂₅/CeO₂: 0.3 wt%. Spectra were normalized by the carrier gas signal to compensate for changes in pressure. Spectra are offset for better visibility.

This may also explain the different activity of the nanocluster catalysts at 250 °C: In case of Au₂₅/CeO₂, due to an earlier on-set of the ligand removal, the Au/oxide interfacial sites are better accessible, leading to significantly higher activity than that of the phosphine-protected cluster catalysts. Raising the pretreatment temperature to 300 °C is sufficient to remove also (most of) the ligands of the latter, diminishing the differences in activity (see Figure 5.17c).

The 250 °C oxidative pretreatment of all catalysts was also followed by *in situ* transmission infrared spectroscopy. Figure 5.5 shows a comparison of the room temperature spectra after pretreatment and Figure 5.6 the difference spectra from 1800-900 cm⁻¹ acquired during pretreatment.

To get insights into the ligand-support interaction and its evolution during pretreatment, one should focus on bands related to hydroxyl, formate and (hydrogen) carbonate species on CeO₂ (e.g.^[58,59]). However, typically several of these species coexist on the support and overlapping features make an accurate assignment difficult. Therefore, a thorough analysis of the pure supports is required for reference.

Pretreated catalysts (Figure 5.5) displayed formate related bands at 2936, 2847, 2725, 1565 (low intensity; only visible in the spectrum of pure CeO₂), 1545, 1372 and 1359 cm⁻¹.^[58,59] Hydrogen carbonate species were observed at 1398, 1225 and 1037 cm⁻¹.^[58,60]

For all samples including the plain support without clusters, intense negative bands were

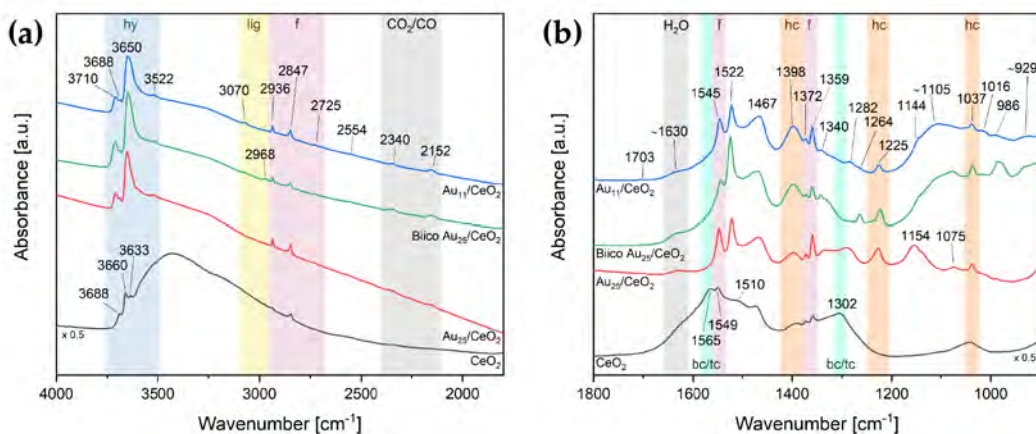


Figure 5.5.: Infrared spectra of the catalysts after oxidative pretreatment at 250 °C: 4000-1800 cm⁻¹ (a) and 1800-900 cm⁻¹ (b). Bands associated with certain species are highlighted: hy = hydroxy species (blue), lig = ligand/other organic residues (yellow), f = formates (violet), CO₂/CO/H₂O (grey), bc/tc = bidentate/tridentate carbonates (turquoise), hc = hydrogen carbonates (orange). Spectra are offset for better visibility and the spectrum of CeO₂ was multiplied with 0.5 to allow for comparison with the cluster catalysts. Au content in catalyst: Au₁₁/CeO₂ and Biico Au₂₅/CeO₂: 1.2 wt%, Au₂₅/CeO₂: 0.3 wt%.

observed in the pretreatment difference spectra (Figure 5.6a-c and Figure 5.24c; as-prepared catalysts in He at RT used as background) at 1565-1560 and 1306-1303 cm⁻¹. These are related to the dissociation of either bidentate^[59-62] or tridentate^[58,61,62] carbonate species upon temperature increase. The negative shoulder at ≈1630 cm⁻¹ corresponds to the H₂O bending vibration.^[59] Simultaneously, bands were starting to appear 1459-1456 and 1404-1400 cm⁻¹, followed by the formate bands (1546-1545, 1372-1371 and 1359 cm⁻¹) and a sharp feature at 1523-1520 cm⁻¹ (Figure 5.6a-c and Figure 5.24c). These bands at 1459-1456 and 1404-1400 cm⁻¹ may indicate formation of polydentate carbonates.^[58,59,62] A third weak feature related to it should be located at around 1065 cm⁻¹,^[58,59] which could not be identified as an increasing band within the presented difference spectra, presumably due to interferences with vibrations of other (carbonate) species. Moreover, it should be noted that the band around 1400 cm⁻¹ might also be associated with the formation of hydrogen carbonates.^[58,60]

There were also changes in the higher wavenumber region (Figures 5.21a-5.23a): Removal of H₂O is evidenced by the reduction of the broad band associated with O-H stretching vibrations (approximately 3300 cm⁻¹).^[63] However, as Figure 5.5a shows, bands at 3710, 3688, 3650 and 3522 cm⁻¹ associated with hydroxylated species^[58,59] were still present in the catalyst samples after pretreatment. Besides the aforementioned bands associated with formate species (2936, 2847, 2725 cm⁻¹), the Au₁₁/CeO₂ and the Biico Au₂₅/CeO₂ samples also showed further absorption features in the C-H stretching region (at 3070 and 2968 cm⁻¹; blue and green curve in Figure 5.5a), which indicates that not all hydrocarbon species (adsorbates/ligand residues) were removed by the pretreatment.

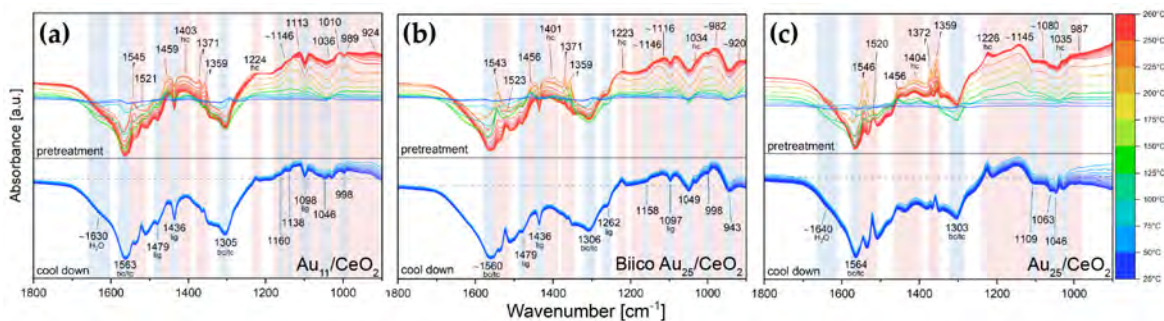


Figure 5.6.: Difference spectra of the cluster catalysts during oxidative pretreatment: (a) $\text{Au}_{11}/\text{CeO}_2$, (b) Biico $\text{Au}_{25}/\text{CeO}_2$ and (c) $\text{Au}_{25}/\text{CeO}_2$. Bands decreasing during the pretreatment are indicated by a light blue background color and marked at the bottom, increasing ones by a light red one and marked on top. Assigned species are indicated by abbreviations: f = formates, hc = hydrogen carbonates, bc/tc = bidentate/tridentate carbonates, lig = ligands. For all samples, the spectra of the as-prepared catalysts in He at RT were used as background. Au content in catalyst: $\text{Au}_{11}/\text{CeO}_2$ and Biico $\text{Au}_{25}/\text{CeO}_2$: 1.2 wt%, $\text{Au}_{25}/\text{CeO}_2$: 0.3 wt%. Difference spectra featuring the frequency region from 3800-2500 cm^{-1} and from 2500-2000 cm^{-1} can be found in Section 5.8 (Figures 5.21-5.23).

Differences among the samples were especially pronounced in the region below 1300 cm^{-1} . The purely thiolate ligand protected cluster $\text{Au}_{25}/\text{CeO}_2$ showed formation of bands in the difference spectrum (Figure 5.6c) at 1226, ≈ 1145 , ≈ 1080 , 1035 and 987 cm^{-1} , as well as negative bands at 1109, 1063 and 1046 cm^{-1} . Several of those were also identified in the difference spectra of CeO_2 without clusters (1223, 1109, 1085, 1063, 1046, 1037 and 984 cm^{-1} , see Figure 5.24c), indicating that these might be related to adsorbed (hydrogen) carbonate species on the support. The broad band formed at around 1145 cm^{-1} , which is not present in the support spectra, could be related to the formation of sulfate species due to the oxidative decomposition of the thiolate protecting ligands.^[64] Previous studies have already shown that residues of thiolate ligands can still be present on the CeO_2 support even after pretreatment at 250 °C, forming sulfate species.^[49,50] However, it cannot be excluded that carbonate species are responsible for the IR bands in this area.^[58]

The removal of the hydrocarbon framework of the ligands of $\text{Au}_{25}/\text{CeO}_2$ can be confirmed by IR spectroscopy: The difference spectrum in Figure 5.23a shows a negative band at 2926 cm^{-1} , which can be attributed to the most intense C-H stretching vibration of the 2-PET ligands (see Figure 5.13c for reference). Moreover, while the absorption spectrum of the as-prepared catalyst still shows weak bands at 3060, 3027 and 2925 cm^{-1} related to the ligands, these are not present anymore for the pretreated catalyst (Figure 5.31a).

The difference spectra acquired during pretreatment of the phosphine-protected clusters, $\text{Au}_{11}/\text{CeO}_2$ and Biico $\text{Au}_{25}/\text{CeO}_2$, depicted in Figure 5.6a-b, clearly show the removal of the ligands (negative bands at 3055, 1479, 1436 and 1098 cm^{-1} for $\text{Au}_{11}/\text{CeO}_2$ and 3060, 2926, 1479, 1436, 1262 and at 1097 cm^{-1} for Biico $\text{Au}_{25}/\text{CeO}_2$). For both of them, the range from

1300-900 cm^{-1} is very complex due to appearing broad absorption features. Dai *et al.*^[65] showed that PO_x on CeO_2 gives rise to IR bands at approximately 1158, 1000 and 950 cm^{-1} . However, the bands appeared very broad and undefined, especially for lower PO_x contents. Thus, formation of phosphate species on the CeO_2 support could be a potential explanation of this considerable increase in absorbance in this region, especially considering that this was only observed for the P-containing cluster catalysts. Once again, however, it should be noted that also IR bands of carbonate species can be found in this wavenumber range,^[58] and might also cause the bands observed for these samples, pointing to a combination of both phosphates and carbonates. Nevertheless, compared to $\text{Au}_{25}/\text{CeO}_2$ and CeO_2 , these two catalysts show a significant increase in IR absorbance below 1200 cm^{-1} . Independent of its exact origin, this strongly indicates the presence of adsorbed species, which may influence the catalyst activity.

The *in situ* IR measurements also showed the removal of the hydrocarbon framework of the ligands for all three cluster catalysts, evidenced by significant formation of gas phase CO_2 during pretreatment (see difference spectra of the catalysts in Figures 5.21b-5.23b). In addition, a band related to adsorbed CO was formed at $\approx 2150 \text{ cm}^{-1}$, for all three. To probe the CO adsorption capability of the pretreated catalysts, 1 % CO in He was flown through the cell at room temperature until no further change was observed in the spectra. Afterwards, 100 % He was used to remove the CO atmosphere. As shown in Figure 5.7a-c, all three catalysts displayed a band of CO adsorbed on $\text{Au}^{\delta+}$ at roughly 2130 cm^{-1} , which agrees with previous studies of Au nanoclusters.^[34,43,44,49] Slight differences in energy were noticed for the three catalysts: Whereas a maximum of 2126 cm^{-1} was detected for $\text{Au}_{25}/\text{CeO}_2$, the band appeared slightly blueshifted for Biico $\text{Au}_{25}/\text{CeO}_2$ (2132 cm^{-1}) and $\text{Au}_{11}/\text{CeO}_2$ (2131 cm^{-1}). For all three, flowing enough He through the cell after CO exposure results in a fully vanishing band.

Furthermore, an additional band evolved with a maximum around 2164 cm^{-1} , which remained after removal of the CO atmosphere. This band was attributed to CO on oxidized Au sites^[43,44,66] and may be explained by some of the Au atoms in ligand-protected nanoclusters bearing a positive charge.^[52,67,68] Moreover, density functional theory (DFT) calculations on gas phase Au nanoclusters suggested a charge transfer from Ce to Au, leading to partially oxidized Au species.^[69] It is possible that a similar phenomenon occurs during ligand detachment increasing interaction between the Au core and the ceria support.

Consequently, it seems that oxidative pretreatment at 250 °C is effective for the removal of the protecting ligands from the Au core of CeO_2 supported gold nanocluster catalysts, thereby providing free Au sites for CO adsorption/reaction. Even though small differences in the frequency and relative intensity of CO adsorbed on the different Au cluster catalysts were noted, the main difference seems to be the presence of further adsorbed species. This is presumably related to the incomplete removal of the ligand sphere, especially concerning the (partially) phosphine-protected clusters. Both $\text{Au}_{11}/\text{CeO}_2$ and Biico $\text{Au}_{25}/\text{CeO}_2$ showed residual weak bands located in the wavenumber region typical of C-H stretching vibrations and development of broad bands below 1200 cm^{-1} .

These findings are in line with a previous study by Longo *et al.*,^[27] who found that the

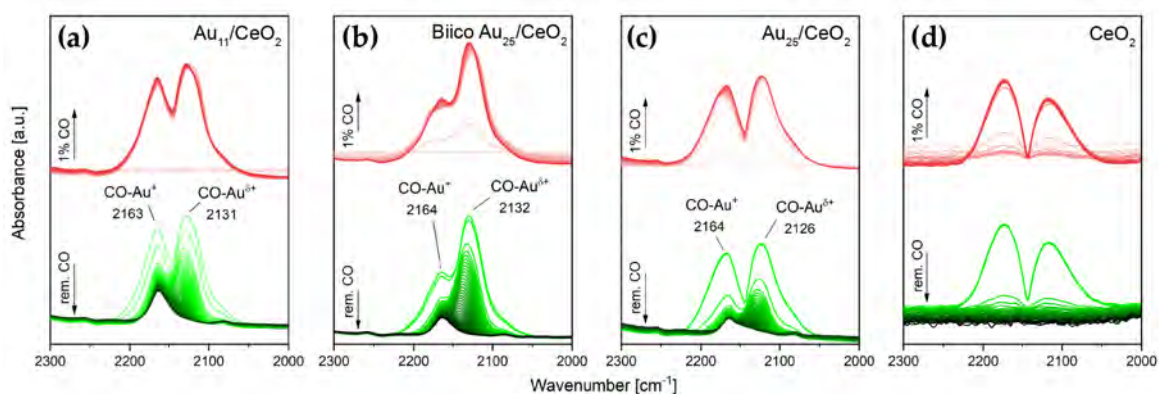


Figure 5.7.: Transmission infrared spectra of room temperature CO adsorption on catalysts after oxidative pretreatment at 250 °C: (a) Au₁₁/CeO₂ (b) Biico Au₂₅/CeO₂, (c) Au₂₅/CeO₂ and (d) CeO₂. The red spectra were obtained during exposure of the sample to an atmosphere of 1 % CO in He (50 ml/min total gas flow), the green spectra upon removal of gas phase CO by flowing 50 ml/min He. Au content in catalyst: Au₁₁/CeO₂ and Biico Au₂₅/CeO₂: 1.2 wt%, Au₂₅/CeO₂: 0.3 wt%.

phosphine ligands of Au_n nanoclusters (n = 1, 8, 9, 101) supported on CeO₂ seemed to migrate to the support at 120 °C. This was explained by the favorable interactions between the phosphine ligands and the Lewis acidic centers of the CeO₂ support. Migration to and oxidation of phosphine ligands on the support has also been described for Au_n (n = 8, 9, 11, 101) nanoclusters on TiO₂ subjected to different activation treatments (e.g. calcination in vacuum or O₂ atmosphere).^[70,71] Thus, phosphine ligands detached from the Au core migrate to the ceria surface, blocking the cluster-support interface. This should have profound influence on the CO oxidation activity of the catalysts, owing to the importance of the interfacial sites,^[72] especially in a Mars-van Krevelen like mechanism.^[27,44]

To remove the phosphine ligands, higher temperatures are required than for thiolate ones, contrary to what is expected taking into account the difference in bond strength (Au-S > Au-P).^[20,67] Thus, the ligand interaction with the support must be considered as well.

5.3.3. Operando Infrared Studies of CO Oxidation

To gain further insight into potential dynamics of the catalysts during CO oxidation at 250 °C, *operando*^[73] infrared studies were performed. CO oxidation was carried out in a transmission IR cell with the catalyst pressed into a thin pellet and CO conversion was followed by gas chromatography (see Figure 5.17). Figure 5.8 first compares the infrared spectra of the used catalysts and Figure 5.9 then displays difference spectra of Au₁₁/CeO₂ acquired during CO oxidation. The difference spectra of Au₂₅/CeO₂ and Biico Au₂₅/CeO₂, as well as of the support, are shown in Section 5.8 (Figures S15-S17).

By following the bands of adsorbed species on the support, an understanding of the dynamics during the catalytic reaction can be obtained. Compared to the pretreated catalysts shown

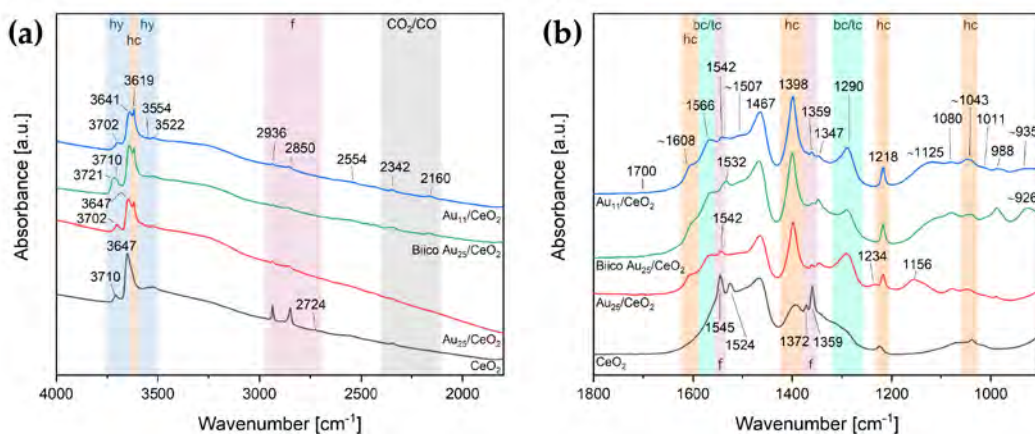


Figure 5.8.: Infrared spectra of the catalysts after CO oxidation at 250 °C: 4000-1800 cm⁻¹ (a) and 1800-900 cm⁻¹ (b). Bands associated with certain species are highlighted: hy = hydroxy species (blue), f = formates (violet), CO₂/CO (grey), bc/tc = bidentate/tridentate carbonates (turquoise), hc = hydrogen carbonates (orange). Spectra are offset for better visibility. Au content in catalyst: Au₁₁/CeO₂ and Biico Au₂₅/CeO₂: 1.2 wt%, Au₂₅/CeO₂: 0.3 wt%.

in Figure 5.5, the bands associated with formates (2936, 2850, 2724, 1545, 1372, 1359 cm⁻¹) decreased for all three cluster catalysts, whereas an increase was noticed for the support (see also the difference spectra during reaction in Figure 5.9 and Figures 5.25-5.27). Moreover, the cluster catalysts also showed evolving bands at 1566 and 1290 cm⁻¹, which have been previously assigned to bidentate^[59-62] or tridentate^[58,61,62] carbonates. As evidenced in the difference spectra during catalytic CO oxidation (Figure 5.9 and 5.25-5.27), the hydrogen carbonate bands at 3619, 1398 and 1218 cm⁻¹ seemed to disappear with increasing temperature during the reaction, but formed again during cool down. Compared to after pretreatment, slight shifts are noticed (1225 → 1218 cm⁻¹ and 1037 → 1043 cm⁻¹). Furthermore, as described by Vayssilov *et al.*,^[58] an additional band at 3619 cm⁻¹, as well as the shoulder at ≈1608 cm⁻¹ could be identified after reaction. As shown in Figure 5.8a, hydroxy species were also still present after CO oxidation for all samples.

During CO oxidation, as clearly evidenced by the difference spectra (Figure 5.9 and Figures 5.25-5.27, a broad band centered at 1467 cm⁻¹ further increased. When compared to spectra of the CeO₂ support at different stages of the catalytic process (Figure 5.32), this particular band seemed to change in unison with another broad band at 1294 cm⁻¹. Similar observations were also reported by other authors,^[61,62] who ascribed the bands to either mono- or polydentate carbonate species. In the spectra of the cluster catalysts, the lower energy band overlapped significantly with the intense hydrogen carbonate band at 1398 cm⁻¹, limiting the assignment. However, formation of polydentate carbonates during CO oxidation seems reasonable. These dynamics show that the clusters are capable of converting such adsorbed (intermediate) species to CO₂, making them active CO oxidation catalysts.

After reaction, no bands related to ligands or their residues in the region of C-H stretching

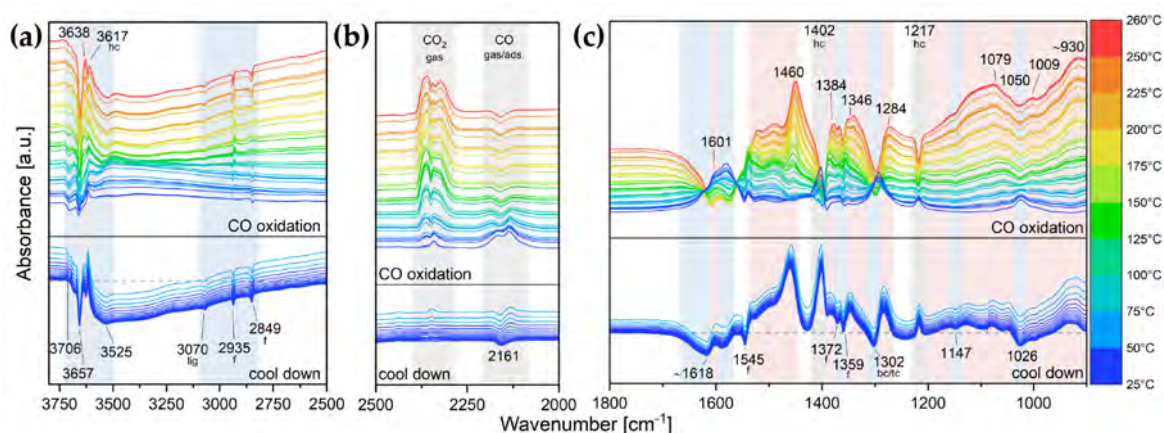


Figure 5.9.: Difference spectra of $\text{Au}_{11}/\text{CeO}_2$ during CO oxidation: (a) $3800\text{--}2500\text{ cm}^{-1}$, (b) $2500\text{--}2000\text{ cm}^{-1}$ and (c) $1800\text{--}900\text{ cm}^{-1}$. Bands decreasing during the pretreatment are indicated by a light blue background color and marked at the bottom, increasing ones by a light red one and marked on top. Bands decreasing during reaction but reforming at cool down are indicated by a grey shaded background. Assigned species are indicated by abbreviations: f = formates, hc = hydrogen carbonates, bc/tc = bidentate/tridentate carbonates. The spectrum of the pretreated catalyst after the CO adsorption experiment in He at RT was used as background. Au content in catalyst: 1.2 wt%. The difference spectra of Biico $\text{Au}_{25}/\text{CeO}_2$ and $\text{Au}_{25}/\text{CeO}_2$ during reaction can be found in Figure 5.25 and Figure 5.26, respectively.

vibrations could be identified anymore for $\text{Au}_{11}/\text{CeO}_2$ and Biico $\text{Au}_{25}/\text{CeO}_2$ (blue and green curve in Figure 5.8a). Analogous to the pretreatment, the spectra of the used catalysts (Figures 5.8a and 5.8b) still showed variations between the three cluster catalysts, whereas no significant differences could be observed in the difference spectra during CO oxidation (Figure 5.9 and Figures 5.25–5.26). This implies that the changes between the clusters that occurred during the oxidative pretreatment were maintained during catalytic CO oxidation (i.e. the broad absorption features below 1200 cm^{-1} for $\text{Au}_{11}/\text{CeO}_2$ and Biico $\text{Au}_{25}/\text{CeO}_2$ and the band at ca. 1156 cm^{-1} for $\text{Au}_{25}/\text{CeO}_2$; see also Figure 5.5b).

The CO adsorption by the catalysts, however, was affected by the reaction. As Figure 5.9b shows, a negative band at 2161 cm^{-1} was observed at the end of the reaction (for all cluster catalysts; see also Figure 5.25b and Figure 5.26b), which indicates reduction of Au^+ during the reaction. However, for $\text{Au}_{11}/\text{CeO}_2$ and Biico $\text{Au}_{25}/\text{CeO}_2$, a weak maximum could still be detected at 2160 cm^{-1} after reaction (Figure 5.8a) which suggests that some oxidized Au sites were still present after CO oxidation.

Upon repeating the room temperature CO adsorption experiment after reaction (same as after pretreatment; see Section 5.3.2), only CO adsorbed on partially oxidized $\text{Au}^{\delta+}$ was observed for all catalysts (Figure 5.28a–c). A comparison with the spectra of the pretreated catalysts (Figure 5.7a–c) shows that the maxima of the $\text{CO-Au}^{\delta+}$ band remained mostly unchanged. The CO-Au^+ band of $\text{Au}_{11}/\text{CeO}_2$ and Biico $\text{Au}_{25}/\text{CeO}_2$ was unaffected by the

adsorption and thus showed no signal in the CO adsorption difference spectra of the used catalysts.

Accordingly, the main changes in the infrared spectra during reaction can be attributed to adsorbed carbonate species on the support. These changes seem to occur for all cluster catalysts. The only significant difference among them is the evolution of the Au sites: Only $\text{Au}^{\delta+}$ was detected for the used $\text{Au}_{25}/\text{CeO}_2$ catalyst, whereas the originally phosphine-protected clusters $\text{Au}_{11}/\text{CeO}_2$ and Biico $\text{Au}_{25}/\text{CeO}_2$ still contained small amounts of oxidized Au^+ species. At this point, it is an open question whether this is related to ligand residues blocking sites near or on the Au particles or not. However, the oxidation state of Au can certainly be considered important for adsorbate binding^[66] and thus also catalytic oxidation of CO, with neutral Au being the main active sites in heterogeneous CO oxidation with Au nanoclusters.^[44]

Moreover, the assumption that oxidized phosphine species on the CeO_2 support block interfacial sites rather than CO adsorption on the Au surface is affirmed by the high intensity of CO adsorbed on Au for both $\text{Au}_{11}/\text{CeO}_2$ and Biico $\text{Au}_{25}/\text{CeO}_2$ (using the intensity of the gas phase CO band as reference; Figure 5.28a-b). This relative intensity difference is considerably less for $\text{Au}_{25}/\text{CeO}_2$ (Figure 5.28c) due to lower Au loading on the catalyst (0.3 wt% compared to 1.2 wt% for $\text{Au}_{11}/\text{CeO}_2$ and Biico $\text{Au}_{25}/\text{CeO}_2$) to ensure comparable activities (see Section 5.8.6.1 in the Supplementary Information). However, the difference in maximum CO conversion of $\text{Au}_{11}/\text{CeO}_2$ and $\text{Au}_{25}/\text{CeO}_2$ in the *operando* IR study was less than 10% (Figure 5.20a), suggesting that the degree of exposed Au surface was not a critical factor.

5.3.4. Electron Microscopy of Used Catalysts

To determine the particle size of the Au clusters after reaction, (scanning) transmission electron microscopy ((S)TEM) images were taken. In line with previous studies, slight sintering of the Au clusters was observed after reaction. Figure 5.10 shows images of all three cluster catalysts after pretreatment and CO oxidation at 250 °C. Both $\text{Au}_{25}/\text{CeO}_2$ and Biico $\text{Au}_{25}/\text{CeO}_2$ mainly feature small particles with average sizes of ≈ 2.1 nm and ≈ 2.7 nm, respectively. Au_{25} clusters should be of ≈ 1.1 nm size.^[28] $\text{Au}_{11}/\text{CeO}_2$, on the other hand, which should have a core diameter of 0.8 nm as a single cluster,^[74] appeared very polydisperse after reaction, but most particles still had sizes of roughly 4-7 nm. Migration of the phosphine ligands to the support during calcination and agglomeration of the bare Au particles was previously reported for Au_{11} on TiO_2 .^[70]

It is worth noting that the Au cluster size is not the predominant factor controlling catalyst activity in this study. $\text{Au}_{25}/\text{CeO}_2$ and Biico $\text{Au}_{25}/\text{CeO}_2$, both having particle sizes between 2-3 nm, show very different CO oxidation activity (see Figure 5.2d). In comparison, Biico $\text{Au}_{25}/\text{CeO}_2$ and $\text{Au}_{11}/\text{CeO}_2$ had similar CO conversion at a given temperature (Figure 5.2d), despite being significantly different in size and distribution on the surface. This confirms the suggestion that ligand residues and/or adsorbed species at the Au cluster-support interfacial sites are causing the observed significant differences in catalytic activity.

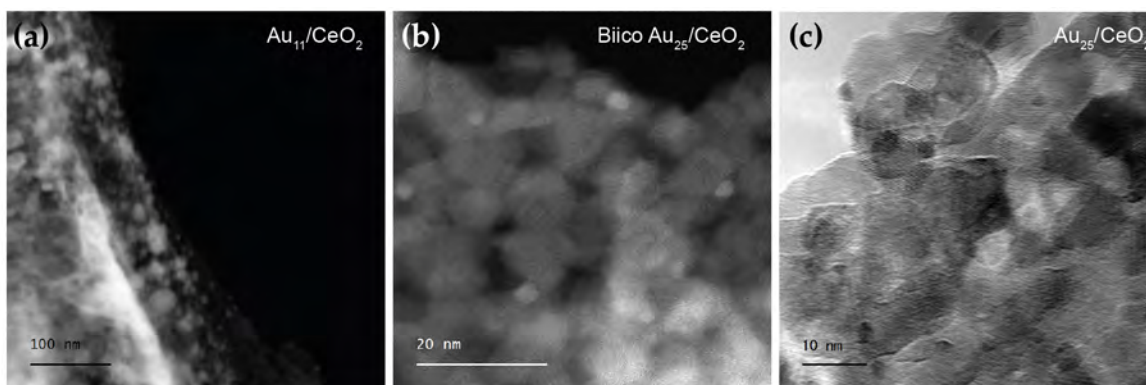


Figure 5.10.: Electron microscopy images of the catalysts (1.2 wt% Au) after pretreatment and reaction at 250 °C: High-angle annular dark-field scanning transmission electron microscopy (HAADF-STEM) of Au₁₁/CeO₂ (a) and Biico Au₂₅/CeO₂ (b); transmission electron microscopy (TEM) image of Au₂₅/CeO₂ (c). HAADF-STEM images of Biico Au₂₅/CeO₂ and Au₂₅/CeO₂ showing a larger sample area can be found in Figure 5.33.

5.4. Materials and Methods

5.4.1. Catalyst Preparation

The Au nanoclusters were synthesized and purified following published protocols.^[54–56,75,76] The supported catalysts were prepared by wet impregnation of the clusters on CeO₂. The gold loading of the catalysts was 1.2 wt%. Further details can be found in the Supplementary Material (Section 5.8).

5.4.2. Catalytic CO Oxidation Experiments

Kinetic studies of the Au nanocluster catalysts in CO oxidation were pursued using a flow reactor coupled to a micro-gas chromatograph (Micro-GC, Fusion 3000A, Inficon). ≈15 mg catalyst was placed between two glass wool plugs in a quartz glass tube, with a Ni/NiCr thermocouple submerged in the catalyst powder connected to a PID controller (EMSR EU-ROTHERM GmbH) of a cylindrical oven. All pretreatments were conducted in an oxidative atmosphere (5 % O₂ in Ar, 50 ml/min total gas flow) with a temperature ramp of 10 °C/min. The maximum temperature (150 °C, 20 °C, 250 °C or 300 °C) was held for 30 minutes before cooling the sample to room temperature in Ar (50 ml/min).

The gas flow composition was subsequently switched to reaction conditions (1 % CO and 2 % O₂ in Ar; 50 ml/min total gas flow). The temperature was then increased to the respective maximum reaction temperature (the same as the maximum temperature of the pretreatment) with a ramp of 5 °C/min. From 50 °C onwards, every 25 °C, the temperature was kept constant for 10 min to achieve steady-state conditions. After reaction, the catalyst was cooled to room temperature in argon (50 ml/min).

To investigate whether there was any deactivation or activation of the catalyst after pre-

treatment and reaction at 250 °C, three consecutive CO oxidation runs were conducted. Therefore, after pretreatment and the first run as described above, once the samples had cooled to room temperature, the gas composition was again changed to reaction conditions and the samples heated another time to 250 °C (same process as in the first run, no further pretreatment). This was then also repeated for a third time.

To compare the activity of the Au nanocluster catalysts, all data were normalized to 15 mg catalyst with a Au loading of 0.3 wt%. It should be noted that the CeO₂ support shows only minor activity above 200 °C (see Figure 5.18).

5.4.3. *In situ/Operando* Transmission Infrared Studies

In situ/Operando transmission Fourier-transform infrared studies (transmission FTIR) were conducted using a Bruker Vertex 70 spectrometer. About 10 mg of catalyst were grinded thoroughly and pressed into a thin pellet using a hydraulic press. The pellet was then mounted in a flow cell with IR transmissible windows and a thermocouple connected to a PID controller. The product gas flow was analyzed by GC chromatography (HP-PLOT Q column, FID detector) and mass spectrometry (Pfeiffer Vacuum, ThermoStar).

The sample was pretreated as described in Section 5.4.2 (10 °C/min to 250 °C, hold for 30 min, 5 % O₂ in He, 50 ml/min total gas flow) while simultaneously recording IR spectra (MIR, resolution 4 cm⁻¹).

After cooling to room temperature in helium, a CO adsorption experiment was performed. Therefore, the sample was exposed to 1 % CO in He (50 ml/min total flow) until the CO IR band did not change significantly anymore. Subsequently, 50 ml/min He was flown through the cell until no further significant changes were observed in the IR spectrum.

Following the CO adsorption experiment, the gases were switched to CO oxidation conditions (1 % CO, 2 % O₂ in He, 50 ml/min total flow) and the reaction conducted as described in Section 5.4.2 (heat up to 250 °C with 5 °C/min, hold every 25 °C for 10 min) while following by IR. The sample was then cooled to room temperature in He and the CO adsorption experiment repeated once more.

5.4.4. Transmission Electron Microscopy (TEM) and High-angle Annular Dark-field Scanning Transmission Electron Microscopy (HAADF-STEM)

Electron microscopy was performed using a 200 kV FEI Tecnai F20 S-TWIN analytical (scanning) transmission electron microscopy [(S)TEM] instrument equipped with a Gatan GIF Tridiem filter. The energy resolution was ≤ 1 eV, the semiconvergence angle ≈ 8 mrad, the semicollection angle ≈ 15 mrad, and the spatial resolution on the order of 0.5 nm. Supported clusters were directly deposited on carbon-coated copper grids and plasma cleaning was applied to remove possible hydrocarbons and adsorbed water.

5.4.5. Molecular Graphic Images

Molecular graphics images were produced using the UCSF Chimera package^[77] from the Resource for Biocomputing, Visualization, and Informatics at the University of California, San Francisco (supported by NIH P41 RR001081).

5.5. Conclusions

Three types of Au nanoclusters with different ligands and supported on CeO₂ were examined. Depending on the cluster structure, type of ligand shell, and pretreatment, significant differences in the catalytic CO oxidation activity were observed. Whereas thiolate-protected Au₂₅/CeO₂ reached 100 % conversion above 20 °C after a 250 °C pretreatment, the cluster catalysts containing phosphines in their ligand shell (Au₁₁/CeO₂ and Biico Au₂₅/CeO₂) exhibited only poor activity (below 30 % conversion at 250 °C). All samples showed stable conversion in three consecutive CO oxidation runs. After pretreatment at 300 °C, all catalysts exhibited comparable activity reaching 100 % above 250-300 °C. This seems related to differences in the catalyst activation process, as temperature programmed oxidation suggested that temperatures above 250 °C are required for oxidative removal of the ligands from Au₁₁/CeO₂ and Biico Au₂₅/CeO₂. Interestingly, this is contrary to the general concept of nanocluster stability, which classifies Au-S bonding stronger than Au-P. However, *in situ* infrared studies indicated that the ligands were mostly decomposed during pretreatment, as related bands decreased and CO adsorbed on Au could be observed after the activation process for all catalysts. In addition, a strong increase in adsorbance below 1200 cm⁻¹ was noticed for Au₁₁/CeO₂ and Biico Au₂₅/CeO₂, which may be related to formation of (oxidized) ligand residues on the support. Reduction of Au⁺ species was observed during CO oxidation and only IR bands related to CO adsorbed on Au^{δ+} were detected for the used Au₂₅/CeO₂ catalyst, whereas the others still additionally possessed a small amount of oxidized Au sites. It thus seems likely that fragments of the phosphine ligands and/or chlorines remained within the catalyst system of Au₁₁/CeO₂ and Biico Au₂₅/CeO₂, blocking active sites on the support-Au interface and causing this striking difference in activity. No correlation was found between the size of the Au particles and the CO oxidation activity, owing to very different CO conversion of the similarly sized Au₂₅-based catalysts (2-3 nm after 250 °C reaction) and the negligible differences in activity between Au₁₁/CeO₂ and Biico Au₂₅/CeO₂ (4-30 nm and ≈2.7 nm, respectively). Consequently, the choice of a particular nanocluster and its ligands must be carefully considered in heterogeneous nanocluster catalysis, as each individual building block will affect the performance of the catalyst system.

5.6. Author Contributions

Synthesis of the Au nanoclusters was performed by V.T. and D.S. IR, TPO, TGA/DSC and kinetic measurements and data evaluation were done by V.T. (S)TEM was measured by

M.S.P. and ESI-TOFMS by H.D. Final interpretation and manuscript preparation was led by V.T., N.B., Y.N. and G.R., with contributions from all authors.

5.7. Acknowledgments

The authors thank Stephan Pollitt, Yukari Imai and Ibuki Kobayashi for helpful discussions about the CO oxidation activity of biicosahedral Au nanoclusters. Pablo Ayla and Peter Kregsamer are acknowledged for TXRF and Ernst Pittenauer for MALDI-MS measurements. This project was also supported by EQ-BOKU VIBT GmbH and the BOKU Core Facility Mass Spectrometry. We further acknowledge support by the Austrian Science Fund (FWF) via grants Single Atom Catalysis (I 4434-N) and Elise Richter (V831-N).

5.8. Supplementary Information

The Supporting Information contains further experimental details and characterization of the nanoclusters (Figures 5.11-5.13), thermogravimetric analysis/differential scanning calorimetry (Figures 5.14-5.16), additional kinetic measurements (Figures 5.17-5.18), additional temperature programmed oxidation spectra (Figure 5.19) and additional spectra of the *in situ/operando* transmission infrared measurements (Figures 5.20-5.32), as well as additional scanning transmission electron microscopy images (Figure 5.33).

5.8.1. Synthesis and Characterization of Au Nanoclusters

The gold nanoclusters were synthesized according to standard procedures, as described in the following. Ultraviolet-visible spectroscopy (UV-Vis) of the nanoclusters in solution (DCM, toluene) was performed on a UV-1600PC spectrometer (VWR collection).

For electrospray ionization-time of flight mass spectrometry (ESI-TOFMS), the samples were dissolved in 100 % ACN, filtered through 0.2 μm PTFE filters (Ref: 4552T, Pall Corporation) and directly injected into the HPLC system (1290 Infinity II UPLC, Agilent Technologies). 5 μl of the sample was introduced into a flow of 5 ml/min with the eluent mixture of 10 % A (99.9 % H_2O , 0.1 % formic acid) and 90 % B (99.9 % ACN, 0.1 % formic acid), passing to the ESI-source over a short flow path (PEEK-capillaries). Mass spectra were recorded on an electrospray ionization-time of flight mass spectrometer (ESI-TOFMS, 6230 B, Agilent Technologies). The TOFMS settings can be found elsewhere.^[78] In brief, the dual AJS ESI-source was set to positive mode with the following settings: gas temperature 200 °C, gas flow 10 l/min, sheath gas temperature 350 °C, sheath gas flow 11 l/min, and nebulizer pressure 35 psig. The fragmentor voltage and the capillary voltages were set to 180 and 3500 V, respectively.

The TOF instrument is specified to an accuracy of ± 1 ppm and a resolution of 10000 at m/z 322. Prior to the measurement, the TOF was calibrated within the mass range of m/z 100 and the upper calibration limit of m/z 2722, and during the entire analysis the reference masses were enabled to ensure the specified values. The measurements were performed in the 1 GHz mode (m/z range: 100-20000) with a scan rate of 2.00. Background subtraction was performed via the software Agilent MassHunter Qualitative Analysis Software (B.10.00).

Matrix-assisted laser desorption ionization (MALDI) mass spectrometric spectra were obtained with a MALDI-7090 MALDI-TOF-MS mass spectrometer (Shimadzu). *trans*-2-[3-(4-*tert*-Butylphenyl)-2-methyl-2-propenylidene]-malononitrile (DCTB) was used as matrix. Spectra were obtained as an average of 500 profiles of single pulses at 50 Hz and with 100 μm spot size. To avoid too much fragmentation, the laser power was reduced as much as possible.

Attenuated total reflection Fourier-transform infrared spectroscopy (ATR-FTIR) of the solid cluster samples was conducted with a Perkin Elmer Spektrum 400 instrument.

5.8.1.1. $\text{Au}_{11}(\text{PPh}_3)_7\text{Cl}_3$

$\text{Au}_{11}(\text{PPh}_3)_7\text{Cl}_3$ (' Au_{11} ') was synthesized following a protocol by McKenzie *et al.*,^[54] with minor adaptations. To a solution of $\text{Au}(\text{PPh}_3)\text{Cl}$ (400 mg) in 20 ml tetrahydrofuran (THF), 152 mg NaBH_4 in 20 ml ethanol (EtOH) were added. After stirring at room temperature (2 h), the red-brown crude product was precipitated in 400 ml pentane (over 2 h). The clusters were filtered and washed four times with hexane (6 ml each) and a 50:50 mixture dichloromethane/hexane (10 ml each). Due a lot of dark brown precipitate, the crude product was subsequently rinsed with THF until the filtrate was colorless. Only red precipitate remained at that point, which was redissolved in dichloromethane (DCM) (in 5 ml portions) and the solvent removed under reduced pressure.

The purified $\text{Au}_{11}(\text{PPh}_3)_7\text{Cl}_3$ was characterized by UV-Vis spectroscopy, ESI mass spectrometry and ATR-FTIR spectroscopy (Figure 5.11). The ESI-TOF mass spectrum (Figure 5.11b) shows peaks corresponding to the two known Au_{11} isomers, $\text{Au}_{11}(\text{PPh}_3)_7\text{Cl}_3$ and $[\text{Au}_{11}(\text{PPh}_3)_8\text{Cl}_2]\text{Cl}$, as well as several products of in-source fragmentation. However, the shape and positions of the maxima of the UV-Vis spectrum in Figure 5.11a are in perfect agreement with those reported by McKenzie *et al.*^[54] for $\text{Au}_{11}(\text{PPh}_3)_7\text{Cl}_3$. Considerable percentages of $[\text{Au}_{11}(\text{PPh}_3)_8\text{Cl}_2]\text{Cl}$ in the sample should lead to shifts in the UV-Vis bands.^[54] Thus, the presence of $[\text{Au}_{11}(\text{PPh}_3)_8\text{Cl}_2]^+$ in the mass spectrum is attributed to be mainly a result of gas phase chemistry during the measurement. Note that the intrinsic positive charge of $[\text{Au}_{11}(\text{PPh}_3)_8\text{Cl}_2]\text{Cl}$ compared to the neutral $\text{Au}_{11}(\text{PPh}_3)_7\text{Cl}_3$ is also expected to have an influence.

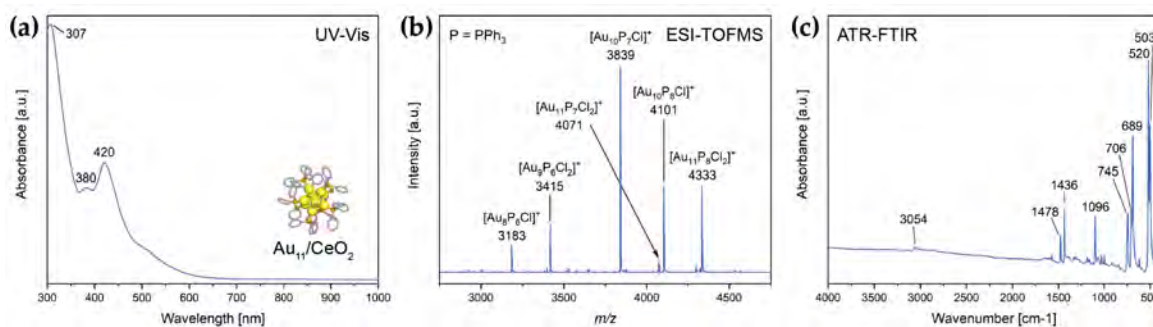


Figure 5.11.: UV-Vis (a), ESI-MS (b) and ATR-FTIR (c) spectrum of $\text{Au}_{11}(\text{PPh}_3)_7\text{Cl}_3$.

5.8.1.2. $[\text{Au}_{25}(\text{PPh}_3)_{10}(\text{SC}_2\text{H}_4\text{Ph})_5\text{Cl}_2]\text{Cl}_2$

The synthesis of $[\text{Au}_{25}(\text{PPh}_3)_{10}(\text{SC}_2\text{H}_4\text{Ph})_5\text{Cl}_2]\text{Cl}_2$ ('Biico Au_{25} ') was conducted as described previously.^[55,56,76] Briefly, 7.6 mg NaBH_4 were added to a solution of $\text{Au}(\text{PPh}_3)\text{Cl}$ (98.5 mg) in 5.5 ml ethanol and the reaction mixture stirred at room temperature for 2 h. Afterwards, the solvent was removed under reduced pressure and the crude product washed with water, hexane and chloroform/hexane (3:2 and 1:1, 2 x 5 ml each). The precursor clusters were then obtained by extraction with chloroform. For transformation to $[\text{Au}_{25}(\text{PPh}_3)_{10}(\text{SC}_2\text{H}_4\text{Ph})_5\text{Cl}_2]\text{Cl}_2$, 20 mg

of the precursor were dissolved in 30 ml chloroform and 41 μ l of 2-phenylethanethiol (2-PET) added. The mixture was stirred at room temperature for 20 h, after which the solvent was removed. The product was washed repeatedly with hexane and then extracted with EtOH, yielding $[\text{Au}_{25}(\text{PPh}_3)_{10}(\text{SC}_2\text{H}_4\text{Ph})_5\text{Cl}_2]\text{Cl}_2$, as confirmed by UV-Vis spectroscopy, ESI mass spectrometry and ATR-FTIR spectroscopy (Figure 5.12).

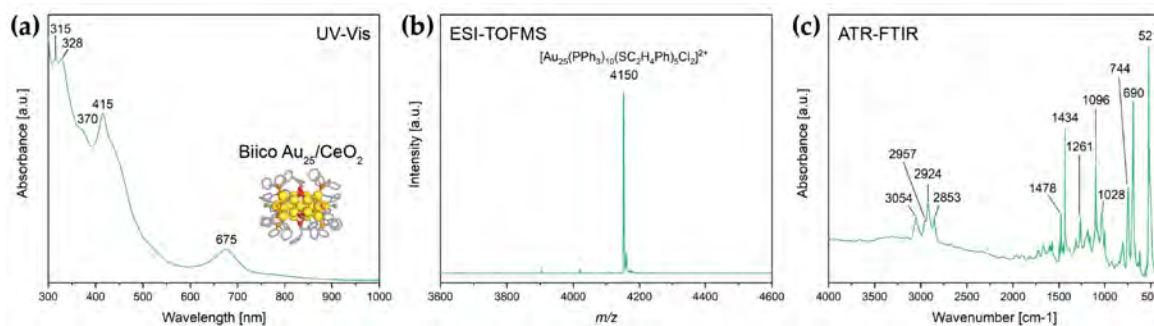


Figure 5.12.: UV-Vis (a), ESI-MS (b) and ATR-FTIR (c) spectrum of $[\text{Au}_{25}(\text{PPh}_3)_{10}(\text{SC}_2\text{H}_4\text{Ph})_5\text{Cl}_2]\text{Cl}_2$.

5.8.1.3. $[\text{Au}_{25}(\text{SC}_2\text{H}_4\text{Ph})_{18}]^-\text{TOA}^+$

$[\text{Au}_{25}(\text{SC}_2\text{H}_4\text{Ph})_{18}]^-\text{TOA}^+$ ("Au₂₅") was obtained according to a procedure by Shivhare *et al.*^[75] 500 mg of $\text{HAuCl}_4 \cdot 3 \text{H}_2\text{O}$ and 833 mg of tetraoctylammonium bromide (TOAB) were dissolved in 50 ml THF. 850 μ l 2-PET were added, leading the color of the orange solution gradually fading out over 1 h. Subsequently, the mixture was reduced by addition of 480 mg NaBH_4 in 10 ml ice-cold H_2O . The reaction was continued for 4 days at room temperature. Then, the solvent was evaporated and the precipitate washed repeatedly with H_2O /methanol (1:1) and methanol (MeOH). The crude product was then extracted with acetone and purified by size exclusion chromatography (Bio-Beads S-X1 in THF). The UV-Vis, MALDI-MS and ATR-FTIR spectra of $[\text{Au}_{25}(\text{SC}_2\text{H}_4\text{Ph})_{18}]^-\text{TOA}^+$ are shown in Figure 5.13. Due to the strong laser power of the mass spectrometer, the main peak in the mass spectrum in Figure 5.13b originates from the $[\text{M}-(\text{Au}(\text{SC}_2\text{H}_4\text{Ph})_4)]^+$ fragment, a typical fragment ion of Au_{25} clusters in MALDI-MS.^[79]

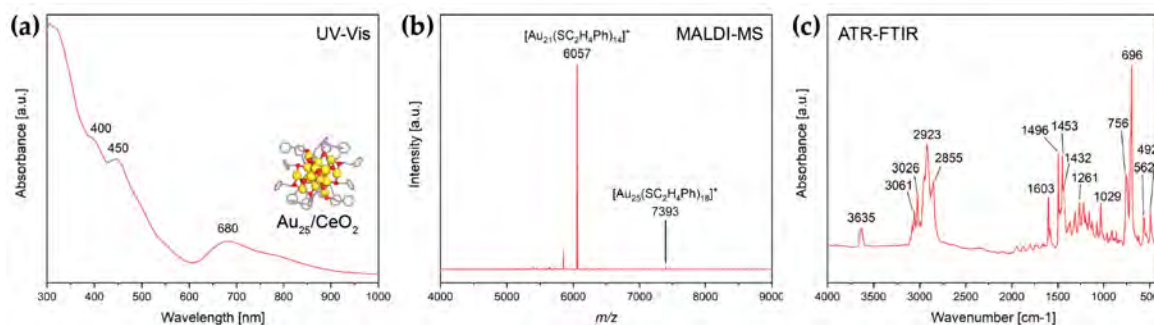


Figure 5.13.: UV-Vis (a), MALDI-MS (b) and ATR-FTIR (c) spectrum of $[\text{Au}_{25}(\text{SC}_2\text{H}_4\text{Ph})_{18}]^{-}\text{TOA}^{+}$.

5.8.2. Preparation of Ceria Supported Au Nanocluster Catalysts

The gold nanoclusters were subsequently supported on CeO_2 (Alfa Aesar, 15-30 nm particle size, 30-50 m^2/g surface area). The clusters were dissolved in toluene (Au_{25}) or MeOH (Au_{11} , Biico Au_{25}) and added dropwise to a stirred suspension of ceria in the respective solvent. After complete addition, stirring at room temperature was continued for 6 h. The supported clusters were then separated from the solution by filtration, the powder dried under reduced pressure and then grinded.

The exact metal loading (wt%) of the gold nanocluster catalysts was determined by total X-ray fluorescence spectroscopy (TXRF), using an ATOMIKA 8030C X-ray fluorescence analyzer. Samples were attached to total reflecting quartz reflectors using 1 mg of sample mixed with 5 μl of 1 % poly-vinyl alcohol solution (for fixation). Blank measurements of the unloaded reflectors were performed prior to each specimen measurement to avoid cross contamination. Detection limits of the quantified elements (Au and Ce) are in the range of 10-100 $\mu\text{g}/\text{g}$.

5.8.3. Thermogravimetric Analysis/Differential Scanning Calorimetry

Simultaneous thermogravimetric analysis (TGA)/differential scanning calorimetry (DSC) was carried out using a Netzsch STA 409 PC/PG Luxx thermal analyzer. Approximately 10 mg of unsupported clusters were transferred to an Al_2O_3 crucible as a concentrated suspension in dichloromethane and dried at room temperature for 24 h to ensure complete evaporation of the solvent. The sample was subsequently transferred to the thermal analyzer and heated to 100 $^{\circ}\text{C}$ with a 5 $^{\circ}\text{C}/\text{min}$ ramp. It was kept at this temperature for 30 min before being heated to 400 $^{\circ}\text{C}$ (also 5 $^{\circ}\text{C}/\text{min}$ and 30 min holding period). The entire heating process was performed with a total gas flow of 50 ml/min of 5 % O_2 in He (i.e., the pretreatment atmosphere).

It should be noted that quantitative errors of up to 10 % apply to the mass loss of all samples and thus, both the TGA and the DSC signals are only interpreted qualitatively. The error is due to the small amounts of sample used (10 mg) or to traces of gold removed from the

crucible during the oxidation of the ligand sphere. Moreover, in lieu of the dynamic nature of oxide supported Au nanoclusters, considering for example potential ligand migration to the support or Au sintering, it should be noted beforehand that TGA and DSC results of unsupported clusters are probably not directly transferable to their immobilized counterparts.

The main mass loss of unsupported $\text{Au}_{11}(\text{PPh}_3)_7\text{Cl}_3$ (Figure 5.14) occurs between 200 °C and 300 °C, with a gradual on-set starting at approximately 150 °C. In addition, the DSC curve shows a sharp negative peak at 157 °C, which could indicate a structural rearrangement process. Further small peaks in the DSC curve are observed at 189 °C and 296 °C, which are approximately at the beginning and end of the period of main mass loss. Overall, the observed TGA curve agrees with the temperature programmed oxidation measurements of the CeO_2 supported clusters catalysts, which showed CO_2 formation above 200 °C (see Figure 5.4 and Figure 5.19). It also indicates that under the pretreatment conditions applied herein, a temperature of 300 °C is necessary to remove all ligands and/or their residues from the unsupported clusters, which correlates with the pronounced increase in reactivity for the 300 °C pretreated catalyst (Figure 5.2a). Compared to TGA of $[\text{Au}_{11}(\text{PPh}_3)_8\text{Cl}_2]\text{Cl}$ reported by Leong and coworkers,^[24] the mass loss proceeds and extends to higher temperatures, which may be related to differences in experimental conditions.

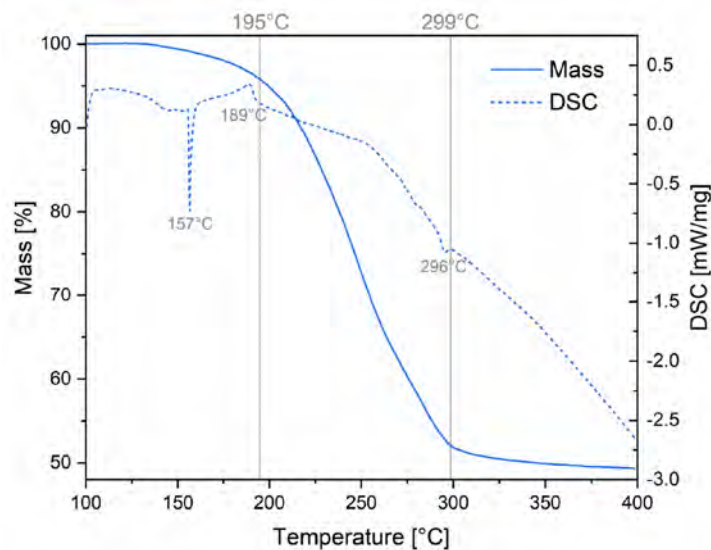


Figure 5.14.: Mass loss (solid line) and differential scanning calorimetric signal (dashed line) of $\text{Au}_{11}(\text{PPh})_3\text{Cl}_3$ at pretreatment conditions.

For $[\text{Au}_{25}(\text{PPh}_3)_{10}(\text{SC}_2\text{H}_4\text{Ph})_5\text{Cl}_2]\text{Cl}_2$, (Figure 5.15), mass loss starts at around 165 °C and continues up to 370 °C, though the loss is marginal above 263 °C. It is accompanied by several negative peaks and small dips in the DSC curve at 265 °C, 192 °C, 244 °C, ≈ 270 °C and ≈ 350 °C. This could indicate several changes to the initial cluster structure during the ligand detachment process. Notably, the major ligand removal process is still ongoing at 250 °C and

also structural changes seem to occur even above 250 °C, which may contribute to the sudden jump in activity after pretreatment at 300 °C (cf. Figure 5.2b). The mass loss curve of the unsupported clusters also compares well to the CO₂ formation and O₂ consumption peaks observed in the temperature programmed oxidation experiments with CeO₂ supported catalyst (see Figure 5.4 and Figure 5.19), which showed an on-set at 165-175 °C and a maximum at 267 °C. Zhu *et al.*^[32] also performed TGA of [Au₂₅(PPh₃)₁₀(SC₂H₄Ph)₅Cl₂]Cl₂ nanoclusters and observed beginning mass loss at 150 °C, which continued up to ≈300 °C. They also reported that the thiolate ligands were removed first, followed by the phosphines and chlorine ligands.

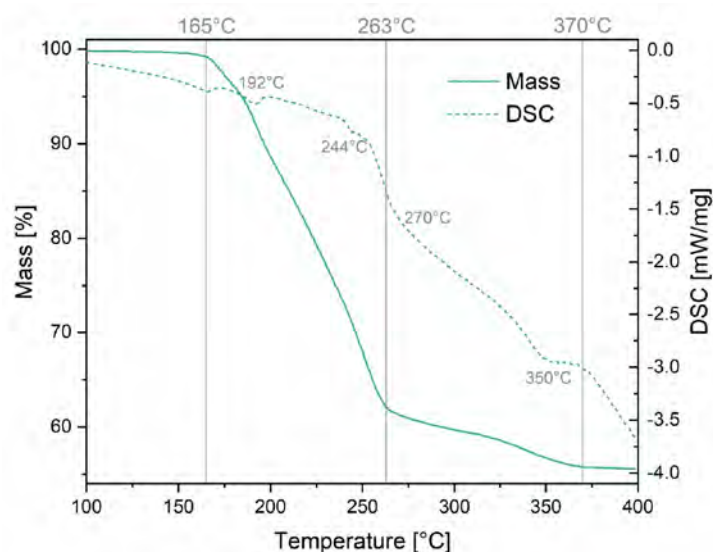


Figure 5.15.: Mass loss (solid line) and differential scanning calorimetric signal (dashed line) of [Au₂₅(PPh)₁₀(SC₂H₄Ph)₅Cl₂]Cl₂ at pretreatment conditions.

Ligand desorption of [Au₂₅(SC₂H₄Ph)₁₈]⁻TOA⁺ started at ≈174 °C, accompanied by a negative DSC peak at 176 °C. The mass loss then occurs up to 298 °C, though most part of the ligand sphere seems already removed when reaching 240 °C. In addition, also DSC only shows significant features below 240 °C. This indicates that most structural changes occur below 250 °C, which may contribute to the significantly increased activity of catalysts pretreated at that temperature (Figure 5.2c). For the CeO₂ supported clusters, similar temperatures were observed by temperature programmed oxidation (Figure 5.4 and Figure 5.19): the CO₂ formation starts between 150-165 °C (slightly lower than in TGA) and peaks at 235-245 °C. Complete removal of the protecting ligands/counterions at 250-300 °C in TGA was reported by Nie *et al.*^[38] and at 250 °C by Zhu *et al.*^[32] However, both reported a slightly higher on-set temperature of ≈190-200 °C.^[32,38]

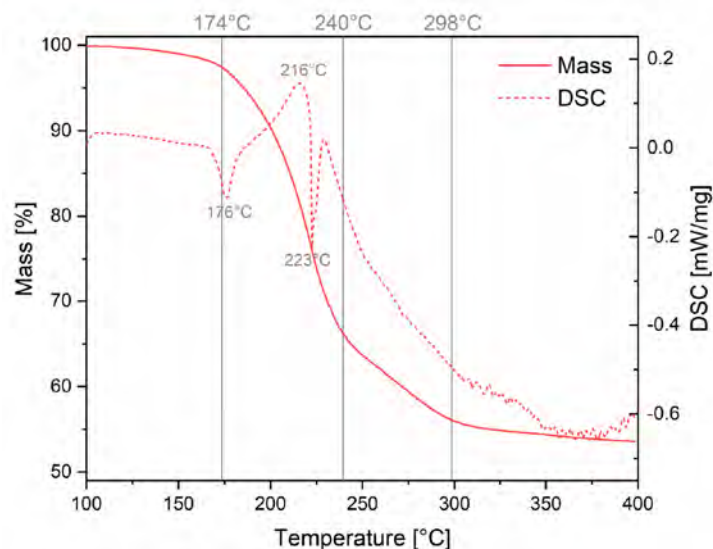


Figure 5.16.: Mass loss (solid line) and differential scanning calorimetric signal (dashed line) of $[\text{Au}_{25}(\text{SC}_2\text{H}_4\text{Ph})_{18}]\text{TOA}$ at pretreatment conditions.

5.8.4. Additional Kinetic Measurements

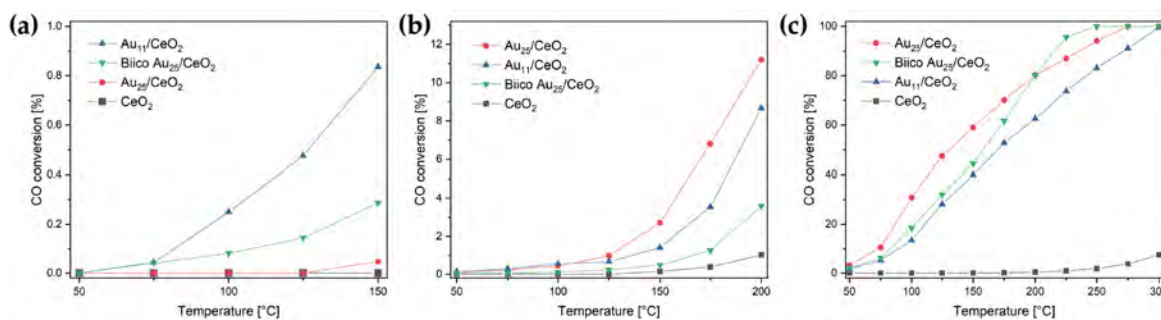


Figure 5.17.: Comparison of the catalytic activity of nanocluster catalysts (0.3 wt% Au loading, 15 mg catalyst) pretreated at (a) 150 °C, (b) 200 °C and (c) 300 °C. Note that the conversion scales differ by two orders of magnitude.

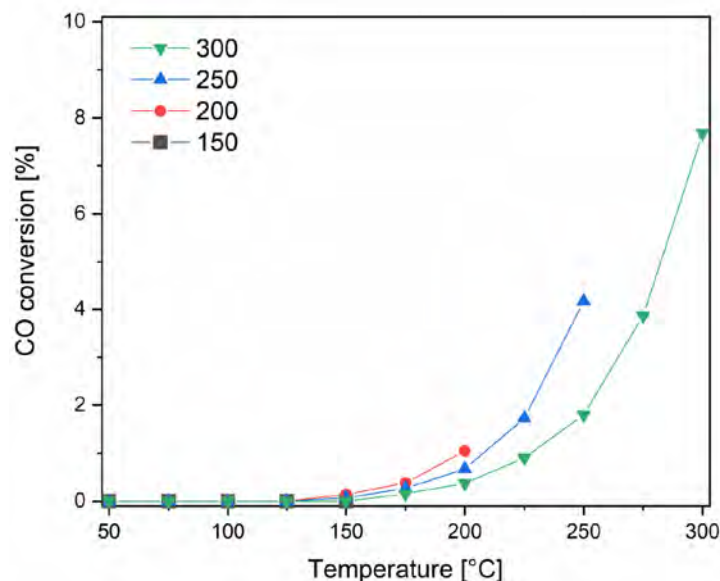


Figure 5.18.: CO conversion of the pure CeO₂ (15 mg) pretreated at different temperatures.

5.8.5. Additional Temperature Programmed Oxidation Spectra

In addition to the CO₂ generation and O₂ consumption spectra obtained for a 250 °C pretreatment during the *in situ* transmission infrared studies, a separate temperature programmed oxidation (TPO) experiment until 300 °C was performed. A reactor set-up comparable to the one used for the catalytic studies (see Section 5.4.2 in the main manuscript) was employed. ≈23 mg of sample was placed in a quartz tube between glass wool plugs and heated to 300 °C (10 °C/min) in an atmosphere of 5% O₂ in Ar (50 ml/min total gas flow). The sample was kept at 300 °C for 30 min. The exhaust gas composition was analyzed by mass spectrometry (Pfeiffer Vacuum QME 200 with SEM detector).

Figure 5.19 shows the CO₂ evolution (a) and O₂ consumption (b) spectra of the different catalysts during pretreatment till 300 °C. As seen in Figure 5.19a, CO₂ desorption from CeO₂ was observed from about 70-130 °C for all samples.^[38] For Au₂₅/CeO₂, CO₂ formation started at approximately 165 °C, with the peak centered at 245 °C. A very broad peak is observed for its O₂ consumption, with an approximate on-set at 140 °C. For Biico Au₂₅/CeO₂ and Au₁₁/CeO₂, CO₂ formation set in at ≈175 °C (center 267 °C) and ≈200 °C (center 275 °C), respectively. Their O₂ consumption peaks were centered at 270 °C (Biico Au₂₅/CeO₂) and 275 °C (Au₁₁/CeO₂). Pure CeO₂ also showed CO₂ evolution and very minor O₂ consumption above 200 °C.

It should be noted that the disturbance in the low-temperature region of the O₂ consumption spectra (Figure 5.19b) of Au₁₁/CeO₂ and Au₂₅/CeO₂ are mainly due to a negative spike in the argon carrier gas pressure, which can also be seen in the CO₂ generation spectra (Figure 5.19a). The distortions of the Biico Au₂₅/CeO₂ spectrum originate from the O₂ mass flow controller.

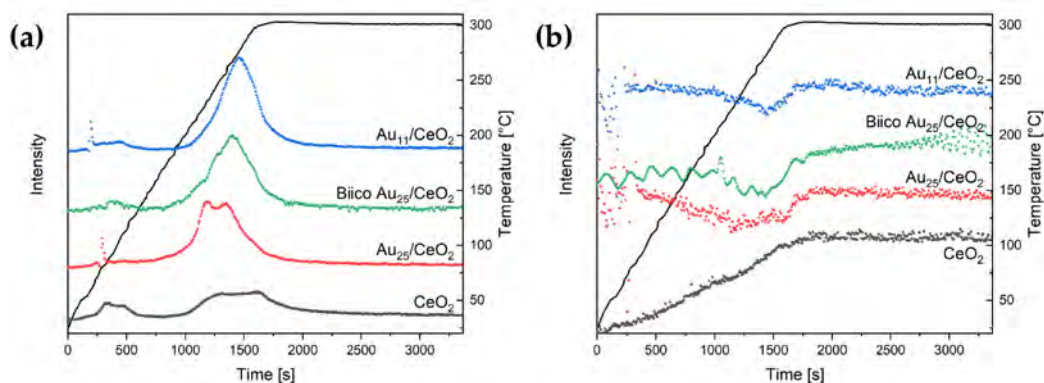


Figure 5.19.: CO₂ generation (a) and O₂ consumption spectra (b) of the different catalysts during oxidative pretreatment up to 300 °C. Au content in catalyst: 1.2 wt% for all cluster catalysts. Spectra were normalized by the carrier gas signal to compensate for changes in pressure. Spectra are offset for better visibility.

5.8.6. Additional Spectra of *In Situ* Transmission Infrared Measurements

5.8.6.1. Catalytic CO Conversion

Figure 5.20 shows the CO conversion (after 250 °C pretreatment) during the *operando* IR measurements determined by gas chromatography. To facilitate a more meaningful comparison of the IR spectra, similar conversion levels (activity) of the clusters catalysts was aimed for. Therefore, in case of Au₁₁/CeO₂ and Biico Au₂₅/CeO₂ catalysts, samples with 1.2 wt% Au loading instead of 0.3 wt% were employed (Au₂₅/CeO₂ still had 0.3 wt%). For all catalysts, a thin wafer with ≈10 mg mass was produced. To show that the activity is similar to that observed in the kinetic experiments with the powdered catalyst in a quartz tube, the CO conversion was normalized to 0.3 wt% and 15 mg catalyst, (Figure 5.20b). Small deviations can be attributed to the different experimental setup (pellet vs. powder).

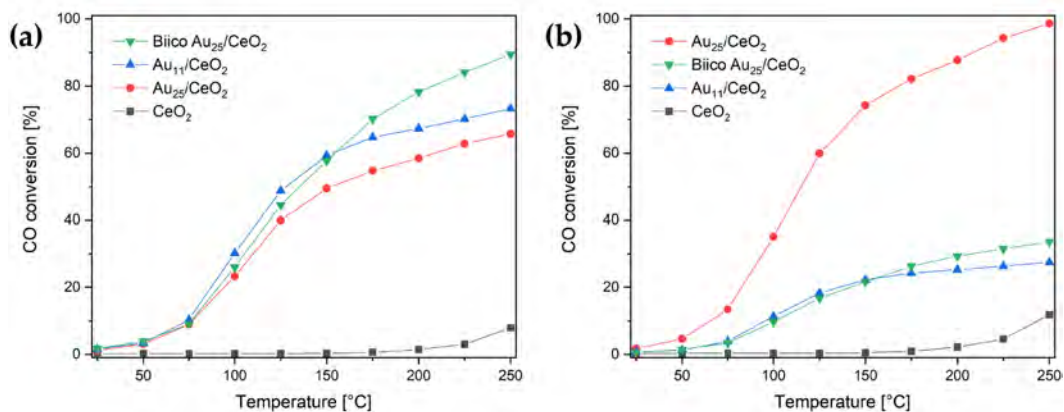


Figure 5.20.: CO conversion during *operando* transmission IR studies: (a) per 10 mg catalyst pellet (Au content in catalyst: Au₁₁/CeO₂ and Biico Au₂₅/CeO₂: 1.2 wt%, Au₂₅/CeO₂: 0.3 wt%) and (b) normalized to 0.3 wt% Au and 15 mg catalyst (cf. kinetic studies). Pretreatment at 250 °C at 5 % O₂ in He.

5.8.6.2. Additional Infrared Spectra of the Oxidative Pretreatment

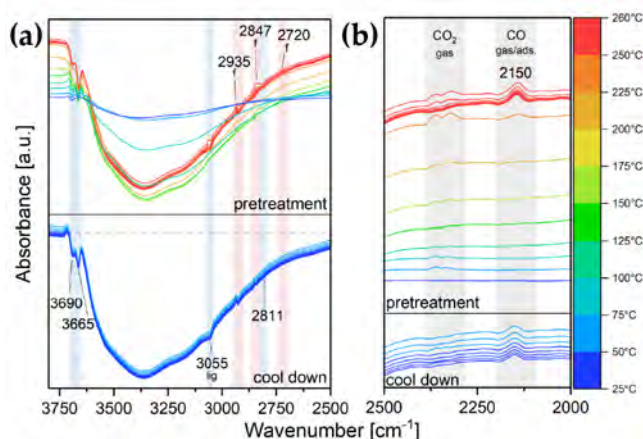


Figure 5.21.: Difference spectra of Au₁₁/CeO₂ during oxidative pretreatment: (a) 3800-2500 cm⁻¹ and (b) 2500-2000 cm⁻¹. Bands decreasing during the pretreatment are indicated by a light blue background color and marked at the bottom, increasing ones by a light red one and marked on top. Assigned species are indicated by abbreviations: f = formates, hc = hydrogen carbonates, bc/tc = bidentate/tridentate carbonates, lig = ligands. The spectrum of the as-prepared catalyst in He at RT was used as background. Au content in catalyst: 1.2 wt%.

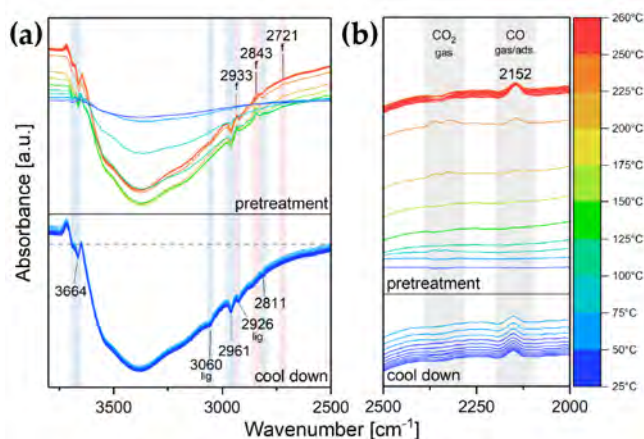


Figure 5.22.: Difference spectra of Biico Au₂₅/CeO₂ during oxidative pretreatment: (a) 3800-2500 cm⁻¹ and (b) 2500-2000 cm⁻¹. Bands decreasing during the pretreatment are indicated by a light blue background color and marked at the bottom, increasing ones by a light red one and marked on top. Assigned species are indicated by abbreviations: f = formates, hc = hydrogen carbonates, bc/tc = bidentate/tridentate carbonates, lig = ligands. The spectrum of the as-prepared catalyst in He at RT was used as background. Au content in catalyst: 1.2 wt%.

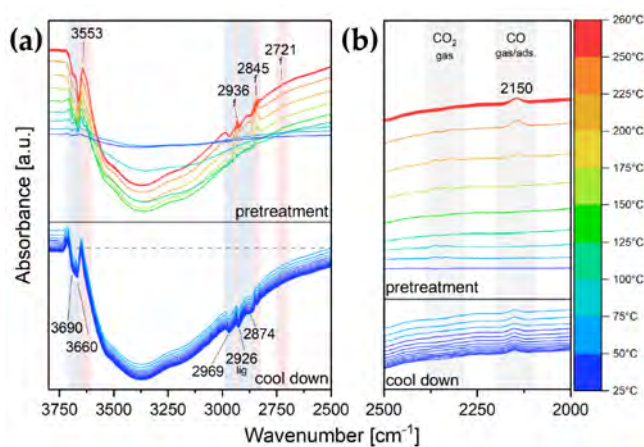


Figure 5.23.: Difference spectra of Au₂₅/CeO₂ during oxidative pretreatment: (a) 3800-2500 cm⁻¹ and (b) 2500-2000 cm⁻¹. Bands decreasing during the pretreatment are indicated by a light blue background color and marked at the bottom, increasing ones by a light red one and marked on top. Assigned species are indicated by abbreviations: f = formates, hc = hydrogen carbonates, bc/tc = bidentate/tridentate carbonates, lig = ligands. The spectrum of the as-prepared catalyst in He at RT was used as background. Au content in catalyst: 0.3 wt%.

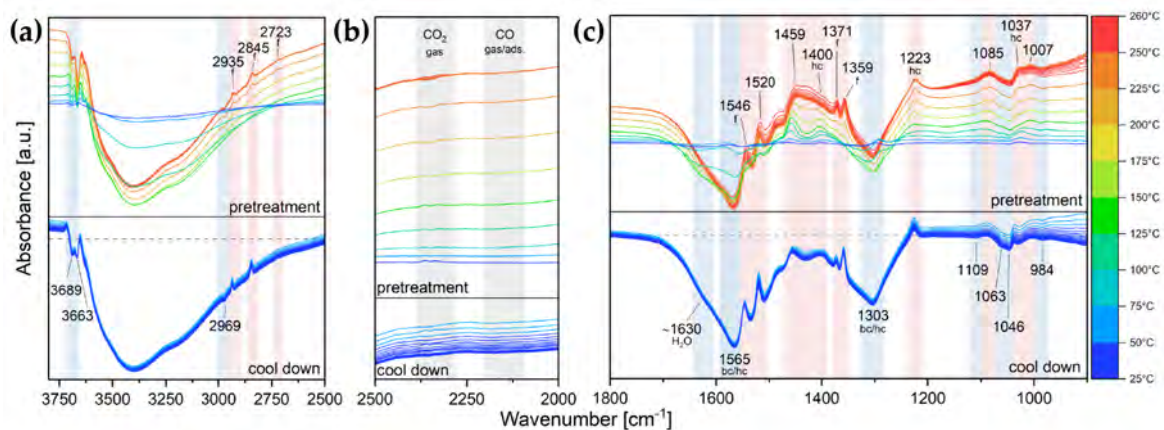


Figure 5.24.: Difference spectra of the CeO_2 support during oxidative pretreatment: (a) $3800\text{--}2500\text{ cm}^{-1}$, (b) $2500\text{--}2000\text{ cm}^{-1}$ and (c) $1800\text{--}900\text{ cm}^{-1}$. Bands decreasing during the pretreatment are indicated by a light blue background color and marked at the bottom, increasing ones by a light red one and marked on top. Assigned species are indicated by abbreviations: f = formates, hc = hydrogen carbonates, bc/tc = bidentate/tridentate carbonates. The spectrum of CeO_2 in He at RT was used as background.

5.8.6.3. Additional Spectra of the CO Oxidation

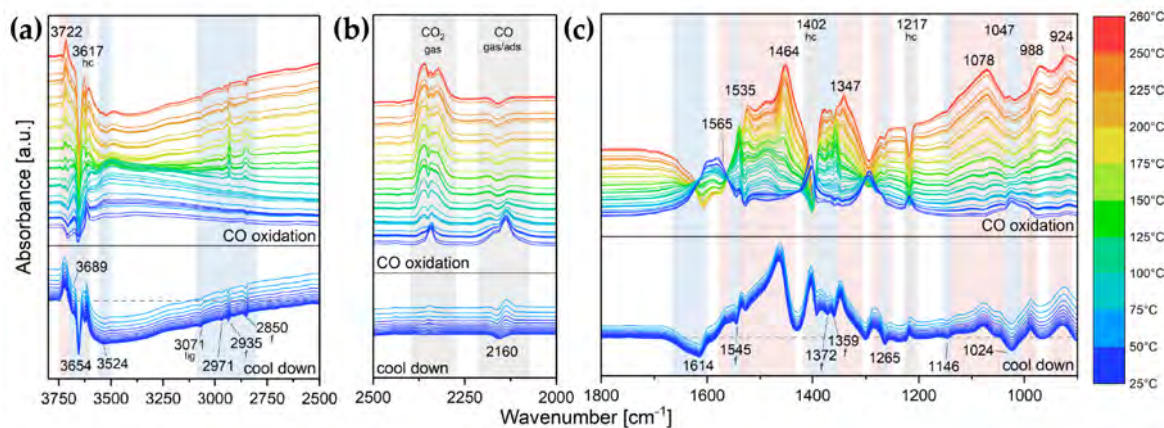


Figure 5.25.: Difference spectra of BiCo $\text{Au}_{25}/\text{CeO}_2$ during CO oxidation: (a) $3800\text{--}2500\text{ cm}^{-1}$, (b) $2500\text{--}2000\text{ cm}^{-1}$ and (c) $1800\text{--}900\text{ cm}^{-1}$. Bands decreasing during the pretreatment are indicated by a light blue background color and marked at the bottom, increasing ones by a light red one and marked on top. Bands decreasing during reaction but restored upon cool down are indicated by a grey shaded background. Assigned species are indicated by abbreviations: f = formates, hc = hydrogen carbonates, bc/tc = bidentate/tridentate carbonates. The spectrum of the pretreated catalyst after the CO adsorption experiment in He at RT was used as background. Au content in catalyst: 1.2 wt%.

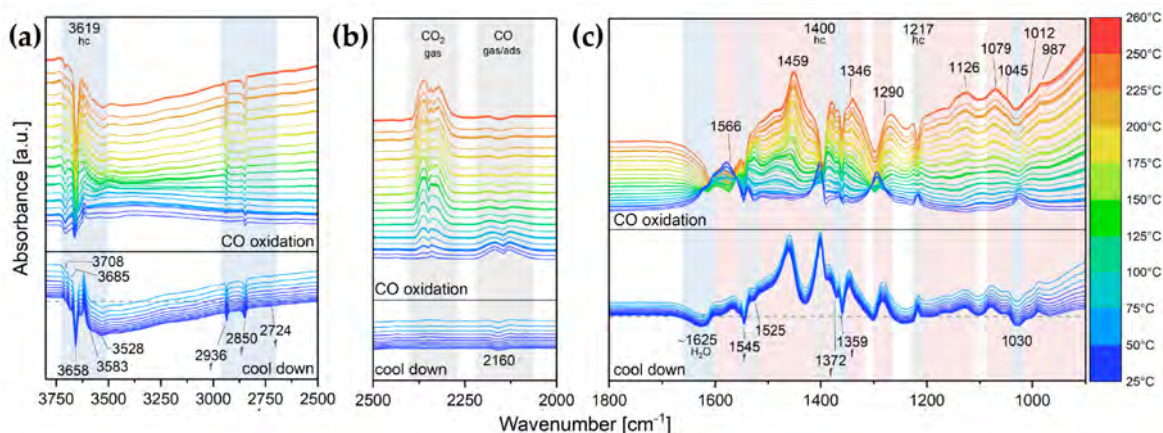


Figure 5.26.: Difference spectra of $\text{Au}_{25}/\text{CeO}_2$ during CO oxidation: (a) $3800\text{-}2500\text{ cm}^{-1}$, (b) $2500\text{-}2000\text{ cm}^{-1}$ and (c) $1800\text{-}900\text{ cm}^{-1}$. Bands decreasing during the pretreatment are indicated by a light blue background color and marked at the bottom, increasing ones by a light red one and marked on top. Bands decreasing during reaction but restored upon cool down are indicated by a grey shaded background. Assigned species are indicated by abbreviations: f = formates, hc = hydrogen carbonates, bc/tc = bidentate/tridentate carbonates. The spectrum of the pretreated catalyst after the CO adsorption experiment in He at RT was used as background. Au content in catalyst: 0.3 wt%.

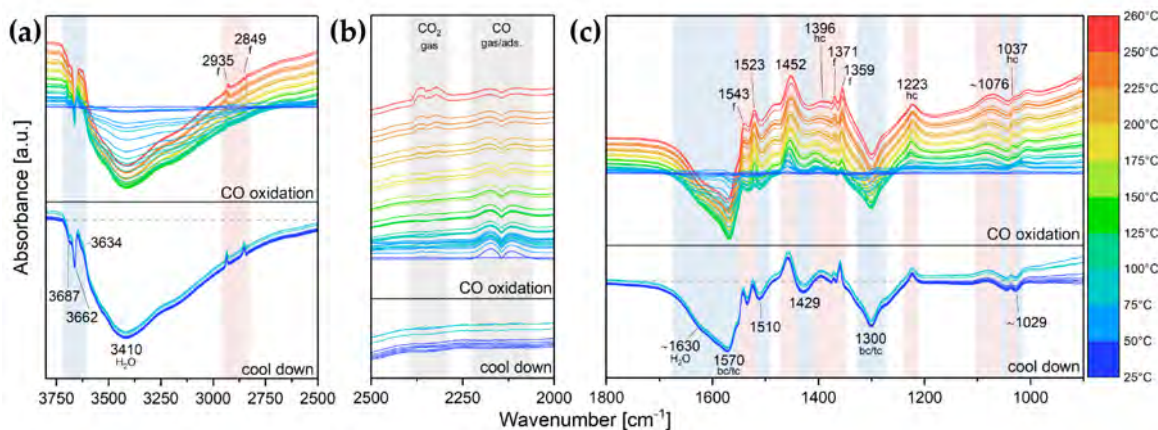


Figure 5.27.: Difference spectra of the CeO_2 support during CO oxidation: (a) $3800\text{-}2500\text{ cm}^{-1}$, (b) $2500\text{-}2000\text{ cm}^{-1}$ and (c) $1800\text{-}900\text{ cm}^{-1}$. Bands decreasing during the pretreatment are indicated by a light blue background color and marked at the bottom, increasing ones by a light red one and marked on top. Assigned species are indicated by abbreviations: f = formates, hc = hydrogen carbonates, bc/tc = bidentate/tridentate carbonates. The spectrum of CeO_2 after pretreatment and the adsorption experiment in He at RT was used as background.

5.8.6.4. Infrared Spectra of Post-Reaction CO Adsorption

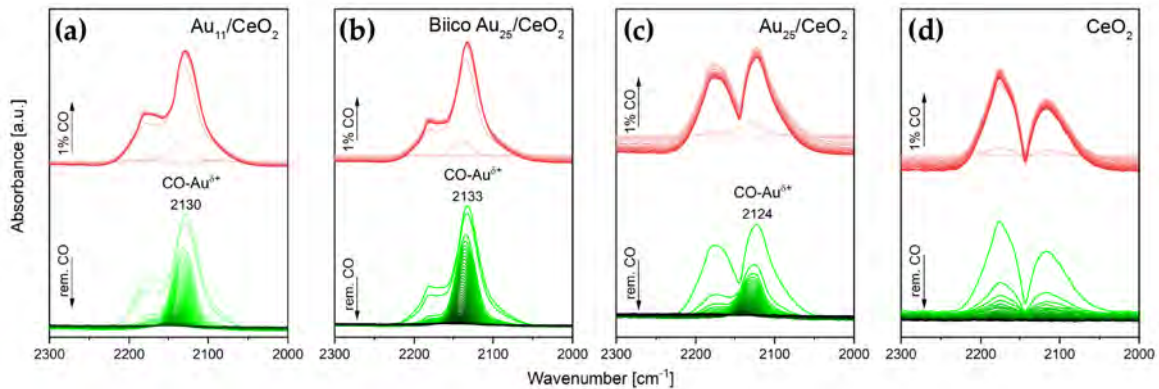


Figure 5.28.: Transmission infrared spectra of room temperature CO adsorption on the used catalysts (250 °C pretreatment and reaction) : (a) Au₁₁/CeO₂ (b) Biico Au₂₅/CeO₂, (c) Au₂₅/CeO₂ and (d) CeO₂. The red spectra were obtained during exposure of the sample to an atmosphere of 1% CO in He (50 ml/min total gas flow), the green spectra upon removal of gas phase CO by flowing 50 ml/min He. Au content in catalyst: Au₁₁/CeO₂ and Biico Au₂₅/CeO₂: 1.2 wt%, Au₂₅/CeO₂: 0.3 wt%.

5.8.6.5. Additional Infrared Spectra at Different Steps of the Reaction

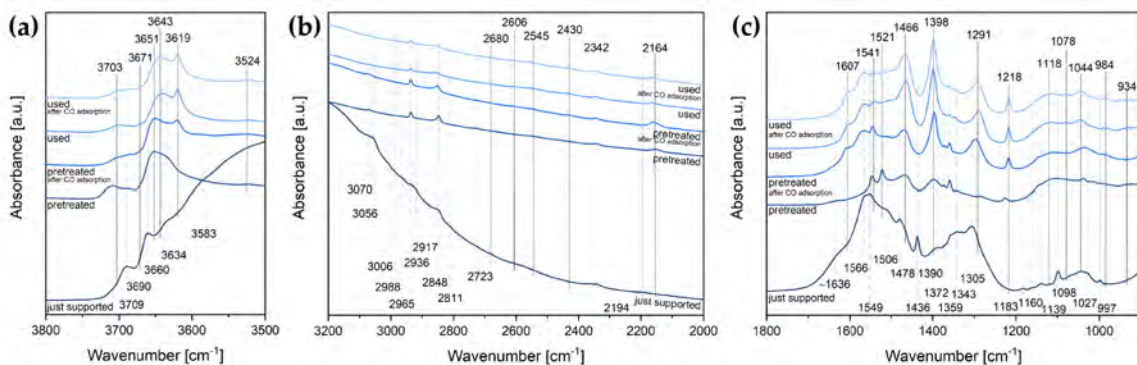


Figure 5.29.: Comparison of infrared absorption spectra of Au₁₁/CeO₂ in He at room temperature at different steps of the catalytic process: (a) 3800-3500 cm⁻¹, (b) 3200-2000 cm⁻¹ and (c) 1800-900 cm⁻¹. Decreasing bands are indicated by dotted lines and marked on the bottom, increasing ones by solid lines and marked on top. Au content in catalyst: 1.2 wt%.

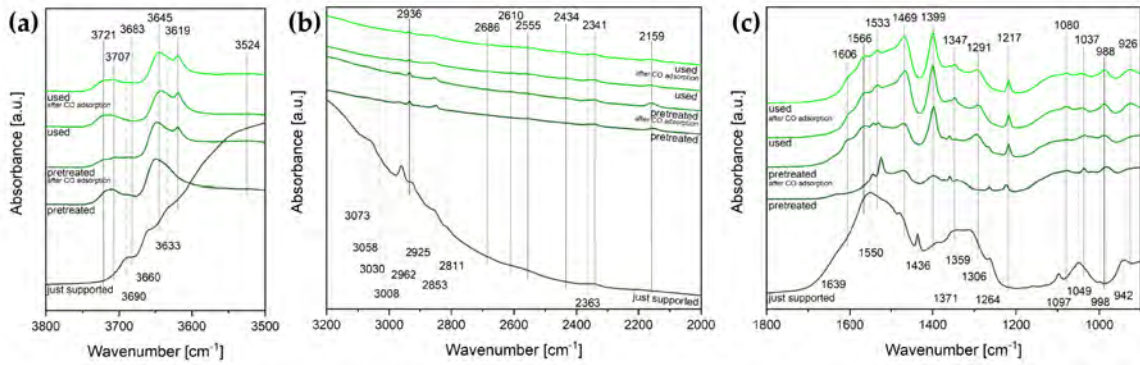


Figure 5.30.: Comparison of infrared absorption spectra of Biico Au₂₅/CeO₂ in He at room temperature at different steps of the catalytic process: (a) 3800-3500 cm⁻¹, (b) 3200-2000 cm⁻¹ and (c) 1800-900 cm⁻¹. Decreasing bands are indicated by dotted lines and marked on the bottom, increasing ones by solid lines and marked on top. Au content in catalyst: 1.2 wt%.

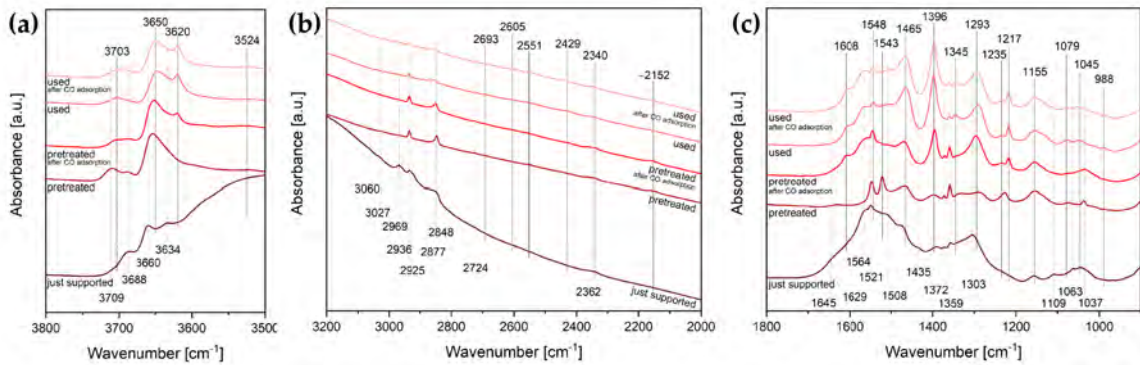


Figure 5.31.: Comparison of infrared absorption spectra of Au₂₅/CeO₂ in He at room temperature at different steps of the catalytic process: (a) 3800-3500 cm⁻¹, (b) 3200-2000 cm⁻¹ and (c) 1800-900 cm⁻¹. Decreasing bands are indicated by dotted lines and marked on the bottom, increasing ones by solid lines and marked on top. Au content in catalyst: 0.3 wt%.

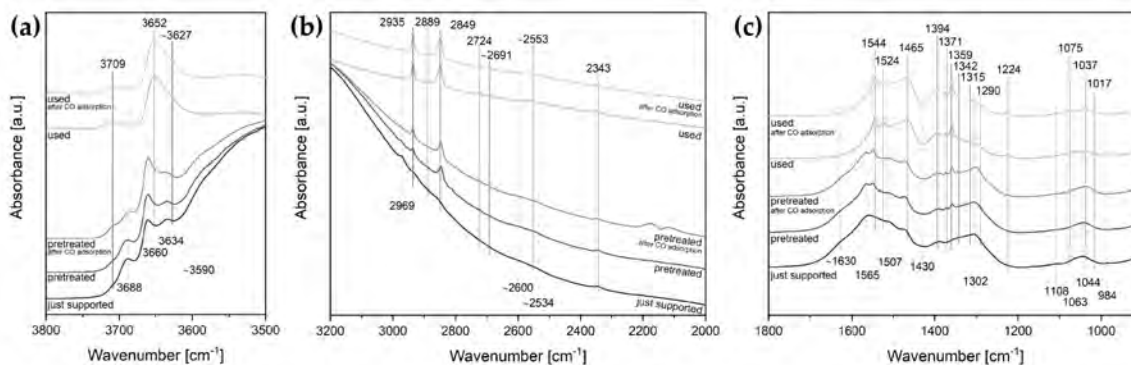


Figure 5.32.: Comparison of infrared absorption spectra of the CeO_2 support in He at room temperature at different steps of the catalytic process: (a) $3800\text{-}3500\text{ cm}^{-1}$, (b) $3200\text{-}2000\text{ cm}^{-1}$ and (c) $1800\text{-}900\text{ cm}^{-1}$. Decreasing bands are indicated by solid lines and marked on the bottom, increasing ones by solid lines and marked on top.

5.8.7. Additional High-angle Annular Dark-field Scanning Transmission Electron Microscopy

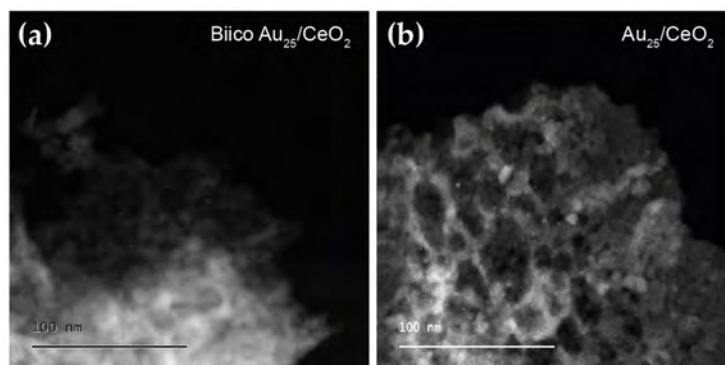


Figure 5.33.: Overview HAADF-STEM images of Biico $\text{Au}_{25}/\text{CeO}_2$ (a) and $\text{Au}_{25}/\text{CeO}_2$ (b) after pretreatment and reaction at $250\text{ }^\circ\text{C}$. Au content in catalyst: 1.2 wt%.

5.9. References

- [1] Lichen Liu and Avelino Corma. Metal Catalysts for Heterogeneous Catalysis: From Single Atoms to Nanoclusters and Nanoparticles. *Chemical Reviews*, 118(10):4981–5079, apr 2018. doi: 10.1021/acs.chemrev.7b00776.
- [2] Masatake Haruta. When Gold Is Not Noble: Catalysis by Nanoparticles. *The Chemical Record*, 3(2): 75–87, apr 2003. doi: 10.1002/tcr.10053.
- [3] Tamao Ishida, Toru Murayama, Ayako Taketoshi, and Masatake Haruta. Importance of Size and Contact Structure of Gold Nanoparticles for the Genesis of Unique Catalytic Processes. *Chemical Reviews*, 120(2):464–525, dec 2019. doi: 10.1021/acs.chemrev.9b00551.
- [4] Masatake Haruta, Tetsuhiko Kobayashi, Hiroshi Sano, and Nobumasa Yamada. Novel Gold Catalysts for the Oxidation of Carbon Monoxide at a Temperature far Below 0 °C. *Chemistry Letters*, 16(2):405–408, feb 1987. doi: 10.1246/cl.1987.405.
- [5] M. S. Chen and D. W. Goodman. The Structure of Catalytically Active Gold on Titania. *Science*, 306(5694):252–255, oct 2004. doi: 10.1126/science.1102420.
- [6] R. Meyer, C. Lemire, Sh. K. Shaikhutdinov, and H. J. Freund. Surface chemistry of catalysis by gold. *Gold Bulletin*, 37(1-2):72–124, mar 2004. doi: 10.1007/bf03215519.
- [7] B. Hammer and J. K. Norskov. Why gold is the noblest of all the metals. *Nature*, 376(6537):238–240, jul 1995. doi: 10.1038/376238a0.
- [8] Jun Fang, Bin Zhang, Qiaofeng Yao, Yang Yang, Jianping Xie, and Ning Yan. Recent advances in the synthesis and catalytic applications of ligand-protected, atomically precise metal nanoclusters. *Coordination Chemistry Reviews*, 322:1–29, sep 2016. doi: 10.1016/j.ccr.2016.05.003.
- [9] Yuanxin Du, Hongting Sheng, Didier Astruc, and Manzhou Zhu. Atomically Precise Noble Metal Nanoclusters as Efficient Catalysts: A Bridge between Structure and Properties. *Chemical Reviews*, 120(2): 526–622, mar 2019. doi: 10.1021/acs.chemrev.8b00726.
- [10] Tatsuya Higaki, Yingwei Li, Shuo Zhao, Qi Li, Site Li, Xiang-Sha Du, Sha Yang, Jinsong Chai, and Rongchao Jin. Atomically Tailored Gold Nanoclusters for Catalytic Application. *Angewandte Chemie International Edition*, 58(25):8291–8302, mar 2019. doi: 10.1002/anie.201814156.
- [11] Rongchao Jin, Gao Li, Sachil Sharma, Yingwei Li, and Xiangsha Du. Toward Active-Site Tailoring in Heterogeneous Catalysis by Atomically Precise Metal Nanoclusters with Crystallographic Structures. *Chemical Reviews*, 121(2):567–648, sep 2020. doi: 10.1021/acs.chemrev.0c00495.
- [12] Zhihe Liu, Zhennan Wu, Qiaofeng Yao, Yitao Cao, Osburg Jin Huang Chai, and Jianping Xie. Correlations between the fundamentals and applications of ultrasmall metal nanoclusters: Recent advances in catalysis and biomedical applications. *Nano Today*, 36:101053, feb 2021. doi: 10.1016/j.nantod.2020.101053.
- [13] Jianbo Zhao and Rongchao Jin. Heterogeneous catalysis by gold and gold-based bimetal nanoclusters. *Nano Today*, 18:86–102, feb 2018. doi: 10.1016/j.nantod.2017.12.009.
- [14] Tokuhisa Kawawaki, Ayano Ebina, Yasunaga Hosokawa, Shuhei Ozaki, Daiki Suzuki, Sakiat Hossain, and Yuichi Negishi. Thiolate-Protected Metal Nanoclusters: Recent Development in Synthesis, Understanding of Reaction, and Application in Energy and Environmental Field. *Small*, 17(27):2005328, feb 2021. doi: 10.1002/sml.202005328.

- [15] Rongchao Jin, Chenjie Zeng, Meng Zhou, and Yuxiang Chen. Atomically Precise Colloidal Metal Nanoclusters and Nanoparticles: Fundamentals and Opportunities. *Chemical Reviews*, 116(18):10346–10413, sep 2016. doi: 10.1021/acs.chemrev.5b00703.
- [16] Tokuhisa Kawawaki, Yukari Imai, Daiki Suzuki, Shun Kato, Ibuki Kobayashi, Taiyo Suzuki, Ryo Kaneko, Sakiat Hossain, and Yuichi Negishi. Atomically Precise Alloy Nanoclusters. *Chemistry – A European Journal*, 26(69):16150–16193, oct 2020. doi: 10.1002/chem.202001877.
- [17] Ricca Rahman Nasaruddin, Tiankai Chen, Ning Yan, and Jianping Xie. Roles of thiolate ligands in the synthesis, properties and catalytic application of gold nanoclusters. *Coordination Chemistry Reviews*, 368:60–79, aug 2018. doi: 10.1016/j.ccr.2018.04.016.
- [18] Sakiat Hossain, Yukari Imai, Daiki Suzuki, Woojun Choi, Zhaoheng Chen, Taiyo Suzuki, Mahiro Yoshioka, Tokuhisa Kawawaki, Dongil Lee, and Yuichi Negishi. Elucidating ligand effects in thiolate-protected metal clusters using $\text{Au}_{24}\text{Pt}(\text{TBBT})_{18}$ as a model cluster. *Nanoscale*, 11(45):22089–22098, 2019. doi: 10.1039/c9nr07117b.
- [19] Katsuaki Konishi. Phosphine-Coordinated Pure-Gold Clusters: Diverse Geometrical Structures and Unique Optical Properties/Responses. In *Structure and Bonding*, pages 49–86. Springer International Publishing, 2014. doi: 10.1007/430_2014_143.
- [20] Bihan Zhang, Jishi Chen, Yitao Cao, Osburg Jin Huang Chai, and Jianping Xie. Ligand Design in Ligand-Protected Gold Nanoclusters. *Small*, 17(27):2004381, jan 2021. doi: 10.1002/smll.202004381.
- [21] Yingwei Li, Yuxiang Chen, Stephen D. House, Shuo Zhao, Zahid Wahab, Judith C. Yang, and Rongchao Jin. Interface Engineering of Gold Nanoclusters for CO Oxidation Catalysis. *ACS Applied Materials & Interfaces*, 10(35):29425–29434, aug 2018. doi: 10.1021/acsami.8b07552.
- [22] Xian-Kai Wan, Jia-Qi Wang, Zi-Ang Nan, and Quan-Ming Wang. Ligand effects in catalysis by atomically precise gold nanoclusters. *Science Advances*, 3(10), oct 2017. doi: 10.1126/sciadv.1701823.
- [23] Yuxiang Chen, Chong Liu, Qing Tang, Chenjie Zeng, Tatsuya Higaki, Anindita Das, De en Jiang, Nathaniel L. Rosi, and Rongchao Jin. Isomerism in $\text{Au}_{28}(\text{SR})_{20}$ Nanocluster and Stable Structures. *Journal of the American Chemical Society*, 138(5):1482–1485, jan 2016. doi: 10.1021/jacs.5b12094.
- [24] Ying-Zhou Li and Weng Kee Leong. A comparative study on atomically precise Au nanoclusters as catalysts for the aldehyde–alkyne–amine (A3) coupling reaction: ligand effects on the nature of the catalysis and efficiency. *RSC Advances*, 9(10):5475–5479, 2019. doi: 10.1039/c9ra00933g.
- [25] Yanan Wang and Thomas Bürgi. Ligand exchange reactions on thiolate-protected gold nanoclusters. *Nanoscale Advances*, 3(10):2710–2727, 2021. doi: 10.1039/d1na00178g.
- [26] Shubo Tian, Yitao Cao, Tiankai Chen, Shuangquan Zang, and Jianping Xie. Ligand-protected atomically precise gold nanoclusters as model catalysts for oxidation reactions. *Chemical Communications*, 56(8): 1163–1174, 2020. doi: 10.1039/c9cc08215h.
- [27] Alessandro Longo, Ewoud J. J. Boed, Nisha Mammen, Marte Linden, Karoliina Honkala, Hannu Häkkinen, Petra E. Jongh, and Baira Donoeva. Towards Atomically Precise Supported Catalysts from Monolayer-Protected Clusters: The Critical Role of the Support. *Chemistry – A European Journal*, 26(31):7051–7058, apr 2020. doi: 10.1002/chem.202000637.
- [28] Clara García, Stephan Pollitt, Marte van der Linden, Vera Truttman, Christoph Rameshan, Rafael Rameshan, Ernst Pittenauer, Günter Allmaier, Peter Kregsamer, Michael Stöger-Pollach, Noelia Barrabés, and Günther Rupprechter. Support effect on the reactivity and stability of $\text{Au}_{25}(\text{SR})_{18}$ and

Au₁₄₄(SR)₆₀ nanoclusters in liquid phase cyclohexane oxidation. *Catalysis Today*, 336:174–185, oct 2019. doi: 10.1016/j.cattod.2018.12.013.

- [29] Yan Zhu, Huifeng Qian, and Rongchao Jin. An Atomic-Level Strategy for Unraveling Gold Nanocatalysis from the Perspective of Au_n(SR)_m Nanoclusters. *Chemistry - A European Journal*, 16(37):11455–11462, aug 2010. doi: 10.1002/chem.201001086.
- [30] Yongmei Liu, Hironori Tsunoyama, Tomoki Akita, Songhai Xie, and Tatsuya Tsukuda. Aerobic Oxidation of Cyclohexane Catalyzed by Size-Controlled Au Clusters on Hydroxyapatite: Size Effect in the Sub-2 nm Regime. *ACS Catalysis*, 1(1):2–6, dec 2010. doi: 10.1021/cs100043j.
- [31] Dan Yang and Yan Zhu. Evolution of catalytic activity driven by structural fusion of icosahedral gold cluster cores. *Chinese Journal of Catalysis*, 42(2):245–250, feb 2021. doi: 10.1016/s1872-2067(20)63659-2.
- [32] Yan ZHU, Huifeng QIAN, Anindita DAS, and Rongchao JIN. Comparison of the Catalytic Properties of 25-Atom Gold Nanospheres and Nanorods. *Chinese Journal of Catalysis*, 32(6-8):1149–1155, jan 2011. doi: 10.1016/s1872-2067(10)60238-0.
- [33] Wataru Kurashige, Rui Hayashi, Kosuke Wakamatsu, Yuki Kataoka, Sakiat Hossain, Akihide Iwase, Akihiko Kudo, Seiji Yamazoe, and Yuichi Negishi. Atomic-Level Understanding of the Effect of Heteroatom Doping of the Cocatalyst on Water-Splitting Activity in AuPd or AuPt Alloy Cluster-Loaded BaLa₄Ti₄O₁₅. *ACS Applied Energy Materials*, 2(6):4175–4187, may 2019. doi: 10.1021/acsaeam.9b00426.
- [34] Clara Garcia, Vera Truttman, Irene Lopez, Thomas Haunold, Carlo Marini, Christoph Rameshan, Ernst Pittenauer, Peter Kregsamer, Klaus Dobrezberger, Michael Stöger-Pollach, Noelia Barrabés, and Günther Rupprechter. Dynamics of Pd Dopant Atoms inside Au Nanoclusters during Catalytic CO Oxidation. *The Journal of Physical Chemistry C*, 124(43):23626–23636, oct 2020. doi: 10.1021/acs.jpcc.0c05735.
- [35] Weili Li, Chao Liu, Hadi Abroshan, Qingjie Ge, Xiujuan Yang, Hengyong Xu, and Gao Li. Catalytic CO Oxidation Using Bimetallic M_xAu_{25-x} Clusters: A Combined Experimental and Computational Study on Doping Effects. *The Journal of Physical Chemistry C*, 120(19):10261–10267, may 2016. doi: 10.1021/acs.jpcc.6b00793.
- [36] Atal Shivhare and Robert W.J. Scott. Au₂₅ clusters as precursors for the synthesis of AuPd bimetallic nanoparticles with isolated atomic Pd-surface sites. *Molecular Catalysis*, 457:33–40, oct 2018. doi: 10.1016/j.mcat.2018.07.015.
- [37] Irene López-Hernández, Vera Truttman, Clara Garcia, Christian Witte Lopes, Christoph Rameshan, Michael Stöger-Pollach, Noelia Barrabés, Günther Rupprechter, Fernando Rey, and A. Eduardo Palomares. AgAu nanoclusters supported on zeolites: Structural dynamics during CO oxidation. *Catalysis Today*, 384-386:166–176, feb 2022. doi: 10.1016/j.cattod.2021.04.016.
- [38] Xiaotao Nie, Huifeng Qian, Qingjie Ge, Hengyong Xu, and Rongchao Jin. CO Oxidation Catalyzed by Oxide-Supported Au₂₅(SR)₁₈ Nanoclusters and Identification of Perimeter Sites as Active Centers. *ACS Nano*, 6(7):6014–6022, jun 2012. doi: 10.1021/nn301019f.
- [39] Zili Wu, Guoxiang Hu, De en Jiang, David R. Mullins, Qian-Fan Zhang, Lawrence F. Allard, Lai-Sheng Wang, and Steven H. Overbury. Diphosphine-Protected Au₂₂ Nanoclusters on Oxide Supports Are Active for Gas-Phase Catalysis without Ligand Removal. *Nano Letters*, 16(10):6560–6567, oct 2016. doi: 10.1021/acs.nanolett.6b03221.
- [40] Jacob Good, Paul N. Duchesne, Peng Zhang, William Koshut, Meng Zhou, and Rongchao Jin. On the functional role of the cerium oxide support in the Au₃₈(SR)₂₄/CeO₂ catalyst for CO oxidation. *Catalysis Today*, 280:239–245, feb 2017. doi: 10.1016/j.cattod.2016.04.016.

- [41] Bei Zhang, Clara García, Annelies Sels, Giovanni Salassa, Christoph Rameshan, Jordi Llorca, Klaudia Hradil, Günther Rupprechter, Noelia Barrabés, and Thomas Bürgi. Ligand and support effects on the reactivity and stability of Au₃₈(SR)₂₄ catalysts in oxidation reactions. *Catalysis Communications*, 130: 105768, oct 2019. doi: 10.1016/j.catcom.2019.105768.
- [42] Guicen Ma, Andrew Binder, Miaofang Chi, Chao Liu, Rongchao Jin, De en Jiang, Jie Fan, and Sheng Dai. Stabilizing gold clusters by heterostructured transition-metal oxide–mesoporous silica supports for enhanced catalytic activities for CO oxidation. *Chemical Communications*, 48(93):11413, 2012. doi: 10.1039/c2cc35787a.
- [43] Zili Wu, David R. Mullins, Lawrence F. Allard, Qianfan Zhang, and Laisheng Wang. CO oxidation over ceria supported Au₂₂ nanoclusters: Shape effect of the support. *Chinese Chemical Letters*, 29(6):795–799, jun 2018. doi: 10.1016/j.ccllet.2018.01.038.
- [44] Zili Wu, De en Jiang, Amanda K. P. Mann, David R. Mullins, Zhen-An Qiao, Lawrence F. Allard, Chenjie Zeng, Rongchao Jin, and Steven H. Overbury. Thiolate Ligands as a Double-Edged Sword for CO Oxidation on CeO₂ Supported Au₂₅(SCH₂CH₂Ph)₁₈ Nanoclusters. *Journal of the American Chemical Society*, 136(16):6111–6122, apr 2014. doi: 10.1021/ja5018706.
- [45] V. Sudheeshkumar, Kazeem O. Sulaiman, and Robert W. J. Scott. Activation of atom-precise clusters for catalysis. *Nanoscale Advances*, 2(1):55–69, 2020. doi: 10.1039/c9na00549h.
- [46] Xiaotao Nie, Chenjie Zeng, Xiangang Ma, Huifeng Qian, Qingjie Ge, Hengyong Xu, and Rongchao Jin. CeO₂-supported Au₃₈(SR)₂₄ nanocluster catalysts for CO oxidation: a comparison of ligand-on and -off catalysts. *Nanoscale*, 5(13):5912, 2013. doi: 10.1039/c3nr00970j.
- [47] Weili Li, Qingjie Ge, Xiangang Ma, Yuxiang Chen, Manzhou Zhu, Hengyong Xu, and Rongchao Jin. Mild activation of CeO₂-supported gold nanoclusters and insight into the catalytic behavior in CO oxidation. *Nanoscale*, 8(4):2378–2385, 2016. doi: 10.1039/c5nr07498c.
- [48] Daria A. Pichugina, Nadezhda A. Nikitina, and Nikolay E. Kuzmenko. On the Mechanism of the Reaction between Thiolate-Protected Gold Clusters and Molecular Oxygen: What is Activated? *The Journal of Physical Chemistry C*, 124(5):3080–3086, jan 2020. doi: 10.1021/acs.jpcc.9b10286.
- [49] Stephan Pollitt, Vera Truttman, Thomas Haunold, Clara Garcia, Wojciech Olszewski, Jordi Llorca, Noelia Barrabés, and Günther Rupprechter. The Dynamic Structure of Au₃₈(SR)₂₄ Nanoclusters Supported on CeO₂ upon Pretreatment and CO Oxidation. *ACS Catalysis*, 10(11):6144–6148, may 2020. doi: 10.1021/acscatal.0c01621.
- [50] Bei Zhang, Annelies Sels, Giovanni Salassa, Stephan Pollitt, Vera Truttman, Christoph Rameshan, Jordi Llorca, Wojciech Olszewski, Günther Rupprechter, Thomas Bürgi, and Noelia Barrabés. Ligand Migration from Cluster to Support: A Crucial Factor for Catalysis by Thiolate-protected Gold Clusters. *ChemCatChem*, 10(23):5372–5376, nov 2018. doi: 10.1002/cctc.201801474.
- [51] Tokuhisa Kawawaki, Yuki Kataoka, Momoko Hirata, Yuki Akinaga, Ryo Takahata, Kosuke Wakamatsu, Yu Fujiki, Miori Kataoka, Soichi Kikkawa, Abdulrahman S. Alotabi, Sakiat Hossain, D. J. Osborn, Toshiharu Teranishi, Gunther G. Andersson, Gregory F. Metha, Seiji Yamazoe, and Yuichi Negishi. Creation of High-Performance Heterogeneous Photocatalysts by Controlling Ligand Desorption and Particle Size of Gold Nanocluster. *Angewandte Chemie International Edition*, 60(39):21340–21350, jul 2021. doi: 10.1002/anie.202104911.
- [52] Michael Walter, Jaakko Akola, Olga Lopez-Acevedo, Pablo D. Jadzinsky, Guillermo Calero, Christopher J. Ackerson, Robert L. Whetten, Henrik Gronbeck, and Hannu Häkkinen. A unified view of ligand-protected gold clusters as superatom complexes. *Proceedings of the National Academy of Sciences*, 105(27):9157–9162, jul 2008. doi: 10.1073/pnas.0801001105.

- [53] Xi Kang, Hanbao Chong, and Manzhou Zhu. Au₂₅SR₁₈: the captain of the great nanocluster ship. *Nanoscale*, 10(23):10758–10834, 2018. doi: 10.1039/c8nr02973c.
- [54] Lallie C. McKenzie, Tatiana O. Zaikova, and James E. Hutchison. Structurally Similar Triphenylphosphine-Stabilized Undecagolds, Au₁₁(PPh₃)₇Cl₃ and [Au₁₁(PPh₃)₈Cl₂]Cl, Exhibit Distinct Ligand Exchange Pathways with Glutathione. *Journal of the American Chemical Society*, 136(38):13426–13435, sep 2014. doi: 10.1021/ja5075689.
- [55] Yukatsu Shichibu, Yuichi Negishi, Takahito Watanabe, Nirmalya K. Chaki, Hiroyuki Kawaguchi, and Tatsuya Tsukuda. Biicosahedral Gold Clusters [Au₂₅(PPh₃)₁₀(SC_nH)_{(2n+1)5}Cl₂]²⁺ (n = 2-18): A Stepping Stone to Cluster-Assembled Materials. *The Journal of Physical Chemistry C*, 111(22):7845–7847, may 2007. doi: 10.1021/jp073101t.
- [56] Lakshmi V. Nair, Sakiat Hossain, Shunjiro Takagi, Yukari Imai, Guoxiang Hu, Shota Wakayama, Bharat Kumar, Wataru Kurashige, De en Jiang, and Yuichi Negishi. Hetero-biicosahedral [Au₂₄Pd(PPh₃)₁₀(SC₂H₄Ph)₅Cl₂]²⁺ nanocluster: selective synthesis and optical and electrochemical properties. *Nanoscale*, 10(40):18969–18979, 2018. doi: 10.1039/c8nr04078h.
- [57] Manzhou Zhu, Christine M. Aikens, Frederick J. Hollander, George C. Schatz, and Rongchao Jin. Correlating the Crystal Structure of A Thiol-Protected Au₂₅ Cluster and Optical Properties. *Journal of the American Chemical Society*, 130(18):5883–5885, apr 2008. doi: 10.1021/ja801173r.
- [58] Georgi N. Vayssilov, Mihail Mihaylov, Petko St. Petkov, Konstantin I. Hadjiivanov, and Konstantin M. Neyman. Reassignment of the Vibrational Spectra of Carbonates, Formates, and Related Surface Species on Ceria: A Combined Density Functional and Infrared Spectroscopy Investigation. *The Journal of Physical Chemistry C*, 115(47):23435–23454, nov 2011. doi: 10.1021/jp208050a.
- [59] Claude Binet, Marco Daturi, and Jean-Claude Lavalley. IR study of polycrystalline ceria properties in oxidised and reduced states. *Catalysis Today*, 50(2):207–225, apr 1999. doi: 10.1016/s0920-5861(98)00504-5.
- [60] Kohei Yoshikawa, Hiroki Sato, Masato Kaneeda, and Junko Nomura Kondo. Synthesis and analysis of CO₂ adsorbents based on cerium oxide. *Journal of CO₂ Utilization*, 8:34–38, dec 2014. doi: 10.1016/j.jcou.2014.10.001.
- [61] A. López Cámara, S. Chansai, C. Hardacre, and A. Martínez-Arias. The water–gas shift reaction over CeO₂/CuO: Operando SSITKA–DRIFTS–mass spectrometry study of low temperature mechanism. *International Journal of Hydrogen Energy*, 39(8):4095–4101, mar 2014. doi: 10.1016/j.ijhydene.2013.05.087.
- [62] Zhibo Ren, Fei Peng, Jianwei Li, Xin Liang, and Biaohua Chen. Morphology-Dependent Properties of Cu/CeO₂ Catalysts for the Water-Gas Shift Reaction. *Catalysts*, 7(12):48, feb 2017. doi: 10.3390/catal7020048.
- [63] Karin Föttinger, Robert Schlögl, and Günther Rupprechter. The mechanism of carbonate formation on pd–Al₂O₃ catalysts. *Chem. Commun.*, (3):320–322, 2008. doi: 10.1039/b713161e.
- [64] M. Waqif, P. Bazin, O. Saur, J.C. Lavalley, G. Blanchard, and O. Touret. Study of ceria sulfation. *Applied Catalysis B: Environmental*, 11(2):193–205, feb 1997. doi: 10.1016/s0926-3373(96)00040-9.
- [65] Qiguang Dai, Zhiyong Zhang, Jiaorong Yan, Jinyan Wu, Grayson Johnson, Wei Sun, Xingyi Wang, Sen Zhang, and Wangcheng Zhan. Phosphate-functionalized CeO₂ nanosheets for efficient catalytic oxidation of dichloromethane. *Environmental Science & Technology*, 52(22):13430–13437, oct 2018. doi: 10.1021/acs.est.8b05002.

- [66] André Fielicke, Gert von Helden, Gerard Meijer, David B. Pedersen, Benoit Simard, and David M. Rayner. Gold Cluster Carbonyls: Saturated Adsorption of CO on Gold Cluster Cations, Vibrational Spectroscopy, and Implications for Their Structures. *Journal of the American Chemical Society*, 127(23): 8416–8423, may 2005. doi: 10.1021/ja0509230.
- [67] Hannu Häkkinen, Michael Walter, and Henrik Grönbeck. Divide and Protect: Capping Gold Nanoclusters with Molecular Gold-Thiolate Rings. *The Journal of Physical Chemistry B*, 110(20):9927–9931, apr 2006. doi: 10.1021/jp0619787.
- [68] Stefan Knoppe and Thomas Bürgi. Chirality in Thiolate-Protected Gold Clusters. *Accounts of Chemical Research*, 47(4):1318–1326, mar 2014. doi: 10.1021/ar400295d.
- [69] Changjun Zhang, Angelos Michaelides, David A. King, and Stephen J. Jenkins. Positive Charge States and Possible Polymorphism of Gold Nanoclusters on Reduced Ceria. *Journal of the American Chemical Society*, 132(7):2175–2182, jan 2010. doi: 10.1021/ja906687f.
- [70] David P. Anderson, Jason F. Alvino, Alexander Gentleman, Hassan Al Qahtani, Lars Thomsen, Matthew I. J. Polson, Gregory F. Metha, Vladimir B. Golovko, and Gunther G. Andersson. Chemically-synthesised, atomically-precise gold clusters deposited and activated on titania. *Physical Chemistry Chemical Physics*, 15(11):3917, 2013. doi: 10.1039/c3cp44005b.
- [71] David P. Anderson, Rohul H. Adnan, Jason F. Alvino, Oliver Shipper, Baira Donoeva, Jan-Yves Ruzicka, Hassan Al Qahtani, Hugh H. Harris, Bruce Cowie, Jade B. Aitken, Vladimir B. Golovko, Gregory F. Metha, and Gunther G. Andersson. Chemically synthesised atomically precise gold clusters deposited and activated on titania. Part II. *Physical Chemistry Chemical Physics*, 15(35):14806, 2013. doi: 10.1039/c3cp52497c.
- [72] Yuri Suchorski, Sergey M. Kozlov, Ivan Bepalov, Martin Datler, Diana Vogel, Zuzana Budinska, Konstantin M. Neyman, and Günther Rupprechter. The role of metal/oxide interfaces for long-range metal particle activation during CO oxidation. *Nature Materials*, 17(6):519–522, may 2018. doi: 10.1038/s41563-018-0080-y.
- [73] Günther Rupprechter. Operando Surface Spectroscopy and Microscopy during Catalytic Reactions: From Clusters via Nanoparticles to Meso-Scale Aggregates. *Small*, 17(27):2004289, mar 2021. doi: 10.1002/smll.202004289.
- [74] Paul A. Bartlett, Barr Bauer, and S. J. Singer. Synthesis of water-soluble undecagold cluster compounds of potential importance in electron microscopic and other studies of biological systems. *Journal of the American Chemical Society*, 100(16):5085–5089, aug 1978. doi: 10.1021/ja00484a029.
- [75] Atal Shivhare, Stephen J. Ambrose, Haixia Zhang, Randy W. Purves, and Robert W. J. Scott. Stable and recyclable Au₂₅ clusters for the reduction of 4-nitrophenol. *Chem. Commun.*, 49(3):276–278, 2013. doi: 10.1039/c2cc37205c.
- [76] Gerd H. Woehrle, Marvin G. Warner, and James E. Hutchison. Ligand Exchange Reactions Yield Subnanometer, Thiol-Stabilized Gold Particles with Defined Optical Transitions. *The Journal of Physical Chemistry B*, 106(39):9979–9981, sep 2002. doi: 10.1021/jp025943s.
- [77] Eric F. Pettersen, Thomas D. Goddard, Conrad C. Huang, Gregory S. Couch, Daniel M. Greenblatt, Elaine C. Meng, and Thomas E. Ferrin. UCSF Chimera – A visualization system for exploratory research and analysis. *Journal of Computational Chemistry*, 25(13):1605–1612, 2004. doi: 10.1002/jcc.20084.
- [78] Vera Truttmann, Stephan Pollitt, Hedda Drexler, Sreejith P. Nandan, Dominik Eder, Noelia Barrabés, and Günther Rupprechter. Selective ligand exchange synthesis of Au₁₆(2-PET)₁₄ from Au₁₅(SG)₁₃. *The Journal of Chemical Physics*, 155(16):161102, oct 2021. doi: 10.1063/5.0062534.

- [79] Amala Dass, Anthony Stevenson, George R. Dubay, Joseph B. Tracy, and Royce W. Murray. Nanoparticle MALDI-TOF Mass Spectrometry without Fragmentation: $\text{Au}_{25}(\text{SCH}_2\text{CH}_2\text{Ph})_{18}$ and Mixed Monolayer $\text{Au}_{25}(\text{SCH}_2\text{CH}_2\text{Ph})_{18-x}(\text{L})_x$. *Journal of the American Chemical Society*, 130(18):5940–5946, apr 2008. doi: 10.1021/ja710323t.

6. Conclusions and Outlook

The impact of protecting ligands on Au nanoclusters has been evaluated, focusing on three main areas: induction of chirality, influence in synthesis/ligand exchange procedures and heterogeneous CO oxidation.

Regarding **(chiral) properties of a test set of Au nanoclusters with a chiral thiol ligand**, (*S*)-2-methylbutanethiol (2-MeBuSH) has been employed in the direct synthesis of Au₂₅, Au₃₈ and Au₁₄₄. The three clusters all exhibited pronounced circular dichroism (CD) signals, which increased in the order Au₂₅ < Au₃₈ < Au₁₄₄. This is consistent with the intrinsically chiral Au₃₈ and Au₁₄₄ being present as single enantiomers, indicating that the chiral ligand is capable of directing the chirality of the overall cluster structure. Moreover, a shift in the typical product distribution after synthesis toward intrinsically chiral clusters was observed for Au₂₅ and Au₁₄₄, corroborating this hypothesis. Furthermore, it was also experimentally demonstrated that Au₁₄₄ produces a significantly stronger CD signal than Au₃₈, which is consistent with earlier theoretical calculations of other authors.

The optical absorption spectra of 2-MeBuS-protected Au₃₈ clusters simulated with time dependent-density functional theory plus tight binding (TD-DFT+TB) were in good agreement with the experimental spectra. Moreover, a comparison of the CD spectra of the two possible Au₃₈ stereoisomers clearly indicated that the isomer with the -S(R)-(Au-S(R))₂-staples in a counter-clockwise arrangement seems to be preferentially formed. However, at the same time, higher energies were calculated for this isomer compared to its clockwise-counterpart, which is contradicting the favorable formation. Thus, further refinement of the model will be undertaken to determine if the same can also be observed for isomers optimized at a different level of theory. It is also possible that kinetic rather than thermodynamic effects in the synthesis are responsible for this discrepancy.

The second objective, namely developing **synthesis strategies for Au nanoclusters**, has been addressed in two different projects: Within the set of experiments employing the chiral ligand 2-MeBuSH, a suprisingly high yield was achieved for both intrinsically chiral clusters, Au₃₈ and Au₁₄₄ compared to reported values by other authors. Thus, this study presents an important first step toward direct synthesis of enantiopure chiral Au nanoclusters in quantities that enable practical applications. It also avoids post-synthetic separation steps e.g. by chiral high-performance liquid chromatography, which require individual method development for each new cluster species and can only be used for low quantities. Moreover, the chiral ligand 2-MeBuSH can be obtained from a commercially available precursor in

a simple two-step procedure, making the overall approach very economical. In a next step, 2-MeBuSH should be employed to synthesize other clusters known to exhibit intrinsic chirality, thus probing its suitability for broader application in metal nanocluster chemistry. A second synthesis strategy involves the preparation of $\text{Au}_{16}(\text{2-PET})_{14}$ from $\text{Au}_{15}(\text{SG})_{13}$ in a two-phase ligand-exchange-induced size/structure transformation (LEIST) process. $\text{Au}_{16}(\text{2-PET})_{14}$ proved to be very stable in presence of large quantities of exchange thiols, which also seemed to be the key factor for its selective formation. This cluster species has not been accessible by direct synthesis from Au salt precursors so far and reports on organic thiolate-protected Au nanoclusters with less than 20 Au atoms are still scarce. Therefore, this LEIST synthesis of $\text{Au}_{16}(\text{2-PET})_{14}$ contributes to the understanding of gold nanocluster structure evolution. Of note, while the composition and charge state of this cluster was determined by mass spectrometry, its crystal structure still has to be elucidated in future studies.

Finally, the **influence of protecting ligands on immobilized Au nanocluster catalysts** was investigated for a Au_{11} , biicosahedral Au_{25} and Au_{25} supported on CeO_2 in heterogeneous CO oxidation. Thereby, the impact of the protecting ligands was investigated using clusters with different ligand shell compositions: thiolates, phosphines, and a mixture of both. The changes of the catalyst systems during oxidative pretreatment at 250 °C were monitored by *in situ* transmission infrared (IR) measurements, revealing (partial) disintegration of the protecting ligands for all clusters. However, in all cases, decomposition products were detected as adsorbates on the support. The only-thiolate protected Au_{25} cluster catalyst then showed significantly higher activity in subsequent CO oxidation compared to the clusters containing phosphines in their ligand shell. Since it was determined that size and CO adsorption capability of the Au particles were not the key factors determining the reactivity of the catalysts, this discrepancy was attributed to phosphine ligand residues blocking the Au-support interfacial sites, which are crucial for the reaction. This demonstrates that the nature of the ligands must be taken into consideration in the design of the catalyst system, even if they are to be removed during activation prior to the reaction, since their decomposition products may also have an influence on the activity.

Appendix

A. Further Publications During PhD Studies

The publications below correspond to projects in which V.T. was significantly involved in both experimental work (such as cluster synthesis and characterization, XAFS measurements or kinetic tests), data evaluation/interpretation and preparation of the manuscript. The complete list of publications at present can be found in the appendix to the CV at the end of this document.

Ligand engineering of immobilized nanoclusters on surfaces: ligand exchange reactions with supported Au₁₁(PPh₃)₇Br₃

Vera Truttmann, Christopher Herzig, Ivonne Illes, Andreas Limbeck, Ernst Pittenauer, Michael Stöger-Pollach, Günter Allmaier, Thomas Bürgi, Noelia Barrabés and Günther Rupprechter

The properties of gold nanoclusters, apart from being size-dependent, are strongly related to the nature of the protecting ligand. Ligand exchange on Au nanoclusters has been proven to be a powerful tool for tuning their properties, but has so far been limited to dissolved clusters in solution. By supporting the clusters previously functionalized in solution, it is uncertain that the functionality is still accessible once the cluster is on the surface. This may be overcome by introducing the desired functionality by ligand exchange after the cluster deposition on the support material. We herein report the first successful ligand exchange on supported (immobilized) Au₁₁ nanoclusters. Dropcast films of Au₁₁(PPh₃)₇Br₃ on planar oxide surfaces were shown to react with thiol ligands, resulting in clusters with a mixed ligand shell, with both phosphines and thiolates being present. Laser ablation inductively coupled plasma mass spectrometry and infrared spectroscopy confirmed that the exchange just takes place on the cluster dropcast. Contrary to systems in solution, the size of the clusters did not increase during ligand exchange. Different structures/compounds were formed depending on the nature of the incoming ligand. The feasibility to extend ligand engineering to supported nanoclusters is proven and it may allow controlled nanocluster functionalization.

Nanoscale, 12, 12809–12816 (2020)

<https://doi.org/10.1039/C9NR10353H>

Collaboration within research group (C. García):

Dynamics of Pd Dopant Atoms inside Au Nanoclusters during Catalytic CO Oxidation

Clara García⁺, Vera Truttmann⁺, Irene López, Thomas Haunold, Carlo Marini, Christoph Rameshan, Ernst Pittenauer, Peter Kregsamer, Klaus Dobrezberger, Michael Stöger-Pollach, Noelia Barrabés and Günther Rupprechter

⁺These authors contributed equally.

Doping gold nanoclusters with palladium has been reported to increase their catalytic activity and stability. PdAu₂₄ nanoclusters, with the Pd dopant atom located at the center of the Au cluster core, were supported on titania and applied in catalytic CO oxidation, showing significantly higher activity than supported monometallic Au₂₅ nanoclusters. After pretreatment, *operando* DRIFTS spectroscopy detected CO adsorbed on Pd during CO oxidation, indicating migration of the Pd dopant atom from the Au cluster core to the cluster surface. Increasing the number of Pd dopant atoms in the Au structure led to incorporation of Pd mostly in the S-(M-S)_n protecting staples, as evidenced by *in situ* XAFS. A combination of oxidative and reductive thermal pretreatment resulted in the formation of isolated Pd surface sites within the Au surface. The combined analysis of *in situ* XAFS, *operando* DRIFTS, and *ex situ* XPS thus revealed the structural evolution of bimetallic PdAu nanoclusters, yielding a Pd single-site catalyst of 2.7 nm average particle size with improved CO oxidation activity.

J. Phys. Chem. C, 124, 43, 23626–23636 (2020)

<https://doi.org/10.1021/acs.jpcc.0c05735>

Collaboration with ITQ Valencia (I. López-Hernández, A.E. Palomares, F. Rey):

AgAu nanoclusters supported on zeolites: Structural dynamics during CO oxidation

Irene López-Hernández, Vera Truttmann, Clara García, Christian Wittee Lopes, Christoph Rameshan, Michael Stöger-Pollach, Noelia Barrabés, Günther Rupprechter, Fernando Rey, Antonio Eduardo Palomares

The bimetallic nanocluster catalyst structure can change during pretreatment and reaction, thus *in situ* characterization techniques are required for a proper analysis of the active sites. *In situ* XAFS and DRIFTS were used to study the dynamic evolution

of the metal active sites in bimetallic $\text{Ag}_x\text{Au}_{25-x}$ nanoclusters supported on ITQ2 zeolite during CO catalytic oxidation. The activity of the bimetallic nanocluster catalyst in this reaction was significantly higher than those of supported monometallic Ag_{25} and Au_{25} nanoclusters. These results were explained by the formation of AgAu alloyed nanoparticles, which favoured reactant adsorption and reaction. Furthermore, the initial activity depended on the catalyst pretreatment, obtaining better conversion, at lower temperatures, with the catalyst pretreated with hydrogen than with the catalyst pretreated with oxygen. This was also associated with an easier formation of a AgAu alloy under hydrogen pretreatment at 150 °C. However, the alloying process seemed to be completed after reaction in both cases, i.e. for the catalyst pretreated with oxygen and with hydrogen, obtaining the same catalytic performance with both catalysts upon reuse. The activity is constant in successive reaction runs, indicating high stability of the active species formed under reaction conditions. The results have shown that the combination of catalytic studies with in situ characterization techniques provides insight into the structural dynamics of the catalysts during activation and reaction.

Catalysis Today, 384–386, 166–176 (2022)
<https://doi.org/10.1016/j.cattod.2021.04.016>

Gold nanoclusters supported on different materials as catalysts for the selective alkyne semihydrogenation

Irene López-Hernández, Vera Truttmann, Noelia Barrabés, Günther Rupprechter, Fernando Rey, Jesus Mengual, Antonio Eduardo Palomares

Catalysts based on gold nanoclusters supported by different materials have been used for the selective semihydrogenation of phenylacetylene to styrene. The most active species were formed by catalyst thermal activation in a reductive atmosphere. It is shown that the activity and selectivity of these catalysts is mainly controlled by the interaction of the gold nanoclusters with the support, as demonstrated by using materials with high surface area and different acidity/basicity, i.e. MgO, Al_2O_3 and Mg/Al hydrotalcite. There is an important influence of the acid/base properties of the support on the selectivity. Higher activity is obtained for gold supported on basic materials (MgO and hydrotalcite) and the best results are obtained with the Au catalyst supported on the MgAl hydrotalcite exhibiting high activity and the best selectivity to the alkene. This was explained by the intermediate basicity of the support that favors the heterolytic cleavage of H_2 while avoiding the overreduction of the alkynes to alkanes.

submitted to *Catalysis Today* on 9 April 2021, in review

B. Information on Images in Introduction and Chapter Title Pages

Unless noted otherwise, the molecular graphics were created using the UCSF Chimera software^[1], developed by the Resource for Biocomputing, Visualization, and Informatics at the University of California, San Francisco, with support from NIH P41-GM103311. If no reference is mentioned, the represented structures were generated using the commercial software packages ChemDraw or ChemDoodle. In some cases, editing of nanocluster structures was performed with MacMolPlt^[2].

Figure 1.2:

The following crystal structures were used to create the molecular structures in this image: $\text{Au}_{11}(\text{PPh}_3)_7\text{Cl}_3$ ^[3] and $[\text{Au}_{25}(\text{SC}_2\text{H}_4\text{Ph})_{18}]\text{TOA}$ ^[4].

Figure 1.3:

The following crystal structures were used to create the molecular structures in this image: $\text{Au}_{11}(\text{PPh}_3)_7\text{Cl}_3$ ^[3], $[\text{Au}_{25}(\text{PPh}_3)_{10}(\text{SC}_2\text{H}_5)_5\text{Cl}_2](\text{SbF}_6)_2$ ^[5], $\text{Au}_{25}(\text{SC}_2\text{H}_5)_{18}$ ^[6] and $\text{Au}_{38}(\text{SC}_2\text{H}_4\text{Ph})_{24}$ ^[7].

Figure 1.5:

The following crystal structure was used to create the molecular structure in this image: $\text{Au}_{11}(\text{PPh}_3)_7\text{Cl}_3$ ^[3].

Figure 1.6:

The following crystal structures were used to create the molecular structures in this image: $\text{Au}_{11}(\text{PPh}_3)_7\text{Cl}_3$ ^[3], $\text{Au}_{25}(\text{SC}_2\text{H}_5)_{18}$ ^[6], $\text{Au}_{38}(\text{SC}_2\text{H}_4\text{Ph})_{24}$ ^[7], $\text{Ag}_{44}(\text{SPhF}_2)_{30}$ ^[8], $\text{Ni}_6(\text{C}_4\text{H}_6\text{S}_2\text{O}_2)_3$ ^[9], L-glutathione^[10], (*S*)-BINAP^[11] and CeO_2 ^[12].

Figure 1.7:

The following crystal structures were used to create the molecular structures in this image: $\text{Au}_{25}(\text{SC}_2\text{H}_5)_{18}$ ^[6], $[\text{Au}_{25}(\text{SC}_2\text{H}_4\text{Ph})_{18}]\text{TOA}$ ^[4], $\text{Au}_{11}(\text{PPh}_3)_7\text{Cl}_3$ ^[3], $[\text{Au}_{25}(\text{PPh}_3)_{10}(\text{SC}_2\text{H}_4\text{Ph})_5\text{Cl}_2](\text{SbF}_6)_2$ ^[13], $\text{Au}_{28}(\text{TBBT})_{20}$ ^[14] and $\text{Au}_{28}(\text{SC}_8\text{H}_{11})_{20}$ ^[15].

Figure 1.8:

The following crystal structures were used to create the molecular structures in this

image: $[\text{Au}_{25}(\text{SC}_2\text{H}_4\text{Ph})_{18}]\text{TOA}$ ^[16], $\text{Au}_{38}(\text{SC}_2\text{H}_4\text{Ph})_{24}$ ^[7], $[\text{Au}_{20}(\text{PP}_3)_4]\text{Cl}_4$ (with $\text{PP}_3 = \text{tris}(2\text{-(diphenylphosphino)ethyl)phosphine}$)^[17] and $\text{Au}_{133}(\text{TBBT})_{52}$ ^[18].

Figure 1.9:

The following crystal structures were used to create the molecular structures in this image: $\text{Au}_{11}(\text{PPh}_3)_7\text{Cl}_3$ ^[3] and CeO_2 ^[12].

Title Figure Chapter 3:

The following structures were used to create the molecular structures in this image: $[\text{Au}_{25}(\text{SC}_2\text{H}_4\text{Ph})_{18}]\text{TOA}$ ^[16], $\text{Au}_{38}(\text{SC}_2\text{H}_4\text{Ph})_{24}$ ^[7] and $\text{Au}_{144}(\text{2-PET})_{60}$ ^[19].

Title Figure Chapter 4:

The following structures were used to create the molecular structures in this image: $\text{Au}_{15}(\text{SG})_{13}$ ^[20] and L-glutathione^[10].

B.1. References

- [1] Eric F. Pettersen, Thomas D. Goddard, Conrad C. Huang, Gregory S. Couch, Daniel M. Greenblatt, Elaine C. Meng, and Thomas E. Ferrin. UCSF Chimera – A visualization system for exploratory research and analysis. *Journal of Computational Chemistry*, 25(13):1605–1612, 2004. doi: 10.1002/jcc.20084.
- [2] Brett M. Bode and Mark S. Gordon. MacMolPlt: a graphical user interface for GAMESS. *Journal of Molecular Graphics and Modelling*, 16(3):133–138, jun 1998. doi: 10.1016/s1093-3263(99)00002-9.
- [3] Lallie C. McKenzie, Tatiana O. Zaikova, and James E. Hutchison. Structurally Similar Triphenylphosphine-Stabilized Undecagolds, $\text{Au}_{11}(\text{PPh}_3)_7\text{Cl}_3$ and $[\text{Au}_{11}(\text{PPh}_3)_8\text{Cl}_2]\text{Cl}$, Exhibit Distinct Ligand Exchange Pathways with Glutathione. *Journal of the American Chemical Society*, 136(38):13426–13435, sep 2014. doi: 10.1021/ja5075689.
- [4] Manzhou Zhu, Christine M. Aikens, Frederick J. Hollander, George C. Schatz, and Rongchao Jin. Correlating the Crystal Structure of A Thiol-Protected Au_{25} Cluster and Optical Properties. *Journal of the American Chemical Society*, 130(18):5883–5885, apr 2008. doi: 10.1021/ja801173r.
- [5] Yukatsu Shichibu, Yuichi Negishi, Takahito Watanabe, Nirmalya K. Chaki, Hiroyuki Kawaguchi, and Tatsuya Tsukuda. Biicosahedral Gold Clusters $[\text{Au}_{25}(\text{PPh}_3)_{10}(\text{SC}_n\text{H})_{(2n+1)5}\text{Cl}_2]^{2+}$ ($n = 2\text{--}18$): A Stepping Stone to Cluster-Assembled Materials. *The Journal of Physical Chemistry C*, 111(22):7845–7847, may 2007. doi: 10.1021/jp073101t.
- [6] Tiziano Dainese, Sabrina Antonello, José A. Gascón, Fangfang Pan, Neranjan V. Perera, Marco Ruzzi, Alfonso Venzo, Alfonso Zoleo, Kari Rissanen, and Flavio Maran. $\text{Au}_{25}(\text{SEt})_{18}$, a Nearly Naked Thiolate-Protected Au_{25} Cluster: Structural Analysis by Single Crystal X-ray Crystallography and Electron Nuclear Double Resonance. *ACS Nano*, 8(4):3904–3912, mar 2014. doi: 10.1021/nn500805n.
- [7] Huifeng Qian, William T. Eckenhoff, Yan Zhu, Tomislav Pintauer, and Rongchao Jin. Total Structure Determination of Thiolate-Protected Au_{38} Nanoparticles. *Journal of the American Chemical Society*, 132(24):8280–8281, jun 2010. doi: 10.1021/ja103592z.

- [8] Huayan Yang, Yu Wang, Huaqi Huang, Lars Gell, Lauri Lehtovaara, Sami Malola, Hannu Hakkinen, and Nanfeng Zheng. CCDC 953878: Experimental Crystal Structure Determination, 2013. doi: 10.5517/CC110L8X.
- [9] Chunhong Tan, Zhenzhen Xue, Xiao Ma, Yanlong Wang, Yong Wang, Shenming Hu, Tianlu Sheng, and Xintao Wu. CCDC 908151: Experimental Crystal Structure Determination, 2014. doi: 10.5517/CCZH06N.
- [10] S.A. Moggach, A.R. Lennie, C.A. Morrison, P. Richardson, F.A. Stefanowicz, and J.E. Warren. CCDC 762192: Experimental Crystal Structure Determination, 2011. doi: 10.5517/CCTL3VB.
- [11] M.D. Jones, F.A.A. Paz, J.E. Davies, and B.F.G. Johnson. CCDC 209977: Experimental Crystal Structure Determination, 2003. doi: 10.5517/CC71HG6.
- [12] Materials Data on CeO₂ by Materials Project, 2020. doi: 10.17188/1195334.
- [13] Lakshmi V. Nair, Sakiat Hossain, Shunjiro Takagi, Yukari Imai, Guoxiang Hu, Shota Wakayama, Bharat Kumar, Wataru Kurashige, De en Jiang, and Yuichi Negishi. Hetero-biicosahedral [Au₂₄Pd(PPh₃)₁₀(SC₂H₄Ph)₅Cl₂]²⁺ nanocluster: selective synthesis and optical and electrochemical properties. *Nanoscale*, 10(40):18969–18979, 2018. doi: 10.1039/c8nr04078h.
- [14] Chenjie Zeng, Tao Li, Anindita Das, Nathaniel L. Rosi, and Rongchao Jin. Chiral Structure of Thiolate-Protected 28-Gold-Atom Nanocluster Determined by X-ray Crystallography. *Journal of the American Chemical Society*, 135(27):10011–10013, jul 2013. doi: 10.1021/ja404058q.
- [15] Yuxiang Chen, Chong Liu, Qing Tang, Chenjie Zeng, Tatsuya Higaki, Anindita Das, De en Jiang, Nathaniel L. Rosi, and Rongchao Jin. Isomerism in Au₂₈(SR)₂₀ Nanocluster and Stable Structures. *Journal of the American Chemical Society*, 138(5):1482–1485, jan 2016. doi: 10.1021/jacs.5b12094.
- [16] Michael W. Heaven, Amala Dass, Peter S. White, Kennedy M. Holt, and Royce W. Murray. Crystal Structure of the Gold Nanoparticle [N(C₈H₁₇)₄][Au₂₅(SCH₂CH₂Ph)₁₈]. *Journal of the American Chemical Society*, 130(12):3754–3755, mar 2008. doi: 10.1021/ja800561b.
- [17] Xian-Kai Wan, Shang-Fu Yuan, Zhi-Wei Lin, and Quan-Ming Wang. A Chiral Gold Nanocluster Au₂₀ Protected by Tetradentate Phosphine Ligands. *Angewandte Chemie International Edition*, 53(11):2923–2926, feb 2014. doi: 10.1002/anie.201308599.
- [18] Chenjie Zeng, Yuxiang Chen, Kristin Kirschbaum, Kannatassen Appavoo, Matthew Y. Sfeir, and Rongchao Jin. Structural patterns at all scales in a nonmetallic chiral Au₁₃₃(SR)₅₂ nanoparticle. *Science Advances*, 1(2), mar 2015. doi: 10.1126/sciadv.1500045.
- [19] Nan Yan, Nan Xia, Lingwen Liao, Min Zhu, Fengming Jin, Rongchao Jin, and Zhikun Wu. Unraveling the long-pursued Au₁₄₄ structure by X-ray crystallography. *Science Advances*, 4(10), oct 2018. doi: 10.1126/sciadv.aat7259.
- [20] De en Jiang, Steven H. Overbury, and Sheng Dai. Structure of Au₁₅(SR)₁₃ and Its Implication for the Origin of the Nucleus in Thiolated Gold Nanoclusters. *Journal of the American Chemical Society*, 135(24):8786–8789, jun 2013. doi: 10.1021/ja402680c.

C. Coordinates of the Calculated Structures

Coordinates of the Lowest Energy Isomers of Au₃₈(2-MeBuS)₂₄

Isomer 1a

Index	Symbol	x (angstrom)	y (angstrom)	z (angstrom)					
1	Au	-2.25050449	9.13961124	21.40570641	59	C	-4.43073702	0.61360413	18.34121513
2	Au	-1.62261558	10.68276215	19.04342270	60	C	-5.72672081	-0.20046198	18.36547470
3	Au	-2.78735828	13.30908108	19.72196007	61	C	-4.93646765	1.85438931	16.16534233
4	Au	-0.47498831	12.95487690	17.75946426	62	H	-2.91108036	2.75337481	18.87184525
5	Au	2.49938011	12.05049515	21.53145409	63	H	-2.43325424	2.28437424	17.21680069
6	Au	-4.29084682	10.75326443	20.23686028	64	H	-5.34171295	2.56073022	18.16347122
7	Au	-0.18833321	12.63096237	20.64192772	65	H	-4.09137392	0.78097689	19.37825966
8	Au	-2.49080849	11.90609837	22.24284935	66	H	-3.63324451	0.02823465	17.84567451
9	Au	-4.33987141	9.97326660	23.21131325	67	H	-6.54433537	0.37245581	18.83141708
10	Au	-3.13672161	8.27631474	18.80020714	68	H	-5.59534454	-1.12748444	18.94425011
11	Au	1.26266420	10.76781464	19.04148483	69	H	-6.04988146	-0.48719195	17.35352898
12	Au	0.48251584	10.04690361	21.77543068	70	H	-4.96154308	2.83994579	15.67655182
13	Au	0.15205055	12.39676476	23.44605827	71	H	-5.92757130	1.39462471	16.04183578
14	Au	1.24284768	14.73297215	21.95830345	72	H	-4.20056772	1.23044276	15.62997437
15	Au	-0.21995199	8.17002392	19.65839767	73	S	-1.01777995	9.33581161	26.40567017
16	Au	-0.22292744	7.41700172	22.59944916	74	C	0.72035104	9.85720348	26.85983086
17	Au	-0.52561080	15.22060680	19.46110153	75	C	0.93975252	9.91841412	28.37740326
18	Au	-2.08292317	10.29452705	16.05222130	76	C	2.28824973	10.61973000	28.64287758
19	Au	-4.89307928	8.03634548	21.16094398	77	C	2.56792903	10.91684532	30.11835480
20	Au	2.06413698	13.64417744	19.18049812	78	C	0.86221892	8.53764820	29.03451538
21	Au	-1.40259457	9.85332584	24.02861404	79	H	0.85704386	10.85346889	26.41527557
22	Au	-4.78126287	5.53897381	18.78040695	80	H	1.42919707	9.16906643	26.37694740
23	Au	-1.58341360	14.60442543	22.26203156	81	H	0.14000133	10.55442524	28.80496216
24	Au	-2.58602047	15.54462814	17.10396957	82	H	2.30559063	11.56662655	28.07566071
25	Au	-2.90254784	7.35788774	23.54168510	83	H	3.10057878	9.99313927	28.23164558
26	Au	-1.29562151	5.46827841	17.93603134	84	H	1.75856876	11.52005577	30.55990028
27	Au	-7.33921766	9.95759201	21.55299950	85	H	3.50481391	11.48382473	30.23070908
28	Au	0.92431223	15.65415287	16.61462593	86	H	2.66582584	9.99680519	30.71315765
29	Au	-2.28484559	6.33032417	20.74123001	87	H	-0.10434513	8.05576324	28.82697678
30	Au	-1.22514164	4.53809500	23.42140388	88	H	0.97611701	8.60354519	30.12692833
31	Au	-4.42339325	13.43409824	24.02822685	89	H	1.65698373	7.87996817	28.64390182
32	Au	-0.40993261	17.51630592	22.04165268	90	S	-3.18625689	8.23881435	16.36356926
33	Au	0.31814504	15.49395084	24.85599709	91	C	-4.95592642	8.49098206	15.84396744
34	Au	4.53028774	11.70686531	18.83138466	92	C	-5.13356590	8.67097569	14.33105183
35	Au	-0.71865678	7.06035566	25.86891556	93	C	-6.63074636	8.89535999	14.03636742
36	Au	-6.29546404	7.68493557	24.10104561	94	C	-6.93373489	9.29878998	12.59126759
37	Au	4.56924343	14.43558216	21.09506226	95	C	-4.56460905	7.48857355	13.54100895
38	Au	3.06055355	8.77224350	22.74677467	96	H	-5.36318684	9.34851742	16.39704514
39	S	0.82292110	6.44658470	18.25320244	97	H	-5.46861935	7.57576323	16.18669510
40	C	1.15046036	7.19223881	16.57147217	98	H	-4.58368921	9.58726215	14.03971100
41	C	1.91979456	6.24220991	15.64137840	99	H	-7.01066971	9.67807674	14.71482182
42	C	2.46709418	7.06353331	14.45645142	100	H	-7.18420267	7.97136164	14.28684902
43	C	3.35606956	6.27320147	13.49319458	101	H	-6.38031244	10.20946980	12.31189823
44	C	1.06442857	5.05980158	15.17898750	102	H	-8.00684166	9.50510788	12.45872974
45	H	1.74137843	8.10042095	16.76455498	103	H	-6.66171694	8.50654125	11.87810230
46	H	0.19239688	7.50301170	16.12925339	104	H	-3.50337720	7.32748127	13.78004360
47	H	2.78676629	5.84776068	16.20667648	105	H	-4.64463282	7.65361261	12.45676708
48	H	3.04060698	7.91614771	14.85933495	106	H	-5.10880232	6.56147194	13.78953838
49	H	1.61457229	7.49851322	13.90317535	107	S	0.46995991	13.29946709	25.69739914
50	H	4.18797731	5.78930922	14.03046322	108	C	-1.15238893	13.05450916	26.58617592
51	H	3.79161215	6.93679476	12.73104954	109	C	-1.09890294	13.50509071	28.05305290
52	H	2.79456377	5.48846960	12.96521664	110	C	-2.28960967	12.87070465	28.80043411
53	H	0.65491301	4.50789165	16.03796959	111	C	-2.28829527	13.11096478	30.31172562
54	H	1.64885867	4.35028696	14.57407475	112	C	-1.07540083	15.02927017	28.19556427
55	H	0.21378826	5.41278410	14.57231331	113	H	-1.34475827	11.97292805	26.52611732
56	S	-3.32755041	4.51259184	17.23644638	114	H	-1.94933748	13.56770420	26.02709961
57	C	-3.23400283	2.74391174	17.82098198	115	H	-0.16885373	13.09627819	28.49477386
58	C	-4.55281258	1.98296750	17.64297104	116	H	-2.27990437	11.78343010	28.60762787
					117	H	-3.22811913	13.25694752	28.36200905

118	H	-1.34474862	12.76607704	30.76497078	196	C	-9.82690144	15.28242970	18.42719078
119	H	-3.11040759	12.56217384	30.79583740	197	C	-9.67123604	12.49567223	19.83190346
120	H	-2.41255951	14.17525005	30.56015205	198	H	-6.33887577	13.52483654	19.60627747
121	H	-0.24635848	15.46665573	27.61805153	199	H	-7.24583054	13.04187202	21.06145096
122	H	-0.95121342	15.33661652	29.24467278	200	H	-8.35138798	12.95036602	18.19044685
123	H	-2.01588869	15.46385479	27.81635857	201	H	-7.73062181	15.25632858	18.94432449
124	S	-4.35150957	14.49506474	18.25144005	202	H	-8.81327724	15.09426308	20.33390617
125	C	-4.92503023	13.19296074	17.04208755	203	H	-9.71607113	14.95333481	17.38161278
126	C	-5.96257496	13.70948505	16.03435707	204	H	-9.86363697	16.38264275	18.42759895
127	C	-6.65638638	12.48980427	15.39217663	205	H	-10.79876614	14.91971397	18.79362679
128	C	-7.80942202	12.83919621	14.44823933	206	H	-9.50630569	11.40873623	19.80506134
129	C	-5.34810734	14.63787842	14.98350716	207	H	-10.59303284	12.70948410	19.27020836
130	H	-5.36537075	12.40448284	17.67012215	208	H	-9.83372784	12.78499031	20.88383675
131	H	-4.04691505	12.76379776	16.53675842	209	S	6.10132217	13.04747009	19.96578217
132	H	-6.72913408	14.27538967	16.59898567	210	C	6.88308382	14.17630672	18.69446945
133	H	-7.03538418	11.84105301	16.20162964	211	C	8.22674465	13.64191437	18.18094254
134	H	-5.89622068	11.89898968	14.84898949	212	C	8.90285969	14.75134373	17.34885216
135	H	-8.56320095	13.46028137	14.95842171	213	C	10.33958054	14.43521595	16.92560768
136	H	-8.31402588	11.92796230	14.09305477	214	C	8.06481266	12.33987713	17.39241028
137	H	-7.46346140	13.38986874	13.56135941	215	H	7.03109598	15.13759327	19.20834160
138	H	-4.82020998	15.47830486	15.46048832	216	H	6.16809654	14.32053089	17.87160301
139	H	-6.11494589	15.05939102	14.31645679	217	H	8.86656094	13.44083240	19.06364250
140	H	-4.61690617	14.08742809	14.36757278	218	H	8.90264130	15.68386078	17.94027519
141	S	-3.39930010	15.52146435	23.62501144	219	H	8.28654289	14.94938374	16.45202446
142	C	-4.51812553	16.33603096	22.37728882	220	H	10.96987247	14.21769333	17.80282402
143	C	-5.89884186	16.70127678	22.93379402	221	H	10.78657150	15.29027176	16.39563942
144	C	-6.76073027	17.24866676	21.77899742	222	H	10.38758469	13.56805515	16.25110245
145	C	-8.22073460	17.51338387	22.15358925	223	H	7.58725166	11.56198788	18.00451851
146	C	-5.80400944	17.68289185	24.10515594	224	H	9.03698063	11.94790077	17.05876541
147	H	-4.60497904	15.66616726	21.51157379	225	H	7.43442535	12.50302696	16.50193787
148	H	-3.97166419	17.23968887	22.05795097	226	S	-8.20174122	8.93657303	23.48879814
149	H	-6.36711073	15.76535892	23.29613495	227	C	-9.36247635	7.62529945	22.84297943
150	H	-6.72698784	16.52577400	20.94616127	228	C	-9.86706161	6.67569065	23.93586349
151	H	-6.30039787	18.17974854	21.39776230	229	C	-10.67347908	5.54430676	23.26726341
152	H	-8.69126892	16.60900879	22.57292557	230	C	-11.10071659	4.42579556	24.22110558
153	H	-8.80195999	17.81489372	21.26904106	231	C	-10.67315960	7.41315365	25.00912857
154	H	-8.31558037	18.31719589	22.89895821	232	H	-8.83430386	7.06412888	22.05991554
155	H	-5.15602493	17.28448296	24.90037346	233	H	-10.20041752	8.17778683	22.38470078
156	H	-6.79130554	17.88212967	24.54685020	234	H	-8.97543144	6.22174120	24.41109467
157	H	-5.38095140	18.64419937	23.76725006	235	H	-10.06209183	5.11018848	22.45725441
158	S	-0.96990710	12.28822327	15.46453190	236	H	-11.56832981	5.98017788	22.78409767
159	C	0.69533318	11.76589298	14.80835819	237	H	-10.22704411	3.98518968	24.72777176
160	C	0.64874256	11.07286167	13.44159698	238	H	-11.61153316	3.62025714	23.67166328
161	C	2.09181237	10.68470001	13.05902672	239	H	-11.79391384	4.78770781	24.99474525
162	C	2.21220827	9.87157726	11.76796818	240	H	-10.09192562	8.24096870	25.44184303
163	C	-0.01819270	11.94357872	12.37347984	241	H	-10.96007442	6.74115372	25.80308101
164	H	1.17479885	11.12472248	15.55972290	242	H	-11.59577084	7.83750916	24.57680893
165	H	1.26992118	12.70577145	14.74515057	243	S	-6.41923428	6.36907339	20.25782394
166	H	0.05899091	10.14252758	13.55672264	244	C	-7.54098558	7.32865572	19.12025833
167	H	2.53033066	10.10915089	13.89183331	245	C	-8.34692764	6.43554258	18.16955566
168	H	2.69554901	11.60778046	12.97142124	246	C	-9.10586739	7.33647966	17.17479134
169	H	1.59791005	8.95842648	11.81438828	247	C	-9.81257534	6.57557106	16.04983521
170	H	3.25570965	9.56529522	11.59854507	248	C	-9.27966976	5.48783302	18.92993355
171	H	1.89253867	10.44805145	10.88716888	249	H	-6.92589045	8.04764652	18.56330490
172	H	-1.03098488	12.24199200	12.68333244	250	H	-8.20628262	7.90607548	19.78581619
173	H	-0.10407333	11.41154480	11.41462708	251	H	-7.62185144	5.82767725	17.59352112
174	H	0.57151055	12.86047840	12.20271778	252	H	-8.38870430	8.04825592	16.73025703
175	S	3.03905249	14.89884281	17.33332443	253	H	-9.84123802	7.94682980	17.73149300
176	C	3.84123302	16.40530968	18.09473228	254	H	-9.10258770	5.93823814	15.49849892
177	C	4.80024242	17.12643242	17.13973236	255	H	-10.26475906	7.27473783	15.33014679
178	C	5.59856415	18.16673470	17.95372391	256	H	-10.61765671	5.93015337	16.43155479
179	C	6.72711372	18.84695625	17.17503357	257	H	-8.71685410	4.88075686	19.65494537
180	C	4.07624388	17.75697708	15.94769859	258	H	-9.79923248	4.79784393	18.24916077
181	H	4.38877869	16.01644516	18.97019577	259	H	-10.04273319	6.06031227	19.48429680
182	H	3.05520511	17.07892609	18.46414757	260	S	-5.71901369	11.52701855	24.49564552
183	H	5.51884127	16.37623024	16.75499344	261	C	-5.47154760	11.09736443	26.28962898
184	H	6.02438116	17.66651535	18.84152603	262	C	-6.14062691	12.07621861	27.26359177
185	H	4.89799452	18.93105698	18.33865929	263	C	-5.88998652	11.57441998	28.70083427
186	H	7.42585707	18.10164833	16.76275826	264	C	-6.29886389	12.56283092	29.79608536
187	H	7.30181742	19.51996040	17.83008003	265	C	-7.63435650	12.25064373	26.97140694
188	H	6.34445286	19.44999695	16.33874321	266	H	-4.39370871	11.01430035	26.48721123
189	H	3.50559330	17.00310326	15.38653088	267	H	-5.92347527	10.09481430	26.38521767
190	H	4.78408146	18.22682190	15.24895573	268	H	-5.64151525	13.05786705	27.14618111
191	H	3.36999750	18.53069878	16.29188919	269	H	-4.81817722	11.33733940	28.81249046
192	S	-6.64490509	11.13396358	19.63679886	270	H	-6.43473148	10.62196922	28.84062958
193	C	-7.16331911	12.89669323	19.97439003	271	H	-5.76635790	13.52078533	29.68356323
194	C	-8.47055531	13.24792099	19.25071716	272	H	-6.06100702	12.16220284	30.79339600
195	C	-8.66475677	14.77717304	19.28603935	273	H	-7.37854719	12.77347660	29.77642059

274	H	-7.79910040	12.59544659	25.94052505	352	H	-0.85630971	4.15728569	27.67289925
275	H	-8.09290123	12.98476887	27.64946365	353	H	-1.01000583	2.03126454	25.46263885
276	H	-8.16554165	11.29118252	27.09250450	354	H	-2.89766288	1.87117672	27.07948112
277	S	-4.59326124	6.26670599	24.88953972	355	H	-1.75536501	1.78814542	28.42954445
278	C	-4.27109146	6.88954306	26.61689377	356	H	-1.92636085	-0.27879634	26.13726234
279	C	-5.39565277	6.55593348	27.60330009	357	H	-2.62938786	-0.48585203	27.75860214
280	C	-5.09748220	7.26239061	28.94114494	358	H	-0.86808044	-0.40674472	27.56265640
281	C	-6.22602749	7.16389227	29.97093582	359	H	1.30716443	2.55512595	26.32751274
282	C	-5.57927370	5.04449797	27.76777458	360	H	0.81389725	0.89499778	26.71874809
283	H	-4.10215139	7.97255230	26.55916405	361	H	0.76478183	2.15719581	27.97721863
284	H	-3.32006884	6.41901731	26.92054558	362	S	4.35548401	10.70986843	22.38433456
285	H	-6.33283138	6.98245907	27.19469452	363	C	4.69545078	11.36560535	24.09396553
286	H	-4.89124203	8.32740402	28.73593712	364	C	5.57370090	10.44282722	24.94719696
287	H	-4.16612673	6.84467125	29.36763382	365	C	5.70468569	11.05839443	26.35464859
288	H	-7.17053127	7.55558157	29.56006241	366	C	6.39512396	10.15129948	27.37639427
289	H	-5.98360538	7.74885511	30.87130356	367	C	6.93578005	10.18567371	24.29661560
290	H	-6.40251589	6.12617016	30.29036331	368	H	3.73207760	11.55793762	24.58580589
291	H	-5.75889158	4.56254482	26.79504967	369	H	5.20133305	12.33119488	23.92073059
292	H	-6.43282938	4.80820942	28.41980171	370	H	5.04002810	9.47707081	25.04327393
293	H	-4.67524672	4.59274578	28.21107674	371	H	4.69560528	11.31120110	26.72350502
294	S	0.25390804	17.78230476	24.28866814	372	H	6.25679922	12.01345634	26.27631760
295	C	-1.24062812	18.37937355	25.23921776	373	H	5.87834644	9.18133640	27.45473099
296	C	-1.43524134	19.90052795	25.17105293	374	H	6.39277077	10.61504173	28.37480736
297	C	-2.39631200	20.31600571	26.30554581	375	H	7.44336987	9.95320797	27.10739326
298	C	-2.58311296	21.82826614	26.45052719	376	H	6.81706381	9.78378296	23.27964783
299	C	-1.93605447	20.36036873	23.79954338	377	H	7.52850771	9.46305466	24.87628365
300	H	-1.03884912	18.07099724	26.27654457	378	H	7.51243401	11.12366104	24.22390747
301	H	-2.12540984	17.83165550	24.88131905	379	S	-2.27739501	3.97579646	21.39199638
302	H	-0.45407423	20.37540436	25.37029457	380	C	-4.05697346	3.62830687	21.82575226
303	H	-2.01090312	19.90943146	27.25765419	381	C	-4.30027866	2.19921255	22.33409309
304	H	-3.37718439	19.83488846	26.13496780	382	C	-5.79268837	1.86078966	22.13383484
305	H	-1.61424267	22.33331299	26.59370422	383	C	-6.17486334	0.42907608	22.51754189
306	H	-3.21401572	22.06057358	27.32215500	384	C	-3.86356020	2.02641916	23.79171753
307	H	-3.06718731	22.26889229	25.56655502	385	H	-4.59310341	3.79733157	20.87623787
308	H	-1.27499604	20.00632477	22.99441147	386	H	-4.40577078	4.37855387	22.55014229
309	H	-1.98478234	21.45719337	23.73231125	387	H	-3.70915008	1.50660014	21.70268822
310	H	-2.94438386	19.95803833	23.60608864	388	H	-6.04725122	2.02980447	21.07299232
311	S	-0.98899674	17.58471870	19.76134872	389	H	-6.40056944	2.57890296	22.71499252
312	C	0.41433737	18.52458191	18.95482063	390	H	-5.55718040	-0.30381978	21.97424889
313	C	0.01203483	19.95380974	18.57356644	391	H	-7.22829247	0.22790743	22.26923752
314	C	1.12699330	20.55179024	17.69050217	392	H	-6.04901218	0.24388778	23.59447861
315	C	0.79349929	21.92150307	17.09439468	393	H	-2.81999445	2.34983206	23.93099594
316	C	-0.28179389	20.81557655	19.80463982	394	H	-3.93815041	0.97859699	24.11715317
317	H	0.66808939	17.94377899	18.05369568	395	H	-4.49423695	2.64346385	24.45406342
318	H	1.27937520	18.51667213	19.63388252	396	S	2.01160765	6.74737883	23.31206512
319	H	-0.90646464	19.88825417	17.95827484	397	C	2.53717041	5.46090221	22.07140541
320	H	1.33323050	19.84603310	16.86754036	398	C	3.97032094	4.95367193	22.27516747
321	H	2.05593276	20.62205124	18.28698730	399	C	4.26859999	3.90863490	21.18040466
322	H	-0.14043605	21.87944031	16.51157761	400	C	5.72405291	3.43685722	21.13610077
323	H	1.59522033	22.25753784	16.41901398	401	C	4.18556261	4.38643694	23.68191719
324	H	0.67397064	22.69013405	17.87162209	402	H	2.39562893	5.86835527	21.06148911
325	H	-1.07791913	20.36909103	20.41764641	403	H	1.81452954	4.63978052	22.21706390
326	H	-0.60970998	21.82647514	19.52008820	404	H	4.65539932	5.81159782	22.12977600
327	H	0.61862445	20.91037560	20.43496895	405	H	3.99860644	4.33796883	20.20088397
328	S	-1.01984906	16.68394089	15.75751686	406	H	3.60115695	3.03918433	21.33117294
329	C	-1.32814384	15.94520664	14.06868267	407	H	6.41169024	4.28675079	20.99921989
330	C	-0.56819004	16.66094017	12.94376659	408	H	5.88235235	2.73845387	20.29992104
331	C	-1.16710877	16.20289612	11.59650326	409	H	6.01501799	2.91381383	22.05928612
332	C	-0.59396476	16.92045021	10.37172699	410	H	3.93616915	5.13044405	24.45273209
333	C	0.94165856	16.42097473	13.01199913	411	H	5.23026419	4.07950640	23.83611298
334	H	-2.41291904	16.05713844	13.91993237	412	H	3.54055834	3.50607586	23.84328270
335	H	-1.09649563	14.87019348	14.10802269	413	S	3.23139691	10.04651737	17.77889633
336	H	-0.76000077	17.74740028	13.04658985	414	C	3.87452793	8.49822140	18.60656548
337	H	-2.25957823	16.36316872	11.62707996	415	C	4.97738743	7.80339956	17.79607010
338	H	-1.01520061	15.11284733	11.49228764	416	C	5.19777679	6.39989901	18.39623642
339	H	-0.70349443	18.01295662	10.46598434	417	C	6.19423676	5.52924633	17.62729645
340	H	-1.12163091	16.60869026	9.45751953	418	C	6.26951694	8.62173748	17.74136353
341	H	0.47340056	16.69835472	10.22755718	419	H	3.00147843	7.83715582	18.70915604
342	H	1.34698427	16.70868492	13.99307537	420	H	4.21947241	8.75653553	19.61863708
343	H	1.47807384	17.00141525	12.24680424	421	H	4.60381651	7.67093229	16.76214218
344	H	1.16977191	15.35332870	12.85627270	422	H	4.22236109	5.88465452	18.43461037
345	S	-0.11098599	4.82544518	25.48133278	423	H	5.53194952	6.51092863	19.44423294
346	C	-1.13021934	3.80304050	26.66470337	424	H	5.90288973	5.43423796	16.56880760
347	C	-0.85293770	2.30113769	26.52457809	425	H	6.23574448	4.51588583	18.05466652
348	C	-1.88811624	1.52501190	27.36303902	426	H	7.21332121	5.94242668	17.66080093
349	C	-1.82013321	0.00490682	27.19638443	427	H	6.08647585	9.62140179	17.32215691
350	C	0.58970362	1.95492291	26.90652275	428	H	7.03030539	8.13184071	17.11575890
351	H	-2.19110298	4.02726936	26.48851967	429	H	6.68671417	8.75219727	18.75403786

430	S	3.29526925	15.99482346	22.30878448	439	H	5.27110815	14.41783810	25.88892746
431	C	3.78297639	15.62432384	24.07088661	440	H	4.92079449	16.02417946	26.53658485
432	C	5.23952150	15.97824287	24.39096451	441	H	7.68839693	15.11719513	25.49642754
433	C	5.55950451	15.48109055	25.81529617	442	H	7.20821810	15.18258858	27.20853615
434	C	7.02937031	15.62686825	26.21748161	443	H	7.33772087	16.68149948	26.26956749
435	C	5.51421356	17.47517776	24.21916389	444	H	5.23995161	17.81241989	23.20820427
436	H	3.58328891	14.56140995	24.25930595	445	H	6.57704592	17.71127892	24.37388039
437	H	3.08645797	16.21655273	24.68771553	446	H	4.92273808	18.06124878	24.94304276
438	H	5.88072014	15.41845703	23.68197250					

Isomer 1b

Index	Symbol	x (angstrom)	y (angstrom)	z (angstrom)	64	C	-0.80115061	9.73964706	26.54297474
1	Au	2.29825670	9.15972786	21.28387360	65	C	-1.37346343	9.08935384	27.80939780
2	Au	1.65888040	10.70996275	18.92198378	66	C	-2.89919370	9.30718720	27.83263301
3	Au	2.81994083	13.29634509	19.55484038	67	C	-3.61800552	8.58935552	28.97845954
4	Au	0.42239799	12.96435640	17.66041202	68	H	-0.83473092	10.83952545	26.61342457
5	Au	-2.42087952	12.11388843	21.59853202	69	H	-1.36743887	9.43602759	25.65155439
6	Au	4.34541910	10.74467396	20.10956735	70	H	-3.10686383	10.39158155	27.88357203
7	Au	0.24844991	12.65154348	20.55776546	71	H	-3.31371702	8.95320511	26.87266323
8	Au	2.57815152	11.91756615	22.12211029	72	H	-3.31618873	8.97927588	29.96175432
9	Au	4.40612378	9.98633949	23.13077282	73	H	-4.70847149	8.71504607	28.89458879
10	Au	3.23064634	8.33677660	18.65065150	74	H	-3.40391555	7.50861225	28.96082519
11	Au	-1.25307872	10.77850930	19.04080281	75	S	3.48247058	8.49256453	16.22018325
12	Au	-0.41919922	10.07474524	21.72571605	76	C	5.19520240	9.11900672	15.82488589
13	Au	0.00201050	12.46664262	23.36348755	77	C	6.16537447	7.98295491	15.47589236
14	Au	-1.10125954	14.79264741	21.92128648	78	C	7.57083801	8.59887097	15.30878867
15	Au	0.26809298	8.22438919	19.54771151	79	C	8.66552516	7.60409735	14.91578081
16	Au	0.25823297	7.40381315	22.44825596	80	H	5.08232123	9.79095542	14.96074349
17	Au	0.56378188	15.24253936	19.34752836	81	H	5.55290268	9.70825325	16.68034522
18	Au	2.12822541	10.40432819	15.97981100	82	H	7.51664668	9.39630058	14.54353475
19	Au	4.93681876	8.05733684	21.09167642	83	H	7.84949770	9.09964183	16.25308504
20	Au	-2.07127694	13.61601192	19.18809715	84	H	8.50463200	7.19687114	13.90672516
21	Au	1.49083615	9.85154335	23.91064324	85	H	9.65370249	8.08988428	14.92245283
22	Au	4.86710935	5.62175832	18.67192973	86	H	8.70390974	6.75517105	15.61559070
23	Au	1.75035747	14.64730977	22.06548658	87	S	-0.29807276	13.30262833	25.64448788
24	Au	2.59478221	15.50593520	16.95221322	88	C	1.36531180	13.15438729	26.47381431
25	Au	2.93580147	7.34963490	23.40702043	89	C	1.52246300	14.10372250	27.66967300
26	Au	1.45834280	5.72377465	17.60322015	90	C	2.98178192	14.05028108	28.16137808
27	Au	7.33735271	10.05564019	21.63438618	91	C	3.32124197	15.08283338	29.23944851
28	Au	-0.96275827	15.65361314	16.64850034	92	H	1.44029869	12.10062297	26.79130236
29	Au	2.35428365	6.37820675	20.53597651	93	H	2.14046107	13.33892056	25.71574634
30	Au	1.24688124	4.52675411	23.21111577	94	H	3.19369379	13.03379942	28.54000729
31	Au	4.48069103	13.45803635	23.86754336	95	H	3.64581017	14.20880680	27.29367732
32	Au	0.53578912	17.54753211	21.99731642	96	H	2.75332532	14.91293153	30.16627920
33	Au	-0.19359927	15.51015975	24.82353791	97	H	4.39109500	15.04172070	29.49591726
34	Au	-4.54368659	11.58955557	19.12302236	98	H	3.10137105	16.10374106	28.88864723
35	Au	0.75950108	7.02447995	25.68709356	99	S	4.38165209	14.44598594	18.06439595
36	Au	6.28782872	7.62552924	24.01918841	100	C	4.94478675	13.16910760	16.82965359
37	Au	-4.43656604	14.52070062	21.09213459	101	C	5.53595158	13.79066043	15.55740684
38	Au	-2.92694355	8.85107302	22.81301138	102	C	5.79152141	12.67063781	14.53058558
39	S	-0.67600932	6.67349626	17.90732585	103	C	6.24631604	13.16766929	13.15577989
40	C	-0.86645125	7.62126778	16.31203321	104	H	5.69744674	12.56338111	17.36188053
41	C	-0.95654363	6.71253642	15.07951458	105	H	4.08829170	12.52029589	16.59404065
42	C	-0.92379957	7.59391230	13.81531619	106	H	6.54493273	11.97379965	14.94147777
43	C	-0.87167469	6.80803678	12.50245863	107	H	4.85856257	12.09186572	14.41265638
44	H	-1.78588718	8.21887405	16.43028907	108	H	7.22758949	13.66284306	13.20119811
45	H	-0.01664541	8.31439545	16.22952147	109	H	6.33174935	12.33057648	12.44576277
46	H	-1.80850497	8.25671436	13.81764303	110	H	5.52460912	13.88718775	12.73752157
47	H	-0.03804157	8.24976504	13.87526678	111	S	3.66995861	15.59166150	23.26182209
48	H	-1.78111037	6.20911251	12.34577052	112	C	4.90349880	16.09200183	21.94846581
49	H	-0.77363090	7.48925243	11.64302594	113	C	4.55930269	17.41179372	21.25296883
50	H	-0.00771561	6.12448935	12.48778873	114	C	5.57927597	17.64717039	20.11996415
51	S	3.50291266	4.74696938	16.95540602	115	C	5.23596719	18.83029922	19.21080753
52	C	3.25071121	2.93607459	17.34479994	116	H	5.87114511	16.16896741	22.47117258
53	C	4.33178591	2.02810697	16.74409378	117	H	4.96151913	15.27505719	21.21749203
54	C	3.84125688	0.56791073	16.83737306	118	H	6.58207244	17.79358692	20.56403714
55	C	4.75286646	-0.45067334	16.14892877	119	H	5.63492443	16.73319859	19.50462157
56	H	3.16727295	2.81362778	18.43482456	120	H	5.25469402	19.78753010	19.75328523
57	H	2.27191330	2.69855333	16.90131926	121	H	5.95576295	18.90663201	18.38117943
58	H	3.72137581	0.29921172	17.90312999	122	H	4.23271039	18.70400261	18.77558747
59	H	2.83402002	0.50756517	16.38781664	123	S	0.78569351	12.23772941	15.34918318
60	H	5.73816210	-0.51463462	16.63340072	124	C	-0.79649458	11.39493916	14.82226023
61	H	4.30445810	-1.45558602	16.17987819	125	C	-1.86641862	12.38582370	14.35081933
62	H	4.91145490	-0.18659706	15.09093408	126	C	-3.19271526	11.62236172	14.15875431
63	S	0.98983369	9.30759820	26.24888010	127	C	-4.39242077	12.52372820	13.85530363

128	H	-0.51562774	10.70945252	14.00631407	206	H	5.82167981	7.98804190	28.83483206
129	H	-1.15877653	10.80149213	15.67183846	207	S	4.63981715	6.02925569	24.52753159
130	H	-3.06561047	10.88223855	13.34599791	208	C	4.31597837	6.15153240	26.36286417
131	H	-3.40158019	11.04839005	15.07806279	209	C	4.98907329	5.01256768	27.14119025
132	H	-4.28159494	13.05236017	12.89647355	210	C	4.42939164	4.99470270	28.57870792
133	H	-5.31965876	11.93298876	13.80149711	211	C	4.88627703	3.79976703	29.41903471
134	H	-4.51751022	13.27708846	14.64848633	212	H	4.64868470	7.13733741	26.71717783
135	S	-3.06424473	14.83920065	17.33620718	213	H	3.21927965	6.10789337	26.46641741
136	C	-3.88215806	16.35839007	18.03961989	214	H	4.71350040	5.93392946	29.08605974
137	C	-4.35453860	17.34433950	16.96421278	215	H	3.32668100	4.99543176	28.52462740
138	C	-4.89177883	18.60819986	17.66537650	216	H	5.97183511	3.81185132	29.59619961
139	C	-5.24012026	19.75747713	16.71632457	217	H	4.39189225	3.80399285	30.40258438
140	H	-4.73050346	15.98485448	18.63787758	218	H	4.63495637	2.84872267	28.92292496
141	H	-3.17800489	16.83731836	18.73149333	219	S	-0.09056924	17.79366460	24.25339380
142	H	-5.78207671	18.33497819	18.26208979	220	C	1.42767100	18.38863286	25.15726048
143	H	-4.13213826	18.95788954	18.38494905	221	C	1.79633178	19.83648572	24.81236149
144	H	-6.06872532	19.49737783	16.04097454	222	C	3.11327759	20.18598168	25.53438251
145	H	-5.54477148	20.65061143	17.28255270	223	C	3.71764988	21.53092263	25.12346692
146	H	-4.37267056	20.03370435	16.09562079	224	H	1.17964565	18.29550151	26.22821625
147	S	6.70484090	11.32572148	19.74409466	225	H	2.25267674	17.70069913	24.92425387
148	C	6.94671611	13.04942726	20.41561784	226	H	2.93391561	20.17639369	26.62616294
149	C	8.41934730	13.38987017	20.67838224	227	H	3.84890552	19.38789252	25.33367143
150	C	8.49188302	14.72892148	21.43825636	228	H	3.06263135	22.37459418	25.38624551
151	C	9.90170062	15.12200001	21.88729847	229	H	4.68295330	21.69368432	25.62699506
152	H	6.51206418	13.72364998	19.65891919	230	H	3.89657257	21.56439784	24.03711200
153	H	6.35133911	13.13482801	21.33578622	231	S	0.96178129	17.61944862	19.68089955
154	H	8.06715671	15.52708403	20.80234824	232	C	-0.52647954	18.56254071	19.07371314
155	H	7.84148760	14.65587005	22.32700063	233	C	-0.39632319	20.06847629	19.34155924
156	H	10.56812432	15.31089004	21.03283022	234	C	-1.75271861	20.74644585	19.06612652
157	H	9.87579615	16.04006312	22.49401744	235	C	-1.79465891	22.23521827	19.42108510
158	H	10.35436203	14.32778586	22.50215594	236	H	-0.59319626	18.35437076	17.99280079
159	S	-6.02452863	12.95694129	20.33817756	237	H	-1.41383807	18.14711646	19.57101627
160	C	-6.97711018	13.85414584	19.00705975	238	H	-2.01249933	20.61181582	17.99985453
161	C	-7.89355090	12.92092300	18.20625429	239	H	-2.52864176	20.21935902	19.64800035
162	C	-8.48972552	13.71198503	17.02480864	240	H	-1.10616603	22.82492066	18.79806343
163	C	-9.29363792	12.86026818	16.03892740	241	H	-2.80586651	22.64336048	19.27232593
164	H	-7.56289686	14.62892600	19.53052026	242	H	-1.51934357	22.39611211	20.47579374
165	H	-6.25360165	14.34285466	18.34211170	243	S	0.95058152	16.73837551	15.79168783
166	H	-9.12815968	14.52391020	17.42135242	244	C	0.99800492	16.18400882	14.00683359
167	H	-7.66396255	14.20134828	16.47967611	245	C	1.94321245	17.03096187	13.14424560
168	H	-10.19482645	12.43314587	16.50325494	246	C	1.63814551	16.73328970	11.66088711
169	H	-9.62035749	13.46492876	15.17939433	247	C	2.41761800	17.60179548	10.67027884
170	H	-8.68420324	12.02825156	15.65197068	248	H	1.26285848	15.11692843	13.97927518
171	S	8.10541593	9.06849496	23.63352199	249	H	-0.03782635	16.29592609	13.65441704
172	C	9.50091575	7.92638825	23.16063198	250	H	1.84439794	15.66528239	11.46118797
173	C	10.75956467	8.68240030	22.71836102	251	H	0.55653214	16.87785549	11.48996004
174	C	11.79810665	7.65820626	22.21877953	252	H	3.49933369	17.40945100	10.71780146
175	C	13.04941342	8.28119071	21.59442870	253	H	2.09239329	17.40167582	9.63796997
176	H	9.70423828	7.32859280	24.06536320	254	H	2.25452481	18.67281157	10.87186122
177	H	9.14404924	7.24926892	22.37260735	255	S	0.17710490	4.77387372	25.30309313
178	H	12.08978572	7.00373260	23.06193924	256	C	1.16894245	3.77278073	26.53055638
179	H	11.31326315	7.00471375	21.47388700	257	C	0.66646884	2.32755433	26.65877889
180	H	13.63461093	8.85171592	22.33068357	258	C	1.28817306	1.70609418	27.92742609
181	H	13.70853012	7.50263125	21.18132918	259	C	0.76986502	0.30566980	28.26339738
182	H	12.78215819	8.96474207	20.77266349	260	H	2.23124594	3.80284483	26.24830002
183	S	6.40606050	6.27482491	20.33812439	261	H	1.04456929	4.30177986	27.48764091
184	C	7.80142964	7.11787555	19.42710254	262	H	2.38687428	1.67489992	27.80702278
185	C	9.01857920	6.20336761	19.23136924	263	H	1.08805614	2.37704206	28.78177627
186	C	10.16961215	7.05413248	18.65457594	264	H	1.03879660	-0.42857457	27.49002153
187	C	11.49277104	6.30361313	18.47997672	265	H	1.19404578	-0.04772114	29.21559010
188	H	7.42162819	7.49111415	18.46509466	266	H	-0.32729414	0.30527128	28.36412539
189	H	8.06681322	7.99117581	20.04709112	267	S	-4.13810277	10.87567495	22.83039173
190	H	9.85204576	7.46830217	17.68086710	268	C	-3.98079394	11.39694042	24.61430951
191	H	10.32799943	7.92202708	19.31888143	269	C	-4.65584996	12.73993322	24.91522375
192	H	11.41984297	5.51742989	17.71396781	270	C	-4.37055168	13.08786728	26.39168058
193	H	12.29282059	6.99290928	18.16949718	271	C	-4.86926970	14.46570023	26.83289937
194	H	11.80901072	5.82649016	19.42131230	272	H	-4.45555673	10.59230202	25.19967595
195	S	5.59075685	11.52780506	24.62961356	273	H	-2.91291159	11.43363952	24.86697209
196	C	4.89051956	11.25902407	26.33619777	274	H	-4.82844546	12.30947189	27.03061667
197	C	5.69520815	10.23040945	27.14032287	275	H	-3.28098731	13.03240169	26.55890378
198	C	4.91922883	9.93493315	28.44060617	276	H	-5.96449486	14.54905999	26.76804497
199	C	5.59311628	8.92270258	29.36945619	277	H	-4.58442162	14.66542592	27.87758733
200	H	4.92409888	12.23801392	26.83845164	278	H	-4.42920778	15.26010230	26.21200171
201	H	3.84069536	10.95328594	26.23193748	279	S	2.22587113	4.01995748	21.13027614
202	H	4.77065403	10.88540753	28.98713773	280	C	3.97319982	3.56605764	21.58679900
203	H	3.91150508	9.57245506	28.17157720	281	C	4.08848368	2.23332643	22.33558341
204	H	6.53644864	9.30880140	29.78384235	282	C	5.55867472	2.04741746	22.76180929
205	H	4.93611278	8.67227357	30.21662995	283	C	5.80855718	0.83042632	23.65578551

284	H	4.51950304	3.53177159	20.62820321	362	H	-2.01965256	13.12698325	15.15678247
285	H	4.39220955	4.38294299	22.18850911	363	C	-1.43485173	13.12670127	13.08181310
286	H	6.18734522	1.97603192	21.85460636	364	H	-1.34293506	12.42363823	12.23545941
287	H	5.88312971	2.95855233	23.29317205	365	H	-0.45975229	13.61498753	13.22192972
288	H	5.59095687	-0.11488517	23.13680036	366	H	-2.16054433	13.90433966	12.80223022
289	H	6.86055313	0.79432760	23.97851279	367	H	-3.46746786	17.63493768	16.36850084
290	H	5.18210746	0.87025842	24.56123954	368	C	-5.38954513	16.71746424	16.02582646
291	S	-2.01632334	6.68970264	23.01416955	369	H	-5.00173475	15.79416342	15.57041331
292	C	-2.63484130	5.77969554	21.50694382	370	H	-5.66304462	17.40197555	15.20943756
293	C	-2.18560328	4.31388460	21.49370177	371	H	-6.30912166	16.46517775	16.58054362
294	C	-2.51934402	3.71028492	20.11451345	372	H	8.82439200	12.60345704	21.34469869
295	C	-1.97787504	2.29393863	19.90248829	373	C	9.23818485	13.40418817	19.38429212
296	H	-3.73420042	5.84763883	21.54212294	374	H	8.89490408	14.21546669	18.72054357
297	H	-2.27590322	6.31229291	20.61656749	375	H	10.30893307	13.55656754	19.58436212
298	H	-3.61772901	3.71314956	19.97854218	376	H	9.13135416	12.45235676	18.84182075
299	H	-2.10476525	4.37153051	19.33443498	377	H	-7.25573662	12.11805080	17.78803008
300	H	-2.43955459	1.56815704	20.58827015	378	C	-8.96966719	12.28278703	19.08906691
301	H	-2.17789046	1.95163192	18.87541070	379	H	-9.57400137	11.55683679	18.52635854
302	H	-0.88792636	2.26615345	20.05999259	380	H	-9.64836787	13.05458780	19.49117988
303	S	-3.28813493	9.99138437	17.93210876	381	H	-8.51953913	11.75195104	19.94142051
304	C	-3.83916549	8.42908124	18.78974587	382	H	10.47622321	9.32707580	21.86356148
305	C	-5.30110684	8.07418078	18.48760312	383	C	11.31285702	9.57035285	23.83715721
306	C	-5.72553734	6.90355661	19.39659167	384	H	10.54611863	10.26664333	24.20805548
307	C	-7.20344035	6.52090023	19.27958001	385	H	12.16757108	10.16854915	23.49059781
308	H	-3.15985494	7.63618994	18.43538510	386	H	11.64953204	8.95309038	24.68747103
309	H	-3.67661199	8.56286437	19.86915894	387	H	9.33075456	5.84078193	20.23124218
310	H	-5.09476456	6.02506984	19.16763932	388	C	8.69980378	4.98287667	18.36389575
311	H	-5.50945997	7.18274893	20.44252173	389	H	8.39181269	5.29343066	17.35204692
312	H	-7.44820048	6.12859999	18.28168711	390	H	7.87945199	4.39386731	18.79800014
313	H	-7.46308658	5.74158363	20.01269545	391	H	9.57213243	4.31948435	18.26743755
314	H	-7.85213988	7.39047215	19.47173380	392	H	5.74745956	9.29679610	26.54590906
315	S	-3.05064504	16.25817730	21.86445111	393	C	7.12383781	10.71477430	27.40575347
316	C	-3.61265092	16.61097783	23.61668576	394	H	7.11366198	11.61497602	28.04437016
317	C	-3.90470307	18.10213953	23.82215502	395	H	7.63279066	10.96870860	26.46419786
318	C	-4.08865881	18.35950581	25.33101352	396	H	7.72451118	9.94472584	27.91077810
319	C	-4.24990271	19.83571446	25.70288605	397	H	4.69960747	4.05979576	26.65476439
320	H	-4.50741567	16.00199709	23.80976935	398	C	6.51689965	5.12062908	27.11087684
321	H	-2.80356708	16.27333262	24.28097155	399	H	6.84997208	6.03873795	27.62270041
322	H	-4.96587409	17.78902891	25.68874927	400	H	6.99220646	4.26117583	27.60701197
323	H	-3.21041340	17.95163780	25.86074330	401	H	6.88951829	5.15880446	26.07669349
324	H	-5.16629958	20.27050712	25.27675661	402	H	1.98159633	19.88138393	23.72210580
325	H	-4.30493939	19.95726764	26.79560621	403	C	0.66870644	20.81413896	25.15736043
326	H	-3.39296191	20.42661945	25.34278272	404	H	-0.26652465	20.53468378	24.65066661
327	H	-0.04896166	6.07846880	15.07235486	405	H	0.47721820	20.81673353	26.24408820
328	C	-2.18868611	5.80481191	15.12889061	406	H	0.91931859	21.84070194	24.85262775
329	H	-2.20190003	5.09435203	14.28938086	407	H	-0.17214668	20.19389543	20.41862029
330	H	-3.11143577	6.40678828	15.08208741	408	C	0.74417764	20.68627510	18.52694090
331	H	-2.20927112	5.22037093	16.06094583	409	H	1.69112309	20.15803743	18.71312773
332	H	4.42484965	2.28489785	15.67035443	410	H	0.52706654	20.61980187	17.44728315
333	C	5.69489327	2.22220799	17.41175227	411	H	0.89721420	21.74482954	18.78225771
334	H	5.65021059	1.92713997	18.47355026	412	H	1.70419814	18.09660482	13.33056531
335	H	6.01276224	3.27408552	17.37010050	413	C	3.41382955	16.78937803	13.49139109
336	H	6.47380410	1.61914857	16.92215819	414	H	4.07953345	17.45460584	12.92166460
337	H	-1.19100563	7.99970364	27.73228190	415	H	3.60674694	16.96149402	14.56081557
338	C	-0.68792704	9.61324752	29.07506331	416	H	3.69193976	15.74727828	13.26306158
339	H	-0.90592490	10.68548722	29.21370642	417	H	-0.43085721	2.36807651	26.80532063
340	H	-1.02901355	9.07675458	29.97242589	418	C	0.96371142	1.49908415	25.40621892
341	H	0.40417102	9.49251123	29.00862149	419	H	0.52744245	0.49163603	25.47571136
342	H	6.19127908	7.27717490	16.32963861	420	H	0.55621164	1.97710558	24.50330395
343	C	5.71177751	7.21599967	14.23025814	421	H	2.05258969	1.39186012	25.26628570
344	H	6.36503913	6.35525738	14.02716020	422	H	-4.17299655	13.50681471	24.28020907
345	H	4.68848617	6.83387962	14.35622662	423	C	-6.15438520	12.71026881	24.60104292
346	H	5.72607151	7.87442156	13.34440113	424	H	-6.66870048	11.97540334	25.24441208
347	H	1.32930181	15.12981061	27.29923002	425	H	-6.62070539	13.69226615	24.76733906
348	C	0.51958342	13.78976627	28.78325878	426	H	-6.33637234	12.42949001	23.55302450
349	H	-0.51216815	13.81020923	28.40059069	427	C	3.47595318	2.31889531	23.25378925
350	H	0.58509038	14.51822362	29.60482819	428	C	3.56379435	1.05696951	21.50764044
351	H	0.70998383	12.78620747	29.19931388	429	H	3.57365918	0.11977284	22.08291683
352	H	4.76809888	14.46652818	15.13537283	430	H	2.52931045	1.23495976	21.17769673
353	C	6.79528115	14.61100279	15.85314211	431	H	4.18811378	0.91093070	20.60964081
354	H	7.16468094	15.12365573	14.95304616	432	H	-1.08421877	4.29774836	21.61132803
355	H	7.60029876	13.95897963	16.23215155	433	C	-2.80602425	3.52114918	22.64809482
356	H	6.59225449	15.37934463	16.61412499	434	H	-2.57569376	3.98690336	23.61803477
357	H	3.56376969	17.29819418	20.78745690	435	H	-2.42541128	2.48975579	22.67720606
358	C	4.50636166	18.58200835	22.23715907	436	H	-3.90404195	3.47795059	22.54048396
359	H	4.19530133	19.51101530	21.73858486	437	H	-5.91711141	8.95267698	18.76089475
360	H	5.49630655	18.75066767	22.69591684	438	C	-5.51517400	7.76724738	17.00236594
361	H	3.78737510	18.38165204	23.04378235	439	H	-4.96003340	6.85902116	16.71447933

440	H	-6.57808263	7.60509051	16.77072438	444	H	-5.27132169	19.64222433	23.07530248
441	H	-5.15993765	8.59813330	16.37422625	445	H	-4.97042188	18.31782046	21.93052740
442	H	-3.01208312	18.66748738	23.49250846	446	H	-6.02862394	18.04895283	23.33918139
443	C	-5.11142756	18.55703240	22.99532976					

Isomer 2a

1	Au	-0.11240000	0.01830000	1.95492995	70	H	8.55097961	0.93640000	4.08050013
2	Au	-0.02853000	0.03835000	-2.23615003	71	H	8.14282036	-0.56819999	4.91307020
3	Au	-1.02493000	-1.69645000	-0.16605000	72	H	10.54642963	-0.16903000	3.01323009
4	Au	-1.09686995	1.70730996	-0.15380999	73	H	10.59624004	-0.37996000	4.77360010
5	Au	1.89905000	0.05633000	-0.10353000	74	H	10.08170986	-1.72904003	3.73444009
6	Au	-2.83603001	-0.10838000	-1.69868004	75	S	-3.46439004	-3.91497993	1.88532996
7	Au	1.23901999	2.51215005	-1.61188996	76	C	-3.38664007	-5.59393978	2.70890999
8	Au	1.31098998	2.42580009	1.40204000	77	C	-4.36620998	-5.70323992	3.88347006
9	Au	1.26275003	-2.41926003	1.38627005	78	C	-4.11368990	-7.03572989	4.61742020
10	Au	-2.89197993	0.03047000	1.32422996	79	C	-4.91332006	-7.19675016	5.91280985
11	Au	1.44511998	-2.32467008	-1.63739002	80	H	-3.64192009	-6.32931995	1.92908001
12	Au	-1.31562996	-2.52151990	-2.94706988	81	H	-2.35108995	-5.77186012	3.02906990
13	Au	-1.59679997	2.42341995	-2.91427994	82	H	-4.34609985	-7.87110996	3.92987990
14	Au	2.73536992	-0.06120000	2.66488004	83	H	-3.03773999	-7.10769987	4.84967995
15	Au	-1.61318004	-2.44773006	2.58846998	84	H	-5.99747992	-7.23043013	5.72796011
16	Au	-1.51554000	2.54671001	2.58691001	85	H	-4.63807011	-8.12932014	6.42900991
17	Au	2.85762000	0.19101000	-2.83628011	86	H	-4.71299982	-6.36114979	6.60228014
18	Au	-1.80332005	-0.21036001	-4.46165991	87	S	-1.82201004	4.87806988	1.84371996
19	Au	0.69314998	1.75901997	-4.39598989	88	C	-3.29627991	5.68996000	2.66062999
20	Au	0.93207002	1.48838997	4.16405010	89	C	-2.89728999	6.53138018	3.87874007
21	Au	0.57656002	-1.65429997	4.15855980	90	C	-4.18099022	7.02564001	4.57528019
22	Au	-1.95106006	0.22719000	4.11343002	91	C	-3.93706989	7.73161983	5.91143990
23	Au	1.13133001	-1.36295998	-4.41556978	92	H	-3.75398993	6.33113003	1.89026999
24	Au	-2.44385004	-4.29664993	-0.19866000	93	H	-4.01495981	4.90458012	2.93206000
25	Au	-2.67102003	4.23720980	-0.25453001	94	H	-4.71927023	7.70542002	3.88772988
26	Au	4.86793995	0.08085000	0.01074000	95	H	-4.84221983	6.15868998	4.74396992
27	Au	-4.38853979	-2.02169991	-4.08450985	96	H	-3.35332990	8.65653992	5.78996992
28	Au	0.43651000	4.87822008	-3.97291994	97	H	-4.89062023	8.00512028	6.38898993
29	Au	3.72308993	2.93692994	3.79232001	98	H	-3.39070010	7.07473993	6.60692978
30	Au	0.45091999	-4.77944994	3.72024012	99	S	4.97664022	1.18454003	-2.06417990
31	Au	-4.57458019	1.91404998	3.60807991	100	C	6.46404982	0.40233999	-2.88527012
32	Au	3.95026994	-2.71254992	-3.91665006	101	C	6.96127987	1.22144997	-4.08229017
33	Au	-1.56067002	-2.92361999	-6.02759981	102	C	8.06779003	0.42260000	-4.80036020
34	Au	-1.84407997	2.99234009	-5.93778992	103	C	8.54747009	1.05403996	-6.10963011
35	Au	3.27507997	-0.01604000	5.71821022	104	H	7.24605989	0.34895000	-2.11033010
36	Au	-1.91004002	-2.91896009	5.64588022	105	H	6.19646978	-0.62119001	-3.18168998
37	Au	-1.84686995	1.91404998	5.63430977	106	H	8.92440033	0.30181000	-4.11011982
38	Au	3.46984005	0.23683999	-5.87140989	107	H	7.68585014	-0.59086001	-5.01000023
39	S	-1.55106997	-4.88501978	-2.29339004	108	H	9.02715969	2.03077006	-5.94568014
40	C	-3.01086998	-5.69723988	-3.13799000	109	H	9.28283978	0.40561000	-6.61020994
41	C	-2.58972001	-6.53088999	-4.35355997	110	H	7.70502996	1.20275998	-6.80364990
42	C	-3.85995007	-7.02265978	-5.07612991	111	S	-5.13204002	-0.77829999	-2.22534990
43	C	-3.59248996	-7.69364977	-6.42543983	112	C	-5.57722998	-2.02995992	-0.91668999
44	H	-3.48135996	-6.34238005	-2.37887001	113	C	-7.00705004	-2.57258010	-1.04753995
45	H	-3.72502995	-4.91031981	-3.41679001	114	C	-7.40748978	-3.19826007	0.30555001
46	H	-4.39812994	-7.72389984	-4.41048002	115	C	-8.85832024	-3.68073010	0.37568000
47	H	-4.52826023	-6.15977001	-5.23584986	116	H	-4.82810020	-2.83640003	-0.92493999
48	H	-2.98691010	-8.60630035	-6.32139015	117	H	-5.46567011	-1.47878003	0.02916000
49	H	-4.53712988	-7.97970009	-6.91337013	118	H	-6.72307014	-4.03819990	0.52144998
50	H	-3.06075001	-7.00639009	-7.10265017	119	H	-7.23651981	-2.44905996	1.09792995
51	S	-3.60224009	3.74505997	-2.36282992	120	H	-9.05405998	-4.50380993	-0.32745001
52	C	-3.56187010	5.32120991	-3.35716009	121	H	-9.09685040	-4.04717016	1.38589001
53	C	-4.80802011	6.19688988	-3.16339993	122	H	-9.55906963	-2.86254001	0.14245000
54	C	-4.86610985	7.22007990	-4.31767988	123	S	1.86924005	4.83095980	-2.10356998
55	C	-6.13152981	8.08059978	-4.33663988	124	C	1.00934994	5.84669018	-0.79636002
56	H	-2.63817000	5.87278986	-3.12869000	125	C	1.30851996	7.34922981	-0.88938999
57	H	-3.50271010	4.97746992	-4.40113020	126	C	0.96480000	7.99069023	0.47187999
58	H	-3.97293997	7.86990976	-4.26389980	127	C	1.30676997	9.47902012	0.57367003
59	H	-4.78913021	6.67216015	-5.27308989	128	H	-0.07014000	5.63918018	-0.83552003
60	H	-6.19679022	8.73491001	-3.45495009	129	H	1.39183998	5.44220018	0.15267999
61	H	-6.14997005	8.72597027	-5.22805023	130	H	-0.11129000	7.83949995	0.67238998
62	H	-7.03622007	7.45207977	-4.35903978	131	H	1.50577998	7.43949986	1.26063001
63	S	4.94175005	-1.00325000	2.10148001	132	H	0.71319997	10.08708000	-0.12517001
64	C	6.24049997	-0.11848000	3.10355997	133	H	1.10748005	9.85513973	1.58870995
65	C	7.67424011	-0.58095998	2.80173993	134	H	2.37240005	9.65620995	0.35404000
66	C	8.57826996	-0.16480000	3.98201990	135	S	2.92682004	4.18518019	1.95931995
67	C	10.03005981	-0.63599998	3.86491990	136	C	4.26484013	4.06443024	0.66430002
68	H	6.12857008	0.96688002	2.96620011	137	C	5.34243011	5.14916992	0.79890001
69	H	5.97849989	-0.35755000	4.14598989	138	C	6.10069990	5.24387980	-0.54233998

139	C	7.13750982	6.36878014	-0.60233003	217	H	7.50030994	-5.20363998	5.71646976
140	H	4.69400978	3.05175996	0.68831003	218	H	7.29180002	-3.62159991	6.50252008
141	H	3.73066998	4.17767000	-0.29091001	219	S	-3.02174997	-0.87645000	6.00480986
142	H	6.58978987	4.27331018	-0.74190003	220	C	-4.73474979	-1.24775004	5.36745024
143	H	5.36152983	5.38920021	-1.34894001	221	C	-5.54968023	-2.16120005	6.29079008
144	H	7.96089983	6.20919991	0.10933000	222	C	-6.88967991	-2.47852993	5.59715986
145	H	7.58013010	6.43702984	-1.60808003	223	C	-7.75640011	-3.49853992	6.34034014
146	H	6.67670012	7.34331989	-0.37323999	224	H	-5.22204018	-0.26284999	5.25554991
147	S	1.93954003	-4.71995020	1.89411998	225	H	-4.63397980	-1.68701005	4.36550999
148	C	1.14303994	-5.75074005	0.55931002	226	H	-7.45554018	-1.53723001	5.46409988
149	C	1.44295001	-7.25117016	0.67750001	227	H	-6.67662001	-2.85654998	4.58323002
150	C	1.13935995	-7.90756989	-0.68647999	228	H	-8.10416031	-3.11437988	7.31106997
151	C	1.49422002	-9.39435959	-0.76551998	229	H	-8.64879990	-3.75602007	5.74947977
152	H	0.06140000	-5.54803991	0.54900002	230	H	-7.19714022	-4.42926979	6.52845001
153	H	1.56660998	-5.35131979	-0.37458000	231	S	0.45980000	2.91312003	6.08432007
154	H	0.06814000	-7.76526022	-0.91727000	232	C	1.04489994	4.59472990	5.52608013
155	H	1.69772005	-7.36038017	-1.46589994	233	C	0.61983001	5.73894978	6.45436001
156	H	0.88595998	-10.00063992	-0.07779000	234	C	1.11452997	7.06448984	5.84049988
157	H	1.32516003	-9.78061008	-1.78222001	235	C	0.62459999	8.31846046	6.56900978
158	H	2.55469990	-9.56190014	-0.51556998	236	H	2.14532995	4.51566982	5.47606993
159	S	-5.23557997	0.59496002	1.76933002	237	H	0.67575002	4.75927019	4.50496006
160	C	-5.70225000	1.81306005	0.43549001	238	H	2.22047997	7.05692005	5.81713009
161	C	-7.16300011	2.27690005	0.51310003	239	H	0.78473002	7.10677004	4.78855991
162	C	-7.54023981	2.90052009	-0.84776002	240	H	1.03639996	8.39151001	7.58683014
163	C	-9.01369953	3.29643011	-0.97302997	241	H	0.92629999	9.22723007	6.02618980
164	H	-4.99949980	2.65962005	0.46454000	242	H	-0.47404000	8.32398987	6.65068007
165	H	-5.52860022	1.26538002	-0.50294000	243	S	2.16031003	2.14326000	-6.29967022
166	H	-6.89841986	3.78280997	-1.02338004	244	C	3.26770997	3.53004003	-5.72473001
167	H	-7.29188013	2.17597008	-1.64251006	245	C	4.45009995	3.80580997	-6.66142988
168	H	-9.28649044	4.09969997	-0.27246001	246	C	5.31190014	4.91976976	-6.03322983
169	H	-9.23443031	3.65681005	-1.98934996	247	C	6.61750984	5.20249987	-6.78067017
170	H	-9.67273998	2.43570995	-0.77395999	248	H	2.60868001	4.41325998	-5.65195990
171	S	3.16476989	-4.00729990	-2.10877991	249	H	3.61494994	3.28899002	-4.71090984
172	C	4.43212986	-3.78391004	-0.75860000	250	H	4.71024990	5.84589005	-5.97399998
173	C	5.59734011	-4.77978992	-0.84021997	251	H	5.54501009	4.63689995	-4.99268007
174	C	6.32085991	-4.78471994	0.52366000	252	H	6.43598986	5.60680006	-7.78788996
175	C	7.43212986	-5.83101988	0.64216000	253	H	7.22683001	5.93979979	-6.23565006
176	H	4.78131008	-2.74009991	-0.76686001	254	H	7.21741009	4.28481007	-6.88970995
177	H	3.86557007	-3.93957996	0.17178001	255	S	-3.88283992	-3.33181000	-5.97909990
178	H	6.73301983	-3.77658010	0.71016997	256	C	-4.51929998	-2.41628003	-7.48028994
179	H	5.57138014	-4.96157980	1.31421006	257	C	-5.96119022	-2.79942012	-7.84146976
180	H	8.25926018	-5.63601017	-0.05621000	258	C	-6.26507998	-2.25661993	-9.25428009
181	H	7.85445976	-5.83725977	1.65910006	259	C	-7.62188005	-2.68794990	-9.81684017
182	H	7.04606009	-6.84230995	0.43516999	260	H	-4.40326023	-1.33497000	-7.31642008
183	S	0.76065999	-2.76556993	-6.37175989	261	H	-3.83652997	-2.71176004	-8.29108047
184	C	1.35192001	-4.44302988	-5.80648994	262	H	-6.20524979	-1.15306997	-9.23301983
185	C	0.98211998	-5.58349991	-6.76275015	263	H	-5.46816015	-2.59715009	-9.93931007
186	C	1.46656001	-6.90890980	-6.14110994	264	H	-8.45825005	-2.28343010	-9.22848034
187	C	1.04103005	-8.16036987	-6.91300011	265	H	-7.74435997	-2.33242011	-10.85116005
188	H	2.44804001	-4.34658003	-5.71305990	266	H	-7.71429014	-3.78595996	-9.82656002
189	H	0.94533002	-4.62381983	-4.80230999	267	S	-0.97551000	5.18435001	-5.83299017
190	H	2.56928992	-6.88242006	-6.05634022	268	C	0.14078000	5.26867008	-7.32296991
191	H	1.07964003	-6.97241020	-5.10999012	269	C	-0.64985001	5.32412004	-8.63669968
192	H	1.51238000	-8.21187973	-7.90596008	270	C	0.33825001	5.19856977	-9.81367970
193	H	1.32669997	-9.07143974	-6.36537981	271	C	-0.33392000	5.06377983	-11.18266010
194	H	-0.05082000	-8.18284035	-7.05831003	272	H	0.74739999	6.18042994	-7.18912983
195	S	-2.94047999	0.93927002	-6.29249001	273	H	0.79973000	4.39019012	-7.30374002
196	C	-4.61543989	1.29821002	-5.55236006	274	H	1.00909996	6.07796001	-9.81474018
197	C	-5.41372013	2.36435008	-6.31252003	275	H	0.97920001	4.31698990	-9.64083004
198	C	-6.68559980	2.68823004	-5.50265980	276	H	-0.90705001	5.96330976	-11.45090961
199	C	-7.49897003	3.86241007	-6.05329990	277	H	0.41786000	4.90483999	-11.97068977
200	H	-5.14602995	0.33008000	-5.55037022	278	H	-1.02314997	4.20432997	-11.19859982
201	H	-4.46165991	1.59995997	-4.50746012	279	S	4.71234989	1.85304999	5.63595009
202	H	-7.32099009	1.78435004	-5.45557022	280	C	4.19417000	2.84457994	7.12645006
203	H	-6.38836002	2.91027999	-4.46294022	281	C	4.57193995	2.16395998	8.44775009
204	H	-7.90082979	3.65293002	-7.05569983	282	C	3.97211003	2.98433995	9.60708046
205	H	-8.35363007	4.08629990	-5.39673996	283	C	4.10981989	2.32326007	10.98087025
206	H	-6.88103008	4.77187014	-6.12099981	284	H	4.70377016	3.81787992	7.02433014
207	S	2.05995989	-2.00137997	6.06154013	285	H	3.10798001	2.99829006	7.07123995
208	C	3.25847006	-3.27934003	5.41855001	286	H	4.45118999	3.98140001	9.62570953
209	C	4.48120022	-3.48101997	6.32114983	287	H	2.90231991	3.15550995	9.39760971
210	C	5.47097015	-4.41675997	5.59813023	288	H	5.16202021	2.21237993	11.28090000
211	C	6.80921984	-4.59520006	6.32004976	289	H	3.60803008	2.92529011	11.75364017
212	H	2.67162991	-4.21096992	5.33221006	290	H	3.64842010	1.32272005	10.98326015
213	H	3.56035995	-2.97728992	4.40619993	291	S	-0.98066998	-5.08420992	5.56618023
214	H	4.99229002	-5.40319014	5.45300007	292	C	0.13750000	-5.12516022	7.05688000
215	H	5.65660000	-4.01261997	4.58794022	293	C	-0.64528000	-5.13493013	8.37576962
216	H	6.68948984	-5.09929991	7.29051018	294	C	0.35323000	-4.98131990	9.54069996

295	C	-0.30682999	-4.80007982	10.91009998	371	H	5.72006989	4.74745989	2.91265011
296	H	0.74089998	-6.04223013	6.94829988	372	C	0.66544998	-7.90862989	1.82053995
297	H	0.79870999	-4.24931002	7.00641012	373	H	0.94586003	-8.96459961	1.95005000
298	H	1.01835001	-5.86474991	9.56285954	374	H	-0.41874999	-7.86231995	1.62198997
299	H	0.99843001	-4.10988998	9.33528996	375	H	0.85268998	-7.39329004	2.77537990
300	H	-0.88515002	-5.68636990	11.20919037	376	H	2.52761006	-7.36576996	0.87322003
301	H	0.45247999	-4.62432003	11.68725967	377	C	-7.40637016	3.24006009	1.67797995
302	H	-0.98885000	-3.93482995	10.90581036	378	H	-8.47266960	3.49048996	1.78346002
303	S	-4.17745018	3.31803012	5.45620012	379	H	-6.84602022	4.17793989	1.52393997
304	C	-4.84873009	2.38256001	6.92226982	380	H	-7.79523993	1.37820995	0.65823001
305	C	-4.59572983	3.11063004	8.24818993	381	H	-7.07002020	2.80241990	2.63013005
306	C	-5.00365019	2.17489004	9.40408993	382	C	6.54852009	-4.46694994	-1.99812996
307	C	-4.67909002	2.71924996	10.79755974	383	H	6.00622988	-4.41882992	-0.65848998
308	H	-5.92983007	2.27390003	6.73297024	384	H	7.33410978	-5.23097992	-2.09753990
309	H	-4.38212013	1.38788998	6.92889977	385	H	7.03632021	-3.49020004	-1.84001994
310	H	-6.08749008	1.96570003	9.33187008	386	H	5.16769981	-5.78911018	-0.99687999
311	H	-4.49006987	1.20766997	9.26766014	387	C	1.53954995	-5.36431980	-8.17183971
312	H	-5.25359011	3.62837005	11.02869987	388	H	2.64258003	-5.35910988	-8.15515041
313	H	-4.91737986	1.97318995	11.57094955	389	H	1.21385002	-6.15709019	-8.86153984
314	H	-3.60810995	2.96247005	10.88547993	390	H	-0.12304000	-5.61945009	-6.82419014
315	S	4.95490980	-1.58754003	-5.72702980	391	H	1.20033002	-4.40266991	-8.58535957
316	C	4.52616978	-2.60590005	-7.22880983	392	C	-5.72513008	1.93748999	-7.74966002
317	C	4.93669987	-1.92972004	-8.54238033	393	H	-4.80520010	1.66385996	-8.28857040
318	C	4.40656996	-2.78186989	-9.71304989	394	H	-6.21716976	2.74228001	-8.31540012
319	C	4.58297014	-2.13615990	-11.08979034	395	H	-6.39577007	1.06197000	-7.75294018
320	H	5.05720997	-3.56378007	-7.09514999	396	H	-4.79005003	3.27871990	-6.34608984
321	H	3.44308996	-2.78811002	-7.21422005	397	C	4.08846998	-3.99784994	7.70782995
322	H	4.91191006	-3.76584005	-9.69769955	398	H	3.62841010	-4.99779987	7.63136005
323	H	3.33406997	-2.97904992	-9.54504013	399	H	4.95983982	-4.07368994	8.37469006
324	H	5.64333010	-2.00622010	-11.35118961	400	H	3.36139011	-3.32485008	8.18599033
325	H	4.12421989	-2.75935006	-11.87240982	401	H	4.97152996	-2.49495006	6.43957996
326	H	4.10054016	-1.14628005	-11.12401009	402	C	-5.74490976	-1.55066001	7.68127012
327	C	-1.67332006	-7.69092989	-3.94938993	403	H	-6.34114981	-0.62503999	7.61660004
328	H	-1.31110001	-8.24551964	-4.82639980	404	H	-4.77726984	-1.30061996	8.14140034
329	H	-0.79622000	-7.32949018	-3.39326000	405	H	-6.26591015	-2.24450994	8.35721970
330	H	-2.21597004	-8.40003967	-3.29989004	406	H	-4.98902988	-3.11021996	6.39859009
331	H	-2.04310989	-5.86283016	-5.04784012	407	H	-0.48732001	5.76141977	6.46782017
332	C	-4.83291006	6.87404013	-1.79075003	408	C	1.11898005	5.54124022	7.88823986
333	H	-3.99770999	7.58933020	-1.70025003	409	H	2.22168994	5.54768991	7.91827011
334	H	-4.72806978	6.13360977	-0.98330998	410	H	0.77278000	4.58057022	8.29819965
335	H	-5.77314997	7.42122984	-1.62511003	411	H	0.75616002	6.33814001	8.55414963
336	H	-5.69605017	5.54067993	-3.25082994	412	C	3.99608994	4.15621996	-8.08108044
337	C	8.18929005	-0.03671000	1.46647000	413	H	3.36047006	3.36193991	-8.49995041
338	H	7.48621988	-0.26719999	0.65047002	414	H	3.41466999	5.09328985	-8.08069038
339	H	9.16586018	-0.46803999	1.20088005	415	H	4.85343981	4.28809977	-8.75732040
340	H	8.29788971	1.06007004	1.51415002	416	H	5.06207991	2.88446999	-6.70511007
341	H	7.66868019	-1.68763995	2.75597000	417	H	-6.00985003	-3.90531993	-7.88813019
342	H	-4.13759995	-4.88108015	4.58984995	418	C	-6.97594023	-2.31002998	-6.80519009
343	C	-5.82002020	-5.57025003	3.41704988	419	H	-6.99806023	-1.20802999	-6.77700996
344	H	-5.97104979	-4.63963985	2.85071993	420	H	-6.72160006	-2.66506004	-5.79595995
345	H	-6.51845980	-5.56474018	4.26577997	421	H	-7.99116993	-2.66509008	-7.03620005
346	H	-6.09122992	-6.41447020	2.75911999	422	H	-1.31234002	4.43722010	-8.65721989
347	C	-1.97424996	7.68944979	3.48500991	423	C	-1.51322997	6.58543015	-8.73246002
348	H	-1.08574998	7.32427979	2.95015001	424	H	-0.87751001	7.48689985	-8.76453018
349	H	-2.50376010	8.39361954	2.81957006	425	H	-2.13877010	6.57758999	-9.63632965
350	H	-1.63028002	8.25020981	4.36538982	426	H	-2.18267012	6.67502022	-7.86394978
351	H	-2.36268997	5.86810017	4.58684015	427	H	4.08765984	1.16802001	8.45203018
352	C	7.44025993	2.61213994	-3.65197992	428	C	6.08543015	1.97525001	8.58518028
353	H	7.72217989	3.22881007	-4.51702976	429	H	6.49409008	1.41268003	7.73277998
354	H	6.65610981	3.14779997	-3.09740996	430	H	6.34092999	1.42402995	9.50152969
355	H	8.32231045	2.52754998	-2.99312997	431	H	6.59561014	2.95323992	8.62100029
356	H	6.11427021	1.33427000	-4.78780985	432	C	-1.51818001	-6.38541985	8.51531982
357	H	-7.67969990	-1.71196997	-1.23403001	433	H	-0.89051998	-7.29193020	8.56348038
358	C	-7.14707994	-3.56456995	-2.20526004	434	H	-2.13391995	-6.34842014	9.42525005
359	H	-6.78205013	-3.12628007	-3.14657998	435	H	-2.19876003	-6.49127007	7.65782022
360	H	-8.19386005	-3.86573005	-2.36040998	436	H	-1.30016005	-4.24217987	8.37362003
361	H	-6.55251980	-4.47245979	-2.00620008	437	H	-3.50502992	3.28555989	8.32499981
362	C	0.56217998	8.01780033	-2.04706001	438	C	-5.31549978	4.46136999	8.30422974
363	H	-0.52595001	7.98473978	-1.86882997	439	H	-6.40959978	4.31835985	8.28310966
364	H	0.76190001	7.50148010	-2.99871993	440	H	-5.04007006	5.09147978	7.44611979
365	H	0.85740000	9.07059956	-2.16932988	441	H	-5.06160021	5.01644993	9.21874046
366	H	2.39779997	7.46863985	-1.05356002	442	H	4.42487001	-0.94849002	-8.57896996
367	H	4.82838011	6.11700010	0.96385002	443	C	6.44841003	-1.69994998	-8.62224007
368	C	6.28400993	4.88970995	1.97783005	444	H	6.80577993	-1.11430001	-7.76315022
369	H	6.98317003	5.72518015	2.13243008	445	H	6.72565985	-1.15344000	-9.53501034
370	H	6.87538004	3.97515011	1.80075002	446	H	6.98726988	-2.66311002	-8.62304974

Isomer 2b

1	Au	0.06985700	0.00573600	1.99666202	77	C	-9.98912811	1.31388104	2.60267591
2	Au	0.04473300	0.07141300	-2.14765096	78	C	-8.23209190	-1.26667297	2.68012691
3	Au	1.04370201	-1.70433497	-0.10872300	79	H	-5.90235186	1.32799196	2.91235709
4	Au	1.07919300	1.75804996	-0.05670900	80	H	-6.19974995	0.00248700	4.06419802
5	Au	-1.94535100	0.06101100	-0.06092700	81	H	-7.66342306	0.36658600	1.38884997
6	Au	2.83780789	-0.00716300	-1.60182798	82	H	-8.06943512	2.20236611	3.03273797
7	Au	-1.28130305	2.50680995	-1.53806698	83	H	-8.59477043	1.02364302	4.24023199
8	Au	-1.33981705	2.42349195	1.47687495	84	H	-9.98094559	1.50274503	1.51737702
9	Au	-1.30532598	-2.40594602	1.40900004	85	H	-10.54009914	2.13795805	3.08149910
10	Au	2.85386705	0.02228700	1.41771495	86	H	-10.55942059	0.38993701	2.78139997
11	Au	-1.40452695	-2.31310606	-1.60603404	87	H	-7.56977320	-2.01339889	2.21845198
12	Au	1.38693404	-2.42633200	-2.88514090	88	H	-9.23155689	-1.38404202	2.23679590
13	Au	1.52563298	2.52509689	-2.80583811	89	H	-8.30744553	-1.49786794	3.75669599
14	Au	-2.77386689	-0.01915500	2.70431995	90	S	3.33679700	-3.99996209	2.03044605
15	Au	1.51117003	-2.47695708	2.64117408	91	C	3.01681709	-5.63740291	2.85936809
16	Au	1.48606300	2.46136808	2.71257401	92	C	3.84763694	-6.78935099	2.28242493
17	Au	-2.81322694	0.15092200	-2.81382489	93	C	3.36178589	-8.11079025	2.91083694
18	Au	1.84163105	-0.07380700	-4.37297392	94	C	3.99653196	-9.36619282	2.30674505
19	Au	-0.70762902	1.75000203	-4.33640814	95	C	5.34925079	-6.56239891	2.48205805
20	Au	-0.94036102	1.46907902	4.24300003	96	H	1.94124699	-5.85109997	2.78686595
21	Au	-0.68803799	-1.65227199	4.19835997	97	H	3.26099300	-5.47412109	3.92282701
22	Au	1.88814604	0.10461800	4.20624924	98	H	3.63815594	-6.83349705	1.19561100
23	Au	-1.01916301	-1.35508502	-4.38158894	99	H	2.26583195	-8.16968727	2.79236293
24	Au	2.50257993	-4.31168079	-0.15611500	100	H	3.55295396	-8.08242989	3.99991298
25	Au	2.61030889	4.32745790	-0.01335200	101	H	3.83110905	-9.40592194	1.21842694
26	Au	-4.92813683	0.09621200	-0.04317700	102	H	3.55705690	-10.27568340	2.74505210
27	Au	4.51777077	-1.79898095	-4.01897621	103	H	5.08112383	-9.40583611	2.48635292
28	Au	-0.56703401	4.91510391	-3.87314200	104	H	5.66017008	-5.59580612	2.05925703
29	Au	-3.74494290	3.01428199	3.86661291	105	H	5.94562006	-7.34830904	1.99639595
30	Au	-0.62105203	-4.83361292	3.72561407	106	H	5.59843683	-6.56045914	3.55729389
31	Au	4.62026691	1.73117495	3.80025101	107	S	1.93136299	4.82026386	2.19171000
32	Au	-3.85348701	-2.83158112	-3.94472694	108	C	3.51603198	5.29077578	3.04914999
33	Au	1.71828794	-2.79963899	-5.97138977	109	C	4.12323809	6.60597277	2.54748297
34	Au	1.72448206	3.11153889	-5.85702085	110	C	5.51171923	6.78139591	3.19517899
35	Au	-3.27602291	0.07655900	5.80136681	111	C	6.30001497	7.98701620	2.67851710
36	Au	1.70221305	-3.07820797	5.71217012	112	C	3.19841290	7.79768085	2.81403804
37	Au	1.90725601	2.84519601	5.78244019	113	H	4.22466898	4.45895481	2.93249893
38	Au	-3.38178802	0.06237500	-5.89448214	114	H	3.25294089	5.36625290	4.11766815
39	S	1.76994896	-4.79259777	-2.34738493	115	H	4.26869583	6.50813103	1.45387101
40	C	3.32407594	-5.34193516	-3.21440601	116	H	6.09799385	5.86344910	3.01354694
41	C	3.82829404	-6.71277905	-2.74661398	117	H	5.38887215	6.85626888	4.29192591
42	C	5.22122908	-6.96178007	-3.35972595	118	H	6.41482210	7.94269323	1.58371401
43	C	5.89827681	-8.24869347	-2.88103294	119	H	7.30833483	8.01194763	3.11993194
44	C	2.83214092	-7.82574320	-3.08653998	120	H	5.80805111	8.93852425	2.92926311
45	H	4.08835793	-4.56624222	-3.06895399	121	H	2.20051003	7.62440777	2.38480997
46	H	3.06595612	-5.36833906	-4.28639984	122	H	3.59625793	8.72457886	2.37549710
47	H	3.94638991	-6.66568804	-1.64627898	123	H	3.08011508	7.95822001	3.89939404
48	H	5.86798620	-6.10213280	-3.11238909	124	S	-5.03699493	1.00294602	-2.21891499
49	H	5.13109207	-6.97467899	-4.46202612	125	C	-6.30361700	-0.06313900	-3.07192707
50	H	5.97540379	-8.26786900	-1.78217995	126	C	-7.72633696	0.11743300	-2.53112102
51	H	6.91752911	-8.32901764	-3.28908300	127	C	-8.63814068	-0.93359101	-3.19555497
52	H	5.34604883	-9.14584064	-3.19697905	128	C	-10.06021595	-0.98396802	-2.63211393
53	H	1.83564198	-7.59856701	-2.67991304	129	C	-8.23565769	1.54753602	-2.73516512
54	H	3.15032005	-8.79408646	-2.67390609	130	H	-5.97943211	-1.10953605	-2.98697996
55	H	2.73814702	-7.93596697	-4.18060207	131	H	-6.25198078	0.22377500	-4.13596392
56	S	3.39186096	4.01056910	-2.21777797	132	H	-7.69672203	-0.09638700	-1.44467795
57	C	3.08897996	5.65962410	-3.03008699	133	H	-8.16938782	-1.92584705	-3.07548594
58	C	3.93975902	6.79505920	-2.44933295	134	H	-8.67381763	-0.73940402	-4.28396702
59	C	3.46881604	8.12839222	-3.06377602	135	H	-10.04700947	-1.16706002	-1.54585695
60	C	4.12368298	9.36953354	-2.45177507	136	H	-10.63714600	-1.79570901	-3.10114908
61	C	5.43678188	6.54918003	-2.66044807	137	H	-10.60738754	-0.04619300	-2.81093311
62	H	2.01696110	5.88719320	-2.94706702	138	H	-7.54995584	2.27793598	-2.28137398
63	H	3.32290196	5.50229502	-4.09658384	139	H	-9.22767544	1.69195497	-2.28320694
64	H	3.73795605	6.83341980	-1.36089599	140	H	-8.31485462	1.77794397	-3.81162810
65	H	2.37437105	8.20091248	-2.93889594	141	S	5.16203785	-0.61221701	-2.08725691
66	H	3.65392494	8.10715580	-4.15406322	142	C	5.56562901	-1.98882496	-0.89854199
67	H	3.96559501	9.40081406	-1.36209798	143	C	6.82275915	-2.77605891	-1.28686297
68	H	3.69367003	10.28893185	-2.87867904	144	C	6.93483877	-4.00438499	-0.36175400
69	H	5.20764399	9.39657688	-2.63775492	145	C	8.07425308	-4.96134186	-0.72018403
70	H	5.73715782	5.57521296	-2.24689507	146	C	8.07616329	-1.89646494	-1.24846494
71	H	6.04680300	7.32319784	-2.17250896	147	H	4.68682909	-2.64710593	-0.83250999
72	H	5.67908382	6.55240202	-3.73713803	148	H	5.69555616	-1.49786997	0.08008700
73	S	-5.02712202	-0.80863899	2.13334489	149	H	6.68197107	-3.14224601	-2.32262993
74	C	-6.25430393	0.29084599	3.00078011	150	H	5.97775316	-4.55207300	-0.39415601
75	C	-7.68710279	0.15004601	2.47492194	151	H	7.05267620	-3.65683794	0.68108600
76	C	-8.56368065	1.22246897	3.15255904	152	H	7.99647188	-5.29390192	-1.76793396

153	H	8.04646873	-5.85759306	-0.08197100	231	C	-5.65504122	-5.91300106	-1.25013494
154	H	9.06162739	-4.49405718	-0.58830601	232	H	-4.57740402	-2.62675309	-0.72513902
155	H	7.95440578	-1.01344204	-1.89406502	233	H	-4.07502079	-4.10836506	0.12680900
156	H	8.96617413	-2.44260001	-1.59367299	234	H	-6.06375313	-4.03004599	-2.21738696
157	H	8.26607800	-1.54295897	-0.22130200	235	H	-6.85785294	-2.80877399	-0.19952001
158	S	-1.92459095	4.83408403	-1.95158398	236	H	-6.58400822	-4.23582888	0.80214101
159	C	-0.94894803	5.83552790	-0.72058898	237	H	-8.57108021	-4.11215401	-1.56596994
160	C	-0.85895097	7.32519579	-1.07290804	238	H	-9.01210022	-3.95981503	0.15006199
161	C	0.08719400	8.00267124	-0.06080900	239	H	-8.36614895	-5.49389505	-0.46348101
162	C	0.38117000	9.47565842	-0.35526800	240	H	-4.85104895	-6.21961880	-1.93636799
163	C	-2.23978710	7.98597002	-1.11987495	241	H	-6.58611298	-6.38817501	-1.59242404
164	H	0.05157500	5.38654900	-0.63375199	242	H	-5.41554308	-6.30727386	-0.24831600
165	H	-1.46947300	5.69157982	0.24079700	243	S	-0.60788101	-2.77786994	-6.32145500
166	H	-0.39848101	7.40521908	-2.07744789	244	C	-1.17158699	-4.44801188	-5.70397091
167	H	1.03581405	7.43985081	-0.04315900	245	C	-1.12224400	-5.55600786	-6.76500511
168	H	-0.34571701	7.90343809	0.95183098	246	C	-1.98656499	-6.73333216	-6.26409388
169	H	0.79289597	9.60314846	-1.36913502	247	C	-2.13091397	-7.88443995	-7.26217079
170	H	1.11886501	9.87583733	0.35722199	248	C	0.31083900	-5.98928881	-7.08411884
171	H	-0.52177602	10.09952831	-0.27820599	249	H	-2.21235895	-4.27549314	-5.37949419
172	H	-2.89862609	7.46739101	-1.83236206	250	H	-0.58479798	-4.71265507	-4.81187296
173	H	-2.17384911	9.03913307	-1.43034005	251	H	-1.58835697	-5.16398811	-7.69041777
174	H	-2.71846390	7.94967890	-0.12672000	252	H	-2.98976707	-6.37958909	-6.01088381
175	S	-2.97784400	4.18037415	1.96876097	253	H	-1.55560100	-7.11235523	-5.31875610
176	C	-4.36135101	3.90282702	0.75257897	254	H	-2.53467989	-7.52663803	-8.22314739
177	C	-5.66427803	4.61321497	1.13824201	255	H	-2.81902790	-8.65101147	-6.87355089
178	C	-6.76866388	4.16106606	0.16157800	256	H	-1.16845000	-8.37733936	-7.46280622
179	C	-8.16672134	4.68367481	0.49995399	257	H	0.92900401	-5.12867594	-7.38076591
180	C	-5.49504185	6.13508701	1.17045295	258	H	0.34041601	-6.72156096	-7.90488005
181	H	-4.51348782	2.81774211	0.65511799	259	H	0.77727002	-6.44801807	-6.19605398
182	H	-3.97910309	4.27961302	-0.21078500	260	S	2.93462992	1.12123895	-6.20031118
183	H	-5.94517612	4.26963711	2.15346408	261	C	4.62559700	1.46756899	-5.49093485
184	H	-6.78793621	3.05785704	0.14787200	262	C	5.54475784	2.27788305	-6.41793585
185	H	-6.49004412	4.47439384	-0.86175901	263	C	7.00829983	1.99250901	-6.01787615
186	H	-8.45532894	4.40610409	1.52668703	264	C	8.05172920	2.67651892	-6.90394878
187	H	-8.91703796	4.25891209	-0.18429901	265	C	5.22377396	3.77438211	-6.38067579
188	H	-8.22877884	5.77920294	0.41754201	266	H	5.04336119	0.46097499	-5.31694889
189	H	-4.67806196	6.42404413	1.84890199	267	H	4.50882196	1.95309401	-4.51052380
190	H	-6.41038799	6.63769293	1.51594996	268	H	5.39936304	1.91044605	-7.45246792
191	H	-5.25207281	6.51612902	0.16434400	269	H	7.16946793	0.90093499	-6.04671383
192	S	-2.00843692	-4.71562099	1.82800901	270	H	7.15490723	2.29701591	-4.96490812
193	C	-1.07983398	-5.74459124	0.58309102	271	H	7.90277004	2.41501498	-7.96387196
194	C	-1.02180099	-7.23512602	0.93868500	272	H	9.06871223	2.36285496	-6.62165689
195	C	-0.10670500	-7.93920803	-0.08366600	273	H	8.00955105	3.77228189	-6.81732702
196	C	0.16161500	-9.41578865	0.21744899	274	H	4.15578222	3.95391703	-6.58278990
197	C	-2.41760111	-7.86180782	1.00637400	275	H	5.80415583	4.33534622	-7.12828302
198	H	-0.06986600	-5.32172394	0.47825900	276	H	5.45180178	4.18691683	-5.38383484
199	H	-1.61238003	-5.58964014	-0.36998799	277	S	-2.12127495	-1.94433296	6.14731789
200	H	-0.54966098	-7.32312393	1.93710494	278	C	-3.33828998	-3.24475002	5.57928181
201	H	0.85313100	-7.39654398	-0.12102800	279	C	-4.24177122	-3.76964307	6.70268488
202	H	-0.55397898	-7.83833790	-1.08981705	280	C	-4.94572115	-5.04588604	6.19462299
203	H	0.58775002	-9.54386090	1.22535396	281	C	-5.76262093	-5.78211784	7.25953388
204	H	0.87865198	-9.83637428	-0.50406599	282	C	-5.24058723	-2.71742511	7.19199324
205	H	-0.75502503	-10.02144146	0.16058400	283	H	-2.70609808	-4.05913782	5.18602180
206	H	-3.05373406	-7.32612896	1.72690296	284	H	-3.92235303	-2.84092903	4.73925400
207	H	-2.37320089	-8.91579342	1.31809497	285	H	-3.59236693	-4.05942011	7.55159712
208	H	-2.90881205	-7.81572199	0.01982000	286	H	-4.18039322	-5.73146677	5.78988123
209	S	5.20643902	0.54655403	1.85141301	287	H	-5.59833002	-4.77754498	5.34347296
210	C	5.62750578	1.92034197	0.66537100	288	H	-5.13845682	-6.03431177	8.13182640
211	C	6.90331221	2.68134308	1.04469502	289	H	-6.17053223	-6.72186708	6.85620022
212	C	7.03592920	3.90443897	0.11521500	290	H	-6.61198187	-5.18067598	7.61475706
213	C	8.19723034	4.83863497	0.46338800	291	H	-4.72588682	-1.80234897	7.51977396
214	C	8.13766384	1.77549505	1.00297999	292	H	-5.83483410	-3.08868909	8.04011536
215	H	4.76153898	2.59638309	0.60947400	293	H	-5.93481588	-2.44063807	6.38090706
216	H	5.73880386	1.42995095	-0.31600299	294	S	2.89683604	-1.08414805	6.08207083
217	H	6.77556801	3.05330300	2.08017707	295	C	4.62049818	-1.44552004	5.46204185
218	H	6.09072590	4.47202015	0.15194499	296	C	5.54857302	-2.03486896	6.53257799
219	H	7.14027214	3.55126595	-0.92724103	297	C	7.00517607	-1.88403106	6.04366207
220	H	8.12983227	5.18043900	1.50876999	298	C	8.06249332	-2.30293012	7.06819010
221	H	8.18709087	5.73075485	-0.18117000	299	C	5.20126200	-3.48810506	6.86557293
222	H	9.17381287	4.34898376	0.33171600	300	H	4.99789715	-0.46257699	5.13007116
223	H	8.00128460	0.89793003	1.65303802	301	H	4.55254698	-2.09268999	4.57493782
224	H	9.04071999	2.30446410	1.34094405	302	H	5.43731117	-1.42538905	7.45081806
225	H	8.31463242	1.41362405	-0.02355200	303	H	7.17289019	-0.82916200	5.76399994
226	S	-3.09542298	-4.02470016	-2.06305099	304	H	7.13153696	-2.47180009	5.11530018
227	C	-4.45687008	-3.71512604	-0.83011699	305	H	7.94155693	-1.74566400	8.01137257
228	C	-5.78258896	-4.38729095	-1.20692503	306	H	9.07496452	-2.10047603	6.86667698
229	C	-6.86542082	-3.91204500	-0.21715599	307	H	8.00720787	-3.37650299	7.30109596
230	C	-8.27897739	-4.39986706	-0.54300201	308	H	4.14463091	-3.58627105	7.15505219

309	H	5.81271076	-3.87137794	7.69594002	378	H	0.31226301	3.60428596	-9.31562996
310	H	5.37039709	-4.13288879	5.98693895	379	S	-4.69186211	1.95927501	5.74826193
311	S	-0.42435199	2.97387409	6.09795904	380	C	-4.14377403	2.96999598	7.21461201
312	C	-0.90736097	4.62724018	5.37828302	381	C	-4.83523417	4.33752203	7.28109598
313	C	-0.64429098	5.82471514	6.30336094	382	C	-4.20083094	5.14944792	8.42807293
314	C	-1.57134199	6.98082876	5.87049198	383	C	-4.71136379	6.58799791	8.54270363
315	C	-1.48505902	8.22628307	6.75487423	384	C	-6.35348320	4.20068502	7.43202305
316	C	0.82861900	6.24279308	6.29766083	385	H	-3.04947400	3.06965709	7.17410898
317	H	-1.98904705	4.51797009	5.18684483	386	H	-4.40343904	2.36046910	8.09667206
318	H	-0.40862900	4.75124598	4.40537024	387	H	-4.62331200	4.86527920	6.33069181
319	H	-0.92612302	5.53246021	7.33404398	388	H	-3.10699701	5.16534281	8.27994442
320	H	-2.61143088	6.61026096	5.86909723	389	H	-4.37510490	4.61700392	9.38242531
321	H	-1.33946800	7.24884987	4.82276106	390	H	-4.57642412	7.13322401	7.59496880
322	H	-1.67543602	7.97485590	7.81067896	391	H	-4.16217709	7.13485098	9.32423592
323	H	-2.23305702	8.97407818	6.44885588	392	H	-5.77940321	6.62523890	8.80396557
324	H	-0.49680501	8.70585823	6.69491720	393	H	-6.77738905	3.58210206	6.62718821
325	H	1.48344100	5.38578892	6.52150011	394	H	-6.85226822	5.17992687	7.39727402
326	H	1.03411603	7.02473211	7.04391003	395	H	-6.60392523	3.72301698	8.39468765
327	H	1.10830998	6.63001919	5.30390882	396	S	0.70065600	-5.21672201	5.64362383
328	S	-2.19833112	2.06860900	-6.23793983	397	C	-0.55341798	-5.23281479	7.02964878
329	C	-3.37379098	3.38964605	-5.63227892	398	C	0.02365600	-5.69089890	8.37594223
330	C	-4.29277611	3.94241309	-6.72951603	399	C	-1.16219199	-5.99828005	9.31592941
331	C	-4.96069479	5.22663784	-6.19307184	400	C	-0.76047802	-6.56295204	10.68059158
332	C	-5.78879118	5.98744822	-7.23184395	401	C	0.98156202	-4.65880489	8.97470093
333	C	-5.32258701	2.91470003	-7.20634508	402	H	-1.32896996	-5.93721914	6.69160795
334	H	-2.71506596	4.18831778	-5.25015116	403	H	-0.99547797	-4.22833920	7.11002922
335	H	-3.94552112	2.99237394	-4.78058481	404	H	0.57600403	-6.63660812	8.20726013
336	H	-3.65753698	4.22851515	-7.59031105	405	H	-1.82956600	-6.71949720	8.81201172
337	H	-4.17323780	5.89411116	-5.80092907	406	H	-1.75085104	-5.07279205	9.45772934
338	H	-5.59788799	4.96219397	-5.32911205	407	H	-0.14042901	-7.46689892	10.56782341
339	H	-5.18036699	6.23767710	-8.11582088	408	H	-1.65198505	-6.83904123	11.26405239
340	H	-6.17086411	6.92997503	-6.81029320	409	H	-0.19119000	-5.83340883	11.27454472
341	H	-6.65637207	5.40431404	-7.57318401	410	H	1.79941499	-4.42430401	8.27789783
342	H	-4.83165789	1.99697495	-7.6076908	411	H	1.43513203	-5.02338696	9.90820885
343	H	-5.93197203	3.30757403	-8.03376961	412	H	0.44883600	-3.71798611	9.19263077
344	H	-6.00000191	2.63773608	-6.38128996	413	S	4.26679707	3.00621510	5.75197792
345	S	4.05446482	-3.10262609	-5.92525578	414	C	4.89610100	1.91893303	7.13430786
346	C	4.64528322	-2.11217690	-7.38883781	415	C	4.98100281	2.65564203	8.47864914
347	C	6.17390299	-2.07961607	-7.50695896	416	C	5.89368916	1.84219301	9.42057610
348	C	6.55192900	-1.12574399	-8.65859890	417	C	6.17525005	2.52063704	10.76333046
349	C	8.05652046	-0.90014303	-8.82644653	418	C	3.59773397	2.90130806	9.08648682
350	C	6.75930500	-3.48246288	-7.69696903	419	H	5.90116978	1.61215699	6.80607796
351	H	4.22053814	-1.10063696	-7.31385994	420	H	4.25548077	1.02671599	7.20237303
352	H	4.20028877	-2.60888290	-8.26793480	421	H	5.47125101	3.63280892	8.29778957
353	H	6.57522821	-1.65619195	-6.56535578	422	H	6.85312414	1.65751505	8.90514755
354	H	6.05875206	-0.15391700	-8.48278809	423	H	5.43500805	0.85105997	9.59415913
355	H	6.12872601	-1.52033997	-9.60191631	424	H	6.60102510	3.52599502	10.61491585
356	H	8.50863171	-0.53203499	-7.89182281	425	H	6.89783478	1.93410802	11.35125065
357	H	8.25278854	-0.15285100	-9.61026764	426	H	5.26380396	2.62455201	11.36996746
358	H	8.58061981	-1.82342696	-9.11425400	427	H	2.94146895	3.43122101	8.38020706
359	H	6.44459391	-4.15616608	-6.88613319	428	H	3.65959191	3.50765800	10.00200653
360	H	7.85862303	-3.46287894	-7.70599413	429	H	3.11190605	1.94348598	9.33740234
361	H	6.41630220	-3.91703105	-8.65162182	430	S	-4.81394005	-1.81548202	-5.84438515
362	S	0.73316097	5.25681877	-5.81275511	431	C	-4.27668619	-2.91331410	-7.25775480
363	C	-0.52785099	5.27005386	-7.19068813	432	C	-5.01690578	-2.60416198	-8.56626511
364	C	0.06311100	5.63019514	-8.56122875	433	C	-4.77904987	-3.77571797	-9.54214382
365	C	-1.10755599	5.99399614	-9.50035954	434	C	-5.58065605	-3.68354702	-10.84294701
366	C	-0.67981702	6.48450613	-10.88586330	435	C	-4.59541607	-1.25990999	-9.16429710
367	C	0.92562503	4.50225401	-9.13163471	436	H	-4.51369476	-3.93432093	-6.92202520
368	H	-1.26058900	6.03176498	-6.88197422	437	H	-3.18631601	-2.82341909	-7.37913895
369	H	-1.02446795	4.28849411	-7.21953201	438	H	-6.10110903	-2.56969404	-8.33979416
370	H	0.69045299	6.53493977	-8.43650246	439	H	-5.03934383	-4.71791792	-9.02809334
371	H	-1.71544898	6.77794123	-9.01492023	440	H	-3.69927907	-3.83317590	-9.77377701
372	H	-1.76339698	5.10986900	-9.60698223	441	H	-6.65911102	-3.59475303	-10.63534355
373	H	-0.00062800	7.34855413	-10.80645847	442	H	-5.43083000	-4.58480787	-11.45705032
374	H	-1.55547905	6.79977894	-11.47331333	443	H	-5.28011322	-2.81765699	-11.45026207
375	H	-0.16454600	5.69974709	-11.45827579	444	H	-4.74768686	-0.44100100	-8.44669628
376	H	1.72625697	4.21901989	-8.43200970	445	H	-5.17531204	-1.02087402	-10.06811810
377	H	1.40112197	4.79642200	-10.07880020	446	H	-3.52577496	-1.27532101	-9.43252468

[Au₂₅(2-MeBuS)₁₈]⁻

Index	Symbol	x (angstrom)	y (angstrom)	z (angstrom)					
1	Au	8.15674581	0.08811668	-0.03184430	76	C	7.89207301	-3.28839743	5.12619602
2	Au	9.00983867	1.00179549	2.51920070	77	H	7.59451445	-4.43502132	6.10083434
3	Au	7.90160416	2.90148753	0.38788774	78	C	7.34942441	-2.37496344	5.42112132
4	Au	6.05078173	0.94397808	1.70123496	79	H	8.96352850	-3.04486846	5.10802843
5	Au	10.63981700	1.47519761	0.22862969	80	C	7.82853542	-3.93275750	7.54018495
6	Au	10.26836271	-1.40541707	1.19414552	81	C	7.39724963	-4.91610251	8.63153634
7	Au	12.31351568	0.79303596	2.80192633	82	C	8.41684290	-5.68798093	5.78374139
8	Au	6.60334259	0.22613335	4.82526126	83	H	6.52052184	-4.68876626	6.00052249
9	Au	10.44744514	3.88018423	2.42944351	84	H	7.27949046	-2.98381012	7.67309622
10	Au	4.14000672	-1.39165841	2.77038125	85	H	8.90007267	-3.68898244	7.66126802
11	Au	7.37851507	-1.52714919	2.16025345	86	H	6.33300452	-5.18060170	8.52327419
12	Au	7.05165667	4.56464211	-2.26961949	87	H	7.53309718	-4.47547685	9.63164032
13	Au	4.78037086	3.90358060	0.46596329	88	H	7.98144841	-5.84777557	8.59908083
14	Au	7.29513018	-0.81404225	-2.58513371	89	H	8.27093234	-5.99918936	4.73901641
15	Au	8.38632964	-2.73049895	-0.46561765	90	H	8.13801449	-6.53309660	6.43139408
16	Au	10.25596313	-0.78520697	-1.76665996	91	H	9.49136959	-5.48478934	5.92782815
17	Au	5.68140671	-1.32338021	-0.31460418	92	C	11.61453157	-2.18055682	4.21450207
18	Au	6.04486539	1.58957185	-1.28651267	93	C	12.71182787	-2.51303546	5.23547036
19	Au	3.98704296	-0.75226399	-2.86386587	94	H	11.05119799	-3.09094077	3.94671879
20	Au	9.69431265	-0.04043719	-4.85725475	95	H	10.90183970	-1.44274667	4.61275184
21	Au	5.83234008	-3.78457043	-2.46704527	96	C	12.09499149	-3.35281499	6.37211158
22	Au	12.20957124	1.52609097	-2.74683096	97	C	13.10744319	-3.88609158	7.38961408
23	Au	8.94463684	1.70210274	-2.23117528	98	C	13.40601701	-1.25342375	5.76193656
24	Au	9.20747408	-4.38963952	2.18363912	99	H	13.46639256	-3.14219170	4.72410016
25	Au	11.42118796	-3.80061569	-0.60710742	100	H	11.55837117	-4.20608927	5.92211504
26	S	4.34802064	-0.45890538	4.93440197	101	H	11.33181025	-2.74385964	6.89118709
27	S	12.57466212	3.11950238	3.10461155	102	H	13.89197248	-4.47704499	6.88986075
28	S	7.31517007	-3.64439639	3.38879918	103	H	12.61516288	-4.53828222	8.12767903
29	S	12.28429891	-1.55865372	2.58842656	104	H	13.59908019	-3.07304040	7.94420572
30	S	5.22901992	5.56286052	-1.15085682	105	H	13.80159437	-0.65165370	4.93017422
31	S	12.66548198	2.54986772	-0.67260726	106	H	14.24316707	-1.50048577	6.43234316
32	S	8.80868534	1.05680899	4.96129233	107	H	12.68847663	-0.62716108	6.31827596
33	S	8.40021063	4.85934609	1.77900771	108	C	3.80815837	5.39705035	-2.34530392
34	S	4.18680447	2.44258430	2.22083464	109	C	2.48763379	5.91640326	-1.76299537
35	S	11.98455389	0.51848693	-4.86972299	110	H	3.71755420	4.33485065	-2.61168682
36	S	3.67596221	-3.08504838	-3.11886116	111	H	4.09623350	5.97406524	-3.24060631
37	S	8.98525519	3.84269769	-3.41297762	112	C	1.34285678	5.53131266	-2.72088455
38	S	4.05609932	1.60583552	-2.73175840	113	C	-0.05659082	5.86167599	-2.19457793
39	S	10.99739913	-5.43276250	1.04821299	114	C	2.53885645	7.42215160	-1.48590659
40	S	3.67635988	-2.35241041	0.66723579	115	H	2.32170622	5.38417868	-0.80619391
41	S	7.46186521	-0.79991095	-5.03453651	116	H	1.40546280	4.44763853	-2.91745212
42	S	7.93096761	-4.67789605	-1.88938035	117	H	1.50216406	6.03587244	-3.69307099
43	S	11.99425300	-2.39200253	-2.41296769	118	H	-0.22589404	5.39228594	-1.21214600
44	C	4.37984481	-1.89673783	6.12992231	119	H	-0.83036457	5.48640636	-2.88245194
45	C	2.99192611	-2.24804674	6.68239888	120	H	-0.20980039	6.94565422	-2.08353374
46	H	5.03783632	-1.57160314	6.94963388	121	H	3.39566201	7.67349781	-0.84272079
47	H	4.84210182	-2.76115951	5.63052335	122	H	1.62637766	7.77239525	-0.98146195
48	C	3.17032432	-3.21000264	7.87558739	123	H	2.64578977	7.98481060	-2.42996040
49	C	1.87993513	-3.51497177	8.64134033	124	C	12.11567573	4.32001632	-0.87047138
50	C	2.07074372	-2.82982203	5.60688341	125	C	13.18029902	5.23264590	-1.49730670
51	H	2.54101000	-1.31136340	7.06640479	126	H	11.89681461	4.64040179	0.16215211
52	H	3.90545727	-2.77203193	8.57420963	127	H	11.17836550	4.34350921	-1.44524390
53	H	3.61428310	-4.15345304	7.50741034	128	C	12.83404826	6.69762981	-1.15833772
54	H	1.40943927	-2.58651189	9.00342749	129	C	13.87349040	7.72019052	-1.62692217
55	H	2.08545977	-4.15093512	9.51659258	130	C	13.30472499	5.00945368	-3.00751915
56	H	1.14630738	-4.04275482	8.01441890	131	H	14.15111423	4.99642141	-1.01871289
57	H	1.98619057	-2.15234565	4.74456484	132	H	12.71750376	6.78115465	-0.06374980
58	H	1.05705857	-3.00932762	5.99551429	133	H	11.84955940	6.94157508	-1.59883260
59	H	2.47173384	-3.78832355	5.23724964	134	H	14.87110949	7.47884187	-1.22493063
60	C	12.56023848	3.31925452	4.95907388	135	H	13.60971350	8.73297120	-1.28353934
61	C	13.87087286	2.86194662	5.61059389	136	H	13.95045457	7.75306636	-2.72385764
62	H	11.71128205	2.74595607	5.35418855	137	H	13.48182650	3.94543405	-3.22902808
63	H	12.38336525	4.39189713	5.14796218	138	H	14.13314086	5.59059666	-3.44030160
64	C	13.68305101	2.83625895	7.14023793	139	H	12.36949623	5.30368666	-3.51287924
65	C	14.86589848	2.24215534	7.90984023	140	C	8.54379600	2.83609958	5.44596723
66	C	15.05085140	3.73925374	5.18077754	141	C	8.19308504	3.01780918	6.92812036
67	H	14.06021010	1.82448704	5.27572197	142	H	7.75807468	3.25215347	4.80197869
68	H	12.77665872	2.25024839	7.37139384	143	H	9.48468298	3.35409913	5.19356762
69	H	13.48721581	3.86577384	7.49575832	144	C	7.83432098	4.49580741	7.17748974
70	H	15.09192516	1.22516717	7.55211824	145	C	7.30871158	4.78952532	8.58543137
71	H	14.63997421	2.17763213	8.98570074	146	C	9.32189046	2.53278653	7.84329494
72	H	15.77604369	2.85043720	7.79846280	147	H	7.28985469	2.40885258	7.12952012
73	H	15.13203288	3.77575917	4.08402981	148	H	7.07105260	4.79812922	6.44077011
74	H	16.00452164	3.35779510	5.57482851	149	H	8.72508517	5.12001325	6.97498106
75	H	14.91626111	4.77173130	5.54716337	150	H	6.43220729	4.16240413	8.81657141
					151	H	7.00052738	5.84269362	8.67633643

152	H	8.07054569	4.60070060	9.35652970	230	H	6.61597203	6.32957667	-7.71929675
153	H	9.58948865	1.49077184	7.61075327	231	H	6.88298581	5.35575774	-9.18467044
154	H	9.03460470	2.57802445	8.90466960	232	H	8.22061591	6.29189501	-8.48827847
155	H	10.22196033	3.15659301	7.70685460	233	H	9.99443682	5.81869053	-5.07744124
156	C	8.82926375	6.28700010	0.65650317	234	H	9.44869397	6.58087325	-6.58876002
157	C	8.92629514	7.62924115	1.39442929	235	H	10.33764835	5.03617867	-6.64317435
158	H	8.01144504	6.31665855	-0.07995269	236	C	4.73978642	2.03717837	-4.40833866
159	H	9.75884684	6.05406299	0.11758575	237	C	3.78553179	1.69958394	-5.56189467
160	C	8.93600818	8.76386908	0.34895027	238	H	5.69106893	1.50112486	-4.52967995
161	C	8.86617034	10.17267504	0.94486165	239	H	4.95151925	3.12090702	-4.37224453
162	C	10.14022933	7.69052487	2.32575316	240	C	4.51584041	1.92548842	-6.89902828
163	H	8.00697621	7.73909820	2.00347407	241	C	3.74138719	1.44935749	-8.13110413
164	H	8.07829701	8.61863909	-0.33109785	242	C	2.47301310	2.48222042	-4.37224453
165	H	9.84596352	8.66810584	-0.27218567	243	H	3.55667375	0.61935894	-5.47927355
166	H	7.97732841	10.28290540	1.58759361	244	H	5.48454796	1.39778217	-6.85868772
167	H	8.80028209	10.93116869	0.14886636	245	H	4.74490696	3.00202468	-3.02053638
168	H	9.75319535	10.40724658	1.55227847	246	H	3.48026825	0.38274673	-8.04107469
169	H	10.13898384	6.84376732	3.02775035	247	H	4.34558952	1.56887063	-9.04417473
170	H	10.15481371	8.61993668	2.91503211	248	H	2.80767329	2.01391006	-8.27474891
171	H	11.07414745	7.63868996	1.74123603	249	H	1.98945542	2.31103103	-4.49486645
172	C	4.72135119	3.42728699	3.70885825	250	H	1.76262424	2.18297780	-6.25366715
173	C	3.77323763	4.59263866	4.02112187	251	H	2.66103221	3.56502931	-5.46819941
174	H	5.74135294	3.79197560	3.52471495	252	C	12.40626833	-5.31726675	2.26853478
175	H	4.74985707	2.70759062	4.54506423	253	C	13.62894629	-6.15719428	1.87063633
176	C	4.40291396	5.47377819	5.11719439	254	H	11.98547216	-5.68996854	3.21514463
177	C	3.62974210	6.76226385	5.41212287	255	H	12.67582015	-4.25716261	2.38908658
178	C	2.37618320	4.09437386	4.40370797	256	C	14.52437110	-6.32259368	3.11690906
179	H	3.69262173	5.20416519	3.10148895	257	C	15.73831873	-7.23192627	2.90977501
180	H	5.42894707	5.73632103	4.80477798	258	C	14.39008039	-5.54122253	0.69397061
181	H	4.49788703	4.87852614	6.04443512	259	H	13.26832610	-7.16338063	1.57752029
182	H	3.50676672	7.36321327	4.49638822	260	H	13.90879264	-6.72776753	3.93989894
183	H	4.16437264	7.38077691	6.15001871	261	H	14.86394053	-5.32187587	3.44331936
184	H	2.62804129	6.55545015	5.81748196	262	H	15.42814118	-8.22897432	2.55633334
185	H	1.97068031	3.43628584	3.62052839	263	H	16.29107960	-7.36632661	3.85280850
186	H	1.67094427	4.92714711	4.54351929	264	H	16.43967688	-6.81493323	2.17215324
187	H	2.41801698	3.51514118	5.34212826	265	H	13.71900893	-5.36095114	-0.15898401
188	C	12.15427311	1.94330867	-6.05964661	266	H	15.20554560	-6.19517419	0.34993990
189	C	13.61305200	2.39108221	-6.21998371	267	H	14.82176616	-4.56824169	0.98263700
190	H	11.53269194	2.77028541	-5.69221477	268	C	4.21987659	-4.11507975	0.91681077
191	H	11.74514878	1.59058021	-7.02167004	269	C	3.34104663	-4.89951703	1.89851658
192	C	13.64356095	3.71837841	-7.00273679	270	H	5.26312072	-4.10044955	1.26030416
193	C	15.03288312	4.35123546	-7.12072039	271	H	4.19151320	-4.56900419	-0.08967865
194	C	14.46667397	1.30051434	-6.87503548	272	C	3.99423538	-6.27091829	2.15749400
195	H	14.01085588	2.58822391	-5.20633386	273	C	3.31430182	-7.09895084	3.25149972
196	H	12.96919106	4.43314407	-6.50047864	274	H	1.89683688	-5.02091230	1.40257817
197	H	13.22525742	3.54908700	-8.01344475	275	C	3.34148813	-4.33827735	2.85273241
198	H	15.47529923	4.51070955	-6.12439886	276	H	5.04869111	-6.10458852	2.43868198
199	H	14.97513276	5.32946824	-7.62319904	277	H	4.00343606	-6.84512595	1.21256619
200	H	15.72412352	3.72139150	-7.70079748	278	H	3.27693467	-6.53894530	4.19961992
201	H	14.38502891	0.35504449	-6.31823777	279	H	3.86771776	-8.03320702	3.43699501
202	H	15.52994397	1.58015571	-6.90482402	280	H	2.28326227	-7.37245064	2.98040053
203	H	14.13050903	1.11720740	-7.91043924	281	H	1.47454009	-4.02772899	1.18760538
204	C	3.67193162	-3.41182177	-4.96149575	282	H	1.25102978	-5.50907670	2.14755143
205	C	2.25851186	-3.50759925	-5.55053146	283	H	1.85846888	-5.61273645	0.47177954
206	H	4.19426039	-4.37217111	-5.08533708	284	C	7.58850646	-2.59032234	-5.55067297
207	H	4.26179064	-2.62872071	-5.46010490	285	C	7.31332037	-2.81537949	-7.04224911
208	C	2.37219244	-4.03029109	-6.99765103	286	H	6.84004794	-3.11558802	-4.93523431
209	C	1.03182127	-4.34072151	-7.66920414	287	H	8.57853188	-2.97250756	-5.26385133
210	C	1.50586667	-2.17722858	-5.47173962	288	C	7.21809546	-4.33410502	-7.29508356
211	H	1.70345768	-4.26222584	-4.95835530	289	C	6.74195392	-4.71650645	-8.69890556
212	H	2.99037879	-4.94558259	-6.99322557	290	C	8.36516291	-2.14594673	-7.93163783
213	H	2.92419516	-3.28552711	-7.60071906	291	H	6.32516111	-2.36926412	-7.27198147
214	H	0.45401450	-5.06821462	-7.07608826	292	H	6.52898595	-4.77097424	-6.55127452
215	H	1.18739717	-4.77176243	-8.67043347	293	H	8.20784455	-4.78720901	-7.10135254
216	H	0.41494529	-3.43794407	-7.78987883	294	H	5.75636478	-4.27292076	-8.91377966
217	H	1.46579496	-1.80400213	-4.43795110	295	H	6.64600390	-5.80946096	-8.79489255
218	H	0.47124343	-2.27674112	-5.83327063	296	H	7.44191639	-4.37719872	-9.47737071
219	H	2.01169430	-1.41193068	-6.08361350	297	H	8.43291079	-1.06982471	-7.71496190
220	C	8.43164964	3.54435809	-5.16381696	298	H	8.12778501	-2.26301477	-9.00011182
221	C	8.27329743	4.83380561	-5.98095890	299	H	9.35851939	-2.58818335	-7.74845312
222	H	7.49252115	2.97718748	-5.13893076	300	C	7.55128689	-6.14964734	-0.81530044
223	H	9.20211050	2.88924735	-5.60446108	301	C	6.87400275	-7.30354447	-1.56517681
224	C	7.71130439	4.47365225	-7.37050839	302	H	6.93071771	-5.81202981	0.02529718
225	C	7.34082664	5.68057526	-8.23721614	303	H	8.52805646	-6.46760024	-0.41295618
226	C	9.58714485	5.61564251	-6.07884084	304	C	6.49813864	-8.39968221	-0.54859256
227	H	7.52681237	5.46524423	-5.46051193	305	C	5.65230239	-9.53700263	-1.12754336
228	H	6.81750777	3.84242748	-7.23479899	306	C	7.75240826	-7.83974148	-2.69952160
229	H	8.45230587	3.84783723	-7.90266338	307	H	5.93727315	-6.90554960	-2.00276357

308	H	5.94464140	-7.92985295	0.28244420	320	C	11.73896768	-4.51241906	-6.02035291
309	H	7.42599334	-8.81226499	-0.10900325	321	C	12.72496482	-5.24610109	-6.93430368
310	H	4.72871596	-9.14660254	-1.58543264	322	C	12.70887337	-5.36712777	-3.81993865
311	H	5.36040013	-10.24836650	-0.33885032	323	H	13.21322213	-3.51445771	-4.80544728
312	H	6.19734447	-10.10337717	-1.89764129	324	H	11.40900745	-3.58624617	-6.52201908
313	H	8.03063553	-7.03069907	-3.39136769	325	H	10.83411233	-5.13191374	-5.87639866
314	H	7.23507543	-8.61796691	-3.28037369	326	H	13.64534039	-4.65519849	-7.07153441
315	H	8.68300390	-8.27314001	-2.29369475	327	H	12.28502685	-5.41841337	-7.92909896
316	C	11.28336548	-3.26407146	-3.90454714	328	H	13.01135970	-6.22641291	-6.52525819
317	C	12.31099592	-4.13555575	-4.63777976	329	H	13.09102995	-5.07174340	-2.83208214
318	H	10.94432788	-2.44717806	-4.56212730	330	H	13.49280949	-5.95428365	-4.32257285
319	H	10.40427525	-3.84722495	-3.59097277	331	H	11.83485886	-6.02077963	-3.65870471

List of Figures

1.1. Transition from bulk metal to a single atom and consequences for the electronic structure.	1
1.2. Simplified representation of Au nanocluster structures: (a) $\text{Au}_{11}(\text{PPh}_3)_7\text{Cl}_3$ as an example for phosphine-protected Au nanoclusters and (b) $\text{Au}_{25}(\text{SC}_2\text{H}_4\text{Ph})_{18}$ as an example for thiolate-protected Au nanoclusters.	3
1.3. Structures of selected Au nanoclusters. The organic ligand framework is omitted for clarity.	4
1.4. Synthesis scheme of a classical Brust procedure followed by size-exclusion chromatography (SEC) and corresponding Au species present in each step. Note that the ligands are omitted in the illustration of the Au species for clarity.	5
1.5. Summary of characterization methods for Au nanoclusters and the provided information.	7
1.6. Overview of the modification possibilities for metal nanoclusters.	8
1.7. Different ligand exchange processes on Au nanoclusters. Top: ligand exchange from $\text{Au}_{25}(\text{SC}_2\text{H}_5)_{18}$ to $\text{Au}_{25}(\text{2-PET})_{18}$, middle: ligand exchange induced size transformation from $\text{Au}_{11}(\text{PPh}_3)_7\text{Cl}_3$ to $\text{Au}_{25}(\text{PPh}_3)_{10}(\text{2-PET})_5\text{Cl}_2^{2+}$, bottom: reversible ligand exchange induced structure transformation between $\text{Au}_{28}(\text{TBBT})_{20}$ and $\text{Au}_{28}(\text{SC}_8\text{H}_{11})_{20}$. Color code: Au = gold, S = magenta, P = orange, Cl = green, C = beige.	11
1.8. Different forms of chirality in Au nanoclusters: (1) chiral ligands, (2) chiral Au-S interface, (3) chiral Au kernel and (4) hierarchical chirality by combining several different motifs. Note that for $\text{Au}_{38}(\text{2-PET})_{24}$, the hydrocarbon backbone of the ligands is omitted for clarity. Similarly, for $[\text{Au}(\text{PP}_3)_4]\text{Cl}_4$, only the chiral core itself is depicted.	14
1.9. Comparison of different catalyst systems.	16
3.1. Exemplary picture of a size exclusion separation after a $\text{Au}_{144}(\text{2-MeBuS})_{60}$ synthesis and corresponding UV-Vis spectra of the isolated products. The insets show exemplary structures of the (<i>S</i>)-2-MeBuS protected Au nanoclusters. Note that the enantiomers chosen in the representation of $\text{Au}_{38}(\text{2-MeBuS})_{24}$ and $\text{Au}_{144}(\text{2-MeBuS})_{60}$ are not necessarily the enantiomers formed during synthesis.	45

3.2.	<i>a</i> : Normalized CD spectra of the $[\text{Au}_{25}(\text{2-MeBuS})_{18}]^-$, $\text{Au}_{38}(\text{S-MeBuS})_{24}$ and $\text{Au}_{144}(\text{S-MeBuS})_{60}$ nanoclusters at RT; <i>b</i> : comparison of the CD spectra of $\text{Au}_{38}(\text{2-MeBuS})_{24}$ and the enantiomer of $\text{Au}_{38}(\text{2-PET})_{24}$ eluting first during a HPLC separation following the procedure by Dolamic <i>et al.</i> ^[21]	46
3.3.	Evolution of the CD spectra with increasing temperature (RT to 80 °C): $[\text{Au}_{25}(\text{2-MeBuS})_{18}]^-$ (a), $\text{Au}_{38}(\text{2-MeBuS})_{24}$ (b) and $\text{Au}_{144}(\text{2-MeBuS})_{60}$ (c) . . .	48
3.4.	Synthesis of 2-MeBuSH.	52
3.5.	¹ H (a) and ¹³ C-NMR spectrum (b) of (<i>S</i>)-2-methylbutyl 4-methylbenzensulfonate.	55
3.6.	¹ H (a) and ¹³ C-NMR spectrum (b) of (<i>S</i>)-2-methylbutanethiol.	55
3.7.	MALDI-MS spectra of $[\text{Au}_{25}(\text{2-MeBuS})_{18}]^-$ (top) and $[\text{Au}_{25}(\text{S-Bu})_{18}]^-$ (bottom). Note that the counterion cannot be identified due to measuring in positive mode.	56
3.8.	MALDI-MS spectra of $\text{Au}_{38}(\text{2-PET})_{24}$ (top), $\text{Au}_{38}(\text{2-MeBuS})_{24}$ (middle) and $\text{Au}_{38}(\text{S-Bu})_{24}$ (bottom).	57
3.9.	MALDI-MS spectra of $\text{Au}_{144}(\text{2-MeBuS})_{60}$ (top) and $\text{Au}_{144}(\text{S-Bu})_{60}$ (bottom).	57
3.10.	CD spectra of two enantiomers of $\text{Au}_{38}(\text{2-PET})_{24}$	58
3.11.	CD spectrum of the (<i>S</i>)-2-methylbutanethiol ligand.	58
3.12.	HPLC chromatograms of $\text{Au}_{38}(\text{2-MeBuS})_{24}$ (a) and $\text{Au}_{38}(\text{2-PET})_{24}$ (b)	59
3.13.	Structures of isomer 1a and 2a: (a) side view and (b) top view. Note that in (b), the hydrocarbon framework of all but the 9 ligands in the dimeric staples on top is not shown to allow for better visualization.	61
3.14.	Theoretical UV-Vis (a) and CD spectra (b) of isomers 1a (crystal structure) and 2a (JACS2010) in gas phase.	62
3.15.	Structures of isomer 2a and 2b: (a) side view and (b) top view. Note that in (b), the hydrocarbon framework of all but the 9 ligands in the dimeric staples on top is not shown to allow for better visualization.	63
3.16.	Theoretical UV-Vis (a) and CD spectra (b) of isomers 2a and 2b in gas phase.	63
3.17.	Theoretical spectra of isomers 2a and 2b in gas phase and experimental spectrum of $\text{Au}_{38}(\text{2-MeBuS})_{24}$: (a) UV-Vis and (b) CD spectra. Note that the experimental UV-Vis spectrum is offset on the intensity axis from the theoretical ones to allow for better visualization.	64
3.18.	Calculated structure of $[\text{Au}_{25}(\text{2-MeBuS})_{18}]^-$	65
3.19.	Theoretical spectra of $[\text{Au}_{25}(\text{2-MeBuS})_{18}]^-$ in gas phase and experimental spectrum: (a) UV-Vis and (b) CD spectra. Note that the experimental UV-Vis spectrum is offset on the intensity axis from the theoretical ones to allow for better visualization.	65
3.20.	Comparison of the UV-Vis (a) and CD spectra (b) of $\text{Au}_{38}(\text{2-MeBuS})_{24}$ isomer 2b obtained by TD-DFT and TD-DFT+TB.	68
3.21.	Calculated linear response TD-DFT+TB spectra of isomer 1a: (a) oscillator strength and optical absorption spectrum and (b) rotatory strength and CD spectrum.	68

3.22. Calculated linear response TD-DFT+TB spectra of isomer 1b: (a) oscillator strength and optical absorption spectrum and (b) rotatory strength and CD spectrum.	69
3.23. Calculated linear response TD-DFT+TB spectra of isomer 2a: (a) oscillator strength and optical absorption spectrum and (b) rotatory strength and CD spectrum.	69
3.24. Calculated linear response TD-DFT+TB spectra of isomer 2b: (a) oscillator strength and optical absorption spectrum and (b) rotatory strength and CD spectrum.	70
3.25. Calculated linear response TD-DFT+TB spectra of $[\text{Au}_{25}(\text{2-MeBuS})_{18}]^-$: (a) oscillator strength and optical absorption spectrum and (b) rotatory strength and CD spectrum.	70
3.26. Calculated linear response TD-DFT+TB spectra of (<i>S</i>)-2-MeBuSH: (a) oscillator strength and optical absorption spectrum and (b) rotatory strength and CD spectrum.	71
4.1. ESI-TOFMS spectrum of the product clusters after the ligand exchange reaction (L: 2-phenylethanethiolate). The top graphic shows an enlarged view of the m/z 5050–5170 area. The comparison of the measured accurate mass (exp) and the calculated exact mass (sim) of the $[\text{Au}_{16}(\text{2-PET})_{13}]^+$ species is shown in the inset.	83
4.2. UV-Vis absorption spectra of the ligand exchange reaction of $\text{Au}_{15}(\text{SG})_{13}$ with 2-PET at defined time intervals: (a) aqueous phase and (b) DCM phase. The optical absorption spectra of the purified clusters before (bottom) and after (top) the ligand exchange are shown in (c). The insets show photographs of the respective cluster solutions.	84
4.3. Attenuated total reflection-Fourier transform infrared spectra of the clusters before and after ligand exchange: (a) mid-infrared and (b) far-infrared regions.	86
4.4. Au L_3 -edge (a) XANES and (b) FT-EXAFS spectra of the $\text{Au}_{15}(\text{SG})_{13}$ and $\text{Au}_{16}(\text{2-PET})_{14}$ nanoclusters.	87
4.5. Absorbance and photoluminescence spectra of (a) $\text{Au}_{15}(\text{SG})_{13}$ and (b) $\text{Au}_{16}(\text{2-PET})_{14}$. The sharp features in the emission spectra at 750 and 840 nm in (a), which are due to 2nd order diffraction from the excitation wavelength, and the ones at 410 and 525 nm in (b) also appear in the PL spectra of the pure solvents and do not originate from the Au nanoclusters (see solvent PL spectra in Figure 4.15).	88
4.6. UV-Vis absorbance of samples of the aqueous phase (a) and dichloromethane phase (b) at defined time intervals of the ligand exchange. The pH of the aqueous phase was adjusted to 2.0 before addition of 2-PET by acidifying with 1 N HNO_3	94

4.7. (a) UV-Vis absorbance of samples of the toluene and aqueous phase of the one-pot ligand exchange synthesis attempt (Section 4.5.1.1.3): 0.5 days and 3 days days after addition of the exchange thiol 2-PET. (b) Fractions obtained after size exclusion chromatography of the toluene phase.	94
4.8. UV-Vis absorbance of samples of the H ₂ O phase before and the dichloromethane phase after a ligand exchange attempt with 2-PET (24 h). Color transfer to the organic phase was complete at the time of measurement.	95
4.9. UV-Vis absorbance of Au ₁₆ (2-PET) ₁₄ dissolved in toluene at defined time intervals. The sample was stored at room temperature.	95
4.10. Photographs of the ligand exchange batch.	96
4.11. ESI-TOF mass spectrum of Au ₁₅ (SG) ₁₃ : m/z range 1300-2700 Dalton (a) and comparison of experimental and simulated isotope patterns of the multiple charged Au ₁₅ (SG) ₁₃ ions (b)-(d).	96
4.12. Comparison of experimental and simulated isotope patterns of the [Au ₁₆ (SG) ₁₄ -K] ⁺ (a) and [Au ₁₆ (SG) ₁₄ -Cu] ⁺ ions (b). For [Au ₁₆ (2-PET) ₁₄] ⁺ and [Au ₁₆ (SG) ₁₄ -Na] ⁺ , the intensity of the peaks was not sufficient for a definite comparison.	97
4.13. ESI-TOF mass spectra of the samples taken during the ligand exchange process (Section 4.5.1.1.1): (a) H ₂ O phase and (b) DCM phase.	97
4.14. Emission decay of the nanocluster samples at 650 nm (a) and at 700 nm (b) after excitation at 375 nm.	98
4.15. Photoluminescence spectra of toluene (a) and H ₂ O (b) after excitation at different wavelengths.	98
5.1. Structures of the three Au nanoclusters employed in this study: (a) Au ₁₁ (PPh ₃) ₇ Cl ₃ , (b) [Au ₂₅ (SR) ₅ (PPh ₃) ₁₀ Cl ₂] ²⁺ and (c) [Au ₂₅ (SC ₂ H ₄ Ph) ₁₈]. Color code: Au = yellow, P = orange, Cl = green, S = red, C = grey. The images are based on structures determined by X-ray crystallography. ^[54,56,57]	106
5.2. Catalytic activity of Au nanoclusters on CeO ₂ (0.3 wt% Au loading, 15 mg catalyst) in CO oxidation depending on the temperature of oxidative pretreatment: (a) Au ₁₁ /CeO ₂ ; (b) Biico Au ₂₅ /CeO ₂ ; (c) Au ₂₅ /CeO ₂ . Comparison of the catalytic activity of the different nanocluster catalysts pretreated at 250 °C (d).	108
5.3. CO conversion of the same catalyst sample (0.3 wt% Au loading, 15 mg catalyst) in 3 consecutive CO oxidation runs after pretreatment at 250 °C: (a) Au ₁₁ /CeO ₂ , (b) Biico Au ₂₅ /CeO ₂ and (c) Au ₂₅ /CeO ₂	109
5.4. CO ₂ generation (a) and O ₂ consumption spectra (b) of the different catalysts during oxidative pretreatment until 250 °C. Au content in catalyst: Au ₁₁ and BiicoAu ₂₅ /CeO ₂ : 1.2 wt%, Au ₂₅ /CeO ₂ : 0.3 wt%. Spectra were normalized by the carrier gas signal to compensate for changes in pressure. Spectra are offset for better visibility.	110

- 5.5. Infrared spectra of the catalysts after oxidative pretreatment at 250 °C: 4000-1800 cm⁻¹ (a) and 1800-900 cm⁻¹ (b). Bands associated with certain species are highlighted: hy = hydroxy species (blue), lig = ligand/other organic residues (yellow), f = formates (violet), CO₂/CO/H₂O (grey), bc/tc = bidentate/tridentate carbonates (turquoise), hc = hydrogen carbonates (orange). Spectra are offset for better visibility and the spectrum of CeO₂ was multiplied with 0.5 to allow for comparison with the cluster catalysts. Au content in catalyst: Au₁₁/CeO₂ and Biico Au₂₅/CeO₂: 1.2 wt%, Au₂₅/CeO₂: 0.3 wt%. 111
- 5.6. Difference spectra of the cluster catalysts during oxidative pretreatment: (a) Au₁₁/CeO₂, (b) Biico Au₂₅/CeO₂ and (c) Au₂₅/CeO₂. Bands decreasing during the pretreatment are indicated by a light blue background color and marked at the bottom, increasing ones by a light red one and marked on top. Assigned species are indicated by abbreviations: f = formates, hc = hydrogen carbonates, bc/tc = bidentate/tridentate carbonates, lig = ligands. For all samples, the spectra of the as-prepared catalysts in He at RT were used as background. Au content in catalyst: Au₁₁/CeO₂ and Biico Au₂₅/CeO₂: 1.2 wt%, Au₂₅/CeO₂: 0.3 wt%. Difference spectra featuring the frequency region from 3800-2500 cm⁻¹ and from 2500-2000 cm⁻¹ can be found in Section 5.8 (Figures 5.21-5.23). . . . 112
- 5.7. Transmission infrared spectra of room temperature CO adsorption on catalysts after oxidative pretreatment at 250 °C: (a) Au₁₁/CeO₂ (b) Biico Au₂₅/CeO₂, (c) Au₂₅/CeO₂ and (d) CeO₂. The red spectra were obtained during exposure of the sample to an atmosphere of 1 % CO in He (50 ml/min total gas flow), the green spectra upon removal of gas phase CO by flowing 50 ml/min He. Au content in catalyst: Au₁₁/CeO₂ and Biico Au₂₅/CeO₂: 1.2 wt%, Au₂₅/CeO₂: 0.3 wt%. 114
- 5.8. Infrared spectra of the catalysts after CO oxidation at 250 °C: 4000-1800 cm⁻¹ (a) and 1800-900 cm⁻¹ (b). Bands associated with certain species are highlighted: hy = hydroxy species (blue), f = formates (violet), CO₂/CO (grey), bc/tc = bidentate/tridentate carbonates (turquoise), hc = hydrogen carbonates (orange). Spectra are offset for better visibility. Au content in catalyst: Au₁₁/CeO₂ and Biico Au₂₅/CeO₂: 1.2 wt%, Au₂₅/CeO₂: 0.3 wt%. 115

5.9.	Difference spectra of Au ₁₁ /CeO ₂ during CO oxidation: (a) 3800-2500 cm ⁻¹ , (b) 2500-2000 cm ⁻¹ and (c) 1800-900 cm ⁻¹ . Bands decreasing during the pretreatment are indicated by a light blue background color and marked at the bottom, increasing ones by a light red one and marked on top. Bands decreasing during reaction but reforming at cool down are indicated by a grey shaded background. Assigned species are indicated by abbreviations: f = formates, hc = hydrogen carbonates, bc/tc = bidentate/tridentate carbonates. The spectrum of the pretreated catalyst after the CO adsorption experiment in He at RT was used as background. Au content in catalyst: 1.2 wt%. The difference spectra of Biico Au ₂₅ /CeO ₂ and Au ₂₅ /CeO ₂ during reaction can be found in Figure 5.25 and Figure 5.26, respectively.	116
5.10.	Electron microscopy images of the catalysts (1.2 wt% Au) after pretreatment and reaction at 250 °C: High-angle annular dark-field scanning transmission electron microscopy (HAADF-STEM) of Au ₁₁ /CeO ₂ (a) and Biico Au ₂₅ /CeO ₂ (b); transmission electron microscopy (TEM) image of Au ₂₅ /CeO ₂ (c). HAADF-STEM images of Biico Au ₂₅ /CeO ₂ and Au ₂₅ /CeO ₂ showing a larger sample area can be found in Figure 5.33.	118
5.11.	UV-Vis (a), ESI-MS (b) and ATR-FTIR (c) spectrum of Au ₁₁ (PPh ₃) ₇ Cl ₃ . . .	123
5.12.	UV-Vis (a), ESI-MS (b) and ATR-FTIR (c) spectrum of [Au ₂₅ (PPh ₃) ₁₀ (SC ₂ H ₄ Ph) ₅ Cl ₂]Cl ₂	124
5.13.	UV-Vis (a), MALDI-MS (b) and ATR-FTIR (c) spectrum of [Au ₂₅ (SC ₂ H ₄ Ph) ₁₈] ⁻ TOA ⁺	125
5.14.	Mass loss (solid line) and differential scanning calorimetric signal (dashed line) of Au ₁₁ (PPh) ₃ Cl ₃ at pretreatment conditions.	126
5.15.	Mass loss (solid line) and differential scanning calorimetric signal (dashed line) of [Au ₂₅ (PPh) ₁₀ (SC ₂ H ₄ Ph) ₅ Cl ₂]Cl ₂ at pretreatment conditions.	127
5.16.	Mass loss (solid line) and differential scanning calorimetric signal (dashed line) of [Au ₂₅ (SC ₂ H ₄ Ph) ₁₈]TOA at pretreatment conditions.	128
5.17.	Comparison of the catalytic activity of nanocluster catalysts (0.3 wt% Au loading, 15 mg catalyst) pretreated at (a) 150 °C, (b) 200 °C and (c) 300 °C. Note that the conversion scales differ by two orders of magnitude.	128
5.18.	CO conversion of the pure CeO ₂ (15 mg) pretreated at different temperatures.	129
5.19.	CO ₂ generation (a) and O ₂ consumption spectra (b) of the different catalysts during oxidative pretreatment up to 300 °C. Au content in catalyst: 1.2 wt% for all cluster catalysts. Spectra were normalized by the carrier gas signal to compensate for changes in pressure. Spectra are offset for better visibility. . .	130
5.20.	CO conversion during <i>operando</i> transmission IR studies: (a) per 10 mg catalyst pellet (Au content in catalyst: Au ₁₁ /CeO ₂ and Biico Au ₂₅ /CeO ₂ : 1.2 wt%, Au ₂₅ /CeO ₂ : 0.3 wt%) and (b) normalized to 0.3 wt% Au and 15 mg catalyst (cf. kinetic studies). Pretreatment at 250 °C at 5 % O ₂ in He.	131

- 5.21. Difference spectra of Au₁₁/CeO₂ during oxidative pretreatment: (a) 3800-2500 cm⁻¹ and (b) 2500-2000 cm⁻¹. Bands decreasing during the pretreatment are indicated by a light blue background color and marked at the bottom, increasing ones by a light red one and marked on top. Assigned species are indicated by abbreviations: f = formates, hc = hydrogen carbonates, bc/tc = bidentate/tridentate carbonates, lig = ligands. The spectrum of the as-prepared catalyst in He at RT was used as background. Au content in catalyst: 1.2 wt%. 131
- 5.22. Difference spectra of Biico Au₂₅/CeO₂ during oxidative pretreatment: (a) 3800-2500 cm⁻¹ and (b) 2500-2000 cm⁻¹. Bands decreasing during the pretreatment are indicated by a light blue background color and marked at the bottom, increasing ones by a light red one and marked on top. Assigned species are indicated by abbreviations: f = formates, hc = hydrogen carbonates, bc/tc = bidentate/tridentate carbonates, lig = ligands. The spectrum of the as-prepared catalyst in He at RT was used as background. Au content in catalyst: 1.2 wt%. 132
- 5.23. Difference spectra of Au₂₅/CeO₂ during oxidative pretreatment: (a) 3800-2500 cm⁻¹ and (b) 2500-2000 cm⁻¹. Bands decreasing during the pretreatment are indicated by a light blue background color and marked at the bottom, increasing ones by a light red one and marked on top. Assigned species are indicated by abbreviations: f = formates, hc = hydrogen carbonates, bc/tc = bidentate/tridentate carbonates, lig = ligands. The spectrum of the as-prepared catalyst in He at RT was used as background. Au content in catalyst: 0.3 wt%. 132
- 5.24. Difference spectra of the CeO₂ support during oxidative pretreatment: (a) 3800-2500 cm⁻¹, (b) 2500-2000 cm⁻¹ and (c) 1800-900 cm⁻¹. Bands decreasing during the pretreatment are indicated by a light blue background color and marked at the bottom, increasing ones by a light red one and marked on top. Assigned species are indicated by abbreviations: f = formates, hc = hydrogen carbonates, bc/tc = bidentate/tridentate carbonates. The spectrum of CeO₂ in He at RT was used as background. 133
- 5.25. Difference spectra of Biico Au₂₅/CeO₂ during CO oxidation: (a) 3800-2500 cm⁻¹, (b) 2500-2000 cm⁻¹ and (c) 1800-900 cm⁻¹. Bands decreasing during the pretreatment are indicated by a light blue background color and marked at the bottom, increasing ones by a light red one and marked on top. Bands decreasing during reaction but restored upon cool down are indicated by a grey shaded background. Assigned species are indicated by abbreviations: f = formates, hc = hydrogen carbonates, bc/tc = bidentate/tridentate carbonates. The spectrum of the pretreated catalyst after the CO adsorption experiment in He at RT was used as background. Au content in catalyst: 1.2 wt%. 133

5.26.	Difference spectra of Au ₂₅ /CeO ₂ during CO oxidation: (a) 3800-2500 cm ⁻¹ , (b) 2500-2000 cm ⁻¹ and (c) 1800-900 cm ⁻¹ . Bands decreasing during the pretreatment are indicated by a light blue background color and marked at the bottom, increasing ones by a light red one and marked on top. Bands decreasing during reaction but restored upon cool down are indicated by a grey shaded background. Assigned species are indicated by abbreviations: f = formates, hc = hydrogen carbonates, bc/tc = bidentate/tridentate carbonates. The spectrum of the pretreated catalyst after the CO adsorption experiment in He at RT was used as background. Au content in catalyst: 0.3 wt%.	134
5.27.	Difference spectra of the CeO ₂ support during CO oxidation: (a) 3800-2500 cm ⁻¹ , (b) 2500-2000 cm ⁻¹ and (c) 1800-900 cm ⁻¹ . Bands decreasing during the pretreatment are indicated by a light blue background color and marked at the bottom, increasing ones by a light red one and marked on top. Assigned species are indicated by abbreviations: f = formates, hc = hydrogen carbonates, bc/tc = bidentate/tridentate carbonates. The spectrum of CeO ₂ after pretreatment and the adsorption experiment in He at RT was used as background.	134
5.28.	Transmission infrared spectra of room temperature CO adsorption on the used catalysts (250 °C pretreatment and reaction) : (a) Au ₁₁ /CeO ₂ (b) Biico Au ₂₅ /CeO ₂ , (c) Au ₂₅ /CeO ₂ and (d) CeO ₂ . The red spectra were obtained during exposure of the sample to an atmosphere of 1 % CO in He (50 ml/min total gas flow), the green spectra upon removal of gas phase CO by flowing 50 ml/min He. Au content in catalyst: Au ₁₁ /CeO ₂ and Biico Au ₂₅ /CeO ₂ : 1.2 wt%, Au ₂₅ /CeO ₂ : 0.3 wt%.	135
5.29.	Comparison of infrared absorption spectra of Au ₁₁ /CeO ₂ in He at room temperature at different steps of the catalytic process: (a) 3800-3500 cm ⁻¹ , (b) 3200-2000 cm ⁻¹ and (c) 1800-900 cm ⁻¹ . Decreasing bands are indicated by dotted lines and marked on the bottom, increasing ones by solid lines and marked on top. Au content in catalyst: 1.2 wt%.	135
5.30.	Comparison of infrared absorption spectra of Biico Au ₂₅ /CeO ₂ in He at room temperature at different steps of the catalytic process: (a) 3800-3500 cm ⁻¹ , (b) 3200-2000 cm ⁻¹ and (c) 1800-900 cm ⁻¹ . Decreasing bands are indicated by dotted lines and marked on the bottom, increasing ones by solid lines and marked on top. Au content in catalyst: 1.2 wt%.	136
5.31.	Comparison of infrared absorption spectra of Au ₂₅ /CeO ₂ in He at room temperature at different steps of the catalytic process: (a) 3800-3500 cm ⁻¹ , (b) 3200-2000 cm ⁻¹ and (c) 1800-900 cm ⁻¹ . Decreasing bands are indicated by dotted lines and marked on the bottom, increasing ones by solid lines and marked on top. Au content in catalyst: 0.3 wt%.	136

5.32. Comparison of infrared absorption spectra of the CeO ₂ support in He at room temperature at different steps of the catalytic process: (a) 3800-3500 cm ⁻¹ , (b) 3200-2000 cm ⁻¹ and (c) 1800-900 cm ⁻¹ . Decreasing bands are indicated by solid lines and marked on the bottom, increasing ones by solid lines and marked on top.	137
5.33. Overview HAADF-STEM images of Biico Au ₂₅ /CeO ₂ (a) and Au ₂₅ /CeO ₂ (b) after pretreatment and reaction at 250 °C. Au content in catalyst: 1.2 wt%. .	137

List of Tables

3.1. Relative energies of the lowest energy structures of each subcategory. A = anti-clockwise and C = clockwise staple rotation. Isomers 1 are crystal structure ^[15] based and isomers 2 were obtained starting from the calculated structure by Lopez-Acevedo <i>et al.</i> ^[23] The energies of all calculated isomers can be found in Table 3.2.	60
3.2. Relative energies of all calculated Au ₃₈ (2-MeBuS) ₂₄ isomers. A = anti-clockwise and C = clockwise staple rotation. Isomers 1 are crystal structure ^[15] based and isomers 2 were obtained starting from the calculated structure by Lopez-Acevedo <i>et al.</i> ^[23]	72
4.1. Instrument settings for the ESI-TOFMS analysis	93
4.2. Emission lifetimes of the nanocluster samples after excitation at 375 nm	98

PERSONAL INFORMATION



Dipl.-Ing. Vera Truttmann

Institute of Materials Chemistry, TU Wien

📍 Getreidemarkt 9/E165, 1060 Vienna, Austria

☎ +43-1-58801-165149

✉ vera.truttmann@gmail.com

Date of Birth 01/05/1993 Innsbruck, Austria | **Nationality** Austria

EDUCATION AND TRAINING

- since 2018
Doctoral programme in Technical Sciences (Technical Chemistry)
 TU Wien, Austria
Supervisor: Prof. Günther Rupprechter / *Co-Supervisor:* Dr. Noelia Barrabés
- 2021 (September to December)
Marshall Plan Fellow (part of PhD studies)
 Kansas State University, Department of Chemistry, Research Group of Prof. Christine M. Aikens
- 2019 (July) & 2018 (July)
Summer School “Solids4Fun Summer School”
 TU Wien, Waidhofen an der Ybbs
- 2015 - 2017
Master's programme Technical Chemistry
 TU Wien, Austria
Dipl.-Ing. Technical Chemistry, with distinction (equivalent to MSc.)
- 2017 (September)
Summer School “3rd G-NMR School”
 Leibniz-Forschungsinstitut für Molekulare Pharmakologie, Berlin
- 2017 (May/June)
Short-term scientific work abroad (part of the Master's Thesis)
 University of Geneva, Department of Physical Chemistry, Research Group of Prof. Thomas Bürgi
- 2016 (August/September)
Summer School “Fundamentals and Trends in Microelectronics”
 TU Wien & Infineon Technologies Austria AG
- 2016 (January to May)
ERASMUS European Exchange Programme (Chemistry)
 Trinity College Dublin, Ireland
- 2011 - 2015
Bachelor's programme Technical Chemistry
 TU Wien, Austria
BSc. in Technical Chemistry, with distinction
- 2003 - 2011
Secondary School
 Bundesgymnasium Geringergasse, Vienna, Austria
Matura, with distinction (equivalent to British A-levels)

CAREER HISTORY

- since 2018 (February)
University Assistant
 TU Wien, Institute of Materials Chemistry, Research Group of Prof. Günther Rupprechter
- 2015 (March to July)
& 2014 (March to July)
Tutor
 TU Wien, Institute of Chemical Technologies and Analytics

- 2014 (August/September) & 2013 (July) [Internship](#)
TU Wien, Institute of Chemical Technologies and Analytics, Research Group of Prof. Bernhard Lendl
- 2011 (September) [Internship](#)
Bio Forschung Austria
- 2011 (August) [Internship](#)
Institute for Higher Studies, Austria, Research Group of Dr. Erich Griessler
- 2010 (August) [Internship](#)
University of Vienna, Department of Structural and Computational Biology, Research Group of Prof. Kristina Djinovic-Carugo

SCHOLARSHIPS AND AWARDS

- 2020 [Scholarship](#) "Marshall Plan Scholarship", Austrian Marshall Plan Foundation (3-month stay at Kansas State University, USA – Sept.-Dec. 2021)
- 2018 [Award](#) "Diplomarbeitspreis", City of Vienna (Master's Thesis Award)
- 2018 [Award](#) "Förderungspreis", Austrian Chemical Society (GÖCH) (Master's Thesis Award)
- 2018 [Second Place](#) EFCATS Young Generation Catalysis Contest
- 2017 [Förderungsstipendium](#), TU Wien
- 2017 [Travel Grant](#) "Kurzfristige Wissenschaftliche Arbeiten im Ausland", TU Wien (stay at the University of Geneva, CH)
- 2016 [ERASMUS Scholarship](#) (stay at Trinity College Dublin, IRE)
- 2014 & 2016 [Merit Scholarship](#), TU Wien
- 2011 [Award](#) "Best Experimental Work", Austrian Chemical Society (GÖCH) (Award for Fachbereichsarbeit (Matura Thesis))
- 2011 [Award](#) "Dr. Hans Riegel-Fachpreis" (3rd place), University of Vienna and Gemeinnützige Privatstiftung Kaiserschild (Award for Fachbereichsarbeit (Matura Thesis))

TEACHING ACTIVITIES

- 2019–2021 Laboratory Course "Chemical Synthesis"
2018–2020 Laboratory Course "Physical Chemistry"
co-supervision of (under)graduate students (3 interns, 3 Bachelor & 2 Master students)

ADDITIONAL INFORMATION

- Languages German (Mother Tongue), English (Fluent), French (Intermediate)
- Scientific (Chemistry) Chemical Synthesis, (*In situ*) Spectroscopy (IR, UV-Vis, NMR, synchrotron XAFS, CD), Metal Nanocluster Chemistry, Catalysis, Chromatography (GC, HPLC, SEC)
- Computer Skills OriginLab, LaTeX, MS Office, Inkscape, basic programming skills in Python
- Volunteerism Mentor for First-year Students (TU Wien, 2017/18)

PROFESSIONAL AFFILIATIONS AND MEMBERSHIPS

- Membership Austrian Chemical Society (GÖCH)
- Board Member Association of Friends of the Austrian Chemistry Olympiad (VFÖC)
- Team Member Young European Catalysis Network (Team Members & Networking)
- Team Member FemChem TU Wien (Team Communication & Information)

RESEARCH ACHIEVEMENTS (see *Publication List*)

9 publications in refereed international journals and 2 submitted; 10 oral and 9 poster contributions

LIST OF PUBLICATIONS Dipl.-Ing. Vera Truttmann

To be Submitted

V. Truttmann, D. Suzuki, M. Stöger-Pollach, H. Drexler, Y. Negishi, N. Barrabés*, G. Rupprechter
 “Ligand Effect on the CO Oxidation Activity of CeO₂ Supported Gold Nanocluster Catalysts”

Submitted

V. Truttmann, A. Loxha, R. Banu, E. Pittenauer, N. Barrabés*
 “Chirality driven synthesis of intrinsically chiral cluster structures in high yield”

I. López-Hernández, V. Truttmann, N. Barrabés*, G. Rupprechter, J. Mengual, F. Rey and A. E. Palomares*
 “Gold Nanoclusters Supported on Different Materials as Catalysts for the Selective Alkyne Semihydrogenation”

Published

I. López-Hernández, V. Truttmann, C. García, C. W. Lopes, C. Rameshan, M. Stöger-Pollach, N. Barrabés*, G. Rupprechter, F. Rey, A. E. Palomares*
 “AgAu Nanoclusters Supported on Zeolites: Structural Dynamics During CO Oxidation”
Catalysis Today **2022**, 3984-386, pp 166-176
 doi: 10.1016/j.cattod.2021.04.016

V. Truttmann, S. Pollitt, H. Drexler, S. P. Nandan, D. Eder, N. Barrabés*, G. Rupprechter
 “Selective Ligand Exchange Synthesis of Au₁₆(2-PET)₁₄ from Au₁₅(SG)₁₃”
Journal of Chemical Physics **2021**, 155, 161102
 doi: 10.1063/5.0062534

C. García[‡], V. Truttmann[‡], I. López-Hernández, T. Haunold, C. Marini, C. Rameshan, E. Pittenauer, P. Kregsamer, K. Dobrezberger, M. Stöger-Pollach, N. Barrabés*, G. Rupprechter
 “Dynamics of Pd Dopant Atoms inside Au Nanoclusters during Catalytic CO Oxidation”
Journal of Physical Chemistry C **2020**, 124(43), pp 23626–23636
 doi: 10.1021/acs.jpcc.0c05735

S. Pollitt, V. Truttmann, T. Haunold, C. García, W. Olszewski, J. Llorca, N. Barrabés*, G. Rupprechter
 “The Dynamic Structure of Au₃₈(SR)₂₄ Nanoclusters Supported on CeO₂ upon Pretreatment and CO Oxidation”
ACS Catalysis **2020**, 10(11), pp 6144–6148
 doi: 10.1021/acscatal.0c01621

V. Truttmann, C. Herzig, I. Illes, A. Limbeck, E. Pittenauer, M. Stöger-Pollach, G. Allmaier, T. Bürgi, N. Barrabés*, G. Rupprechter
 “Ligand Engineering with Immobilized Nanoclusters on Surfaces: Ligand Exchange Reactions with Supported Au₁₁(PPh₃)₇Br₃”
Nanoscale **2020**, 12(24), pp 12809–12816
 doi: 10.1039/C9NR10353H

I. López Hernández, C. García, V. Truttmann, S. Pollitt, N. Barrabés, G. Rupprechter, F. Rey, A.E. Palomares*
 “Evaluation of the Silver Species Nature in Ag-ITQ2 Zeolites by the CO Oxidation Reaction”
Catalysis Today **2020**, 45, pp 22–26
 doi: 10.1016/j.cattod.2019.12.001

C. García, S. Pollitt, M. van der Linden, V. Truttmann, C. Rameshan, R. Rameshan, E. Pittenauer, G. Allmaier, P. Kregsamer, M. Stöger-Pollach, N. Barrabés*, G. Rupprechter
 “Support Effect on the Reactivity and Stability of Au₂₅(SR)₁₈ and Au₁₄₄(SR)₆₀ Nanoclusters in Liquid Phase Cyclohexane Oxidation”
Catalysis Today **2019**, 336, pp 174–185
 doi: 10.1016/j.cattod.2018.12.013

B. Zhang, A. Sels, G. Salassa, S. Pollitt, V. Truttmann, C. Rameshan, J. Llorca, W. Olszewski, G. Rupprechter, T. Bürgi*, N. Barrabés*
 “Ligand Migration from Cluster to Support: A Crucial Factor for Catalysis by Thiolate Protected Gold Clusters”
ChemCatChem **2018**, 10(23), pp 5372–5376
 doi: 10.1002/cctc.201801474

S. Pollitt, E. Pittenauer, C. Rameshan, T. Schachinger, O. V. Safonova, V. Truttmann, A. Bera, G. Allmaier, N. Barrabés*, and G. Rupprechter
 “Synthesis and Properties of Monolayer-Protected $\text{Co}_x(\text{SC}_2\text{H}_4\text{Ph})_m$ Nanoclusters”
Journal of Physical Chemistry C **2017**, *121*(20), pp 10948–10956
 doi: 10.1021/acs.jpcc.6b12076

Conferences, Seminars and Workshops

Oral Communications

V. Truttmann, N. Barrabés* and G. Rupprechter (2021) – Online Talk
 “The ligand shapes the cluster: Influences and modification possibilities of protecting ligands on Au nanoclusters”.
 Institute of Materials Chemistry Seminar, 20/10

V. Truttmann (2021)
 “Dopant and ligand effects of Au nanoclusters: Modification possibilities and influence on heterogeneous catalysis”.
 Departmental Seminar of the Department of Chemistry, Kansas State University, 14/10, Manhattan, KS, USA

V. Truttmann, P. Hans, N. Barrabés* and G. Rupprechter (2020) – Online Talk
 “Ligand engineering as a tool for heterogeneous gold nanocluster catalyst design”. EFCATS Summer School, 15/09-19/09, Portorož-Portorose, Slovenia

V. Truttmann, N. Barrabés* and G. Rupprechter (2019)
 “Chiral Au Nanoclusters for Catalytic Applications”. 2nd FemChem Scientific Workshop, 24/10, Vienna, Austria

V. Truttmann, N. Barrabés* and G. Rupprechter (2019)
 “Atomically Designed Chiral Au Nanoclusters in Asymmetric Catalysis: First Steps Towards Heterogeneous Nanocluster Catalysts”. 14th European Congress on Catalysis (Europacat), 18/08-23/08, Aachen, Germany

V. Truttmann, N. Barrabés* and G. Rupprechter (2019)
 “Chiral Au Nanoclusters: Catalyst Design for Asymmetric Catalysis”. Solids4Fun Summer School, 01/07-05/07, Waidhofen an der Ybbs, Austria

V. Truttmann, N. Barrabés* and G. Rupprechter (2019)
 “Chiral Au Nanoclusters – A Step Towards Heterogeneous Asymmetric Catalysis”. 5th Vienna Young Scientist Symposium, 13/06-14/06, Vienna, Austria

V. Truttmann, N. Barrabés* and G. Rupprechter (2019)
 “Chiral Au Nanoclusters and Their Application in Asymmetric Catalysis”. 8th Annual SFB FOXSI PhD Workshop, 20/03-23/03, Haus im Ennstal, Austria

V. Truttmann, N. Barrabés*, T. Bürgi and G. Rupprechter (2018)
 “Modification of Au Nanoclusters Through Ligand Exchange”. 1st FemChem Scientific Workshop, 25/06, Vienna, Austria

V. Truttmann, N. Barrabés*, T. Bürgi and G. Rupprechter (2017)
 “Ligand Exchange Reaction Studies on Au Nanoclusters”. Institute of Materials Chemistry Seminar, 28/06, Vienna, Austria

Posters

V. Truttmann, P. Hans, N. Barrabés* and G. Rupprechter (2020)
 “Understanding heterogeneous Au nanocluster materials: Reactivity and structure stability of supported Au_{11} upon exposure to thiolates”. GRC Atomically Precise Nanochemistry, 09/02-14/02, Galveston, Texas, USA

V. Truttmann, N. Barrabés* and G. Rupprechter (2019)
 “Controlled Functionalization of Supported Au Nanoclusters by Ligand Exchange: Reactivity of Immobilized Au_{11} Nanoclusters with Thiolates”. 6th International Symposium on Monolayer Protected Clusters (ISMPC), 23/09-26/09, Xiamen, China

V. Truttmann, N. Barrabés* and G. Rupprechter (2019)

"Reactions of Supported Au₁₁ Nanoclusters with Thiolates". 34th Workshop on Novel Materials and Superconductors, 10/02-15/02, Schladming, Austria

V. Truttmann, N. Barrabés*, T. Bürgi and G. Rupprechter (2018)

"Ligand Exchange Reactions of Au₁₁ Nanoclusters on Surfaces". Solids4Fun Summer School, 02/07-06/07, Waidhofen an der Ybbs, Austria

V. Truttmann, N. Barrabés*, T. Bürgi and G. Rupprechter (2018)

"Functionalization of Supported Au₁₁ Nanoclusters Through Ligand Exchange and Comparison to Liquid Phase Reactions". 4th Vienna Young Scientist Symposium, 07/06-08/06, Vienna, Austria

V. Truttmann, N. Barrabés*, T. Bürgi and G. Rupprechter (2018)

"Ligand Exchange Reaction Studies of Au₁₁ Nanoclusters on Surfaces". 7th Annual SFB FOXSI PhD Workshop, 31/01-03/02, Haus im Ennstal, Austria

V. Truttmann, N. Barrabés*, T. Bürgi and G. Rupprechter (2017)

"Ligand Exchange Reactions on Au-Nanoclusters". 17th Austrian Chemistry Days, 25/09-28/09, Salzburg, Austria

V. Truttmann, N. Barrabés*, T. Bürgi and G. Rupprechter (2017)

"Ligand Exchange Reaction Studies on Supported Au Nanoclusters". 5th International Symposium on Monolayer Protected Clusters (ISMPC), 13/08-16/08, Monte Verità, Switzerland

V. Truttmann, N. Barrabés*, and G. Rupprechter (2017)

"Ligand Exchange Reactions of Au₂₅(SR)_m Nanoclusters on Surfaces". 6th Annual SFB FOXSI PhD Workshop, 01/02-04/02, Haus im Ennstal, Austria